

The Development of Nickel-based Heterogeneous Catalysts with Ultrasonic Irradiation for the Hydrogenation of Plant-based Feedstock

Mitchell Shyan Wei Lim

Department of Chemical and Environmental Engineering

A thesis submitted to the University of Nottingham in partial fulfilment of the requirements for the degree of Doctor of Philosophy.

July 2021

Abstract

Nickel-based heterogeneous catalysts are characterised by their widespread utilisation in the hydrogenation of fats and oleochemicals. Nevertheless, various aspects of the catalyst are still in continuous development and improvement. Therefore, bridging these knowledge gaps concerning the functionality of the catalyst motivated the investigations constituting this thesis.

This thesis pertains to a coherent study in relation to the life cycle of nickel-based heterogeneous catalysts as the central theme. Several aspects and problem statements concerning the development of the catalyst are raised and addressed: (i) What are the predominant deactivation modes of nickel-based catalysts in the hydrogenation of palm-based liquid organic media? (ii) What are the improvements that can be made to nickel-based catalysts, and if so, can the incorporation of innovative technologies such as power ultrasound into the synthesis of such catalysts be of significance? (iii) What are the effects imparted by different ultrasonic synthesis configurations on nickel-based catalyst composites? (iv) How can the recovery of nickel from spent hydrogenation catalysts be improved?

To address problem (i), the hydrogenation of various organic media using nickel-based catalysts was studied to ascertain the dominant deactivation modes of the catalyst. Nickel lixiviation with Ostwald ripening and poisoning were found to be the principal deactivation mechanisms affecting the catalytic performance in the hydrogenation of palm-based liquid organic media. Nickel lixiviation increased 7-fold and 8-fold during the hydrogenation of split-refined, bleached and

deodorised palm stearin (S-RBD-PS) when compared to that of refined, bleached and deodorised palm stearin (RBD-PS) at reaction temperatures of 195 and 210 °C, respectively. On the other hand, catalyst poisons such as S, P, Cl and N in the S-RBD-PS and RBD-PS feeds affected the catalytic activity negatively, as compared to the relatively clean distilled fatty acid blend feed.

To address problem (ii), silica-supported nickel catalysts were synthesised by introducing an alkaline metal dopant and ultrasonic irradiation. A Ni:Mg ratio of 3:1 showed the best catalyst properties, in which the catalyst was chosen for further studies by incorporating ultrasonic irradiation into its synthesis. Sonicated catalysts exhibited geometrical and electronic alterations, leading to improved reducibility, surface area and active site dispersion. The catalysts were evaluated for the partial hydrogenation of sunflower oil to ascertain their catalytic performance. At an ultrasonic intensity of 20.78 W cm^{-2}, the nickel catalyst achieved a 22.6 % increase in hydrogenation activity, along with a 28.5 % decrease in *trans*-C18:1 yield at IV = 70.

To address problem (iii), the synthesis of nickel-silica composites was performed with ultrasonic irradiation incorporated into two different stages of the synthesis: the co-precipitation stage or the support loading/ageing stage, which were characterised for discrepancies in their textural, structural, morphological, reduction and surface composition properties. It was determined that sonication during the co-precipitation stage resulted in composites with wide pores of Type II and IV(a) isotherms, rough morphology, enriched superficial Mg and Si contents and increased reducibility. On the other hand, composites synthesised with

sonication during silica loading/ageing had narrower pores of Type IV(a) isotherms, smooth morphology, decreased superficial Mg and Si contents and lowered reducibility. Ultimately, it was ascertained that the usage of ultrasound at different stages of the synthesis had profound impacts on the final properties of materials, establishing that the configuration of sono-syntheses also plays a significant role in influencing material characteristics, which is an important factor for future material scientists to consider when applying ultrasound for synthesis. It is also suggested that ultrasonic technology can be adopted to optimise and fine-tune the properties of nickel-silica composites for catalytic purposes.

To address problem (iv), acid leaching experiments were performed to assess the effectiveness of applying ultrasound irradiation in the recovery of nickel from spent catalysts. It was established that sonication expedited nickel recovery, allowing a 2 h time reduction in recovering ca. 70 % nickel. Besides, Ni recovery was more efficient when nitric acid was used as the leaching reagent compared to sulphuric acid, in which the former recovered ca. 20 % more nickel than the latter. Lastly, the process optimisation of nickel leaching via response surface methodology enabled a 99.37 % nickel recovery in 2 h.

List of Publications

Refereed journals:

- Lim, M.S.W., Yang, T.C.K., Tiong, T.J., Pan, G.T., Chong, S., Yap, Y.H. 2021. **Ultrasound-assisted sequentially precipitated nickel-silica catalysts and its application in the partial hydrogenation of edible oil**, *Ultrasonics Sonochemistry*, *73*, 105490. 10.1016/j.ultsonch.2021.105490
- Lim, M.S.W., Yang, T.C.K., Yap, Y.H., Pan, G.T., Chong, S., Tiong, T.J., 2021. **Intensification and optimisation of nickel recovery from spent hydrogenation catalysts via ultrasound-augmented hydrometallurgy**, *Journal of Environmental Chemical Engineering*, *9*(4), 105771. 10.1016/j.jece.2021.105771
- Chu, J.K., Lim, M.S.W., Tiong, T.J., Yap, Y.H., Lim, L.Y., Yeoh, P.S.J., et al., 2019. **One-pot co-precipitation of copper-manganese-zinc oxide catalysts for the oxidation of CO and SO_2 in the presence of ultrasonic irradiation**, *Research in Chemical Intermediates*, *45*, 6003-6019. 10.1007/s11164-019-04016-7
- Yap, Y.H., Lim, M.S.W., Lee, Z.Y., Lai K.C., Jamaal, M.A., Wong, F.H., et al., 2018. **Effects of sonication on co-precipitation synthesis and activity of copper manganese oxide catalyst to remove methane and sulphur dioxide gases**, *Ultrasonics Sonochemistry*, *40* (Part A), 57-67. 10.1016/j.ultsonch.2017.06.032

Under review/In preparation:

- Lim, M.S.W., Yang, T.C.K., Yap, Y.H., Pan, G.T., Chong, S., Tiong, T.J. **Textural, morphological, compositional and reduction properties of mesoporous nickel-silica composites synthesised at varied ultrasonic configurations**.
- Lim, M.S.W., Yang, T.C.K., Tiong, T.J., Asli, U.A., Yap, Y.H. **Deactivation of nickel catalysts during the hydrogenation of organic liquid media: Extent of leaching and poisoning in palm-based feedstock.**

Awards:

- Three Minute Thesis® Competition, University of Nottingham Malaysia. Overall winner and People's Choice award (June 2019)
- Postgraduate 1-Min-Rapid-Fire Competition, University of Nottingham Malaysia Faculty of Science & Engineering (FOSE) Postgraduate Research Showcase.

  Grand prize (September 2019)

Acknowledgements

First and foremost, I'd like to express my sincerest gratitude towards my supervisors – Dr Tiong Timm Joyce and Dr Yap Yeow Hong. I am indebted to them for their unfaltering support, mentorship, guidance, insights, encouragement, opportunities and advice throughout the years. One simply could not wish for better, friendlier and more amazing supervisors and I truly am grateful for them. I'd also like to thank my lovely co-supervisor Dr Lim Siew Shee for her input and support on my work.

My special thanks to Prof Thomas Yang Chung-Kuang, Dr Faye Chong and Dr Pan Guan-Ting for granting me the opportunity to partake in the Visiting Researcher Programme to the National Taipei University of Technology. I am extremely grateful for the kind and friendly people I have met there who made my stay in Taipei pleasant, memorable and fulfilling.

I am also thankful and grateful towards all the laboratory and administration officers for their time and assistance in various technicalities. My special thanks to Mr Ng for believing and investing in this project.

Finally, I'd like to extend my deepest appreciation to my loving parents and family members for the immense support and encouragement they have given me all this while, through thick and thin. Words can never express how grateful and loved I am to have their unwavering support and blessings in pursuing my academic goals. My special thanks to my brother-in-law, Dr Alim Impira for his invaluable insights and motivation throughout my PhD studies.

Table of Contents

Abstract ..... *ii*

List of Publications ..... *v*

Acknowledgements ..... *vii*

Table of Contents ..... *viii*

List of Tables ..... *xiii*

List of Figures ..... *xv*

List of Notations and Abbreviations ..... *xxi*

1. Introduction and Background *1*

1.1. Catalysts and catalysis **1**

1.1.1. Catalysis: A historical perspective 1

1.1.2. Principles of catalysis 2

1.2. Catalyst classifications **6**

1.2.1. Homogeneous catalysis 6

1.2.2. Heterogeneous catalysis 7

1.2.3. Synthesis of unsupported catalysts 13

1.2.4. Synthesis of supported catalysts 15

1.3. Catalytic activity of heterogeneous catalysts **16**

1.4. Nickel as a heterogeneous catalyst **17**

1.4.1. Nickel catalysts: Hydrogenation of fats and oils 19

1.4.2. Deactivation of nickel catalysts 23

1.5. Ultrasound in chemistry **29**

1.5.1. The sound wave and the ultrasound wave 29

1.5.2. Applications of ultrasound/sonochemistry....33
1.5.3. Ultrasound in catalysis....34
1.6. Ultrasound for nickel catalysts....42
1.7. Recovery of nickel from spent catalyst....44
1.8. Project rationale....46
1.9. Research aim and objectives....48
1.10. Thesis overview....49
2. Materials and Methodology....50
2.1. Introduction....50
2.2. Ultrasonic equipment....50
2.2.1. Calorimetry....52
2.3. Materials....56
2.4. Analytical techniques....57
2.4.1. Field emission scanning electron microscopy (FE-SEM)....57
2.4.2. Energy dispersive X-ray (EDX) analysis....57
2.4.3. X-ray powder diffraction (XRD)....58
2.4.4. Fourier transform infrared spectroscopy (FT-IR)....59
2.4.5. Brunauer-Emmett-Teller (BET) analysis....59
2.4.6. Temperature programmed reduction (H_2-TPR)....59
2.4.7. Hydrogen pulse chemisorption....60
2.4.8. X-ray photoelectron spectroscopy (XPS)....62
2.4.9. Atomic absorption spectrometry (AAS)....62
2.4.10. Thermogravimetric analysis (TGA)....63
2.5. Product analysis....63
2.5.1. Determination of iodine value (IV)....63
2.5.2. Gas chromatography (GC) analysis....64

3. Deactivation of Nickel Catalysts in Liquid Organic Media.....65

3.1. Introduction..... 65

3.2. Experimental..... 69

3.2.1. Partial hydrogenation of palm-based liquid organic media.....69

3.2.2. Catalyst characterisation and product analyses.....70

3.3. Results and discussion 71

3.3.1. Catalytic hydrogenation and leaching studies.....71

3.3.2. Catalytic poisoning studies.....85

3.3.3. Coking studies.....88

3.4. Concluding remarks..... 92

4. Synthesis and Characterisation of Silica-supported Nickel Catalysts 94

4.1. Introduction..... 94

4.2. Experimental..... 99

4.2.1. Sample synthesis.....99

4.3. Results and discussion 102

4.3.1. Ultrasonic probe calorimetry.....102

4.3.2. Effects of incorporating Mg as a catalyst promoter during catalyst synthesis 102

4.3.3. Effects of ultrasound irradiation during catalyst synthesis.....122

4.4. Concluding remarks.....145

5. Catalytic Performance of Nickel-silica catalysts in the Partial Hydrogenation of Sunflower Oil.....148

5.1. Introduction.....148

5.2. Experimental.....150

5.2.1. Catalyst reduction 151
5.2.2. Partial hydrogenation 151
5.3. Results and discussion 152
5.3.1. Hydrogenation activity 152
5.3.2. Hydrogenation selectivity and product distribution 156
5.4. Concluding remarks 164
6. Characterisation of Nickel-silica Composites Synthesised via Varied Ultrasonic Configurations 167
6.1. Introduction 167
6.2. Experimental 170
6.2.1. Sample synthesis 170
6.3. Results and discussion 172
6.3.1. Textural and structural characterisation 172
6.3.2. Morphological characterisation 185
6.3.3. Composition and surface properties characterisation 187
6.3.4. Reducibility and active site characterisation 201
6.3.5. Summary of the effects of ultrasonic irradiation on the mechanisms of composite formation 210
6.4. Concluding remarks 216
7. Recovery of Nickel from Spent Catalysts via Ultrasound-assisted Hydrometallurgy 218
7.1. Introduction 218
7.2. Experimental 222
7.2.1. Pre-treatment of spent catalysts 222
7.2.2. Acid leaching under conventional mechanical stirring 222
7.2.3. Acid leaching under ultrasonic irradiation 223

7.2.4. Sample characterisation....223

7.3. Results and discussion....228

7.3.1. Pre-treatment of spent catalysts....228

7.3.2. Ultrasonic bath calorimetry....229

7.3.3. Comparison of ultrasonic and conventional mechanical stirring techniques for nickel leaching from spent catalysts....230

7.3.4. Effects of temperature on leaching....236

7.3.5. Effects of ultrasonic amplitudes on leaching....238

7.3.6. Comparison of nitric acid and sulphuric acid for nickel leaching from spent catalyst 241

7.3.7. Characterisation of spent catalyst and leach residues....245

7.3.8. Model validation and statistical analysis....250

7.3.9. Response surface analysis plots and leaching optimisation....255

7.3.10. Leaching kinetics study....259

7.3.11. Process analysis....263

7.4. Concluding remarks....265

8. Conclusions and Recommendations for Future Work....268

8.1. Conclusions....268

8.2. Recommendations for future work....271

Bibliography....273

Appendices....322

I. Iodine value (IV) test....322

II. Gas chromatography....324

III. Deconvoluted TPR graphs....326

List of Tables

Table 1.1: Various general characteristics of homogeneous catalysis/catalysts and heterogeneous catalysis/catalysts. 11

Table 1.2: Mechanisms of catalyst deactivation. 24

Table 1.3: Summary of various catalysts synthesised with the assistance of ultrasonic irradiation obtained from the literature. 36

Table 3.1: Concentration of catalyst poisons present in the organic feeds. 85

Table 4.1: Synthesis parameters of the catalysts involved. 100

Table 4.2: Ultrasonic power output, intensity and density acquired for the 20 kHz ultrasonic probe 102

Table 4.3: Elemental compositions and crystallite sizes for the catalysts prepared under different conditions 112

Table 4.4: Results obtained from BET analysis performed on the catalysts. 115

Table 4.5: Hydrogen pulse chemisorption results obtained for the catalysts. 120

Table 4.6: Elemental composition of the catalysts obtained from EDX and XPS. 127

Table 4.7: Molar ratio of the catalysts calculated using the EDX and XPS data ... 128

Table 4.8: H_2-TPR and H_2-pulse chemisorption results for the catalysts. 135

Table 4.9: XPS analysis results for the calcined catalysts. 137

Table 4.10: Textural properties of calcined catalysts from N_2 physisorption. 144

Table 5.1: Fatty acid composition of the sunflower oil used in this study. 150

Table 5.2: Yield and selectivity of catalysts for the sunflower oil hydrogenation reaction. 159

Table 5.3: Comparison of the present work to other studies in the literature 164

Table 6.1: Structural properties of the synthesised samples. 177

Table 6.2: Sample compositions obtained from EDX and XPS. 189

Table 6.3: Summary of the observed change in elemental atomic ratios with increasing ultrasonic intensity. 191

Table 6.4: Results for the XPS analysis of samples A – G. 199

Table 6.5: Further insight into the reduction properties of the samples and results for the H_2-pulse chemisorption analysis. 205

Table 6.6: Summary of composite properties as a result of the mechanisms involved in the synthesis of the composite. 214

Table 7.1: Experimental factors at different levels for the ultrasonic leaching and recovery of Ni from spent catalysts for 2 h. 226

Table 7.2: Experimental plan based on CCD and the results of nickel recovery. 227

Table 7.3: Ultrasonic densities acquired for the ultrasonic bath operating at different amplitudes. 229

Table 7.4: ANOVA results for the model developed for the ultrasonic leaching of Ni from spent catalysts. 255

Table 7.5: Optimisation of leaching parameters and results from model validation. 259

Table 7.6: Comparison of Ni recoveries of this present work with relevant investigations from the literature. 263

Table 7.7: Economic analysis for recycling 1 kg of spent Ni hydrogenation catalysts. 265

List of Figures

Figure 1.1: Reaction coordinates for catalysed and uncatalysed reactions. 5

Figure 1.2: Illustration of a typical catalytic reaction cycle. 6

Figure 1.3: Key events occurring during a heterogeneous catalytic cycle. 8

Figure 1.4: Typical process pathway of the processing of crude palm oil and its derivatives 28

Figure 1.5: Graphical summary of the event of bubble formation, growth and collapse over several acoustic cycles. 30

Figure 1.6: General applications involving ultrasound. 34

Figure 1.7: Flowchart of the overview of the entire thesis. 49

Figure 2.1: Schematic diagram of the 20 kHz ultrasound probe setup. 51

Figure 2.2: Schematic diagram of the 35 kHz ultrasonic bath setup. 52

Figure 3.1: Flowchart of a typical oleochemical fatty acid processing plant. 69

Figure 3.2: Change of IV with reaction time for the hydrogenation of RBD-PS at 195 and 210 °C. 72

Figure 3.3: Change of IV with reaction time for the hydrogenation of S-RBD-PS at 195 and 210 °C. 73

Figure 3.4: (a) Reaction scheme of Ni leaching to form Ni soap; (b) Molecular structure of glyceryl tripalmitate present in RBD-PS 75

Figure 3.5: Concentration of leached Ni present in the hydrogenation products at different time intervals. Standard deviation represents variation of data obtained from repeating measurements three times. 76

Figure 3.6: Concentration of dissolved Ni present in the hydrogenation products of citral and benzyl alcohol at different time intervals. 79

Figure 3.7: TEM images of the (A) fresh catalyst; (B) spent catalyst from the hydrogenation of RBD-PS at 195 °C; and (C) spent catalyst from the hydrogenation of S-RBD-PS at 195 °C. 81

Figure 3.8: Crystallite size distribution of (A) fresh nickel catalysts and spent nickel catalysts recovered from hydrogenating (B) RBD-PS and (C) S-RBD-PS at 195 °C. 82

Figure 3.9: Schematic flow diagram of Ni lixiviation followed by the redeposition of Ni onto the catalyst particles via Ostwald ripening. 83

Figure 3.10: Change of IV with reaction time for the hydrogenation of the distilled fatty acid blend at 195 and 210 °C. 87

Figure 3.11: TGA and DTG curves of the spent nickel catalysts used for the hydrogenation of S-RBD-PS. 89

Figure 3.12: TGA and DTG curves of the spent nickel catalysts used for the hydrogenation of RBD-PS. 89

Figure 3.13: FT-IR spectrum of the spent nickel catalysts used for the hydrogenation of (a) S-RBD-PS and (b) RBD-PS. 91

Figure 4.1: Schematic flow chart for the synthesis of catalysts A – E. 100

Figure 4.2: Schematic flow chart for the synthesis of catalysts D_US20, D_US30 and D_US40.....101

Figure 4.3: XRD diffractograms of the catalysts with their respective identified compounds, where samples A, B, C, D and E correspond to the Ni:Mg:Si ratio of 0:4:1, 1:3:1, 2:2:1, 3:1:1 and 4:0:1, respectively. 104

Figure 4.4: XRD diffractograms of (A) pure NiO sample; and (B) pure Ni sample. 107

Figure 4.5: FT-IR spectrum for the catalysts, where samples A, B, C, D and E correspond to the Ni:Mg:Si ratio of 0:4:1, 1:3:1, 2:2:1, 3:1:1 and 4:0:1, respectively. 108

Figure 4.6: Nitrogen isotherms obtained for catalysts A – E. 113

Figure 4.7: Pore size distributions obtained for the catalysts. 115

Figure 4.8: TPR profiles at temperatures 30 – 1000 °C obtained for the catalysts. 117

Figure 4.9: SEM scans for catalysts (A) D; (B) D_US20; (C) D_US30; and (D) D_US40. 124

Figure 4.10: Conceptualisation of the formation of the nickel-silica porous network during the ultrasound-assisted synthesis of the catalysts. 127

Figure 4.11: XRD diffractograms of catalysts (A) D; (B) D_US20; (C) D_US30; and (D) D_US40 and their respective identified compounds. 131

Figure 4.12: TPR profiles at temperatures 30 – 900 °C obtained for catalysts (A) D; (B) D_US20; (C) D_US30; and (D) D_US40. 132

Figure 4.13: Ni $2p_{3/2}$ XPS spectra fitting for catalysts (a) D; (b) D_US20; (c) D_US30; and (d) D_US40 137

Figure 4.14: State of the nickel-silica network/particles upon first 10 min of ageing with and without ultrasonic irradiation. 141

Figure 4.15: Nitrogen isotherms obtained for catalysts (a) D; (b) D_US20; (c) D_US30; and (d) D_US40. 142

Figure 4.16: Pore size distributions obtained for catalysts (A) D; (B) D_US20; (C) D_US30; and (D) D_US40. 145

Figure 5.1: General reaction pathway for the hydrogenation of oils from linolenic acid (C18:3) to stearic acid (C18:0). 153

Figure 5.2: Change of iodine value (IV) over time using different catalysts over the course of partial hydrogenation using sunflower oil 155

Figure 5.3: Evolution of fatty acid compositions with the iodine value (IV) during the partial hydrogenation reaction using catalysts (A) D; (B) D_US20; (C) D_US30; and (D) D_US40. 157

Figure 5.4: Percentage of trans fatty acids and saturated fatty acids formed at IV = 70 for catalysts (A) D; (B) D_US20; (C) D_US30; and (D) D_US40. 160

Figure 6.1: Schematic flow chart for the synthesis of samples A – G. 172

Figure 6.2: BET isotherms obtained for the samples via N_2 physisorption. 174

Figure 6.3: Pore size distribution plots for samples B – D with sample A as a reference 175

Figure 6.4: Pore size distribution plots for samples E – G with sample A as a reference 176

Figure 6.5: XRD diffractograms for samples A – G. 181

Figure 6.6: FT-IR spectra of samples A – G. 184

Figure 6.7: SEM images for samples A – G 187

Figure 6.8: Ni $2p_{3/2}$ XPS spectra fitting for samples A – G. 197

Figure 6.9: Reduction profiles obtained for the samples A – G via H_2-TPR. 202

Figure 6.10: Mechanisms of nickel-silica composite formation at varied synthesis configurations for (A) Sample A; (B) Samples B – D; and (C) Sample E – G. 211

Figure 7.1: Thermogravimetric analysis (TGA) performed on spent catalysts, in flowing air. 228

Figure 7.2: Effect of mechanical stirring speed on the recovery on nickel recovery via nitric acid leaching. 231

Figure 7.3: Effect of time on nickel recovery via ultrasound-assisted nitric acid leaching (Ultrasonic density = 0.00825 W cm^{-3}, 70 °C) and conventional mechanical stirring nitric acid leaching (500 rpm, 70 °C). 232

Figure 7.4: Schematic diagram of cavitation events near the surface of spent catalyst particle.....234

Figure 7.5: Effect of temperature on nickel recovery via ultrasound-assisted nitric acid leaching and conventional mechanical stirring nitric acid leaching (Ultrasonic density = 0.0825 W cm^{-3}).....237

Figure 7.6: Effect of ultrasonic amplitude on nickel recovery via ultrasound-assisted nitric acid leaching with conventional mechanical stirring (500 rpm) nitric acid leaching as a reference (Temperature = 70 °C).....239

Figure 7.7: Percentage recovery of nickel via ultrasound-assisted leaching (ultrasonic density = 0.0825 W cm^{-3}) and conventional mechanical stirring leaching (500 rpm) with nitric acid and sulphuric acid as the leaching reagents. 242

Figure 7.8: XRD diffractograms for (a) spent catalyst; (b) ultrasonic leaching residue at US density = 0.0825 W cm^{-3}; and (c) conventional leaching residue, with their corresponding compounds at specific peaks.....246

Figure 7.9: FT-IR spectra of (a) spent catalyst; (b) ultrasonic leaching residue at US density = 0.0825 W cm^{-3} and (c) conventional leaching.....249

Figure 7.10: SEM images for (A) spent catalyst; (B) ultrasonic leaching residue at US density = 0.0825 W cm^{-3}; and (C) conventional leaching residue. 250

Figure 7.11: Diagnostic plots obtained from Design Expert: (a) predicted vs. actual Ni recovery; (b) internally studentised graph; (c) internally studentised outlier t plot; (d) studentised residuals and predicted response plot. 252

Figure 7.12: Combined effects of (a) ultrasonic amplitude and temperature (acid concentration 10 vol%, pulp density 10 %); (b) ultrasonic amplitude and acid concentration (temperature 50 °C, pulp density 10 %); (c) ultrasonic amplitude and pulp density (temperature 50 °C, acid concentration 10 vol%); (d) temperature and acid concentration (ultrasonic amplitude 60 %, pulp density 10 %); (e) temperature and pulp density (ultrasonic amplitude 60 %, acid

concentration 10 vol%); and (f) acid concentration and pulp density (ultrasonic amplitude 60 %, temperature 50 °C) on the Ni percentage recovery. 256

Figure 7.13: Shrinking core model with (a) diffusion control and (b) reaction control.....261

List of Notations and Abbreviations

Symbol	Definition	Unit
ΔG	Change in Gibbs free energy	kJ mol^{-1}
R	Gas constant	J K^{-1} mol^{-1}
T	Temperature	°C or K
ΔH	Change in enthalpy	J
S	Entropy	J K^{-1} mol^{-1}
t	Time	s
K	Equilibrium constant	Dimensionless
IV	Iodine value	Dimensionless
I	Intensity	W cm^{-2}
p/p°	Relative pressure	Dimensionless
D_{Ni}	Dispersion of nickel	%
SA_{Ni}	Metallic surface area of nickel	m^2 g_{Ni}^{-1}
Q	Total heat generated	J
m	Mass	kg
C_p	Heat capacity	J kg^{-1} K^{-1}
ΔT	Change in temperature	°C or K
Δt	Change in time	s
λ	Wavelength	m
A	Absorbance	Dimensionless
β	Full width at half maximum	rad
θ	Bragg's diffraction angle	°
V_m	Volume of hydrogen gas chemisorbed	cm^3 g^{-1} STP
V_{mol}	Molar volume of the adsorptive	cm^3 $mole^{-1}$ STP
F_s	Stoichiometry factor	Dimensionless
N_A	Avogadro's constant	Dimensionless
A_g	Cross-sectional area of the active adsorptive atom	nm^2
ρ	Metal density	g cm^{-3}
I_{US}	Ultrasonic intensity	W cm^{-2}
ρ_{US}	Ultrasonic density	W cm^{-3}
CPO	Crude palm oil	
RBD-PS	Refined, bleached and deodorised palm stearin	
S-RBD-PS	Split-refined, bleached and deodorised palm stearin	
FFA	Free fatty acid	

1. Introduction and Background

1.1. Catalysts and catalysis

1.1.1. Catalysis: A historical perspective

One can trace the roots of catalysis back to the early days of civilisation, when human beings began to engage in the noble task of producing alcohol via fermentation. Investigations of this then seemingly unfamiliar phenomenon comprised several limited observations of events that were not confidently grasped. In the course of time, several other applications of catalysis began to manifest. For instance, during the Middle Ages, sulphur and humid air in the presence of nitric acid led to the manufacture of sulphuric acid. Following the production of sulphuric acid in 1552, it was utilised in the catalytic conversion of alcohol to ether (Davis et al., 1997). A fundamental doctrine of catalysts or catalysis is that the catalytic species in question is preserved throughout the whole reaction. Scottish chemist Elizabeth Fulhame in 1794 initiated the demonstration of this concept when she took into account the catalytic property of water, which remained unaltered after catalysing the oxidation of carbon monoxide (Lindström and Pettersson, 2003). In another scenario, Humphry Davy and his cousin Edmund Davy in 1820 discovered that particular metals have the ability to function as catalysts in gaseous reactions while maintaining their chemical and structural integrity (Edmund, 1820). In that moment, Davy was studying the chemical reaction between coal gas and oxygen in the presence of hot platinum and palladium wires (Wisniak, 2010). Ensuing that, in the 1830s, Swedish chemist Jöns Jacob Berzelius dedicated his time to gathering and cataloguing these historical

observations and dubbed these foregoing phenomena as *catalysis*, which stemmed from the Greek words *kata*, defined as "down"; and *lyein*, defined as "loosen" (Lindström and Pettersson, 2003; Wisniak, 2010).

1.1.2. Principles of catalysis

To put it simply, a catalyst is a chemical substance that brings about the acceleration or retardation of the rate of a chemical reaction, or catalysis, occurring in a reaction medium. A more explicit definition of a catalyst and catalysis is given by IUPAC as "*A substance that alters the rate of a reaction without modifying the overall standard Gibbs energy change in the reaction; the process is called catalysis*" (McNaught and Wilkinson, 1997). Moreover, the catalyst is typically incorporated into the reacting system in relatively small amounts, and as mentioned in the previous section, is not consumed by the reaction. Catalysis in the modern day is ubiquitously exploited for their practical use for accelerating reaction rates and is of paramount importance in many industries because rate acceleration commonly equates to the manufacture of cleaner and more economic chemical products.

Ostwald's definition of catalysis presents a number of significant inferences, one being the position of the chemical equilibrium within a catalysed reaction. To further elaborate, the equilibrium position in a catalysed system will reach a similar point as a reaction eventually occurring in the absence of a catalyst (Bond et al., 2006). This phenomenon owes to the fact that the equilibrium constant, **K**, depends on the Gibbs free energy of the reaction:

$$K = e^{-\frac{\Delta G}{RT}} \quad \text{Eq. (1.1)}$$

where:

ΔG is the change in Gibbs free energy (kJ mol^{-1}); R is the gas constant (J K^{-1} mol^{-1}); T is the temperature (K).

Which is itself governed by the enthalpy and entropy changes of the process:

$$\Delta G = \Delta H - T\Delta S \quad \text{Eq. (1.2)}$$

where:

ΔG is the change in Gibbs free energy (kJ mol^{-1}); ΔH is the change in enthalpy (J); T is the temperature (K); S is the entropy (J K^{-1} mol^{-1}).

A catalyst is only permitted to enhance the rate of a reaction that is thermodynamically allowed under a given set of conditions, when there is a negative change in Gibbs free energy (Bond et al., 2006), in which Gibbs free energy is defined as the maximum amount of work done in a thermodynamic system when conditions such as temperature and pressure are kept constant.

Principally, in order for a reaction, whether catalysed or not catalysed, to proceed, the reactants must possess sufficient potential energy to overcome the energy barrier and reach the product stage. The rate of reaction refers to the amount of reactant consumed, or product formed per unit of time at a given pressure and temperature. One simple way to enhance such a reaction rate is to

increase the temperature of the system. Arrhenius' hypothesis on the effects of temperature on a non-catalysed gaseous reaction is considered in this case, in which the following equation is introduced:

$$r = Ze^{\frac{-E}{RT}} \qquad \text{Eq. (1.3)}$$

He proposed that the rate of reaction, **r**, is reliant on the number of molecular collisions possessing energy levels greater than a threshold termed the *activation energy*, **E**. The activation energy is the energy difference between the potential energy of the reactants and that of the transition state of the reaction. Ultimately, the proportion of collisions happening above this level, **Z**, increases exponentially with the increase in temperature with respect to the Boltzmann distribution fraction (Bond et al., 2006).

In addition to manipulating the temperature, catalysts that are apt for the system can also be employed to achieve a similar, or in some cases, better effect. A catalyst does not alter the energetic characteristics of the reactants and products and the barriers between them. Instead, an alternate reaction pathway is sought by the catalyst, which has a lower activation energy to bridge the reactants and products more effectively and quickly (Ball, 1996). This results in a faster reaction rate as the reactants are now provided with a different pathway with lower energy demands to form products, as demonstrated in Figure 1.1.

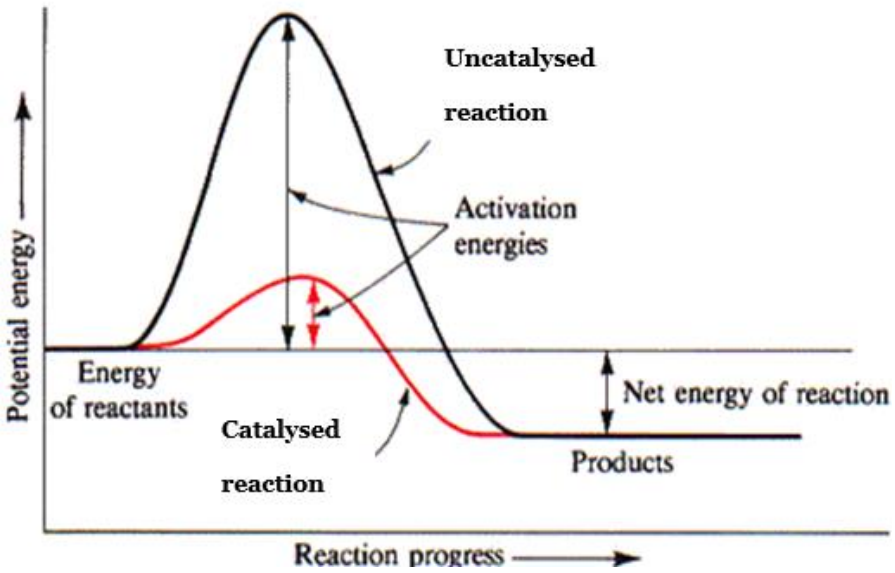


Figure 1.1: Reaction coordinates for catalysed and uncatalysed reactions.

Note: The black line describes the potential energy barrier existing for an uncatalysed reaction; the red line represents an analogous catalysed reaction.

Image adapted from Flowers et al., (2015).

Albeit considered as a reactant, a catalyst is regenerated in its unaltered form at a later stage in the catalytic process. Subsequently, the regenerated catalyst is then liberated and allowed to take part in more chemical reactions, as illustrated in Figure 1.2. This is the very principle as to why catalysts are only necessitated in relatively minuscule proportions to generate copious amounts of product.

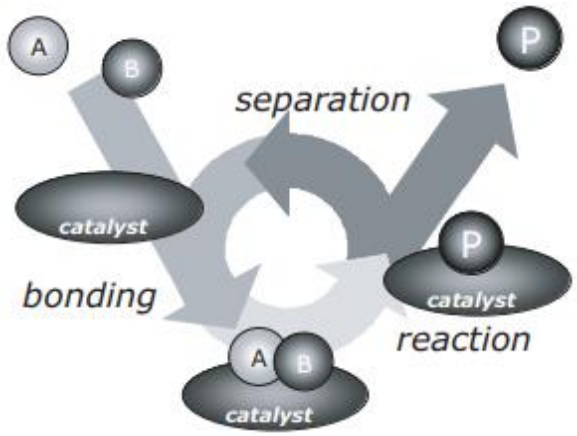


Figure 1.2: Illustration of a typical catalytic reaction cycle.

Image adapted from Chorkendorff and Niemantsverdriet (2003).

1.2. Catalyst classifications

Catalyst systems are generally differentiated into two distinct categories: homogeneous catalysis and heterogeneous catalysis.

1.2.1. Homogeneous catalysis

Homogeneous catalysis involves a catalytic system whereby both the catalyst and reactants are present in the same phase, i.e. a liquid phase or a gaseous phase. Homogeneous catalysts are commonly liquid or soluble in the solvent or reactants used in the reaction. This results in a homogeneous distribution of the catalyst in the system, which allows the active participation of virtually all catalytic molecules in the process. Therefore, homogeneous catalysts conventionally yield high catalytic activity.

Organometallic compounds are extensively used as homogeneous catalysts since they possess a variety of metal centres and organic ligands, hence allowing the execution of a vast range of reactions. Nevertheless, the major disadvantages of this form of catalysis are the tremendous effort required to separate the catalyst from the reaction product and its subsequent complications in recovery and recycling, which are customarily time-consuming processes that come with a hefty price tag.

For instance, organometallic complexes homogeneously catalyse the polymerisation, addition and oxidation of olefins. Another omnipresent homogeneous catalytic reaction occurs in the stratosphere of planet Earth. Ozone is converted into oxygen via the catalytic action of chlorine atoms generated by the photochemical destruction of chlorofluorocarbon refrigerants (Daniel et al., 1999).

Contrary to homogeneous catalysis, heterogeneous catalysis is a process whereby a catalytic reaction comprises components of two distinct phases, i.e. a solid catalyst is utilised in a gaseous- or liquid-phase reaction. In fact, heterogeneous catalytic reactions are at the heart of modern energy and chemical industries (Munnik et al., 2015).

1.2.2. Heterogeneous catalysis

In contrast to homogeneous reactions, heterogeneous catalytic reactions are equipped with specific distinguishing traits due to the fact they occur in entirely dissimilar phases. Nevertheless, the chemical processes involved in

heterogeneous reactions are more complex. With reference to a general heterogeneous catalytic reaction, the reactants and products involved partake a chain of events over the catalyst as illustrated in Figure 1.3.

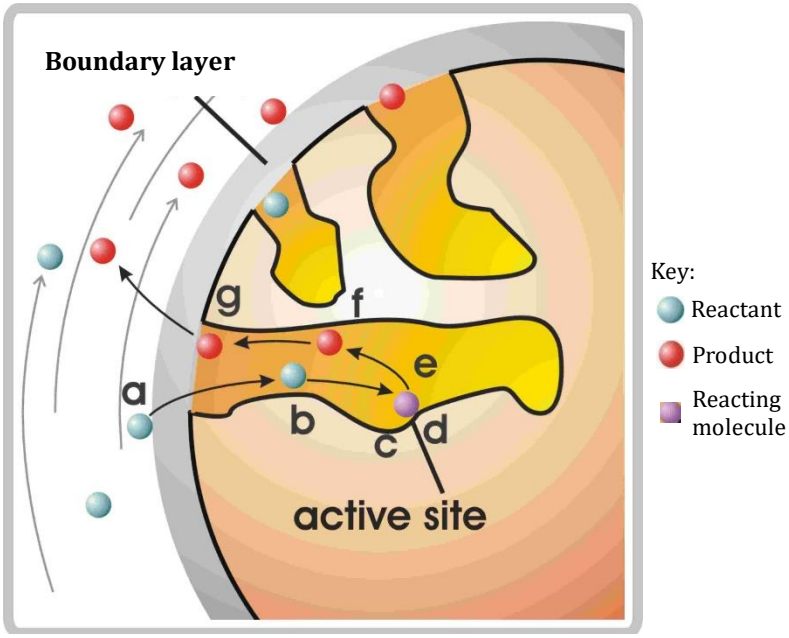


Figure 1.3: Key events occurring during a heterogeneous catalytic cycle.

Image adapted from Ruhr-Universitat (2010).

Based on Figure 1.3, in step **a**, reactants diffuse across the boundary layer surrounding the catalyst particle. Step **b** involves the intra-particle diffusion of reactants into the catalyst pores and subsequently to the active sites, while step **c** involves the adsorption of reactants onto the active sites. In step **d,** surface chemical reactions including the formation or conversion of the adsorbed intermediates take place, feasibly through surface diffusion steps. At the end of the reaction, products desorb from the active sites and subsequently diffuse through the catalyst pores in steps **e** and **f**, respectively. Lastly, the reaction products diffuse out of the boundary layer into the surrounding bulk region in step **g** (Dumesic et

al., 2008). Correspondingly, various distinct regimes of catalytic rate control can manifest, including: (i) film diffusion control (i.e. steps **a** and **g**); (ii) pore diffusion control (i.e. steps **b** and **f**); and (iii) intrinsic reaction kinetics control (i.e. steps **c** to **e**) of catalyst performance (Dumesic et al., 2008). The separation process of heterogeneous catalysts from their reaction mixtures are relatively straightforward and can commonly be achieved by simple filtration. In addition, handling and recycling them are also typically uncomplicated.

Heterogeneous catalysts are made up of two dominant sub-categories: unsupported catalysts and supported catalysts. Unsupported catalysts generally comprise the main active catalytic metal without any supplemental metal or component as an inactive "anchoring site" (Richardson, 1989; Schlögl, 1997). These catalysts represent a large category and are utilised in many industrial processes. On the other hand, supported heterogeneous catalysts are predominantly composed of two main features: a catalytically active phase and a support matrix, which can either be inert or have the capacity to interact with the active phases in certain ways. The active sites, which are loaded and anchored to the support matrix, are accountable for catalytic activity (Deutschmann et al., 2009). It is well established that a good support should be able to offer a large surface area in order to accommodate a significant quantity of active sites and at the same time impart excellent thermal and mechanical stability to the catalyst as a whole. Over and above that, some supports have the ability to modify the catalytic properties of the active phase by imparting strong metal – support interactions (SMSI) throughout the catalyst, as a result of the strong adhesion and reaction between the active and support phases. For instance, these interactions can affect

the chemisorption or reduction capacity of supported metals (Courty and Marcilly, 1983). Broadly employed supports include alumina, silica, aluminosilicates, activated carbon, titania and zinc oxide (Stiles and Koch, 1995).

The overall properties and characteristics carried by homogeneous and heterogeneous catalysis or its catalysts are highlighted below in Table 1.1. Generally, heterogeneous catalysis has a few essential features worth highlighting, in addition to having an upper hand in some cases when contrasted with homogeneous catalysis. In terms of catalyst recoverability, the separation of heterogeneous catalysts from their products is typically relatively straightforward and hassle-free, which diminishes the effort in recycling. Besides, heterogeneous catalysts generally have better thermal stability when compared to homogeneous catalysts, which promotes greater versatility for the former when it comes to various reaction conditions (Farnetti et al., 2009).

Table 1.1: Various general characteristics of homogeneous catalysis/catalysts and heterogeneous catalysis/catalysts.

Property	Homogeneous	Heterogeneous
Catalyst availability	Industrially less relevant.	Commercially available for general reactions.
Catalyst preparation	Generally simple to replicate in laboratories.	Relatively simple, occasionally requiring specialised knowledge.
Catalyst reproducibility	Good, with the ability to fine-tune catalyst properties using various ligands/additives.	Good, with attention paid to raw materials
Catalyst separation	Challenging and expensive separation of products and catalysts/additives.	Generally easy (gravity or vacuum filtration), associated with low costs.
Catalyst re-use	Tough due to complex separation processes.	Easy recovery and re-use, while maintaining activity.
Reaction apparatus	Usually require apparatus for mild reaction conditions.	Special reactors required for high-pressure reactions.
Catalyst characterisation	Investigation of reactions by spectroscopic methods (i.e. NMR, MS, IR, UV-Vis).	Various methods available (texture, thermoanalysis, phase, surface, etc.), although understanding the phenomena on the solid is challenging.
Active sites (species)	Active sites generally well defined. Catalysts are typically single atom transition metal stabilised by ligands.	Tough to synthesise single types of active sites and in most cases, not well defined. Active sites might only comprise few percent of the total metal amount and different zones of the same particle might have different catalytic properties.

1.2.2.1. Heterogeneous catalysis in the industry

A crucial breakthrough in the sphere of heterogeneous catalysis was the discovery and establishment of the Haber-Bosch process in 1905 (Haber, 1905). In brief, this process utilises promoted iron (Fe-based) catalysts to transform N_2 and H_2 gases to ammonia on an industrial scale, which permits the mass production of fertilisers to promote agricultural and economic growth. Thereafter, heterogeneous catalysis has stimulated the advancement of several key industries and has become the workhorses of the chemical and petrochemical industry. Some of the most expansive industrial processes, which are centred on heterogeneous catalysis are, but not limited to: Al_2O_3/SiO_2 catalysts in the cracking and hydrotreating of crude oil, Pt/Al_2O_3 catalysts in gasoline production from naphtha, Ni/Al_2O_3 catalysts in methane steam reforming, V_2O_5 catalysts in the production of sulphuric acid, Ni-based catalysts in the hydrogenation of oils and fatty acids, etc (Chorkendorff and Niemantsverdriet, 2003).

With regards to the previously mentioned industrial applications of heterogeneous catalysts, the advancement of heterogeneously catalysed processes in the manufacture of myriad chemicals demand the preparation or synthesis of their respective catalysts on an industrial or technical scale. It has been established that the catalytic properties of solid catalysts have an intimate relationship with the preparation method, synthesis conditions and the type and quality of the raw materials. For that reason, it is imperative that the production step and physical or mechanical properties of all intermediates are regulated as accurately as possible.

Generally, the techniques used to synthesis these heterogeneous catalysts play a significant role in dictating the final catalyst functionality and properties.

1.2.3. Synthesis of unsupported catalysts

1.2.3.1. Mechanical treatment

One of the most straightforward preparation routes for unsupported catalysts via mechanical treatment is the continuous mixing, milling or kneading of catalytically active materials or their precursors with appropriate promoters, structural stabilisers or pore-forming agents (Courty and Marcilly, 1983; Richardson, 1989). For instance, Au-CeO_2-CoO_x catalysts prepared via milling are applied for the oxidation of benzene. Nevertheless, it is noted that this method presents several major drawbacks in terms of the product's catalytic activity, selectivity or thermal stability because intimate contact between catalyst components is relatively hard to attain. However, by-products such as wastewater is commonly circumvented, which reduces production costs.

1.2.3.2. Sol-gel treatment

This process consists of the formation of a sol, subsequently the production of a gel. The sol, which is a liquid suspension of solid particles less than 1 μm, is acquired by hydrolysing and partly condensing an inorganic salt or metal alkoxide. Next, the gel is generated by condensing the sol particles into a three-dimensional network. The sol-gel synthesis technique can be used to synthesise monometallic catalysts such as TiO_2 and multi-metallic composite catalysts such as $CoAl_2O_4$,

which are applied for catalytic processes such as the oxidation of organics in the liquid phase (Landau, 2008). Generally, the overall conditions of the formation process (i.e. temperature, coagulation conditions and post-treatment) determines the mechanical properties of the gel (Ko, 1997).

1.2.3.3. Precipitation and co-precipitation

One of the most widely used methods for the preparation of unsupported catalysts is precipitation or co-precipitation. Starting materials are typically metal salts in their nitrate or sulphate form, in which the alkali metal nitrates or sulphates generated as precipitation by-products must be washed out of the precipitate to prevent catalyst poisoning. Basic precipitation agents are hydroxides or carbonates (Richardson, 1989). For the homogeneous dispersion of two or more metal precursors and their subsequent defined crystalline structure, it is greatly recommended to partake the co-precipitation method (Schüth and Unger, 1997). Throughout the precipitation process, various parameters have to be tightly regulated as they play a crucial role in determining the properties of the precipitate. Some of these parameters are temperature, stirring speed, pH, aging time and concentration of starting solutions (Schüth and Unger, 1997; Stiles and Koch, 1995).

The synthesis procedure of precipitated catalysts is commonly in the following order: preparation of precursor metal salt solutions and precipitating agent, optional mixing of two or more metal salt solutions, precipitation by dosing precipitating agent under constant stirring, aging of precipitate suspension,

filtration and washing of precipitate, drying by oven drying or spray drying, calcination, shaping and activation. For example, unsupported CoMo catalysts synthesised via co-precipitation are used in decarboxylation reactions for biodiesel upgrading (Shim et al., 2015).

1.2.4. Synthesis of supported catalysts

1.2.4.1. Impregnation

This process is carried out by filling the pores of a carrier component with the active phase metals. The solution containing the catalyst precursor is introduced into the pores of the carrier, with the preferred metal loading controlled by the concentration of the salt solution (Che et al., 1997). A particularly common catalyst prepared via impregnation is the Ni on α-Al_2O_3 catalyst, employed for a wide range of reactions such as steam reforming, hydrogenation and hydrotreating. In cases whereby a higher loading is required, the impregnation process has to be repeated after drying or calcination of the precursor, which is highly time and energy consuming for some instances (Courty and Marcilly, 1983; Richardson, 1989).

1.2.4.2. Adsorption

The adsorption method is useful in attaining a uniform deposition and distribution of small amounts of active phases onto a support medium. The metal salt solutions are exposed to the support medium composed of particles or powders, with the support particles adsorbing equilibrium quantities of salt ions

in conformity with their respective adsorption isotherms. The properties of the carrier surface govern the anionic or cationic adsorption of species. For instance, alumina supports adsorbs both anions and cations depending on adsorption conditions, while silica supports adsorbs cations weakly (Richardson, 1989). A case in point would be the adsorption of Pt species on Al_2O_3 supports, thus used in automobile exhaust oxidation.

1.2.4.3. Precipitation or co-precipitation onto the support medium

This method is accomplished through similar means as that of the precipitation or co-precipitation of unsupported catalysts, as described in Section 1.2.3.3. Supports in their powder form, such as kieselguhr, contains silica and alumina and is slurried into the salt solutions and precipitated (Richardson, 1989). On the other hand, supports initially in their liquid form, such as sodium metasilicate, is added after the precipitation of metal salt solutions. This method requires rapid mixing to ensure that bulk precipitation does not occur and is utilised extensively in the manufacture of catalytically active Ni – SiO_2 or Ni – Al_2O_3 catalysts, employed in various catalytic reactions such as hydrogenation or hydrotreating (Geus and van Dillen, 1997).

1.3. Catalytic activity of heterogeneous catalysts

As previously mentioned in Section 1.2.2., various regimes occurring during the catalytic reaction will impart mass transfer effects that govern the catalytic activity of heterogeneous catalysts. The commencement of diffusion-limited regimes can be tailored by altering the reactor design, the catalyst pore structure,

the catalyst particle size and the homogeneity of active sites throughout the catalyst particles. For example, a catalyst can be designed to offer an acceptable diffusion rate, while providing high active surface areas, by detailed design of specific pore size distributions (Dumesic et al., 2008). From a broader perspective, the following attributes will have a significant impact on the activity of a catalyst: pore size, pore volume, total surface area, total active metal surface area, pore and particle size distribution, uniformity of active sites throughout the catalyst, resistance to poisons and inhibitors and particle or crystallite size. It should be noted that the mentioned features are non-exhaustive and various other factors will have an effect on the overall catalytic activity, as different reactions might necessitate different catalyst properties.

1.4. Nickel as a heterogeneous catalyst

With regards to heterogenous catalysis, nickel has been employed in the industry for various processes due to not only its high availability and activity, but also its economic attractiveness. Nickel might come across as an impoverished sibling of palladium to the unfamiliar in the field of transition metal catalysis (Tasker et al., 2014). However, throughout recent decades the low-cost alternative of palladium has established its niche in various chemical processing industries based on its abundant and diverse usage in myriad nickel-catalysed reactions as reported in many literatures. In fact, the famous scientist and Nobel Laureate Paul Sabatier has dubbed nickel the *spirited horse* of transition metal catalysis in 1922 as he reviewed the state of the art of catalysis in organic chemistry and highlighted the specific functionalities of nickel catalysts. He observed that nickel has *an*

excessive activity along with maximum alterability (Sabatier, 1922). In the subsequent texts, conversely, Sabatier noted that the properties and usage of the catalyst could be tailored by manipulating its preparation methods as it is deemed to be able to do all kinds of work and maintains its activity for a long time (Sabatier, 1922). Since then, nickel's exceptional catalytic capability has effectively fuelled the advancement of nickel-related catalytic processes.

Historically, the utilisation of nickel metal as a catalyst in organometallic reactions predates many other instances in transition metal catalysis (Tamaru, 2005; Wilke, 1988). In 1751, nickel was extracted and isolated from its copper-nickel ore and more than one century later, German chemist Ludwig Mond discerned an uncommon reactivity pattern of the metal. Elemental nickel was able to react with CO at room temperature to form $Ni(CO)_4$, a particularly toxic, low-boiling liquid, which can in turn purify the metal (Mond et al., 1890). Soon thereafter, Sabatier and Senderens (1897) have also reported nickel as a heterogeneous catalyst for gas-phase hydrogenation, for which the Nobel Prize in Chemistry was bestowed upon Sabatier in 1912.

Nickel is pervasively used as a catalyst in the steam reforming or catalytic conversion of hydrocarbons, alcohols and light oil fractions. This process includes reacting steam with methane, ethane, natural gas, liquefied petroleum gas (LPG), naphtha, gasoline and alcohols over nickel catalysts at elevated temperatures and pressures to generate hydrogen gas and carbon monoxide, or carbon dioxide if a water-gas-shift reaction ensues (Mathure et al., 2007). The hydrogen gas produced can then be used for other important industrial processes such as hydrocracking,

hydrodesulphurisation, ammonia production, etc. On the other hand, nickel is also employed in the oleochemical industry as a catalyst for the hydrogenation of fats and oils. In this reaction, unsaturated fats, which contain carbon-carbon double bonds, will be converted to saturated or partially saturated fats, which contain more carbon-carbon single bonds. Together with hydrogen gas as the source of hydrogen atoms for the C=C double bonds present in unsaturated fats, nickel catalysts facilitate this reaction at elevated temperatures and pressures (Dijkstra, 2012).

1.4.1. Nickel catalysts: Hydrogenation of fats and oils

While vapour phase hydrogenation is commonly traced to Sabatier and his associates, hydrogenation in its liquid phase is credited to the German chemist Wilhelm Normann, who filed a British patent on the process in 1903 (Normann, 1903). What followed ever since is the introduction and application of industrial hydrogenation or hardening of vegetable fats and oil, which paved the way for the increase in versatility and variability of said chemical substances throughout the years. In some instances, vegetable oils, such as palm, soybean and sunflower are partially hydrogenated to an appropriate consistency for margarine, shortening and other edible products. Besides, animal fats such as lard can be mildly hydrogenated to enhance its consistency and storage qualities, while tallow is hardened for industrial purposes (Wurster, 1940). The principal motive to hydrogenate fats and oils is to increase their flavour stability since the resulting product will be less prone to oxidation and thermal decomposition, hence

prolonging the shelf life. On the other hand, the saturated product will possess more practicality via the alteration of physical characteristics (Allen, 1978).

Naturally occurring fats and oils comprise mixtures of triglycerides with different compositions of saturated and unsaturated fatty acids. In practice, the hydrogenation process is typically executed in a three-phase slurry reactor through a semi-batch process, whereby hydrogen gas is injected to a reacting mixture composing of unsaturated constituents of fats or oils at an elevated temperature and pressure. The typical operating temperatures and pressures are in the range of 100 – 240 °C and 3 – 5 bar, respectively (Allen, 1978; Patterson, 2011). Depending on the reacting conditions, this results in a product containing highly or completely saturated triglycerides (Wurster, 1940), in which the extent of saturation is expressed as the Iodine Value (IV). The IV is described as the mass of iodine consumed by every 100 g of fats, whereby a high degree of unsaturation would be represented by a high IV, vice versa. It should be established that the foregoing process can only proceed in the presence of a catalyst, which expedites the reaction. Essentially, nickel is ubiquitously employed as a catalyst on an industrial scale except for the production of some special products (Veldsink et al., 1997). Nickel catalysts are considered to be more suited for such processes compared to precious catalytic metals such as Pt or Pd as they are superior in terms of their production costs and comparable in catalytic activities (Balakos and Hernandez, 1997; Dijkstra, 2006; Fernández et al., 2007).

Several important factors govern the velocity and extent of the hydrogenation reaction as well as its selectivity: reactor design, hydrogen gas

purity, feedstock quality, operating conditions (viz. temperature, pressure, catalyst loading level, and agitation intensity) and last but not least, the catalyst efficiency (Hastert, 1979). Throughout the decades, myriad efforts were made to improve and modify the properties and performance of nickel catalysts in various fields and industries, including its application for the hydrogenation of fats and oils. Quite a substantial amount of research at this present-day still revolves around this subject matter, as it is only human nature to yearn for constant improvement, which is tantamount to contemporary science and technology.

For example, Konkol and associates (2016b) have investigated the influence of hydrogen pressure on the kinetics of canola oil hydrogenation using co-precipitated nickel alumina catalysts. They provided findings that revealed comprehensive information on to what extent the increasing hydrogen pressure facilitates hydrogenation over *cis/trans* isomerisation. To illustrate, fatty acid profiles of canola oil samples hydrogenated to the same iodine value were found to be dependent on the hydrogenation pressure. Firstly, elaidic acid, 9t-C18:1 and other positional isomers decreased by approximately 37 % by increasing the pressure from 2.5 to 21 bar(a). Secondly, this was supplemented by a simultaneous increase in stearic acid content, from 13 to 22 wt%. This study goes to show that the research and development of nickel-based hydrogenation processes are still ongoing, in which a lot of parameters or properties of said reaction can still be tweaked in order to favour a particular desired outcome.

Furthermore, in a more recent investigation, Ryabchuk and colleagues (2018) have reported a stable and highly active intermetallic nickel silicide catalyst

prepared by a relatively straightforward high-temperature thermal reduction reaction, which can be utilised in a broad range of hydrogenation reactions, including the saturation of carbon-carbon double bonds found in unsaturated fats and oils. They suggested that said catalyst could be a promising alternative to standard Raney nickel and noble metal-based catalysts. Evaluation from various hydrogenation reaction tests show that the material exhibits outstanding catalytic activity for diverse hydrogenation processes, along with several other attractive advantages such as: long-term stability, ease in handling and recyclability.

1.4.1.1. Sunflower oil

Sunflower oil, a type of vegetable oil, is extracted from seeds which are produced on the sunflower capitulum. These seeds accumulate oil in the kernel, yielding high quality oil that is widely used and appreciated by consumers.

Regular sunflower oil is rich in linoleic and oleic fatty acids, which is easily extracted by a combination of physical and solvent methods, followed by degumming, neutralisation, bleaching, deodorisation and clarification.

The oil, highly transparent with a mild smell and aroma, has been used for various purposes such as frying, retailing and the manufacture of sauces and emulsions (Salas et al., 2021).

1.4.1.2. Hydrogenation of sunflower oil

Sunflower oil is also commonly used in partial hydrogenation reactions to produce high-stearic content sunflower oil, which is used in the formulations of food products that require confectionery fats to reach their proper consistency or texture.

For instance, sunflower oil can be utilised in the production of cocoa butter equivalents (CBEs), which is used to manufacture chocolate products. On the other hand, partially hydrogenated sunflower oil can also be used a in bakery products such as margarine and fat fillings (Salas et al., 2021).

1.4.2. Deactivation of nickel catalysts

Catalyst deactivation, the deterioration of catalytic activity and/or selectivity as a function of time, is an issue of significant and ongoing concern for industrial processes involving the usage of catalysts, in which high costs are commonly inflicted due to the frequent replacement and process shutdown associated (Argyle and Bartholomew, 2015). Compared to gas-solid catalytic reactions, however, studies regarding catalyst stability and deactivation in liquid media have been relatively scarce, likely due to the fact that gas phase catalytic processes are more widespread in the industry (Sádaba et al., 2015).

1.4.2.1. Mechanisms of deactivation

In a gas-phase environment, five types of mechanisms take place for the deactivation of catalysts, and it is noted that deactivation that occurs in a liquid

medium are comparable to those of the gas-phase (Bartholomew, 2001). These mechanisms are compiled in Table 1.2.

Table 1.2: Mechanisms of catalyst deactivation.

Type	**Nature**	**Mechanism**	**Description**
Fouling/coking	Physical	Lowered accessibility to active sites	Physical deposition of foreign chemical species on catalytic sites thus blocking them
Mechanical attrition	Physical	Loss of catalytic material and active sites	Crushing, abrasion and/or erosion of catalyst particles
Sintering	Thermal/ Chemical	Decrease in the number of exposed active sites	Loss of active catalytic area and metal-support reactions due to growth of crystallite size
Poisoning	Chemical	Decline in intrinsic activity	Binding of foreign species on catalytic sites through strong chemisorption
Leaching	Chemical	Loss of active sites	Reaction and dissolution of active components into reaction medium

Fouling involves the physical deposition of chemicals present in the reaction medium on to the surface, and particularly, the active sites of the catalyst. Reactants, principal products, by-products or impurities can be deposited due to heavy molecular weight, insolubility in the reaction medium, steric effects and adsorption. In some cases, the conversion product molecule might be larger than the reactants, hence leading to the occlusion of porous networks. On the other hand, coke refers to heavy hydrocarbons generated in reactions that cause the blockage of pores as well (Sádaba et al., 2015).

Mechanical attrition in a liquid medium causes the reduction in particle size, thus breaking up the catalyst particles into smaller aggregates. This can hinder the catalyst recovery process as the fine particles are difficult to retain, as in some cases even lead to clogging and the subsequent build up in reactor pressure (Bartholomew, 2003).

Sintering is the thermodynamically-driven growth and agglomeration of crystallites, which leads to the decline in active surface area and the collapse of porous structures in supported metal catalysts (Adibi, 2014). Generally, two types of sintering mechanisms are reported: particle migration and atomic migration. The former is known as thermal sintering, which involves the movement of particles on the support surface, with their subsequent coalescence, resulting in nanoparticle growth. The latter is a form of chemical sintering, also known as Ostwald ripening, whereby larger crystallites grow at the expense of smaller crystallites, in which over time the smaller crystallites completely disappear. It describes the migration of adatoms or mobile molecular species, which is a process fuelled by discrepancies in free energy and local adatoms on the support surface (Hansen et al., 2013). The atomic or molecular species migrate either via a second phase (i.e. gas phase or liquid solution) or a catalytic support.

Poisoning is related to the strong chemisorption of impurities onto catalyst that hampers the normal function of the active sites. Besides physically blocking the adsorption sites, adsorbed poisons may also prompt changes in the electronic and geometric structure of the catalyst surface (Bartholomew, 2001). For instance,

catalyst poisons such as sulphur, phosphorus and chlorine have a deleterious effect on nickel catalysts during fatty acid hydrogenation (Klimmek, 1984).

Leaching or the lixiviation of active phases is specific to liquid-based reactions as it is related to the dissolution of active components into the reaction medium. As a result, the activity of a catalyst will decline over time as more and more active metal dissolves into the reaction medium, which also causes potential health risks or complications in subsequent processes as the medium is contaminated by trace amounts of metals (Sádaba et al., 2015).

Clearly, it is imperative to be acquainted with deactivation mechanisms that are highly associated with supported nickel catalysts. By doing so, relevant and appropriate measures can be taken in order to prevent or reduce the extent of deactivation in nickel catalysts for the hydrogenation of fats and oils, which is highly beneficial for any industrial usage of the catalyst.

Investigations into the deactivation of nickel catalysts in plant-based (palm) fatty acid hydrogenation have revealed that it is more often related to poisoning, and in some cases, sintering (Ostwald ripening) and leaching might occur (Hansen et al., 2013; Irandoust and Edvardsson, 1993; Klimmek, 1984). It should also be important to not rule out the simultaneous occurrence of all three mechanisms. Nevertheless, it has not been deciphered which mechanism is more dominant.

1.4.2.2. Palm oil in Malaysia

Malaysia is the world's second largest palm oil producer, with an estimated production capacity of 19.6 million tonnes in 2021 (Wong, 2021). The palm oil industry is also one of Malaysia's well-diversified primary industries and constitutes the largest share of its agricultural sector. Being one of the most widely used plant-based oils in the world – roughly one-third of the global consumption – the consumption rate of palm oil is expected to rise to 72 million tonnes a year.

Palm oil trees only require half as much land as other crops, e.g. soybeans, to produce a given quantity of oil. In addition, the entirety of palm – from its fruit to its waste – can be fully utilised for a purpose. Its woody trunks can be made into furniture or building materials, its leaves or fruit bunches can be processed into fertilisers or fuel, its wastes can be transformed into biomass as an alternative energy source and its fruit can be processed into a variety of oils and chemicals of edible and non-edible purposes (Rosner, 2018).

In particular, the palm fruit can be processed via mechanical means and physical extraction to obtain crude palm oil from its mesocarp. The extracted crude palm oil is then further processed into a myriad of palm oil derivatives as shown in the flowchart (Figure 1.4) below.

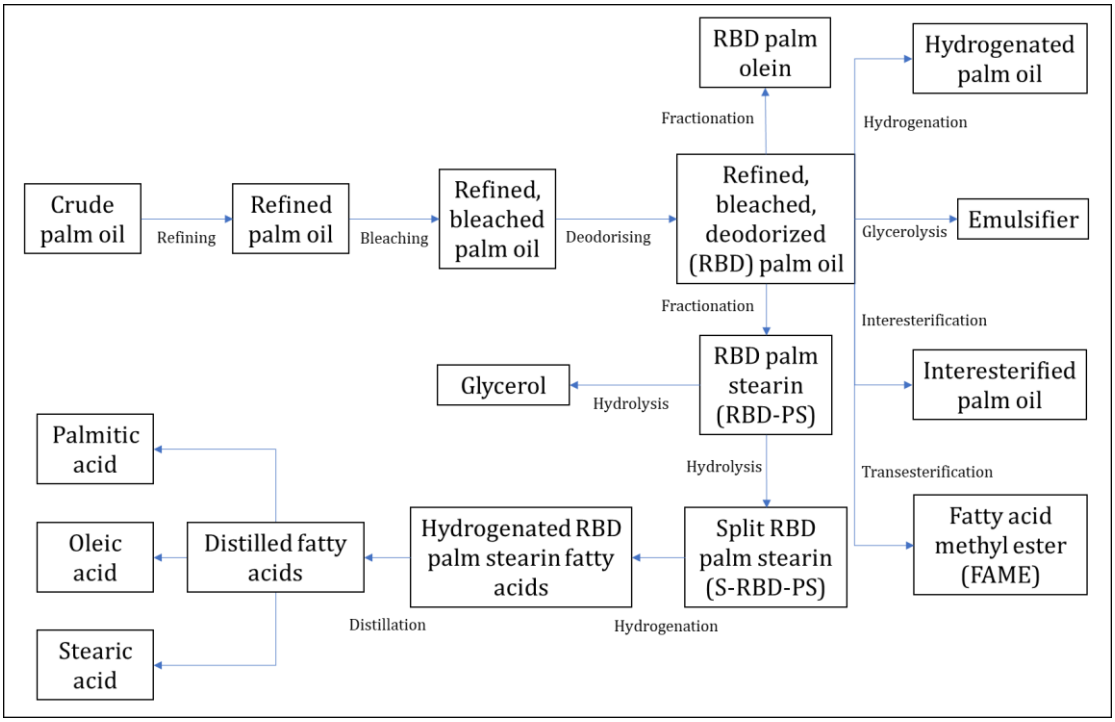


Figure 1.4: Typical process pathway of the processing of crude palm oil and its derivatives.

1.4.2.3. Palm oil processing

Crude palm oil is typically pre-treated by refining, bleaching and deodorising before being sent for further processing. Treated crude palm oil is then fractionated to produce palm olein, the liquid fraction, and palm stearin, the solid fraction. Common uses of palm olein include liquid cooking or frying oil, while palm stearin is used to produce margarine, shortening or vegetable ghee. Palm-based oils are highly desirable in food applications due to its overall quality and stability. The oil is cholesterol-free and has a unique fatty acid and triacylglycerol profile, while its high carotenoids and tocopherols contents create a high resistance against oxidative deterioration, which allows the end products to have longer shelf lives (Pande et al., 2012).

Chemical processes can also be applied to palm oil and its derivatives to alter their properties. For instance, catalytic hydrogenation is used to modify the characteristics of liquid palm oil. In the non-food sector, palm oil is used to manufacture soaps and detergents, cosmetics and oleochemicals. For instance, RBD-palm stearin (RBD-PS) is used to manufacture soaps, while the transesterification of refined palm oil transforms it into oleochemicals used as replacements for petrochemicals and biofuels, i.e. fatty acid methyl esters (FAMEs) (Yeong et al., 2012).

Looking at the significance of palm oil-based processing, a more circumstantial study into the deterioration of nickel catalysts during the hydrogenation of palm-based feedstock might provide valuable understanding on the various mechanisms involved. Subsequently, insights can be obtained to modify the nickel catalysts in order to counter these deactivation processes or tailor them for specific reactions, thus serving as the motivation for the content presented in Chapter 3.

1.5. Ultrasound in chemistry

1.5.1. The sound wave and the ultrasound wave

Sound waves are conventionally described as a mechanical wave generated by a vibrating object and propagated by a medium, in which the dictionary definition of *sound* is *vibrations carried in air, water, etc*. (Kremkau, 1975). Ultrasound is sound whose frequency is above the human audible range (i.e. > 20

kHz). Ultrasound waves, just like standard sound waves, allow their energy to be propagated through longitudinal waves, which induces a disparity of pressure within the medium. Said pressure oscillation travels in fluid (liquid or air) with the speed of sound (Kinsler et al., 1999).

As depicted in Figure 1.5, when a liquid body is subjected to ultrasonic waves, the rarefraction phases induce negative pressures in the liquid, hence causing the liquid medium to undergo rectified diffusion and subsequently cavitation occurs (Crum, 1984).

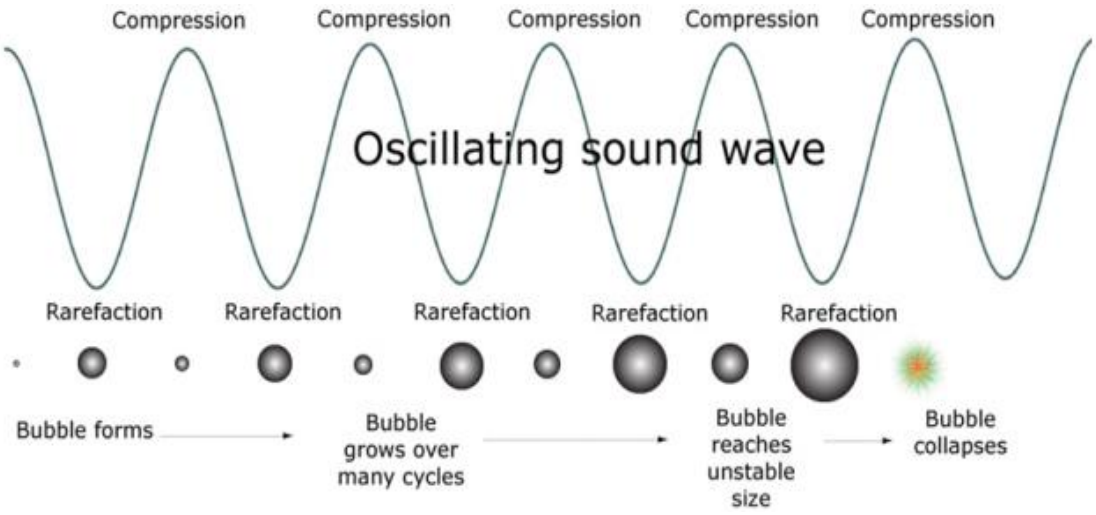


Figure 1.5: Graphical summary of the event of bubble formation, growth and collapse over several acoustic cycles.

Image adapted from Leong et al. (2011).

Sonochemistry, which is one of the branches in power ultrasound, describes the usage of ultrasound energy to induce or enhance chemical, physical and thermal effects occurring in various processes or solutions (Barzureau and Draye, 2011; Mason and Peters, 2002; Suslick et al., 1986). The chemical effects of

ultrasound do not come about from an immediate interaction of sonic energy with species on a molecular level (Suslick, 1990). The wavelength produced by the vibrations in water would be placed in a range of 7.5 to 0.015 cm, for frequencies ranging from 20 – 10000 kHz.

Discernible consequences of ultrasound energy could be deduced by how its sound waves propagate through a medium. A cyclic series of compressions and expansions (rarefractions) (i.e. areas of high and low local pressure, respectively) are produced by the longitudinal mechanical vibration of molecules in a medium. The positive pressure cycle that forces liquid molecules together is wielded by the compression cycles. On the other hand, a negative pressure that forces liquid molecules apart is generated by the rarefraction cycles (Wu et al., 2013). It was discovered that tiny and minute vapour-filled cavities materialise in the rarefraction sections when the pressure amplitude applied overcomes the tensile strength threshold of the liquid (Abramov, 1998; Margulis, 1995).

These observable effects are owed to the cavitation phenomenon, elucidated as the formation, growth and subsequent collapse of minute ultrasonically-induced gaseous micro-bubbles in the liquid phase (Mason and Peters, 2002; Neppiras, 1980; Suslick et al., 1986; Young, 1999). As aforementioned, when liquids are subjected to high intensity ultrasonic energy, the ultrasonic sound waves propagate through the liquid medium and generate alternating compression and rarefraction cycles, in which their rates are influenced by the chosen frequency. During the low-pressure cycle, the ultrasonic waves create tiny vacuum voids or bubbles in the liquid. During the compression

cycle, the micro-bubbles collapse in an intense manner when they reach a volume whereby they can no longer further absorb ultrasonic energy. In a system with abundant acoustic power, cavitation bubbles of several micrometres in diameter are materialised when the expansion cycle surpasses the attractive forces governing the liquid molecules. It is during this expansion stage whereby gaseous matter present in the system can diffuse into the micro-bubbles. The gaseous matter is not completely discharged during the compression stage. The repetition of these cycles brings about the growth of the bubbles until an equilibrium size is attained, in line with the applied frequency. At this very instant, the abrupt collapse of the micro-bubbles culminates potent local isolated reactions, at the birth of all sonochemical events, resulting in extremely intense pressures of up to 1000 bar and temperatures of 5000 K (Gogate and Pandit, 2011; Luche, 1998; Mason, 1992). In addition, these severe states initiated by the bubble collapse also lead to other phenomenon such as the occurrence of sonoluminescence, production of radical species and the generation of shockwaves in the liquid system (Suslick et al., 1990).

Besides generating intense pressures and temperatures, this collapse also delivers divergent shock waves and shear forces adjacent to the bubble, along with acoustic micro-currents and high-speed liquid micro-jets up to 100 ms^{-1} (Pecha and Gompf, 2000; Suslick et al., 1986; Suslick and Crum, 1997). These strong forces and waves generate substantially vigorous turbulences in the neighbouring medium. Moreover, these micro-bubbles encounter asymmetric distortions when solid particles or surfaces are present, thus projecting high-speed jets of liquid into the bubbles. This phenomenon is very prominent in the case of processing suspensions containing metal particles (Yasui et al., 2005). In heterogeneous

systems, the effects arising from the collapse are anticipated to be involved in a pivotal role to bring about major alterations in the morphology and composition of the solid particles concerned such as metal catalysts. In this paradigm, remarkable impacts to such systems are made possible via the following effects contributed by cavitational collapse: dramatic changes in local temperatures and pressures; generation of intense shock waves and micro-jets; development of turbulence and shear forces; improvement of mass transport from rigorous mixing and acoustic streaming; and formation of free radical species.

1.5.2. Applications of ultrasound/sonochemistry

In recent decades, the utilisation of ultrasound in various fields of research disciplines and industrial practices has garnered a considerable amount of attention. By simply manipulating its operating parameters, ultrasonic irradiation can be applied to a plethora of processes in order to bring about positive and desired effects. As a case in point, ultrasonic waves emitted in the kHz to MHz frequency range are known to be effective when applied in sonochemistry. Figure 1.6 schematically illustrates the principal areas of ultrasound applications (Cavalieri et al., 2010; Mason and Petrier, 2004; McClements, 1995; Pazos-Perez et al., 2012; Price, 1992; Schäferhans et al., 2011; Skorb et al., 2013, 2010) in diverse fields including, but not limited to, the following: chemical reactions and processes, surface processing, medical, as well as food processing.

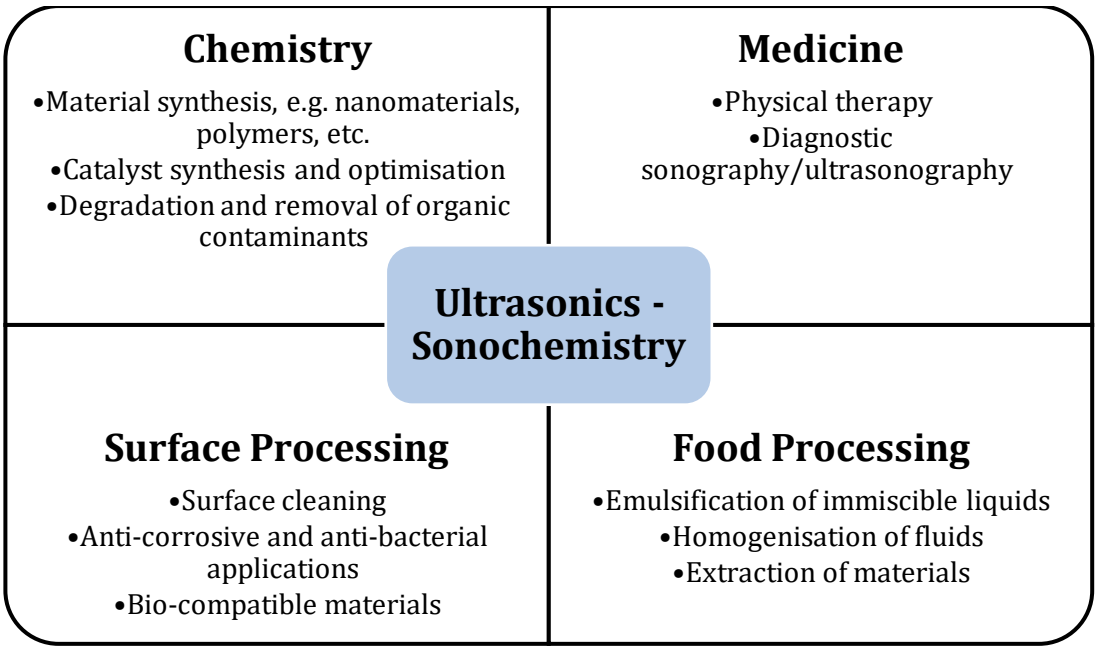


Figure 1.6: General applications involving ultrasound.

1.5.3. Ultrasound in catalysis

The aftermath of applying ultrasonic irradiation to chemical reactions was first documented by Richards and Loomis (1927). Since then, there has been a steady increment in the number of investigations undertaken which are dedicated to studying the reactions that have an appreciable change in their rates or direction when subjected to an ultrasonic field. Concerning their sensitivity to acoustic vibrations, all sonochemical reactions can be differentiated into two main categories: chemical reactions that are accelerated when subjected to ultrasonic irradiation but can still occur independently, notwithstanding at a reduced rate of reaction; and reactions that are completely dependent on the presence of an ultrasound source. For both categories, ultrasound waves of low frequency (> 10 Hz), medium frequency (20 – 100 kHz) and high frequency (2 – 10 MHz) are applied (Hunicke, 1990; Mason and Lorimer, 1988; Suslick and Nyborg, 1990).

Catalytic processes coupled with ultrasonic irradiation are commonly segregated based on the type of catalysis: homogeneous catalysis or heterogeneous catalysis. Furthermore, one should also be able to categorise them based on the type of catalyst used and the nature of the reaction (i.e. oxidation, hydrogenation, polymerisation, etc.) (Gates, 1992; Mason and Lorimer, 1988). The actions and mechanisms of acoustic vibrations are complex and diverse (Bremner, 1990). Through various mechanisms, ultrasonic waves can accelerate chemical reactions: emulsification of liquid constituents, efficient dispersion of solid constituents and catalysts, erosion of solid surfaces, degassing, prevention of sedimentation or coagulation of products, vigorous mixing, etc. When compared to particles obtained after grinding solely, solid catalysts treated with ultrasound present much higher activities, more often not just due to dispersion (Margulis, 1995; Mason and Lorimer, 1988). Extreme surface friction between solid and liquid phases and the fragmentation of solid phase particles would result in an increased active surface area for reactions to take place, which forms the basis of dispersion (Lindley et al., 1987; Suslick and Casadonte, 1987). Furthermore, application of ultrasound could effectively reduce the diffusion boundary layer thickness, resulting in more effective collisions between reactant particles (Sulman, 2000). In a high- and medium- frequency ultrasonic field, large particles break apart and forms smaller particles with rough surfaces, whereas smoothing and polishing of the surfaces occur in a low frequency ultrasonic field (Sulman, 2000).

1.5.3.1. Ultrasonic treatment during catalyst synthesis

Ultrasonic irradiation can be incorporated during the synthesis of catalysts in effort to impart changes onto their catalytic characteristics and activities. Table 1.3 summarises various heterogeneous catalysts synthesised with the aid of ultrasonic irradiation.

Table 1.3: Summary of various catalysts synthesised with the assistance of ultrasonic irradiation obtained from the literature.

No.	Catalyst	Synthesis method	Ultrasonic source	Ultrasonic parameters	Reaction	Ref.
1	Pt/SiO_2	Impregnation	Ultrasonic bath	20 kHz, 30 W	Hydrogenation cinnamaldehyde	(Szöllösi et al., 1998)
2	$(Cu/Zn)_2$	Co-precipitation	Ultrasonic bath/probe	1 – 90 W cm^{-2}, 20 – 35 kHz	N/A	(Kunz et al., 1995)
3	Cu-Mn-O	Co-precipitation	Ultrasonic probe	11.5 – 29.7 W cm^{-2}, 20 kHz	Oxidation of CH_4 and SO_2	(Yap et al., 2018)
4	Fe-TiO_2	Sol-gel	Ultrasonic bath	250 W, 25 kHz	Degradation of coloured dye	(Ambati and Gogate, 2018)
5	S-ZrO_2/ MCM-41	Hydrothermal synthesis	Ultrasonic probe	30 – 90 W, 20 kHz	Biodiesel conversion	(Dehghani and Haghighi, 2017)
6	La-HY (zeolite)	Precipitation	Ultrasonic probe	200 W, 20 kHz	Cracking of hydrocarbons	(Oruji et al., 2019)
7	CuO/ZnO /ZrO_2/Al_2O_3	Co-precipitation	Ultrasonic probe	30 – 90 W, 20 kHz	Steam methanol reforming	(Ahmadi et al., 2016)
8	SAPO-34	Hydrothermal synthesis	Ultrasonic probe	70 W, 20 kHz	Methanol-to-olefin	(Ahmadova et al., 2018)
9	Ni-Mo/ Al_2O_3	Hydrothermal	Ultrasonic probe	90 W, 20 kHz	Glycerol reforming	(Yu et al., 2021)
10	Ni-Ca/ CeO_2	Wet impregnation	Ultrasonic probe	90 W, 20 kHz	Hydrogenolysis of glycerol	(Syuhada et al., 2021)
11	Ni/H-Y zeolite	Hydrothermal	Ultrasonic probe	90 W, 20 kHz	Reforming of sorbitol/glycerol	(Shahbudin et al., 2021)

In fact, this has directly instigated beneficial effects when applied during the synthesis of catalysts with various supports such as alumina, silica, biopolymers or carbon nanotubes (CNT) (Coşkuner et al., 2014; Manzoli and Bonelli, 2018; Suslick et al., 1996).

To illustrate, the Pt/SiO_2 catalyst was ultrasonically treated for the hydrogenation of cinnamaldehyde. It was discovered that the sonochemical pre-treatment was extremely favourable for the selective formation of cinnamyl alcohol (up to 80 %). In addition, the reaction rate also improved twice as much. Ultrasound was said to impart relatively productive metal-support active centres onto the catalyst, which subsequently bestows the catalyst with stronger C=O adsorption sites, hence allowing a higher catalytic turnover rate (Szöllösi et al., 1998).

Furthermore, research was also devoted to investigating the action of acoustic waves during the precipitation of catalysts and their precursors. Low pressure methanol synthesis catalysts, copper/zinc hydroxycarbonates $(Cu/Zn)_2(OH)_2CO_3$, were studied by Kunz and co-workers (1995) in order to determine the properties of the agglomerates in their stirred suspensions. Overall, ultrasound influences the size and total surface area of the agglomerates. On the one hand, coprecipitation of precursors subjected to low intensity ultrasonic irradiation (ultrasonic bath) resulted in lower surface areas and smaller agglomerates. On the other hand, co-precipitation of precursors subjected to high intensity ultrasound (ultrasonic probe horn) produced agglomerates of larger sizes and higher surface areas. In addition to the aforementioned catalyst, the

influence of ultrasound on MnO_2 catalysts were also studied, in which the catalyst was tested for its activity in the decomposition of hydrogen peroxide to oxygen. Similarly, sonicated MnO_2 catalysts exhibited a substantial increase in catalytic activity when high intensity ultrasound was used during synthesis, relative to their non-sonicated counterparts. Their study further evinces that ultrasound indeed has a considerable effect on the properties of catalysts, even if it was incorporated during the precipitation or co-precipitation step of the synthesis procedure.

In recent investigations, Yap and colleagues (2018) have discovered that exposing copper manganese oxide catalysts (Hopcalite) to ultrasonic irradiation of different intensities during the aging step effectively alters and enhances their morphology and hence their catalytic activities, in comparison to that of unsonicated samples. In their investigation, the catalyst was used to oxidise and remove methane and sulphur dioxide gases from compressed natural gas (CNG). Akin to aforementioned investigations, structural modifications were imparted onto the catalyst after ultrasonic treatment. For instance, particle clouds with copper oxide as the primary constituent were noticeably smoothened and well-dispersed, amorphicity of the catalyst was increased, the increase in total surface area resulted in an improved conversion rate and the surface oxide passivating layer was effectively decreased.

Ambati and Gogate (2018) have investigated the effect of ultrasound on the characteristics and performance of the iron doped TiO_2 catalyst, which was compared to its conventionally prepared counterpart. After a comprehensive series of characterisation tests, they established the significant role that

ultrasound plays in improving the overall characteristics and performance of the catalyst. The ultrasonically treated catalyst was demonstrated to have smaller particle and crystallite sizes. The minimum particle size for the ultrasonically synthesised and conventionally synthesised catalysts were 99 nm and 325 nm, respectively. On the other hand, the crystallite size for the ultrasonically synthesised and conventionally synthesised catalysts were 25.42 nm and 31.15 nm, respectively. They also identified a higher degree of agglomeration in the conventionally prepared catalysts, while the ultrasonically synthesised catalysts possess a more uniform surface morphology and average particle size. All these factors subsequently contributed to the substantial increase in BET surface area for the ultrasonically synthesised catalysts, which was reported to be 49.14 $m^2 g^{-1}$, as opposed to a mere 23.13 $m^2 g^{-1}$ for the conventionally prepared catalysts. Besides, utilising ultrasound also significantly reduced the reaction time from 4 h to 60 min. The effectiveness of ultrasound was even more pronounced when the photocatalytic degradation of Acid Blue 80 dye was performed. The ultrasonically prepared Fe doped TiO_2 catalyst resulted in a degradation of 38.0 %, whereas the conventionally prepared catalyst showed a degradation of 31.1 %. Overall, they have successfully established the significance of employing ultrasound in effort to obtain Fe doped TiO_2 catalysts with superior morphological properties and catalytic performance.

Dehghani and colleagues (2017) investigated the preparation of a sono-sulfated zirconia nanocatalyst supported on MCM-41 by using an ultrasound-assisted impregnation/hydrothermal hybrid method. The performance of the catalyst was used in the esterification of oleic acid in soybean oil to simulate the

production of biofuel. They reported an improvement in morphology, particle size, surface area and particle size distribution compared to the non-sonicated samples. Besides, they noted the strong interaction of sulphate groups with the dispersed zirconia located on the pore walls, thus forming stable "sulphated zirconia". In the reaction tests, the sample irradiated at the highest intensity (90 W) performed the best, in which a biodiesel conversion of 96.9 % was achieved, while displaying a good recyclability. For comparison purposes, the unsonicated counterpart achieved a conversion of 81.6 % under the same conditions.

A novel technique to prepare La-modified Y zeolite catalysts, used in the catalytic cracking of bulky hydrocarbons, was presented (Oruji et al., 2019). The ultrasound-assisted precipitation method to synthesise the catalysts was compared to that of the conventional wet impregnation and precipitation methods. The ultrasonic method was far superior to the other two methods, with improved external surface area and mesopore volumes, while preserving the crystalline structure of Y zeolite after La incorporation. Furthermore, the small La particles were well-dispersed on the zeolite support, leading to a uniform coverage of acid sites, which prevented bulk coke formation that blocks the micropore opening mouth. In this case, superior catalytic activity in the catalytic cracking reaction was achieved, with increases in gasoline, kerosene and diesel yields. Furthermore, a 22.9 % reduction in coke formation rate was also observed. This innovative technique is an attractive way to replace classical synthesis techniques for catalytic cracking catalysts.

Ahmadi and associates (2016) investigated the sonochemical co-precipitation of $CuO/ZnO/ZrO_2/Al_2O_3$ catalyst for the production of fuel cell grade hydrogen via steam methanol reforming. The catalysts were synthesised with a range of ultrasonic powers (30 – 90 W) and compared to an unsonicated one. The application of ultrasound effectively allowed homogeneous nucleation that prevents the excessive growth of crystals and aggregations, with the sample synthesised at 90 W exhibiting the best properties. Said sample had the high Cu dispersion and BET surface area, with the lowest extent of agglomeration. In the reaction tests, the sample achieved a 100 % methanol conversion at 200 °C, with the lowest selectivity for undesired CO. Additionally, the catalyst was also tested for its stability, which lasted up to 24 h without any significant decrease in activity.

Ahmadova and co-workers (2018) synthesised SAPO-34 catalysts via a sonochemical method at different ultrasonic powers of 40, 70 and 100 %, while comparing them to the non-sonicated hydrothermally prepared counterpart. The sample synthesised at 40 % (SAPO-34-U40) showed the best properties and activity. Overall, the sonicated catalysts had smaller crystallite sizes, uniform particles and higher BET surface areas, with SAPO-34-U40 having the highest surface area among all samples. For instance, the unsonicated catalyst had a surface area of 434 $m^2\ g^{-1}$, while SAPO-34-U40 had an area of 987.9 $m^2\ g^{-1}$. In the catalytic process of methanol-to-olefin, SAPO-34-U40 had the highest yield of 97 wt% light olefins at 375 °C. Furthermore, coke formation was also less apparent in the sonicated samples.

As evidenced by recent investigations, ultrasonic irradiation has been introduced into the synthesis of various heterogeneous catalysts that are utilised for a wide range of applications such as hydrogenation, oxidation, photocatalytic degradation, alkene reduction, esterification, catalytic cracking, steam reforming, methanol-to-olefin (MTO), etc.

1.6. Ultrasound for nickel catalysts

In recent years, the incorporation of ultrasound in the synthesis of several supported nickel catalysts have been explored, in an endeavour to study and constantly improve the functionality of nickel catalysts for their widespread application. Wang and colleagues (2009) have concluded that Ni-Mo-B catalysts synthesised via an ultrasonic route exhibited an improved catalytic activity in the hydrodeoxygenation of phenol, in comparison to that synthesised regularly using the chemical reduction method. They noted modifications in terms of the particle size, agglomeration tendency, total surface area and elemental compositions of the sonicated catalysts.

Similarly, Vargas and his associates (2016) synthesised nickel catalysts supported on m-ZrO_2 through a simple ultrasonic process. Through characterisation tests, it was determined that the application of ultrasound resulted in a more effective dispersion of the nickel particles; hence, the catalyst exhibited excellent activity and selectivity in the CO_2 methanation reaction. They have also suggested that this preparation method has the potential to be applied on a wider scale.

In an investigation led by Rahbar Shamskar and colleagues (2017), the physical and catalytic properties of ultrasound-assisted co-precipitated NiO-Al_2O_3 powders were evaluated. They were successful in demonstrating the positive effects imparted on the catalysts through sonication. On the one hand, sonicated samples displayed a higher BET surface area as well as a higher activity in the dry reforming of CH_4. On the other hand, the sonicated catalysts also possessed higher stability with a lower degree of carbon formation, thus experiencing a lesser extent of catalyst deactivation.

In recent studies carried out by Ameen and associates (2019), they have revealed that incorporating power ultrasound into the synthesis of the bimetallic solid acid catalyst Ni-Mo supported on γ-Al_2O_3 had substantial effects on the morphology and physicochemical properties of the catalyst. For instance, the surface area, pore size and pore volume increased with the application of ultrasound. Upon further hydrodeoxygenation reactions with rubber seed oil, they discovered that the sonicated catalysts were more active than the conventionally synthesised catalysts in terms of the yield of hydrocarbons, in which the former presented a 17.8 % increase in yield compared to the latter. They ascribed this improvement to the lower binding energy and reduction temperatures of the catalysts, as well as the higher surface area and the homogeneous dispersion of metal particles onto the catalyst support. Furthermore, enhancements in crystallinity were also recorded, which modified the oxidation states of the active sites.

While there have been studies on the ultrasound-assisted synthesis of nickel catalysts supported on various supports such as alumina, molybdenum, boride and zirconia, research in this area is still relatively scarce and limited. On top of that, the widely used silica-supported nickel catalyst still remains unexplored in that matter. Literature reported the sonochemical deposition and characterisation of nickel on silica microspheres, in which the potential of the sonochemical method as a deposition tool of amorphous metal clusters on morphologically fascinating substrates was investigated (Ramesh et al., 1997). Considering the fact that this area in nickel catalysis remains relatively unexplored, this enkindles the initiation to delve into this topic in order to further ascertain the possibility of ultrasound as a useful alternative for the synthesis, characterisation and functionality enhancement of nickel catalysts.

1.7. Recovery of nickel from spent catalyst

In Malaysia, spent catalysts including nickel-based catalysts are considered as scheduled wastes, according to the Department of Environment's Environmental Quality (Scheduled Wastes) Regulations 2005, under the Environmental Quality Act (1974). Furthermore, wastes of such nature are obliged to undergo appropriate processing and treatment by a licensed waste treatment facility prior to proper landfill disposal, as the spent catalysts are hazardous to the environment due to the presence of soluble or leachable organic and inorganic compounds (Idris et al., 2010). This naturally more often poses a disposal problem, as extra expenses will be incurred in order to treat such wastes. Nevertheless, it is also desirable to recover and recycle precious or active metals from spent catalysts

to offset its cost. It should also be noted that this practice is greatly recommended as opposed to disposal due to its myriad benefits from economic and environmental standpoints.

In this case, it is of utmost importance to ensure that the recovery process is constantly being improved and optimised for the recovery of catalyst active metals. This is highlighted by the fact that various investigations have been carried out in recent years in efforts to explore different possibilities in the recovery of metals from spent catalysts. For instance, platinum group metals are recovered from spent catalysts via several hydrometallurgical and pyrometallurgical processes, as revealed in a comprehensive review by Dong and colleagues (2015). In addition to precious platinum metals, the recovery of many other base metals such as V, Ni, Co and Mo from petrochemical wastes were also studied and reviewed excellently by Akcil and co-workers (2015). Green and eco-friendly processes which employs chelating agents such as ethylene diamine tetraacetic acid (EDTA) are also developed for the recovery of heavy metals (Chauhan et al., 2013a). Moreover, the extraction of catalytic metals exclusive for fatty acid hydrogenation processes, such as Ni, is also an area of growing interest. Researchers have manipulated various process parameters such as temperature, reagent concentration, digestion time, agitation rate, etc. in order to determine the most efficient conditions for Ni recovery (Idris et al., 2010; Lee et al., 2010).

Considering the mechanisms associated with ultrasonic irradiation, as mentioned in Section 1.6, it is therefore reasonable to speculate that appreciable effects can be harnessed when it is applied for the recovery of Ni from spent

catalysts. Nevertheless, this aspect of metal recovery has not been greatly investigated, which serves as the motivation for the content which follows in Chapter 7 of this thesis.

1.8. Project rationale

The rationales behind the investigations presented in this thesis were derived based on the background information and literature search described in previous subsections. Firstly, catalyst deactivation is still a major issue affecting most heterogeneous catalytic reactions to date. While those of certain hydrogenation reactions and processes have been studied extensively, such as those concerning petroleum hydrotreating or hydrogenation reactions, those of bio-based feedstock such as plant oils and fats remain relatively undefined. Therefore, it is crucial to bridge the knowledge gap in this area so that appropriate further measures can be taken to prolong or even avert nickel catalyst deactivation in those processes.

The improvement and discovery of novel nickel catalysts are constantly underway. From a perspective of innovative applications, the effect of combining unusual techniques with conventional synthesis techniques might yield surprising and positive results. This culminated in the idea of incorporating a metal dopant and ultrasonic irradiation into the synthesis of nickel catalysts, which can be subsequently tested in catalytic reactions such as the partial hydrogenation of edible oil to determine the feasibility and effectiveness of the technique.

This led to the realisation that investigations present in the literature pertaining to ultrasound-assisted composite synthesis did not explore the effects of sonication at different stages in the synthesis procedure. Essentially, the usage of ultrasound appeared to be rather random and unmethodical, which is further demonstrated by the fact that no justifications or explanations were provided as to why ultrasound was applied at these specific steps during synthesis. Consequently, this instigates further uncertainties: what is the significance and consequence of incorporating ultrasonic irradiation at these different points (i.e. co-precipitation, support loading, aging etc.) during material synthesis? Subsequently, will this result in the formation of final composites with varying structures and properties?

Lastly, it is crucial to recover and recycle useful and reusable components from spent catalysts, especially on an industrial scale due to its associated economic and environmental benefits. The recovery of nickel from spent hydrogenation catalysts is still a topic that is not largely explored. This could entail the usage of various technologies to achieve better or rapid recovery, which has yet to be optimised and applied efficiently on an industrial scale. Therefore, it will be interesting to see the effect of applying ultrasonic irradiation as a means of process intensification in the recovery of nickel from spent industrial catalysts.

In this case, it is apparent that there is a need to fill these gaps in the literature and promote a better understanding of these areas, as well as build on existing research to expand scholarly knowledge of these contemporary problems.

1.9. Research aim and objectives

The overall aim of this research project is to develop new knowledge based on nickel-based heterogeneous catalysts that are primarily used in the hydrogenation of plant-based feedstock, as well as to improve the functionality and properties of the catalyst. In that respect, the entirety of this thesis is regarded as describing the life cycle of the nickel catalyst – from investigating (i) its deactivation mechanisms in plant-based liquid organic media, to (ii) its ultrasound-assisted synthesis, characterisation and catalytic evaluation in the hydrogenation of edible oil and lastly to (iii) its enhancement in recovery from spent catalyst through ultrasound-augmented hydrometallurgy.

The objectives of this thesis are as follows:

a) Investigate and ascertain the dominant deactivation mechanisms of nickel catalysts in the hydrogenation of plant-based liquid organic media.
b) Synthesise, characterise and evaluate MgO-doped silica-supported nickel catalysts enhanced with a dopant and ultrasonic irradiation.
c) Evaluate the catalytic activity of selected catalyst samples via the partial hydrogenation of edible (sunflower) oil.
d) Evaluate the impacts on the textural, structural, morphological, reduction and surface composition properties of catalytic composite materials when applying ultrasonic irradiation at different stages during the synthesis process.
e) Study and optimise the recovery of nickel from spent industrial catalyst waste via ultrasound-assisted hydrometallurgy.

1.10. Thesis overview

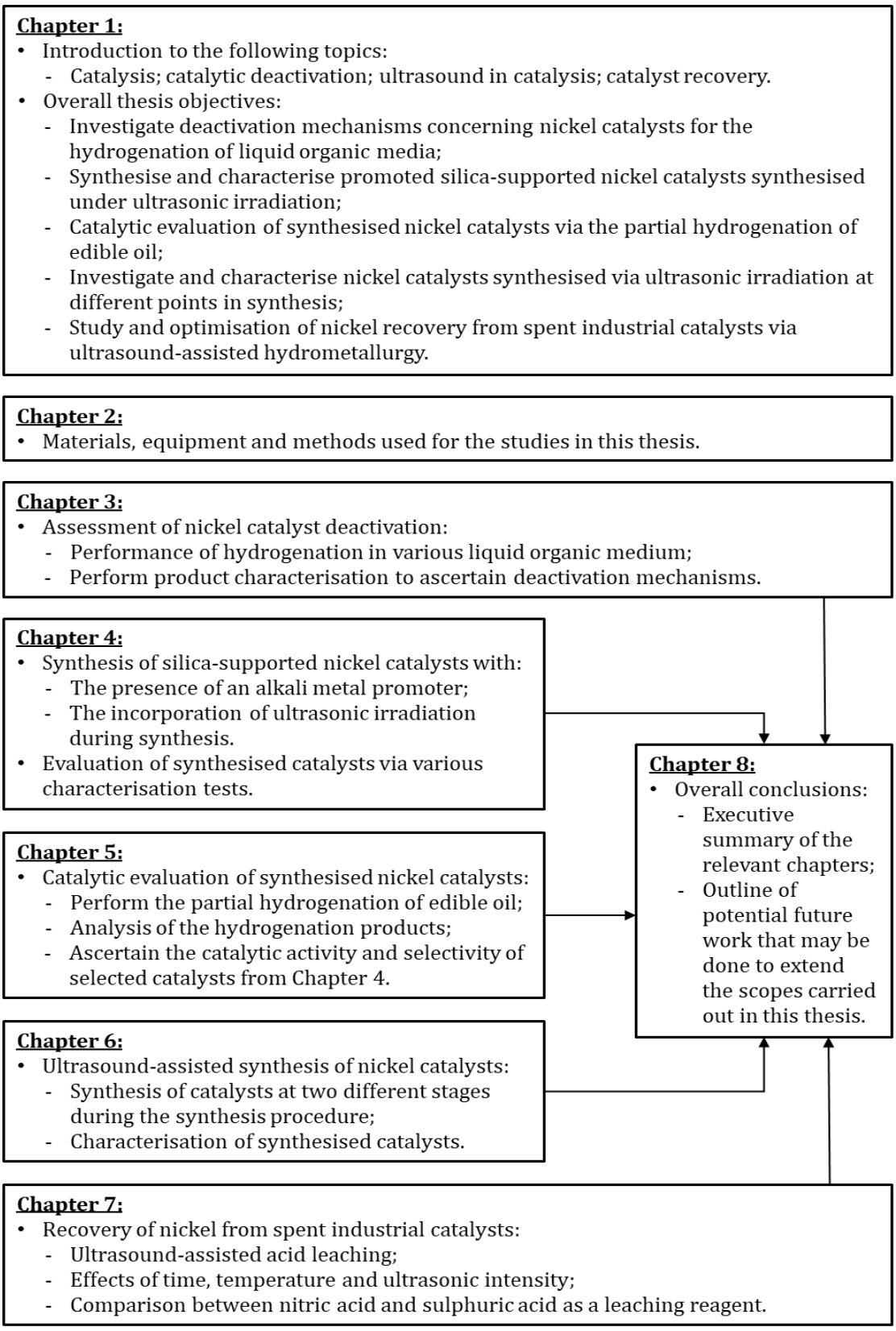


Figure 1.7: Flowchart of the overview of the entire thesis.

2. Materials and Methodology

2.1. Introduction

This chapter provides detailed information on the materials and methodology utilised and employed in this work, which includes various characterisation tests and product analyses. As the contents of Chapters 3 – 7 differ significantly in the contexts of content and experiment, this present chapter will therefore serve as an "umbrella" chapter to describe the materials and methods commonly shared by the individual chapters. Contrariwise, materials and methods exclusive to each chapter are described separately under the experimental section of the respective chapters.

2.2. Ultrasonic equipment

A high intensity 20 kHz ultrasonic probe (Sonics and Materials, VCX 750, 750 W) with a diameter of ca. 1 cm, was used for the investigations in this thesis pertaining to the synthesis of catalytic materials, such as those in Chapters 4 and 6. The experimental setup is shown in Figure 2.1. In a standard experimental setup, the piezoelectric casing of the ultrasonic probe is clamped steadily using the built-in holder. During standard operations, the probe tip is immersed into the sonicated solution at a depth of approximately 2 cm.

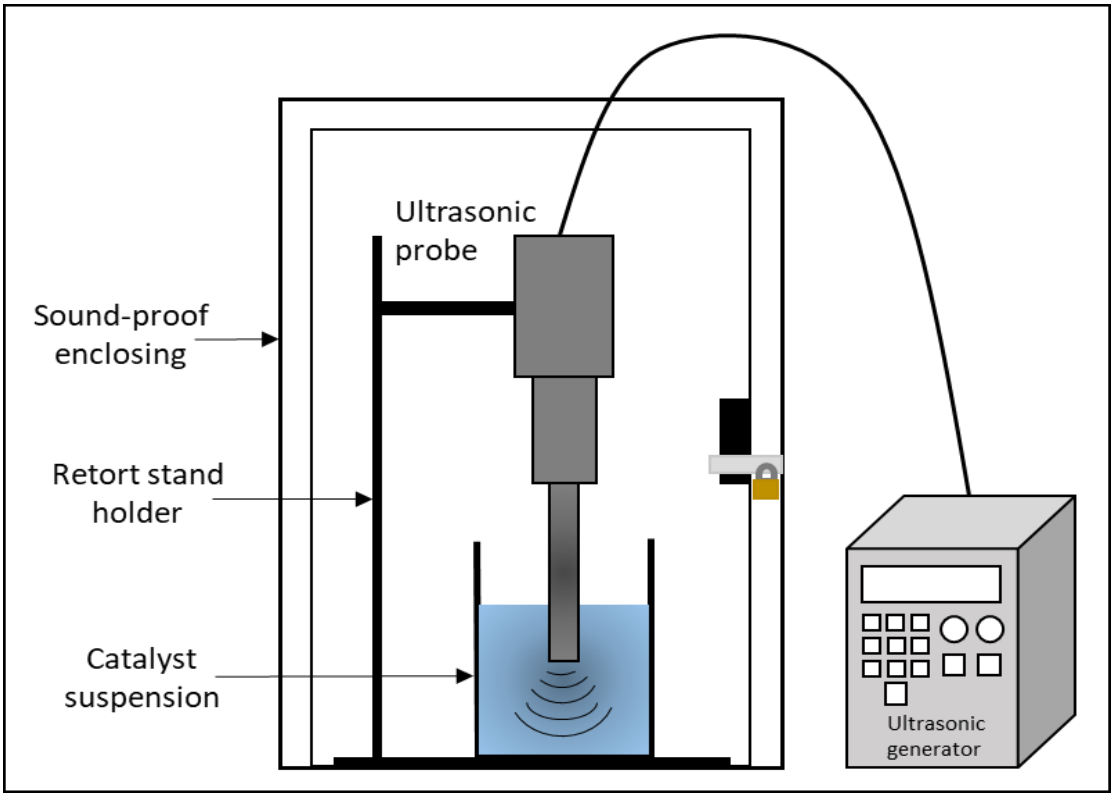


Figure 2.1: Schematic diagram of the 20 kHz ultrasound probe setup.

The ultrasonic bath used in this research for catalytic recovery in Chapter 7 had an operating frequency of 35 kHz (Elma; Transsonic TI-H-15; 200 – 800 W), with the schematic setup shown in Figure 2.2. In a standard experimental setup, the sample will be contained in a conical flask and placed in a water bath inside the ultrasonic bath, with the water level of the bath exceeding the level of the sample in the conical flask at all times.

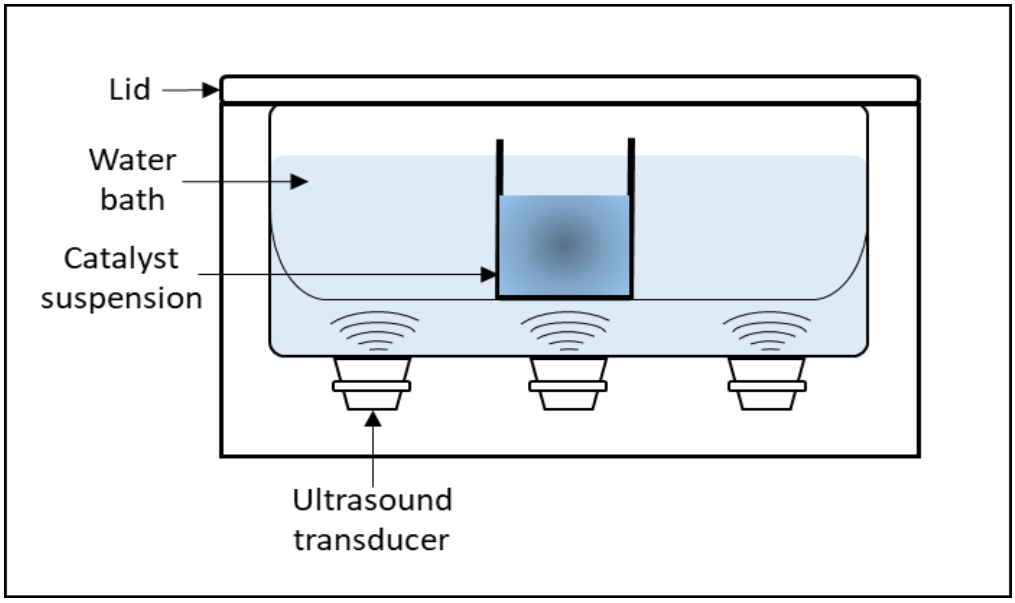


Figure 2.2: Schematic diagram of the 35 kHz ultrasonic bath setup.

2.2.1. Calorimetry

It is not uncommon to see a vast majority of literature sources lack critical information regarding the sonochemical energy output in the ultrasonic systems employed, whereby only the electric powers specified by the ultrasonic generators (as provided by manufacturers) are detailed. However, it should be emphasised that this practice provides only an estimate of the energy dissipated into the system, which could considerably underestimate or overestimate the actual energy supplied by the ultrasonic source. Therefore, it is imperative to perform routine calibration experiments to obtain data that reflects the actual acoustic power dissipated by the ultrasonic source. By doing so, proper replication or comparison between systems or experiments can be executed in a standardised manner, which enhances experimental reliability and consistency. In this work, calorimetry for both the ultrasonic probe and ultrasonic bath was carried out, with

procedures described below, based on the heat energy dissipated by the ultrasonic sources (Koda et al., 2003; Mentler et al., 2017; Tiong et al., 2017a, 2017b).

2.2.1.1. Ultrasonic probe

To obtain the calorimetry data for the ultrasonic system used, a beaker of 200 ml deionised water was subjected to irradiation with ultrasonic amplitudes of 20, 30 and 40 %, total duration being 30 min. The temperature of the system was not regulated. The power output of the ultrasonic system, Q, was obtained using the following equation:

$$Q = \frac{mC_p\Delta T}{\Delta t} \qquad \text{Eq. (2.1)}$$

where:

m is the total mass of water, C_p specific heat capacity of water (4.18 kJ kg^{-1} °C^{-1}), $\Delta T/\Delta t$ (°C s^{-1}) is the temperature gradient. Temperature readings were repeated at 30 s intervals and taken at three varied positions in the beaker, noting the mean value.

To ascertain the heat dissipated by the system, water at an equal volume to the ultrasonic set was heated using a portable electric heater of 1000 W, while being stirred. Similarly, the process took 30 min and readings were repeated at 30 s intervals and taken at three varied positions in the beaker, noting the mean value. The power output due to heating, Q_H, can be acquired using Eq. (2.2). Hence, the heat dissipated, Q_{HL}, can be obtained using the following equation:

$$Q_{HL} = Q_H - Q \quad \text{Eq. (2.2)}$$

Subsequently, the acoustic energy intensity provided by the probe, I_{US}, is calculated via the following equation:

$$I_{US} = \frac{Q+Q_{HL}}{A} \quad \text{Eq. (2.3)}$$

where:

$Q + Q_{HL}$ is the output power, P_{out}, and A is the cross-sectional area of the surface producing ultrasonic waves, determined as 0.8 cm^2 for the ultrasonic probe.

In addition, the ultrasonic density provided by the probe to the liquid body, ρ_{US}, is calculated via the following equation:

$$\rho_{US} = \frac{Q+Q_{HL}}{V} \quad \text{Eq. (2.4)}$$

where:

V is the volume of water (cm^3) in the beaker used for the calorimetry test.

Results of the calorimetry performed for the 20 kHz ultrasonic probe are presented in Section 4.3.1.

2.2.1.2. Ultrasonic bath

A preliminary calibration of the ultrasonic bath was executed using the typical calorimetry method to determine the temperature rise. The calibration was

performed over a period of 14 min, in which there were three time domains (t_1 + t_2 + t_3) throughout the entire period of temperature measurement (Uchida and Kikuchi, 2013). The first 3 min, t_1, is the time before ultrasonic irradiation. The subsequent 3 min, t_2, is the time during ultrasonic irradiation. The last 8 min, t_3, is the time after ultrasonic irradiation. This calibration was also repeated at amplitudes of 20, 40, 60 and 80 % to ascertain the ultrasonic density of the respective amplitudes. Temperatures were recorded every 30 s and said calibration was repeated thrice in order to assess its consistency. All experiments were carried out at a fixed position in the ultrasonic bath to ensure consistent ultrasonic treatment. The total heat generated (Q) by the transducers translates to its total power output, and was calculated based on the following equation:

$$Q = mCp\Delta T \qquad \text{Eq. (2.5)}$$

where:

m is the mass of water (g); C_p is the specific heat capacity of water (J g^{-1} K^{-1}); ΔT is the temperature difference (K).

The ultrasonic power (W) was then calculated by dividing the heat generated (Q) over the total time taken (s) for heating to occur:

$$\text{Ultrasonic power} = \frac{\text{Heat generated}}{\text{Total time taken}} \qquad \text{Eq. (2.6)}$$

Lastly, the ultrasonic density (W cm^{-3}) sustained by the beaker of water is calculated by dividing the ultrasonic power (W) by the total volume (cm^3) of water in the beaker (calculated as 50 cm^3).

$$\text{Ultrasonic density} = \frac{\text{Power}}{\text{Total Volume}} \qquad \text{Eq. (2.7)}$$

Results for the calorimetry performed for the ultrasonic bath is presented in Section 7.3.2.

2.3. Materials

Deionised water used in this work was acquired from the Milli-Q® Advantage A10 Ultrapure Water Purification System. The resistivity of the deionised water obtained always exceeded 18 MΩ cm, indicating the absence of dissolved salts and a corresponding neutral pH of approximately 7. Sulphuric acid (H_2SO_4, 96 w/v%) and nitric acid (HNO_3, 65 w/v%) employed were of reagent grade, purchased from R&M Chemicals (Malaysia) and used without any supplemental purification. Nickel sulphate hexahydrate ($NiSO_4.6H_2O$), magnesium sulphate heptahydrate ($MgSO_4.7H_2O$), sodium metasilicate pentahydrate ($Na_2SiO_3.5H_2O$) and sodium carbonate (Na_2CO_3) employed were of analytical grade, purchased from R & M Chemicals (Malaysia) and used without supplemental purification.

2.4. Analytical techniques

2.4.1. Field emission scanning electron microscopy (FE-SEM)

In this thesis, the surface morphology of all powdered samples was characterised using a field emission scanning electron microscopy (FE-SEM, Fei Quanta 400F). The micrographs were taken using a Fei Quanta 400F microscope at a beam current of 1 μA and an accelerating voltage of 20 kV. Prior to the analysis, the powdered samples were coated with platinum to increase their conductivity for clearer imaging using a rotary pumped coater (Quorum Q150RS PLUS) for 60 s.

2.4.2. Energy dispersive X-ray (EDX) analysis

The elemental composition of the powdered samples was acquired using a field emission scanning electron microscope (FE-SEM) equipped with an Oxford Instruments X-MAX energy dispersive X-ray (EDX) analyser at an accelerating voltage of 20.0 kV and an acquisition live-time of 45 s. It is noted that this EDX system is interfaced to the SEM system in Section 2.4.1. The emission of X-rays occurs after the lowering in energy of electrons from the outer shell of atoms, which then proceeds to fill the holes in the lower shell. The detected signals are presented as the emitted X-ray intensities versus their energies. Identification of the elements present in the sample is based on the energies of the characteristic X-rays, while the concentrations of said elements are based on the intensities of the X-ray peaks (Razeghi, 2009).

2.4.3. X-ray powder diffraction (XRD)

X-ray diffraction patterns were acquired using a PANalytical X'Pert-PRO diffractometer in order to determine the bulk crystalline phase structures and their constituents in the samples, displayed in the 2-theta range of 10 – 90 °. The wavelength of the Cu-Kα X-ray radiation applied was 1.54060 Å while the beam current and voltage were 40 mA and 45 kV, respectively. XRD patterns acquired were compared to standard patterns obtained from the literature. The crystallite size, *D* (nm), of the powdered samples can be estimated using the Debye-Scherrer's formula (Singh et al., 2012):

$$d = \frac{K\lambda}{\beta \cos\theta} \qquad \text{Eq. (2.8)}$$

where:

K is the shape factor (0.89); λ is the wavelength of the X-ray source (0.154 nm); β is the full width at half maximum of the diffraction peak (rad); θ is the Bragg's diffraction angle (°).

It should be noted that the term crystallite in this thesis refers to the individual Ni constituents that make up the whole catalyst or composite particle. In other words, catalyst or composite particles comprise the Ni crystallites as well as the support phases.

2.4.4. Fourier transform infrared spectroscopy (FT-IR)

Fourier transform-infrared (FT-IR, Perkin Elmer Frontier) spectra were recorded at wavenumbers of 4000 – 400 cm^{-1}, with the powdered samples pressed onto and completely covering the quartz sample holder. A resolution of 4 cm^{-1} was used with an average of 64 spectra scans for each powdered sample.

2.4.5. Brunauer-Emmett-Teller (BET) analysis

One of the most crucial characterisation tests for supported heterogeneous catalysts is the surface area and porosity measurement. The surface analyses of the samples were performed using a Micromeritics 3Flex Surface and Catalyst Characterisation by employing the Brunauer-Emmett-Teller (BET) and Barrett-Joyner-Halenda (BJH) methods. The adsorption and desorption experiments were executed at -195.681 °C (77 K) using nitrogen (N_2). Prior to the analysis, the samples were pre-treated by degassing at 150 °C for 4 h.

2.4.6. Temperature programmed reduction (H_2-TPR)

The reduction properties of the powdered samples were determined via the temperature programmed reduction of hydrogen (H_2-TPR), carried out using the Micromeritics AutoChem II 2920 chemisorption analyser equipped with a thermal conductivity detector (TCD). In a typical experiment, approximately 30 mg of powdered samples were placed in the quartz U-tube reactor in a tubular furnace. Prior to the analysis, the samples were pre-treated with Ar at a flow rate of 20 cm^3/min and heated from room temperature to 100 °C with a temperature ramp

of 10 °C/min and held for 60 minutes to remove physisorbed and/or weakly bound species. Following, the samples were subjected to 9.47 % of H_2 in Argon at an injection rate of 25 cm^3/min from room temperature to 900 °C with a heating ramp of 10 °C/min. The vapour produced is removed via a cold trap filled with chilled coolant. The amount of hydrogen consumed by each sample was measured by a TCD and calculated from the peak area of the H_2-TPR profile. The H_2-TPR profiles were processed using the OriginPro software.

2.4.7. Hydrogen pulse chemisorption

The dispersion properties of the powdered samples were acquired via hydrogen pulse chemisorption, which was conducted using the Micromeritics AutoChem II 2920 chemisorption analyser. Calcined and unreduced powdered samples were degassed in an inert argon gas flow for 1 h, followed by reduction at 500 °C in hydrogen gas for 2 h and degassed once more for 30 min prior to the chemisorption analysis. For the analysis, hydrogen gas was pulsed every 6 min until no further uptake was detected. The Ni metal dispersion (%) is calculated with the following equation:

$$\%\text{Dispersion} = \left(\frac{\frac{V_m}{V_{mol}}}{\frac{M_{\%}}{W_a}}\right)(F_s)(100)(100) \qquad \text{Eq. (2.9)}$$

where:

V_m is the volume of hydrogen gas chemisorbed (cm^3 g^{-1} STP); V_{mol} is the molar volume of the adsorptive (cm^3 $mole^{-1}$ STP); $M_{\%}$ is the percentage of Ni metal by

weight as grams of Ni per gram of sample; W_a is the atomic weight of Ni (g mole^{-1}); F_s is the stoichiometry factor, taken as 2 for hydrogen on Ni.

The active metal surface area (m^2 g^{-1}) is calculated with the following equation:

$$\text{Metal surface area} = F_s n_a N_A A_g \qquad \text{Eq. (2.10)}$$

where:

F_s is the stoichiometry factor, taken as 2 for hydrogen on Ni; n_a is the number of moles of gas adsorbed (cm^3 g^{-1} STP); N_A is Avogadro's constant; A_g is the cross-sectional area of the active adsorptive atom (nm^2) (with the assumption that Ni has the proportion of low index plane fcc (111):(100):(110) = 1:1:1, with a single Ni atom occupying 0.0649 nm^2 (Bergeret and Gallezot, 2008).

The average particle size (nm) is calculated with the following equation (Webb and Orr, 1997):

$$\text{Average particle size} = \frac{6}{(A_{Sm})(\%\text{Dispersion})(\rho)} * 100 \qquad \text{Eq. (2.11)}$$

where:

A_{Sm} is the active metal surface area (m^2 g^{-1}); ρ is the density of the metal (g cm^{-3}).

Compared to the BET physisorption analysis as described in Chapter 2.4.5, which measures the overall surface area of the pre-reduced samples, the hydrogen

pulse chemisorption measures the Ni dispersion as well as the active Ni surface area of the samples that are reduced in-situ. This analysis could serve as a good indication of the activity of the samples, prior to carrying out activity tests.

2.4.8. X-ray photoelectron spectroscopy (XPS)

The superficial properties of the calcined powdered samples were analysed via XPS, conducted with the JEOL JPS-9030 photoelectron spectrometer. Al Kα (1486.6 eV) was used as the excitation source to probe the sample surface information at a depth of 1 – 12 nm. The pressure in the analysis chamber during experiments was less than 5×10^{-10} Torr. A hemispherical electron-energy analyser working at a pass energy of 30 eV was used to collect core-level spectra. The samples were dispersed in ethanol and placed on silicon wafers, which were mounted on a sample holder and directly transferred into the analysis chamber. Step size was adjusted to 0.1 eV, dwell time was set at 100 ms and the high-resolution spectra were recorded with 10 scans. Charge effects were corrected by using the C 1s peak at 285 eV. A Shirley background was applied to subtract the inelastic background of core-level peaks. The model peak to describe XPS core-level lines for curve fitting was a product of Gaussian functions. The XPS spectra were processed using the OriginPro software.

2.4.9. Atomic absorption spectrometry (AAS)

Atomic absorption spectrometry (AAS) analysis was conducted with a Perkin Elmer AAnalyst 400 to obtain the concentration of leached nickel from the

hydrogenated oil sample. Prior to the analysis, the oil samples were first dissolved in a fixed amount of organic solvent. Three readings were taken for each sample and a wash time of 120 s was allocated between analyses.

2.4.10.Thermogravimetric analysis (TGA)

Thermogravimetric analysis (TGA) for the spent catalysts was conducted on a Mettler Toledo TGA/DSC 1 thermal analyser at ambient conditions. The heating rate was 10 °C/min.

2.5. Product analysis

2.5.1. Determination of iodine value (IV)

The iodine value measures the degree of unsaturation of fats and oils, which represents the mass (g) of iodine consumed per 100 g of oil. Hydrogenation products collected from the reactor were subjected to iodine value tests, in accordance with the American Oil Chemist's Society (AOCS) Official Method Tg 1a-64, performed 3 times to obtain average values. In essence, the resulting iodine value was calculated with the following formula:

$$\text{Iodine value} = \frac{(\text{B}-\text{S})\text{x N x } 12.691}{\text{mass of sample,g}} \qquad \text{Eq. (2.12)}$$

where:

B is the volume of titrant of blank set, mL; *S* is the volume of titrant of sample set, ml; *N* is the normality of the sodium thiosulphate solution. Detailed procedures of

the sample preparation and a sample calculation for a hydrogenation product is presented in Appendix I.

2.5.2. Gas chromatography (GC) analysis

The gas chromatography analysis was performed on the hydrogenation products to determine their respective fatty acid compositions. A PerkinElmer Clarus 500 gas chromatograph fitted with a PerkinElmer COL-ELITE-2560 capillary column (100 m x 0.25 mm ID x 0.20 μm df) was used for the analysis. Helium gas was used as carrier gas at 1.3 ml/min. Prior to the analysis, the hydrogenation products were esterified into fatty acid methyl esters (FAME) according to the standard procedure by Jham et al. (1982). Detailed procedures of the sample preparation and a sample calculation for a hydrogenation product are presented in Appendix II. The oven, injector and flame ionisation detector (FID) temperatures were set at 175, 210 and 250 °C, respectively. Volume per injection was 1 μL with a split ratio of 100:1. The composition and concentration of the fatty acid species were acquired by noting the relative area under the curve of their respective peaks.

3. Deactivation of Nickel Catalysts in Liquid Organic Media

3.1. Introduction

In recent years, the eventual depletion of fossil fuels and subsequent expansion of alternative energy have fuelled the demand for bio-based materials in the synthesis of sustainable and renewable chemicals and fuels. Concerning the modern catalysis industry, this has resulted in the prevalence of processing bio-based liquid feedstock for various applications. In particular, the catalytic hydrogenation reaction is a commonplace process route for the synthesis of myriad chemical intermediates or end products (Lima et al., 2017). These encompass various liquid-phase catalytic reactions such as the manufacture of liquid alkanes from biomass-based carbohydrates (Chheda and Dumesic, 2007), biodiesel production via triglyceride esterification (Chheda and Dumesic, 2007), conversion of aromatics such as toluene and benzene (Rufete-Beneite and Román-Martínez, 2019), oil quality enhancement through biodiesel (FAMEs) partial hydrogenation (Adu-Mensah et al., 2019), bio- and petroleum-based catalytic hydrotreating of heavy oils (Rodríguez et al., 2018; Vásquez et al., 2017), partial hydrogenation of edible oils and fats (Wong et al., 2018), etc.

Perhaps the most ubiquitous issue faced by these hydrogenation catalytic systems is the deterioration of catalyst activity and/or selectivity over time, due to the deactivation of the catalysts employed. The catalysts used in various industrial processes account for a substantial portion of overall operation costs – replacing

spent catalysts coupled with process shutdown cost billions of dollars per annum (Rodríguez et al., 2018). While catalyst deactivation is fundamentally unavoidable, it is still crucial to understand and grasp the mechanisms behind catalyst deactivation in order to curb with its negative effects as well as to formulate innovative solutions to overcome these phenomena, which could prolong catalyst lifetime and subsequently reduce operation costs of chemical processes.

For instance, in the petroleum hydrotreating industry, extensive research has been carried out to ascertain the associated deactivation mechanisms. Coking and the presence of feedstock impurities such as metals (Ni, V, Fe, Ti) or poisons (S, P, N) have been determined to be the largest contributors to the deactivation of hydrotreating catalysts (Amora et al., 2019; Harrhy et al., 2019; Kohli et al., 2019, 2016; Novaes et al., 2017; Pimerzin et al., 2018; Rodríguez et al., 2018; Tian et al., 2018; Torres-Mancera et al., 2018; Wang and Wang, 2016). Undesirable short cycle lengths may occur if these deactivators are present in substantial quantities, which lead to rapid deactivation that results in the consequential process shutdown and replacement, both of which are costly in terms of time and money (Amora et al., 2019). These investigations could then enable researchers to device efficient solutions to counter or delay catalyst deactivation for these processes. Practical applications of these studies could be observed in modern oil refineries, where impurity guard beds containing Ni-Mo/Al_2O_3 catalysts are installed to avert silicon poisoning caused by the presence of silicon compounds such as polydimethylsiloxanes (compound utilised to aid in crude oil recovery and refining processes) (Nadeina et al., 2019).

The hydrogenation of other renewable bio-based feedstock such as glucose or cellulose have been carried out to manufacture myriad commodity products such as sorbitol, which is utilised in food, pharmaceutical and chemical industries, as well as additives in various end-products (Besson and Gallezot, 2003). In those studies, nickel-based catalysts were determined to pose severe leaching issues, where the nickel active sites of the catalysts dissolved due to the acidic conditions of the reaction. This resulted in a loss of activity and a high nickel concentration in the reactant, which affected the end-products adversely (Kusserow et al., 2003; Lange, 2015).

On the other hand, in processes such as the hydrogenation of fats and oils such as palm-based oils, the mechanisms of catalyst deactivation remain inconclusive and relatively scarce in their investigations – different theories have been proposed for the deactivation of catalysts such as nickel-based catalysts that are commonly employed for the hydrogenation of fats and oils or its derivatives. In particular, catalyst coking (Edvardsson et al., 2001), poisoning (Irandoust and Edvardsson, 1993), Ostwald ripening (Lok, 2018), sintering (Hoffer et al., 2003) have been proposed as the mechanisms. In addition, a brief literature survey would yield no studies regarding deactivation experienced by nickel catalysts for the hydrogenation of palm-based feedstock (i.e. palm stearin). Therefore, further research into the deactivation of these catalysts is needed in order to gain a better understanding of the factors that influence how the catalyst behaves in a particular organic media, which could be of great importance due to its practicality in the industrial manufacturing and processing of oleochemicals that involve the usage of nickel catalysts.

Palm oil is an important source of many food products and oleochemicals (Pande et al., 2012; Yeong et al., 2012), thus it is important that the deactivation mechanisms present in the hydrogenation of palm-based organic media are well understood, as many studies report catalytic activity but do not account for any possible deactivation effects such as leaching. More importantly, while there are numerous investigations regarding enhancing the activity and selectivity of various heterogeneous catalysts available in the literature, those that discuss and study the productivity or stability of those catalysts are often neglected (Scott, 2018). Furthermore, the importance of deactivation studies is amplified by their relevance to industry practitioners, whereby catalyst resilience is a highly sought-after metric in their operations to reduce costs. This is particularly applicable for countries with significant oil-palm plantations such as Malaysia, the second largest producer of palm oil in the world with an expected crude palm oil (CPO) production of 19.6 million tonnes in 2021 (Wong, 2021).

In this section, the deactivation mechanisms undergone by nickel catalysts in the hydrogenation of palm-based liquid organic media were demonstrated. Experimentally, a few palm-based feeds were employed, i.e. refined, bleached and deodorised palm stearin (RBD-PS), split – refined, bleached and deodorised palm stearin (S-RBD-PS), distilled blend fatty acids, benzyl alcohol and citral. It is noted that the latter two feeds were employed to establish the negative effect of feed acidity on nickel lixiviation. On the other hand, the distilled blend fatty acids were formulated by blending fatty acids with varying compositions in order to match the composition of S-RBD-PS. However, the former is considered to be a “clean”

organic feed (i.e. free from catalyst poisons), which is used to demonstrate the effect of catalyst poisoning in this study.

3.2. Experimental

3.2.1. Partial hydrogenation of palm-based liquid organic media

In this study, comparison is made between the hydrogenation of unsplit fats (using RBD-PS) and split fats (using S-RBD-PS). A flowchart illustrating the origin of the unsplit and split fats is shown in Figure 3.1. Apart from the comparison between hydrogenation of split and unsplit fats, hydrogenation was also performed on the blend of distilled pure fatty acids with the same fatty acid composition as S-RBD-PS.

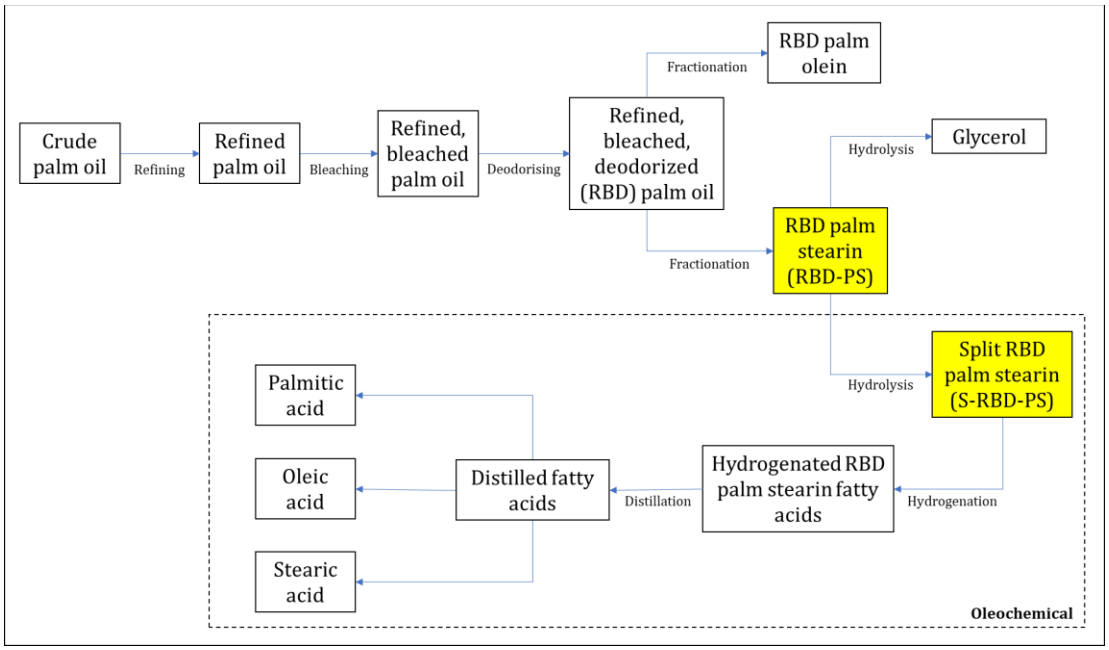


Figure 3.1: Flowchart of a typical oleochemical fatty acid processing plant.

Hydrogenation reactions were carried out in a pressure slurry reactor (1.5 L Buchiglasuster Eco-Clave) connected to a temperature regulator (Huber Unistat Tango Nuevo). The batch hydrogenation reactor was operated at conditions of 195 ˚C, 5 bar and a stirring rate of 2000 rpm. The commercial PRICAT nickel catalyst (Ni = 22 wt%) loading was 0.25 g L^{-1}, which is at a level sufficiently low to observe and compare catalyst deactivation phenomena. The magnitude of IV drop will determine the severity of catalyst deactivation in each case. To investigate the extent of deactivation at higher temperatures, the hydrogenation of split, unsplit fats and distilled fatty acids blend were also performed at 210 ˚C, with other conditions maintained. Hydrogenation of citral and benzyl alcohol were performed at temperatures of 170 and 180 ˚C.

The spent catalysts were recovered via filtration following the termination of hydrogenation reactions. Solvents such as methanol or butanol was added to the fat-coated catalyst residues at an elevated temperature to dissolve the coated fats on the spent catalysts. The spent catalysts were then removed via filtration and dried for further analysis.

3.2.2. Catalyst characterisation and product analyses

3.2.2.1. Transmission electron microscopy (TEM)

Transmission electron microscopy (TEM) analysis was conducted on the fresh and spent catalysts using a 200 kV JEOL JEM-ARM200F transmission election microscope. The image analysis was carried out using the ImageJ image processing software, with an average crystallite size taken from 20 areas on the scan.

3.2.2.2. Ion chromatography

The anionic catalyst poisons were extracted using an ultrasound-assisted technique described by Campos and Cassella (2018). Briefly, 5 g of fat sample was weighed and transferred to a polyethylene tube pre-rinsed with deionised water and dried thoroughly. 40 ml of deionised water was added to the tube and placed in an ultrasonic bath for 15 min at 100 % ultrasonic intensity. The tubes were subsequently vigorously mixed with a vortex mixer for 5 min. The aqueous phase was extracted and filtered for ion chromatography.

To determine concentration of anionic poisons present in the organic samples, ion chromatography was carried out using the Metrohm 930 Compact IC Flex ion chromatographer equipped with a Metrohm Metrosep A Supp 5 – 150/4.0 150X4mm column and a conductivity detector. Standard anion solutions of Cl, N, P and S were prepared with a concentration range of 10 – 50 ppm.

3.3. Results and discussion

3.3.1. Catalytic hydrogenation and leaching studies

It is noted that IV = 0 indicates total saturation of the fatty acids. It can be seen that an IV of < 1 can be achieved at a catalyst dosage of 4 times for the hydrogenation of S-RBD-PS. This represents the minimum IV achievable when an infinitesimally small amount of catalyst that does not experience deactivation is used. Figure 3.2 illustrates the decrease in IV for the RBD-PS feed at 195 °C and at an elevated temperature of 210 °C. With a starting value of 36.5, the IV for the feed

hydrogenated at 195 °C decreased to 15.9 over time; while the IV of RBD-PS hydrogenated at an elevated temperature of 210 °C dropped to 4.9 at the end of the reaction. The increase in reaction temperature from 195 – 210 °C led to a difference in IV drop of 11 points. At a higher hydrogenation temperature, the mass transfer between the reactants and the catalyst surface was considerably enhanced, thus leading to an improvement in the reaction kinetics during the reaction. Consequently, better catalytic activity can be achieved, hence resulting in a greater hydrogenation rate (i.e. the steepness of the hydrogenation curve) and a larger drop in IV at 210 °C. In both cases, it is observed that there is a continued downward trend even after the termination of the reaction, indicating that the catalyst was still actively converting reactant molecules to product molecules. In other words, the catalyst experienced negligible deactivation.

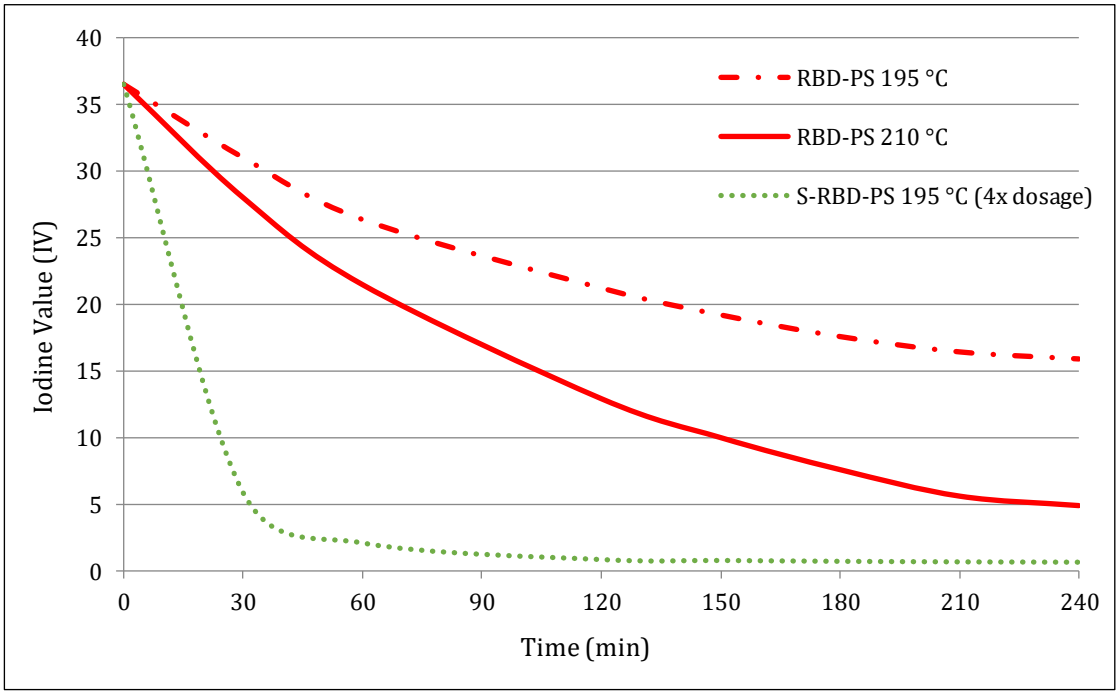


Figure 3.2: Change of IV with reaction time for the hydrogenation of RBD-PS at 195 and 210 °C.

Figure 3.3 depicts the decrease in IV for the S-RBD-PS feed at 195 °C and an elevated temperature of 210 °C. In contrast to the reaction in Figure 3.2 for RBD-PS, the IV for S-RBD-PS decreased to 17.5 at 120 min, in which the conversion plateaued after ca. 120 min with no further reaction. This signifies that the catalyst was virtually deactivated after a reaction time of 120 min, thus unable to further the reaction. On the other hand, despite having a higher initial hydrogenation rate (i.e. steeper hydrogenation curve) at 210 °C, it can be observed that the catalytic activity started to decline ca. 60 min and similar to the reaction carried out at 195 °C, which plateaued at ca. 120 min at an IV of 13.8. In this case, the increase in reaction temperature from 195 – 210 °C registered a further drop in IV of only 3.7.

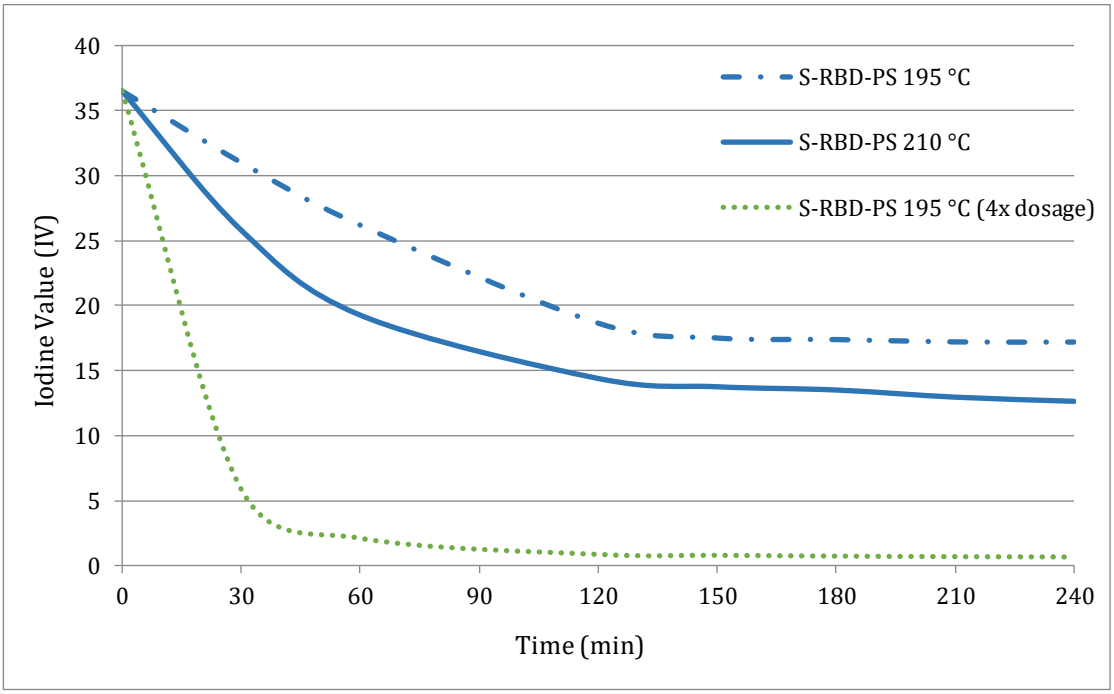


Figure 3.3: Change of IV with reaction time for the hydrogenation of S-RBD-PS at 195 and 210 °C.

The deactivation experienced by the catalyst in this case could be elucidated by the fact that the phenomenon of Ni soap formation (Ariaansz, 1993)

was more apparent in the acidic S-RBD-PS feed, thus causing severe Ni leaching. In heterogeneous metal catalysis, the lixiviation tendency of active metal phases is influenced by the conditions of the reaction medium, e.g. pH, oxidation potential, molecule cheating properties (Besson and Gallezot, 2003). Split palm stearin contains a high proportion of free fatty acids (FFA), which are mostly palmitic, stearic and oleic FFAs in the S-RBD-PS feed used in this present study, as per Figure 3.1. The extent of dissociation of acids, or in other words how readily an acid gives up its protons (H^+), can be represented by the acid dissociation constant, pK_a. An acid with a low pK_a would give up its protons more readily, hence resulting in a feed of higher acidity. With regards to the FFAs present in the S-RBD-PS feed for this study, the palmitic, oleic and stearic acids have pK_a values of 8.6, 9.85 and 10.15, respectively (Kanicky and Shah, 2002). As a reference, the pK_a of pure water is 14 (Meister et al., 2014). Therefore, these FFAs could readily dissociate to release hydrogen ions (H^+), consequently increasing the acidity of the feed. This efficacy in acid dissociation in turn resulted in the dissolution or leaching of Ni metal into the solution to form Ni soap, which can remain dissolved in the reactants. The lixiviation reaction can be described by the equations below:

$$Ni + 2RCOOH \leftrightarrow (RCOO)_2Ni + H_2 \qquad \text{Eq. (3.1)}$$

$$NiO + 2RCOOH \leftrightarrow (RCOO)_2Ni + H_2O \qquad \text{Eq. (3.2)}$$

where:

RCOOH represents fatty acids.

In addition, a visual scheme of this transformation is shown in Figure 3.4(a), which illustrates the dissociation of palmitic acid and the subsequent attack on Ni crystallites. Consequently, the higher dissolution of Ni into the solution led to a more rapid loss of Ni active sites on the catalyst, thus affecting the performance of the catalyst negatively, as per the case of S-RBD-PS hydrogenation. Contrariwise, for unsplit fats such as the RBD-PS feed used in this study, the glycerol molecules are attached to the fatty acid molecules. This constitutes triglyceride molecules (glyceryl tripalmitate, glyceryl trioleate and glyceryl tristearate) that make up the bulk of the RBD-PS, as shown in Figure 3.4(b) with the molecular structure of glyceryl tripalmitate as an example. This effectively suppressed the dissociation of H^+ into the reactant, thus averting Ni leaching and lowering the tendency of Ni soap formation, which allowed the catalyst to function normally with minimal Ni leaching.

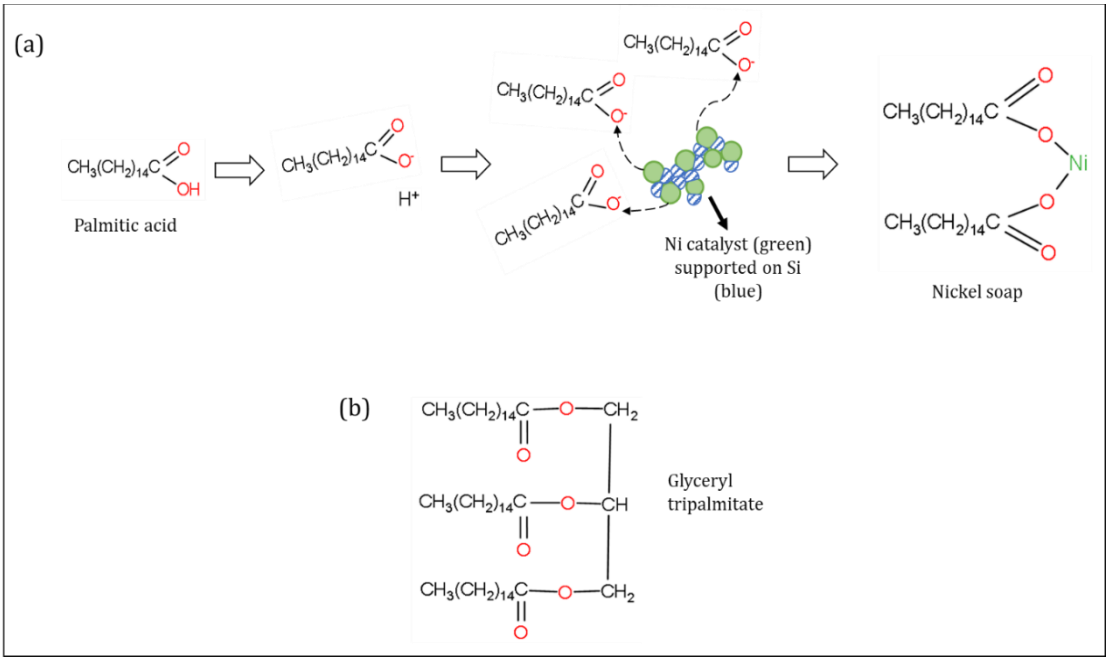


Figure 3.4: (a) Reaction scheme of Ni leaching to form Ni soap; (b) Molecular structure of glyceryl tripalmitate present in RBD-PS.

In order to verify the presence and extent of Ni leaching for the split and unsplit fats, AAS was carried out on the hydrogenation products at different reaction time intervals to determine the concentration of Ni leached into the hydrogenation products. Figure 3.5 demonstrates the strong correlation between the amount of Ni leached and the corresponding hydrogenation activity reported previously. From the figure, the concentration of Ni found in the S-RBD-PS hydrogenation products was higher than that of RBD-PS in all instances. As a case in point, at the time interval of 120 min and reaction temperature of 195 °C, the Ni concentrations found in S-RBD-PS and RBD-PS products were 0.07377 and 0.01011 mg/g_{oil}, respectively. In a more acidic solution, the Ni leached into the hydrogenation products has increased by ca. 7-fold.

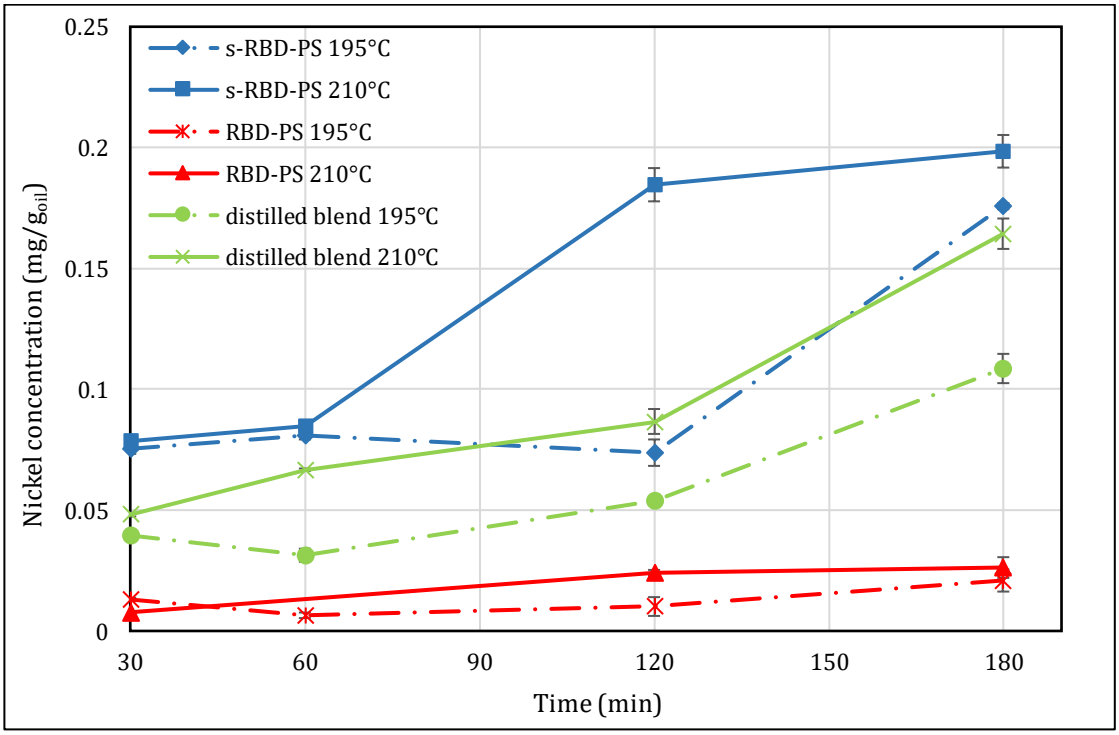


Figure 3.5: Concentration of leached Ni present in the hydrogenation products at different time intervals. Standard deviation represents variation of data obtained from repeating measurements three times.

Furthermore, this leaching behaviour can be further amplified by studying the identical experiment carried out at a reaction temperature of 210 °C. As evidenced by the hydrogenation experiments, the difference in the IV drop achieved between hydrogenating RBD-PS and S-RBD-PS was greater for the reaction ran at the elevated temperature compared to that ran at 195 °C. For example, at 195 °C and 150 min, the difference in IV was 1.7; while at 210 °C, the difference was 3.8. This larger difference also indicates that the deactivation of the Ni catalyst was more severe in the case of S-RBD-PS. At a higher hydrogenation temperature, the mass transfer between the reactant and the catalyst surface was considerably enhanced, which led to an improvement in the reaction kinetics during the hydrogenation process (Alsobaai et al., 2012), causing the greater drop in IV for both split and unsplit reactants due to better reaction rates. However, this also led to the undesirable side-effect of more hydrogen ions being dissociated into the reactant, which increased its acidity. As a higher acidity increases metal solubility, this caused the hastening of Ni dissolution, which increased the Ni concentration in the hydrogenation products. Consequently, this rapidly deactivated the catalyst due a higher degree of loss in nickel active sites, thus resulting in the poorer hydrogenation performance in S-RBD-PS at 210 °C.

Similarly, the AAS results in Figure 3.5 validated this, showing that the Ni concentration in the hydrogenated S-RBD-PS was significantly higher than that of the hydrogenated RBD-PS. This denotes the dissolution of Ni from the catalyst into the hydrogenation products was more severe, thus supporting the Ni soap formation theory mentioned previously.

According to Figure 3.5, at the time interval of 120 min and reaction temperature of 210 °C, the Ni concentrations found in S-RBD-PS and RBD-PS products were 0.1846 and 0.02403 mg/g_{oil}, respectively, thus representing an 8-fold increase. This also shows that Ni leaching was accelerated by the reaction temperature, as the increase in temperature from 195 to 210 °C has increased the Ni dissolved from 7-fold to 8-fold. On the contrary, the increase in temperature did not substantially affect the Ni leaching experienced during the hydrogenation of RBD-PS. As indicated by the AAS study, the difference in leached Ni concentrations between both reaction sets was relatively insignificant throughout the entire hydrogenation reaction, with Ni levels below 0.03 mg/g_{oil} for both temperature sets. During the reaction, the triglyceride molecules in the RBD-PS remain as is due to the lack of favourable conditions for hydrolysis to occur (presence of water and acid or base as a catalyst), ergo the acidity of the feed is unaffected. Consequently, the reaction temperature would be an irrelevant parameter affecting the extent of leaching for RBD-PS. Hence, this highlights the deactivation of the catalysts by Ni leaching due to the acidity of S-RBD-PS caused by the presence of FFAs in the feed.

It should also be noted that while more Ni was leached at 210 °C for the reaction using S-RBD-PS, its performance was also better than that for the S-RBD-PS reaction at 195 °C. This may be due to the fact that while more Ni species were leached out at higher temperatures, the leached Ni species are still active and are capable of catalysing the hydrogenation reaction, as determined by researchers (Sádaba et al., 2015). This phenomenon could explain why the hydrogenation reaction at 210 °C achieved a comparatively better IV drop than that at 195 °C.

Additional experiments were carried out to further demonstrate the role of feed acidity in Ni lixiviation. In order to achieve this, similarly the catalyst was used in the hydrogenation of neutral organic liquid feeds, i.e. citral and benzyl alcohol, at two reaction temperatures of 170 and 180 °C. For reference, the pKa values for citral and benzyl alcohol are 16.33 and 15.02, respectively, indicating that the feeds are non-acidic. Ultimately, the hydrogenation products were similarly analysed using AAS for the presence of dissolved Ni, with results presented in Figure 3.6. As observed from the results, the amount of Ni present in the hydrogenation products of both citral and benzyl alcohol were negligible. In all cases, the concentration of dissolved Ni was less than 0.03 mg/g_{oil}, comparable to that of the RBD-PS hydrogenation products.

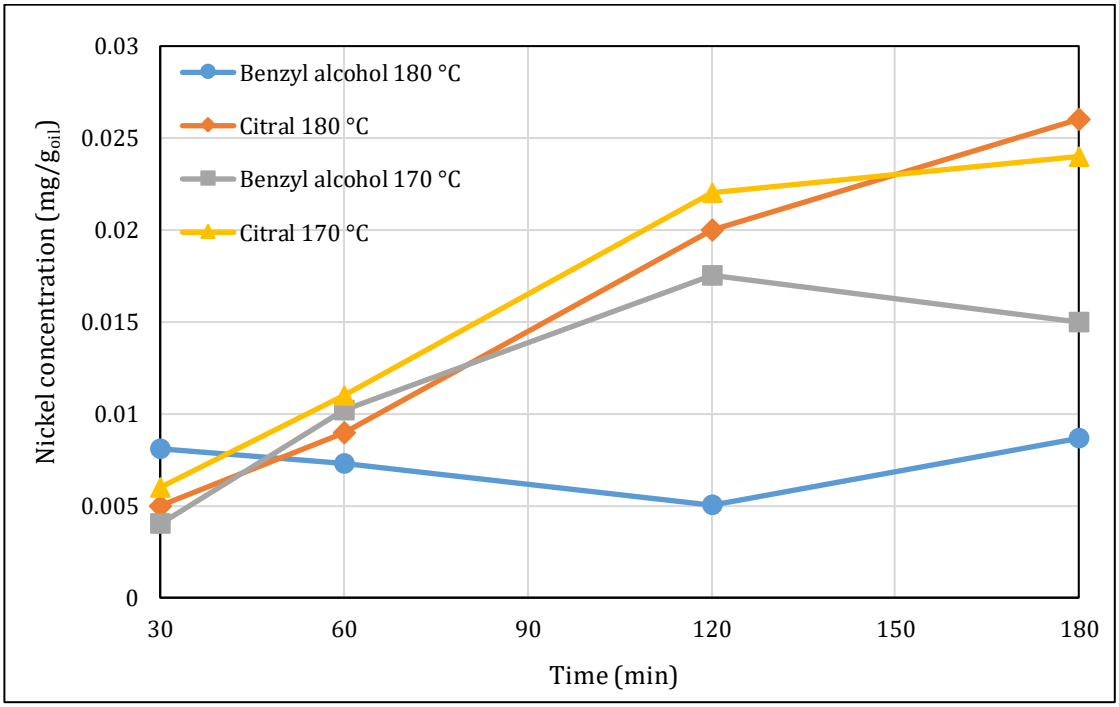


Figure 3.6: Concentration of dissolved Ni present in the hydrogenation products of citral and benzyl alcohol at different time intervals.

The catalyst powders used in the hydrogenation of both RBD-PS and S-RBD-PS were also recovered at the end of the experiments for TEM analysis, with bright field TEM images presented in Figure 3.7. It can be seen that the scan for the spent catalyst used for the hydrogenation of RBD-PS appear similar to that of the fresh catalyst, with minimal and uniform appearances of black globules, indicating the Ni crystallites were largely unaffected post-hydrogenation. For the fresh Ni catalyst, an average crystallite size of 5.497 nm was obtained, with its size distribution presented in Figure 3.8(A). Meanwhile, the spent catalyst from the hydrogenation of RBD-PS recorded an average crystallite size of 5.291 nm, with its size distribution shown in Figure 3.8(B), which appeared similar to that of the fresh catalyst. With a similar average crystallite size (3.7 % difference), it can be said that the Ni crystallites were largely unaffected throughout the hydrogenation process with minimal lixiviation phenomenon. On the other hand, the TEM scan for the spent catalyst used for the hydrogenation of S-RBD-PS looked vastly dissimilar to that of the fresh catalyst. On the scan, large black globules can be observed (indicated by red arrows on the diagram), representing the severe growth of Ni crystallites. In this case, the enlarged Ni crystallites can be obviously distinguished from the Si support material at average crystallites sizes of 31.78 nm, with the crystallite size distribution presented in Figure 3.8(C). Note that the measuring scale of the image in Figure 3.7(C) is at 200 nm, as compared to 50 nm for that of Figures 3.7(A) and (B).

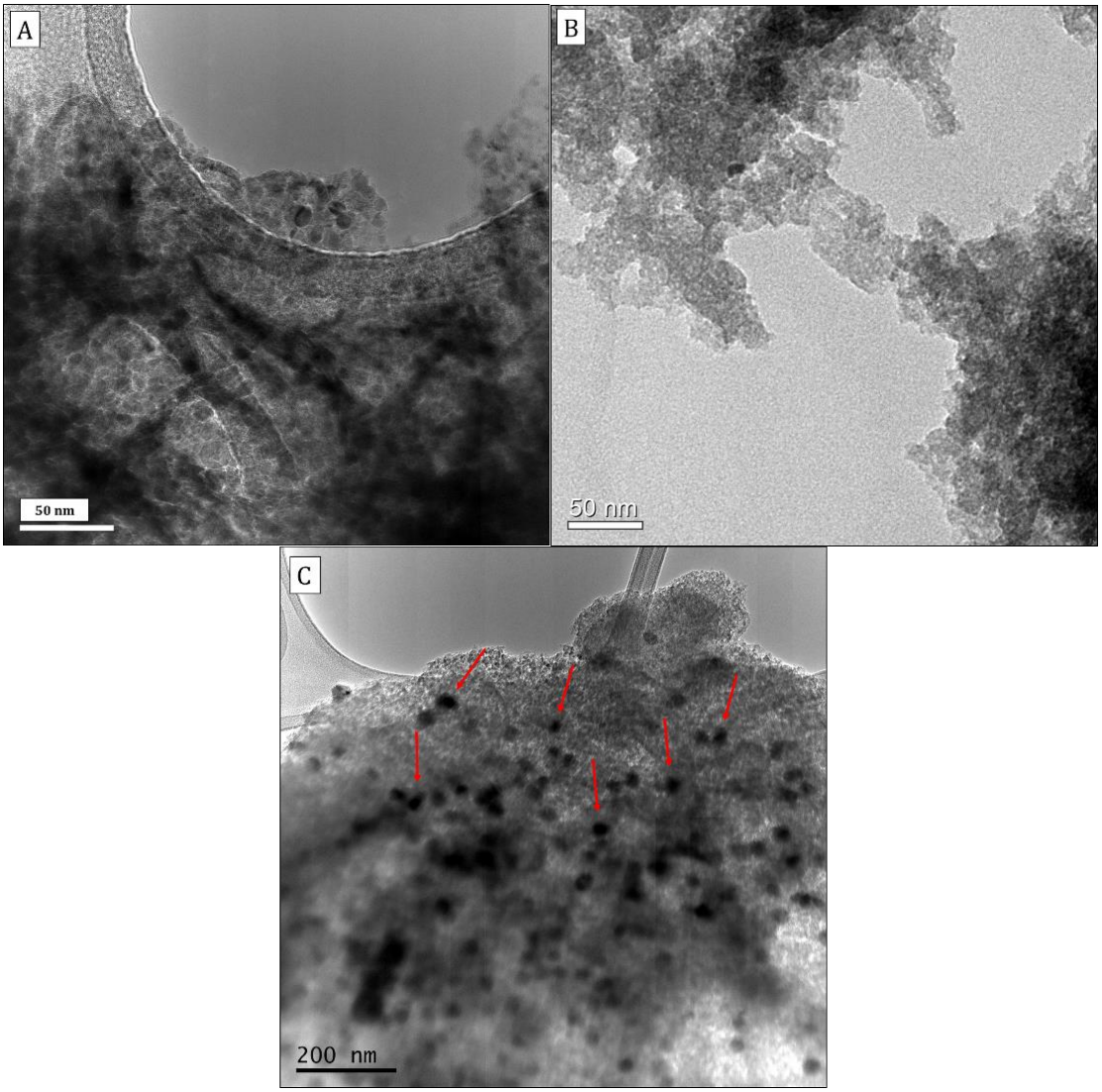


Figure 3.7: TEM images of the (A) fresh catalyst; (B) spent catalyst from the hydrogenation of RBD-PS at 195 °C; and (C) spent catalyst from the hydrogenation of S-RBD-PS at 195 °C.

Note: Images (A) and (B) are presented with a 50 nm scale; Image (C) is presented with a 200 nm scale.

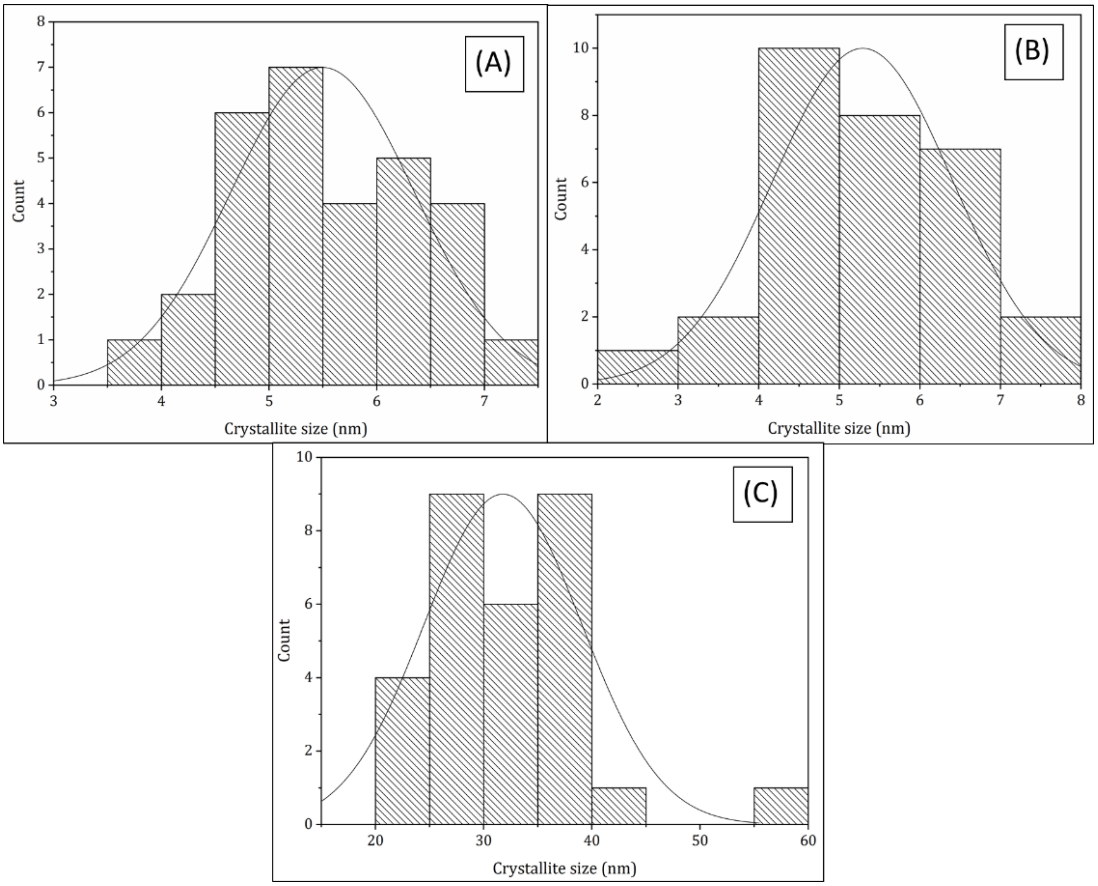


Figure 3.8: Crystallite size distribution of (A) fresh nickel catalysts and spent nickel catalysts recovered from hydrogenating (B) RBD-PS and (C) S-RBD-PS at 195 °C.

In the reversible reactions indicated in Eqs. (3.1) and (3.2), the dissolved Ni could redeposit on existing Ni crystallites (Ariaansz, 1993). As illustrated by the schematic flow in Figure 3.9, the dissolution of Ni occurs initially due to the acidity of the S-RBD-PS feed as mentioned previously. Over time, small crystallites dissolve away and disappear, while concurrently redepositing on existing larger crystallites, resulting in the formation of large globules as observed in Figure 3.7(C). This crystallite growth mechanism is essentially characterised by the Ostwald ripening phenomenon; whereby large crystallites grow at the expense of smaller crystallites, with the liquid organic feed acting as a medium to transport the dissolved Ni phases onto the larger crystallites. Here, Ostwald ripening is

determined as the principal growth mechanism of the crystallites as significant levels of dissolved Ni was detected in the S-RBD-PS hydrogenation products (van Haasterecht et al., 2016), as indicated in Figure 3.5. Secondly, even after extensive crystallite growth whereby larger crystallites are apparently visible, smaller crystallites can still be observed on the scans. This is due to the fact that during Ostwald ripening, it is expected that both enlarged and small crystallites co-exist, as the enlarged crystallites grow at the expense of shrinking crystallites (van Haasterecht et al., 2016).

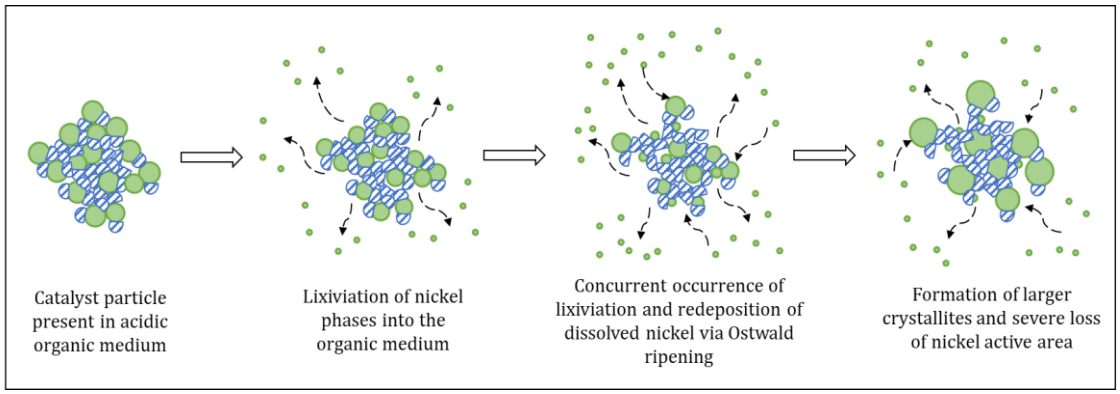


Figure 3.9: Schematic flow diagram of Ni lixiviation followed by the redeposition of Ni onto the catalyst particles via Ostwald ripening.

Therefore, it was once again substantiated that certain conditions of the organic reaction medium, which is the acidity in this case, play a significant role in affecting catalyst stability and deactivation. An acidic reaction medium would promote the lixiviation and the simultaneous occurrence of Ostwald ripening. As a consequence, the rapid loss of catalyst active sites would take place, resulting in a substantial decline in catalytic activity. Furthermore, another significant issue arises as the Ni dissolved in the hydrogenation products are highly toxic, which poses severe threats and concerns to overall product safety. Therefore, further

processing of the products to remove the contaminants will be necessary, i.e. removal of nickel soaps via citric acid chelation (Vavra and Koseoglu, 1994), thus incurring extra costs for the entire production process related to employing S-RBD-PS as the hydrogenation reaction feed.

While the market price of RBD-PS is approximately USD 1143 per metric tonne (as of July 2021), the pricing of S-RBD-PS is typically not provided in the literature, but it can be estimated. The hydrolysis (see Figure 3.1) of triglycerides (RBD-PS) to fatty acids (S-RBD-PS) and glycerol is typically carried out via the Colgate-Emery fat splitting process, with steam being the only reactant other than the fats (Thirunavukarasu and Panda, 2015). In particular, steam and triglyceride at a molar ratio of 21 to 1 enter a counter-current splitting tower with reaction temperatures of 250 °C and high pressures of 50 bar, where hydrolysis occurs rapidly at a reaction time of 2 – 3 h without the need for a catalyst. Considering the molar ratio required for the reaction and the price of steam generation at USD 30 per metric tonne (Jones et al., 2019), the estimated price of S-RBD-PS would be USD 1156.44 per metric tonne.

With the extra costs associated with splitting RBD-PS into S-RBD-PS and further purifying the products due to nickel leaching, it is suggested that RBD-PS can be hydrogenated to its target IV before splitting is carried out in order to improve operation economics.

3.3.2. Catalytic poisoning studies

Another prominent deactivation mechanism present in the hydrogenation of liquid oil is the poisoning of the catalyst due to the impurities present in the oil feed. Catalyst poisons such as sulphur (S), phosphorous (P), chlorine (Cl) and nitrogen (N) compounds are present in plant-based oils, which are either natural constituents of plant-based oils or introduced during processing. These impurity compounds with elements from groups V, VI and VII hold lone electron pairs, which could irreversibly chemisorb onto the active sites of the catalysts, thereafter limiting their capability to bind with reactant molecules (Klimmek, 1984), thus negatively affecting the activity of the catalysts. Table 3.1 shows the concentration of the anionic poisons present in the organic feeds using ion chromatography. Among all the feeds used in this study, the distilled blend contained the lowest amount of impurities. Next, both the RBD-PS and S-RBD-PS feeds contain approximately similar quantities of impurities, however noting that the S-RBD-PS had slightly lesser impurities.

Table 3.1: Concentration of catalyst poisons present in the organic feeds.

Feed	**Cl (ppm)**	**N (ppm)**	**P (ppm)**	**S (ppm)**
Distilled blend	7.67	1.21	0	6.92
RBD-PS	10.1	4.76	5.95	27.8
S-RBD-PS	9.51	4.47	0	15.9

In this present work, hydrogenation reactions using the distilled fatty acid blend can accentuate the effect of poisons and impurities on the catalytic performance. Figure 3.10 shows that the IV drop achieved during the

hydrogenation of the distilled fatty acids blend. At the end of the reaction at 195 °C, the IV dropped to 3.7, which was the lowest among all the feeds tested. Meanwhile, the IV for the feed hydrogenated at 210 °C achieved a slightly lower IV drop, with the end point at 5.9. However, based on the AAS analysis for the distilled blend hydrogenation products in Figure 3.5, it is noted that the catalyst experienced a substantial extent in leaching, although not as severe than that used for the hydrogenation of S-RBD-PS. While containing approximately equal fatty acid compositions as S-RBD-PS, the distilled fatty acids contained the lowest quantity of impurities such as S, P, N and Cl compounds that could tremendously poison and deactivate the Ni catalysts, as shown in Table 3.1. The poisoning of the catalyst occurs via a diffusion process, in which substances other than the oil reactants, such as those mentioned beforehand, are attracted to nickel active centres, blocking or eliminating their activity to a considerable extent (Wise, 1991). In most cases, poisons like S compounds such as those commonly found in fatty acids are irreversibly chemisorbed to catalytic surface sites (Bartholomew, 1987). Klimmek (1984) demonstrated that Cl and S anions have the most detrimental effects on catalyst poisoning, which reflects the ineffectiveness of the nickel catalyst in hydrogenating the RBD-PS feed that possesses the highest concentration of anion poisons, particularly that of Cl and S. These mechanisms by which a poison may affect catalytic activity are multi-fold, hence in this case might overwhelm the deactivation caused by Ni leaching (Argyle and Bartholomew, 2015). Comparing Figures 3.2 and 3.10, the hydrogenation rate for the distilled blend at 195 °C is greater than that of the RBD-PS feed that experienced minimal nickel leaching, demonstrating the role of poisons in hampering the hydrogenation activity over time, however not completely rendering the catalyst deactivated, as the catalyst

was still actively converting reactant molecules towards end of the reactions. On the other hand, as expected, temperature also played a big role in influencing the Ni leaching in distilled fatty acid hydrogenation experiments by increasing the dissolution of fatty acids, which once again corroborates the nickel soap formation theory. As per Figure 3.5, at 180 min the leached Ni concentration for reactions at 195 and 210 °C are 0.11 and 0.16 mg/g, respectively. Consequently, the catalyst used for the higher temperature experienced greater deactivation due to the higher extent of nickel lixiviation, resulting in the rapid decrease in activity and the subsequent plateau at ca. 180 min.

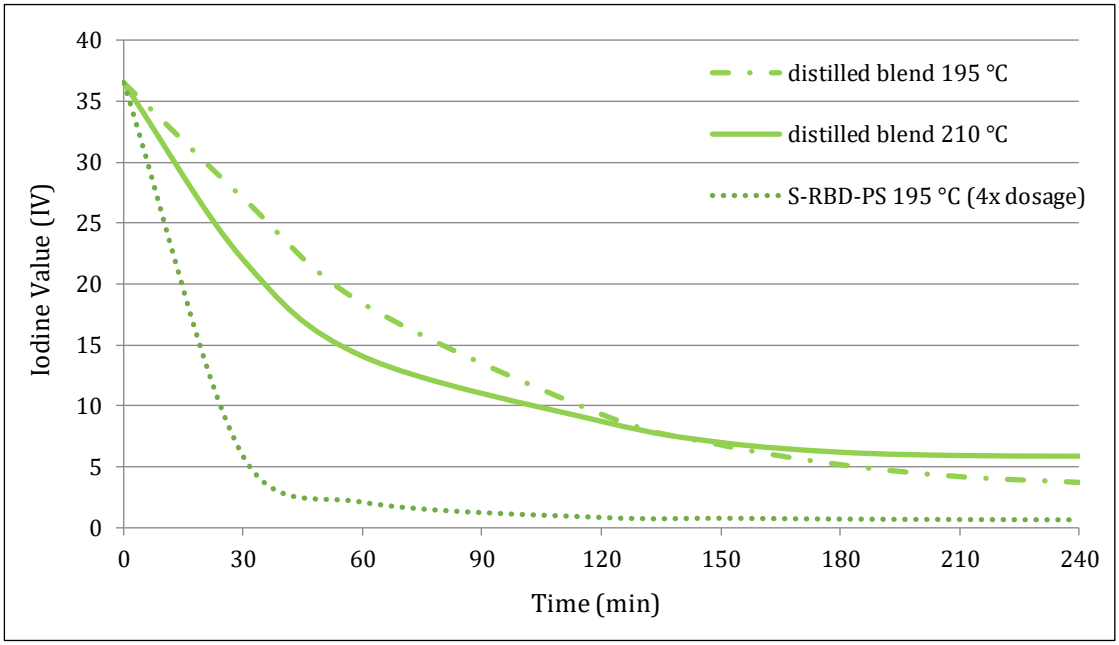


Figure 3.10: Change of IV with reaction time for the hydrogenation of the distilled fatty acid blend at 195 and 210 °C.

3.3.3. Coking studies

In this present study, deactivation due to coke formation or carbonaceous deposits are ruled out since coking is typically associated with gas-phase reactions at high operating temperatures. Moreover, silica-based supports are known to be highly resistant to the coking phenomenon, due to the lack of acidic sites, compared to the more acidic alumina supports (O'Brien, 1997). To support this, temperature programmed oxidation (TPO) of the spent catalysts was conducted using a thermogravimetric analyser (TGA), which was performed in compressed dried air to validate the absence of carbonaceous compounds. In Figures 3.11 and 3.12, the marginal weight loss at the region before 250 °C is due to the loss of adsorbed moisture and volatile species. Next, a single peak was observed ca. 300 – 360 °C for both TPO studies, which is ascribed to the decomposition of remaining fatty acids undissolved by the solvent (Raba et al., 2018). On the other hand, a net weight increase was observed after 360 °C for the catalyst used in the hydrogenation of S-RBD-PS, as indicated in Figure 3.11. This could be explained by the oxidation of metallic Ni that was lixiviated by the S-RBD-PS feed, as mentioned in Chapter 3.3.1., into NiO (Quitete et al., 2016; Shinde and Madras, 2014; Wu and Williams, 2010a). After the coated fatty acids were completely decomposed up to 360 °C, the exposed lixiviated metallic Ni subsequently undergoes oxidation into NiO, resulting in the overall weight gain experienced during the TPO study. Nevertheless, the derivative weight of both S-RBD-PS and RBD-PS samples remained stable and unchanged after the decomposition and oxidation phases were completed at ca. 400 °C, signifying no further changes in weight after that point onwards.

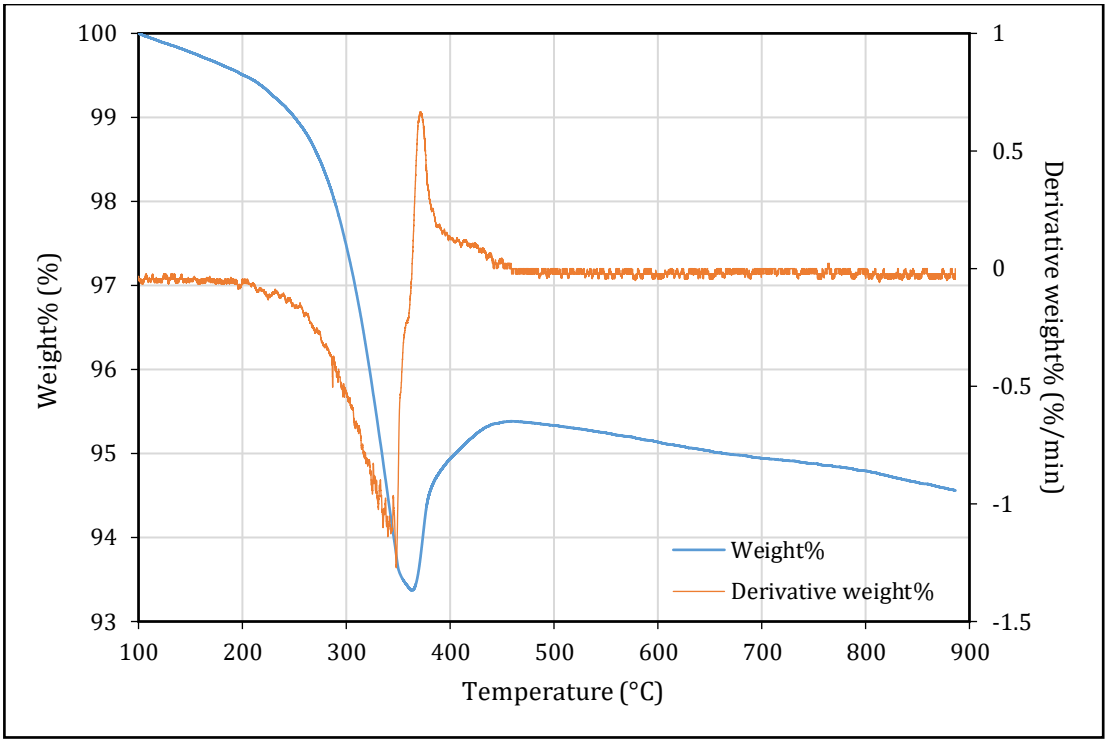


Figure 3.11: TGA and DTG curves of the spent nickel catalysts used for the hydrogenation of S-RBD-PS.

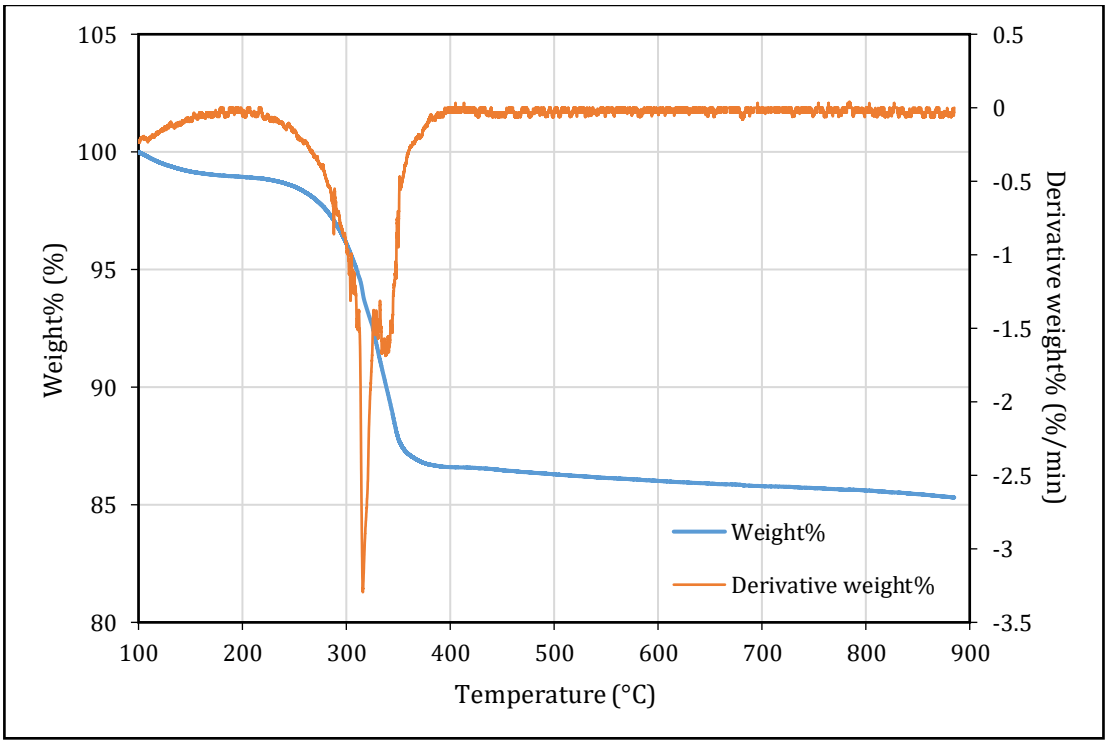


Figure 3.12: TGA and DTG curves of the spent nickel catalysts used for the hydrogenation of RBD-PS.

In this study, the presence of coke was undetected by the TGA as amorphous coke typically manifests in oxidation temperatures above 400 °C (Al-Swai et al., 2017; Lu et al., 2019; Quitete et al., 2016; Shinde and Madras, 2014; Wang et al., 2018). The absence of any peaks after 400 °C in the TPO studies suggests the non-existence of amorphous carbonaceous compounds in the spent catalysts. On the other hand, the presence of filamentous coke is typically characterised at even higher temperatures above 600 °C (Elbaba and Williams, 2014), which was also absent in the TPO studies in this work, signifying the non-formation of filamentous coke on the spent catalysts. In addition, the phenomenon of coking is also accompanied by the presence of visible carbon layers or filaments on TEM scans of spent catalysts (Elbaba and Williams, 2014), which in this study was undetected as per Figure 3.7, further confirming that coking did not take place during the hydrogenation reactions.

FT-IR was also carried out to identify the bonding characteristics present in the spent catalysts, with the spectrum shown in Figure 3.13. It can be observed that both infrared spectra appeared similar, indicating that the spent catalysts for both reactants have similar bonding characteristics after the reaction. The broad peak ca. 3300 cm^{-1} is ascribed to the stretching vibration of structural O-H groups of interlayer water molecules. The peaks ca. 3000 – 2800 cm^{-1} is assigned to the C-H stretching vibrations of the $–CH_2$ and $–CH_3$ groups of the fat molecules (Che Man et al., 1999). Furthermore, the peaks ca. 1700 – 1500 cm^{-1} are assigned to the C=O stretching vibration of ester linkages (Hayeemasae et al., 2020). Peaks at 1500 – 1300 cm^{-1} can be ascribed to the C-H bending vibrations of the $–CH_2$ and $–CH_3$ groups. The detection of absorbance peaks related to the existence of fat molecules

further substantiate the presence of reactant and product molecules on the spent catalysts that were undissolved by the solvent, corroborating the previous TPO studies. Furthermore, the lack of any other visible absorption peaks that are related to coke formation such as Ni-C bonds or C=C 'coke bonds' at ca 1600 cm^{-1} (Gayubo et al., 1993) further signify that coking mechanisms were not present during the reaction. Therefore, this solidifies the inference that coking is not a mechanism associated with the deactivation of nickel catalyst used in this study for the hydrogenation of palm-based liquid organic media.

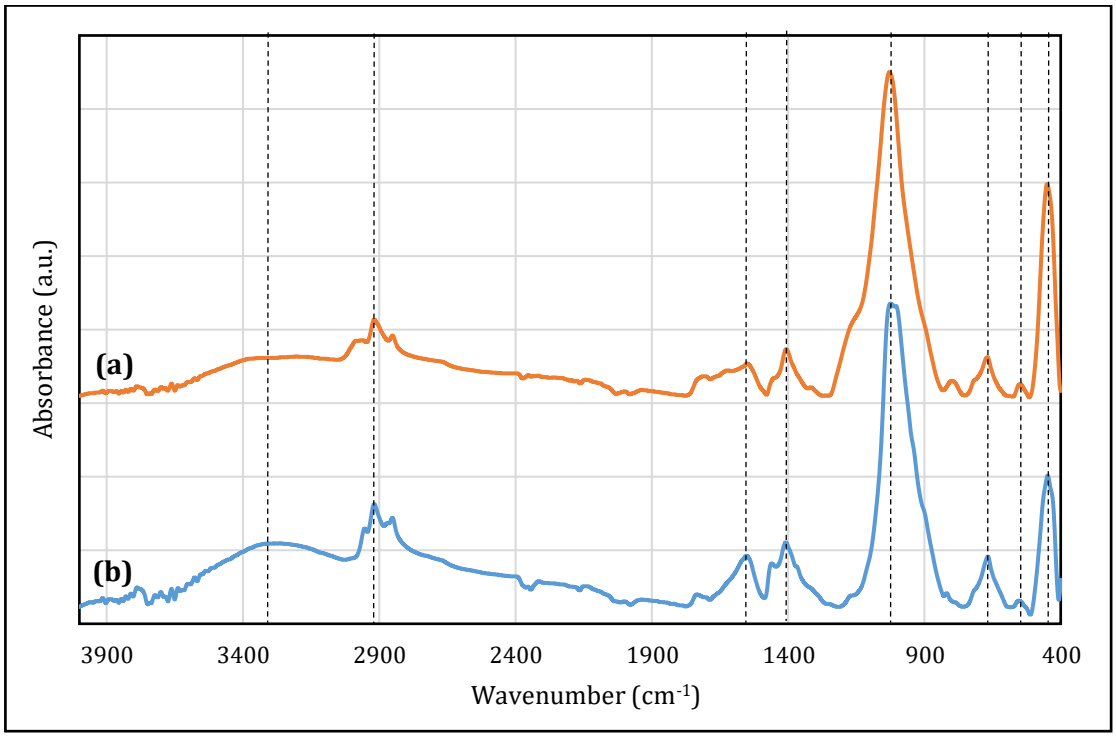


Figure 3.13: FT-IR spectrum of the spent nickel catalysts used for the hydrogenation of (a) S-RBD-PS and (b) RBD-PS.

In addition, peaks at 1000 cm^{-1} is owed to the Si-O stretching vibration mode, indicative of the amorphous silica support of the spent catalysts (Blanco et al., 2014). Peaks ca 700 – 600 cm^{-1} are characteristic of $Ni_3Si_2O_5(OH)_4$ phases in the

spent catalysts, representing the Si-O-Ni stretching vibrations (Korytkova et al., 2005). Moreover, the Si-O rocking vibrations were detected ca. 540 cm^{-1} (Capeletti and Zimnoch, 2016). Finally, absorption peaks ca. 450 – 400 cm^{-1} are ascribed to Ni-O bond vibrations (El-Kemary et al., 2013).

3.4. Concluding remarks

In this chapter, catalytic hydrogenation experiments were performed using several liquid organic media (i.e. RBD-PS, S-RBD-PS, distilled fatty acid blend, benzyl alcohol and citral) as reaction feeds, with the motive of ascertaining the deactivation behaviour of nickel hydrogenation catalysts.

It was found that nickel catalysts are prone to deactivation in acidic liquid media, such as the S-RBD-PS and distilled fatty acid blend feeds used in the study for this chapter. The high free fatty acid (FFA) content in the aforementioned feeds could result in the acidification of the organic feeds due to the dissociation of the fatty acids by releasing their protons (H^+). Consequently, nickel lixiviation would occur via the reaction between the nickel species present on the catalyst and the free fatty acids, forming dissolved nickel soap that concurrently contributes to the phenomenon of Ostwald ripening. This process severely eliminates the active sites on the catalysts, thereby causing the deterioration in catalytic activity.

On the other hand, the presence of poisons in the liquid organic feeds also played a significant role in hampering catalytic activity. Catalyst poisons such as S,

P, Cl and N in the S-RBD-PS and RBD-PS feeds affected the catalytic activity negatively, as compared to the relatively clean distilled fatty acid blend feed.

Coking is ruled out as a deactivation mechanism based on TPO, TEM and FT-IR observations that did not detect the presence of coke on the spent catalysts. Therefore, catalytic deactivation in the hydrogenation of palm-based liquid organic media such as RBD-PS and S-RBD-PS is determined to be strongly affected by mechanisms involving active site lixiviation, Ostwald ripening and catalytic poisoning.

4. Synthesis and Characterisation of Silica-supported Nickel Catalysts

4.1. Introduction

In practice, the hydrogenation process is typically executed in a three-phase slurry reactor through a semi-batch mode, whereby hydrogen gas is bubbled into fatty acids at an elevated temperature and pressure (Allen, 1978). One of the most imperative aspects of the process is the usage of a catalyst to catalyse the reaction. In recent decades, supported nickel (Ni) catalysts have garnered considerable attention due to the fact that Ni is a transition metal that has 'excessive activity along with maximum alterability' (Ananikov, 2015). This led to the application of Ni catalysts in a wide range of reactions, e.g. steam reforming, catalytic cracking of hydrocarbons, water-gas-shift, ammonia synthesis, etc. Although Ni catalysts are vastly applied in industrial processes, there are still plenty of room for improvement in terms of its structural and physico-chemical properties, thus constantly being the subject of various investigations. Recently, researchers have manipulated various preparation parameters such as the support type (Gabrovska et al., 2006), active metal content (Stanković et al., 2017), reduction temperature (Bhering et al., 2002), presence of doping agents (Konkol et al., 2016a) and synthesis method (Ryabchuk et al., 2018; Toshtay et al., 2014). In theory, properties such as the pore volume, pore length, particle size, total surface area and Ni crystallite size play a crucial role in determining the activity of the catalysts (Cepeda et al., 2016; Coenen, 1986).

Various techniques have been developed for the synthesis of heterogeneous Ni catalysts. A common method would be the impregnation of Ni active phases on an inert carrier support such as alumina (Che et al., 1997). In addition, highly-loaded Ni catalysts can be synthesised via the sol-gel method (Ermakova and Ermakov, 2003). The co-precipitation of Ni salt and silica source using an alkali source such as sodium carbonate is also one of the common and conventional routes to synthesise Ni catalyst precursors, i.e. silica-supported Ni carbonate. The aforementioned substance yields supported Ni catalysts, upon reduction (Nitta et al., 1985). Nitta and colleagues (1985) have concluded that compounds of Ni, particularly hydroxide or carbonate compounds of Ni, tend to form strong interactions with the silica carrier or support. Consequently, this results in the generation of Ni hydrosilicate phases, particularly nickel phyllosilicates, on the external layers of the support phase, which function as anchoring sites for Ni crystallites, leading to their stabilisation and dispersion (Burattin et al., 1999). This phenomenon is also supported by various other work concerning the synthesis of silica-supported Ni catalysts (Burattin et al., 1998; Ghuge and Babu, 1995; Mile et al., 1988; Stanković et al., 2017). The presence of these metal-support interactions (MSI) could potentially influence the properties and performance of heterogeneous supported catalysts in terms of their active metallic area and dispersion, reducibility and stability or resistance to thermal sintering, and subsequently the activity and selectivity (Bhering et al., 2002; Campbell, 2012; Mejía et al., 2018). As described in some studies, many factors could influence these properties, including the catalyst synthesis technique. For instance, it was reported that the ageing step is of substantial significance in dictating fundamental catalyst properties, which controls the degree of formation

of less reducible silicates, therefore affecting final metallic dispersion and surface area properties (Liu et al., 2008; Nele et al., 1999). In particular, ageing time and ageing temperature were reported to play an important role in tuning nickel silicate formation, ultimately influencing catalyst activity and applicability (Nele et al., 1999).

Alkaline, alkaline-earth and rare-earth metals are favourably utilised as catalyst promoters. The benefits of such promoters include: varying the acid-base property of the catalyst, enhancing dispersion of active species, increasing the interaction and synergy between the active species and their support and improving the catalytic stability of the catalyst (Feng et al., 2019; Khairudin et al., 2018; Qiu et al., 2007). Additionally, alkaline earth metals could also potentially influence the morphology, reducibility and electronic properties of heterogeneous catalysts (Zhu et al., 2011). In this regard, incorporating an alkali earth metal such as Mg might bring about positive changes in the metal-support structure and overall properties of Ni catalysts.

On the other hand, ultrasonic technology has emerged over the years as an innovative method to effectively modify the properties and performance of heterogeneous catalysts (Estifaee et al., 2014; Pokhrel et al., 2016; Rahmani et al., 2016). The incorporation of ultrasonic irradiation into catalyst synthesis could result in various changes in particle morphology, surface composition, metal dispersion, structural or geometric properties, electronic configurations and catalyst reactivity (Chatel, 2019; Rahmani et al., 2016; Suslick, 1989). In some cases, the use of ultrasound is able to activate less reactive, but also less costly,

catalytic metals (Suslick et al., 1999b). To illustrate, in liquids irradiated by ultrasound, the phenomenon known as acoustic cavitation induces the formation and subsequent implosion of numerous short-lived micro-bubbles with extremely high temperatures and pressures (Suslick and Price, 1999). These transient, localised hot-spots facilitate various physical and chemical reactions during catalyst synthesis, which brings about the enhancement and promotion of nucleation rates and dispersion of active metals on the support surface (Allahyari et al., 2014b). In addition, besides being an environmentally friendly and green synthesis technique, it offers unique reaction conditions that could rarely be achieved by conventional means (Ashokkumar, 2016; Chatel, 2019; Mahmoodi et al., 2019). Nevertheless, it is also imperative to understand the underlying mechanisms involved in driving the positive effects demonstrated by ultrasonic irradiation in catalyst synthesis, which is an aspect that many literature sources lack. For instance, in various catalysts synthesised via ultrasound for photocatalytic, catalytic cracking and gas reforming applications, authors have reported the increase in reducibility, metal dispersion, particle uniformity, BET surface area etc. (Ahmadi et al., 2016; Ameen et al., 2019; Daroughegi et al., 2017; Khoshbin and Haghighi, 2013; Moradiyan et al., 2018; Oruji et al., 2019; Pérez et al., 2011; Rahmani et al., 2016; Zhuang et al., 2018). However, detailed explanations for the reasons behind the improvement via sonication were generally lacking, thus posing a significant knowledge gap.

Furthermore, it is also important to note that performing routine calibration experiments is imperative to accurately reflect the actual acoustic power dissipated by the ultrasonic source, which could allow effective replications

as well as comparisons between different bodies of work. This in fact is a critical aspect that a large majority of literature sources lack, whereby only the electric powers specified by the ultrasonic generators (as provided by manufacturers) are detailed (Ahmadi et al., 2016; Ameen et al., 2019; Daroughegi et al., 2017; Khoshbin and Haghighi, 2013; Pérez et al., 2011; Rahmani et al., 2016; Zhuang et al., 2018).

Galvanised by the potential advantages based on these considerations, this chapter focuses on investigating the influence of incorporating Mg into co-precipitated silica-supported Ni catalysts, as well as identifying the influence of ultrasonic irradiation on the aforementioned catalyst. Mg was chosen as the alkali-earth metal as the element is a cost-effective and widely available material. To achieve this, Ni-Mg/SiO_2 catalysts of varying stoichiometric molar ratios were synthesised and characterised. Moving forward, the optimal sample is selected based on its characterisation results and further investigated for its synthesis using an ultrasonic technique at varying ultrasonic intensities during the ageing step, whereby the actual acoustic power supplied was determined. Lastly, the catalysts were evaluated based on several characterisation tests, in which the variation in catalyst phase compositions due to sonication was analysed and the ultrasonic irradiation synthesis mechanism was outlined.

For clarity, it is noted that "Ni" in the samples exist in the form of its oxide, NiO, post-calcination, which is the unactivated form of the Ni catalyst. Only after a reduction process by H_2, the NiO is reduced to Ni, which is the active form of the Ni-MgO/SiO_2 catalyst. While in the final form of the catalysts, the Mg dopant exists as "MgO", as MgO is inherent difficult to reduce under given conditions.

4.2. Experimental

4.2.1. Sample synthesis

All samples were synthesised and labelled based on the stoichiometric molar ratios as shown in Table 4.1. Figure 4.1 illustrates the schematic flow diagram to ease the understanding of the catalyst synthesis procedure. In essence, nickel sulphate hexahydrate ($NiSO_4.6H_2O$) and magnesium sulphate heptahydrate ($MgSO_4.7H_2O$) solutions were prepared according to the molar ratio. The mixture was then heated to 50 °C. Then, 10 wt% sodium carbonate (Na_2CO_3) was dosed until the pH of the precipitated suspension was 8.8, in a duration of 10 min. The suspension was then heated to 90 °C, followed by the addition of 2 wt% sodium metasilicate pentahydrate ($Na_2SiO_3.5H_2O$) solution, in a duration of 10 min. The suspension was then allowed to age for 30 min at 90 °C. Throughout the whole synthesis process, the suspension was continuously stirred. After terminating the synthesis procedure, the resulting mixture was filtered and thoroughly rinsed three times using deionised water. Next, the filtered precipitate was dried at 100 °C for 5 h in an oven. Lastly, the dried precipitate was calcined in a chamber furnace at 400 ˚C for 4 h.

Table 4.1: Synthesis parameters of the catalysts involved.

Sample	A	B	C	D	E	D_US20	D_US30	D_US40
Molar ratio (Ni:Mg:Si)	0:4:1	1:3:1	2:2:1	3:1:1	4:0:1	3:1:1	3:1:1	3:1:1
Ultrasonic amplitude (%)	-	-	-	-	-	20	30	40

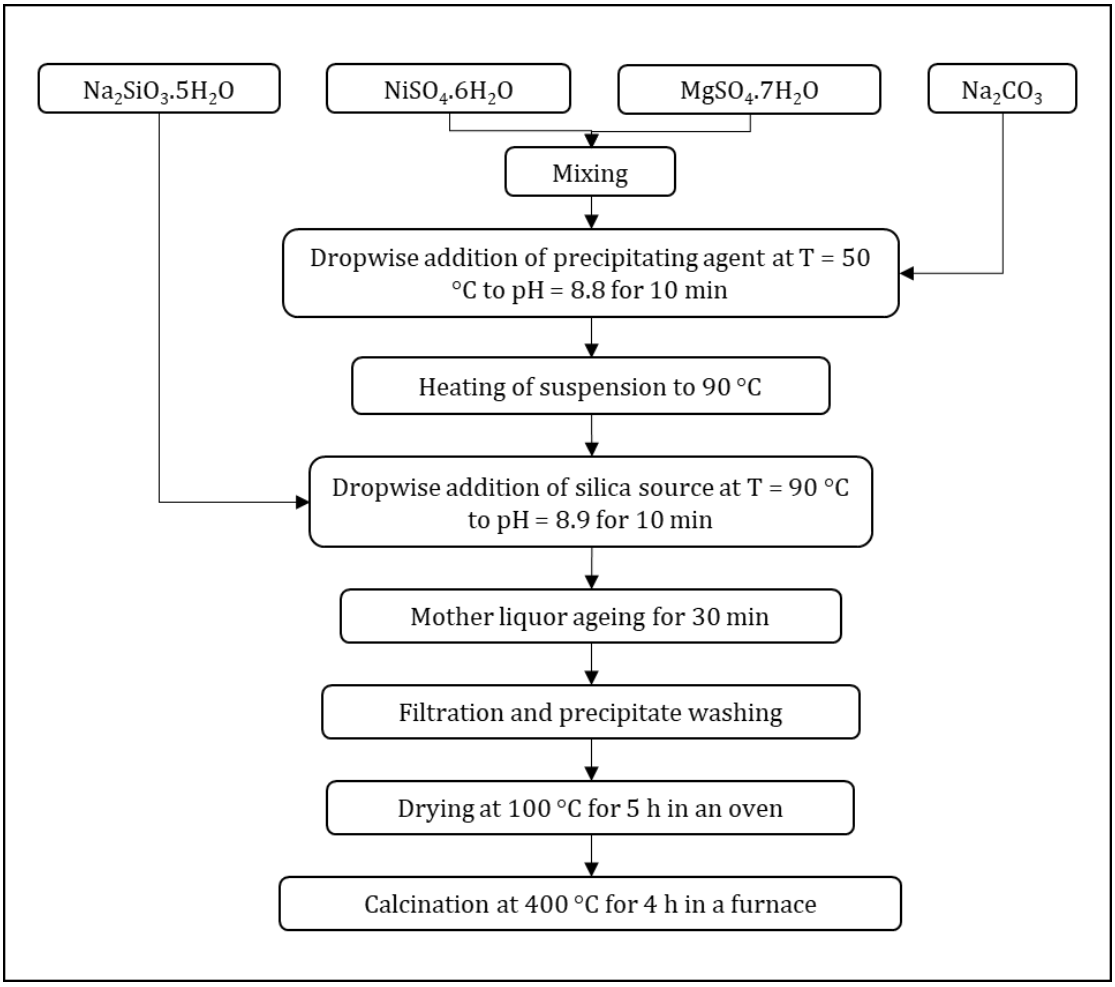


Figure 4.1: Schematic flow chart for the synthesis of catalysts A – E.

For catalysts subjected to ultrasonic irradiation, the dosing of 2 wt% $Na_2SiO_3.5H_2O$ solution was delivered under the influence of a sonicator, in the same duration of 10 min as the unsonicated sample for consistency. The probe was

immersed at a depth of 2 cm, pulsed at 2 s on/off, under temperature-controlled conditions. Three sonicated catalysts were synthesised with ultrasonic amplitudes of 20, 30 and 40 %, corresponding to ultrasonic intensities of 7.07, 20.78 and 27.72 W cm^{-2}, labelled as D_US20, D_US30 and D_US40, respectively. The aforementioned ultrasonic amplitudes were chosen considering their interesting impacts on catalyst synthesis in a previous work (Yap et al., 2018). Similarly, the catalyst synthesis procedure for this set of catalysts is illustrated in Figure 4.2.

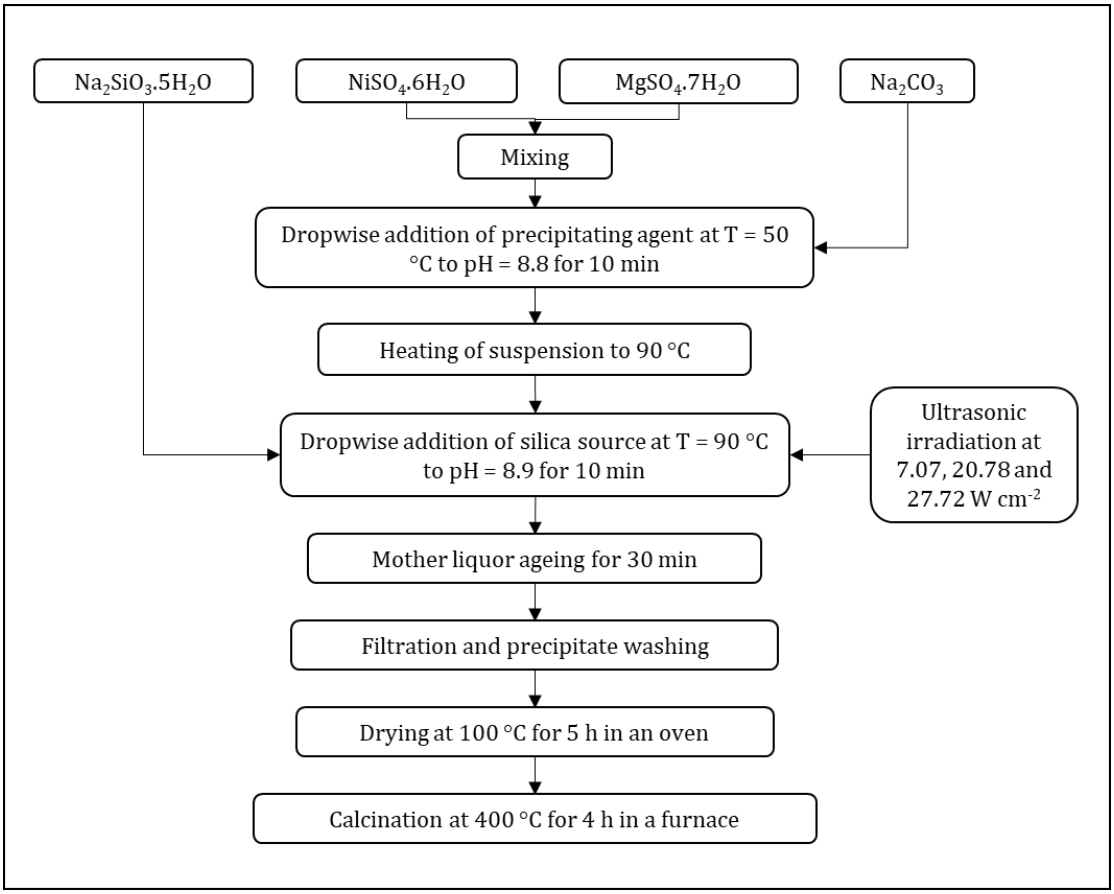


Figure 4.2: Schematic flow chart for the synthesis of catalysts D_US20, D_US30 and D_US40.

4.3. Results and discussion

4.3.1. Ultrasonic probe calorimetry

The ultrasonic system was assessed for its calorimetry and results are presented in Table 4.2. The heat loss, Q_{HL}, calculated was 0.8 W.

Table 4.2: Ultrasonic power output, intensity and density acquired for the 20 kHz ultrasonic probe.

Ultrasonic amplitude (%)	**Rate of increase in temperature, $\frac{\Delta T}{\Delta t}$ (K s^{-1})**	**Power output, Q (W)**	**Total power, $Q+Q_{HL}$ (W)**	**Ultrasonic intensity, I_{US} (W cm^{-2})**	**Ultrasound density, ρ_{US} (W cm^{-3})**
20	0.005778	4.853	5.653	7.07	0.0283
30	0.01883	15.82	16.62	20.78	0.0831
40	0.02544	21.37	22.17	27.72	0.111

4.3.2. Effects of incorporating Mg as a catalyst promoter during catalyst synthesis

4.3.2.1. Characterisation of synthesised catalysts

Powder XRD analyses were carried out to ascertain the phases and structures present in the calcined samples. The wide-angle XRD graphs (Figure 4.3) for all samples show a broad peak around the 2θ value of 22 °, which signifies an amorphous nature of the structure, caused by the presence of the SiO_2 support structure (JCPDS 84-0384) (Cai et al., 2014; Krstić et al., 2005; Pettiti et al., 2015; Thyssen et al., 2015). In particular, this denotes the low degree of crystallisation of

the silica support (Cho et al., 2002). In general, the XRD diffractograms register reflections that are broad and weak, indicating the poorly crystallised state of the samples, which in turn suggests the presence of small, well-dispersed particles and highly developed surfaces (Echeverria and Andres, 1990; Gabrovska et al., 2005). This observation is in accord with the physisorption and chemisorption analyses, which will be discussed in the later sections. The diffractograms of the Ni-containing samples (B – E) exhibit NiO peaks at 2θ values of 37 °, 43 °, 63 °, 75 ° and 79 °, which correspond to the presence of free (111), (200), (220), (222) and (311) NiO planes (ICDD: 01-073-1523), respectively. This finding is in good agreement with the results of several other works (Cai et al., 2014; Cho et al., 2002; Rynkowski et al., 1993; Thyssen et al., 2015; Zhang et al., 1992). In addition, previous investigations have identified the peaks at 2θ = 35 °, 37 ° and 61 ° as reflections characteristic of Ni silicate hydroxide ($Ni_3Si_2O_5(OH)_4$; ICDD: 01-083-1648) (Gabrovska et al., 2005; Liao et al., 2021; Zhang et al., 2017). In this case, peaks identified at those positions in the XRD diffractograms can be ascribed to said compounds.

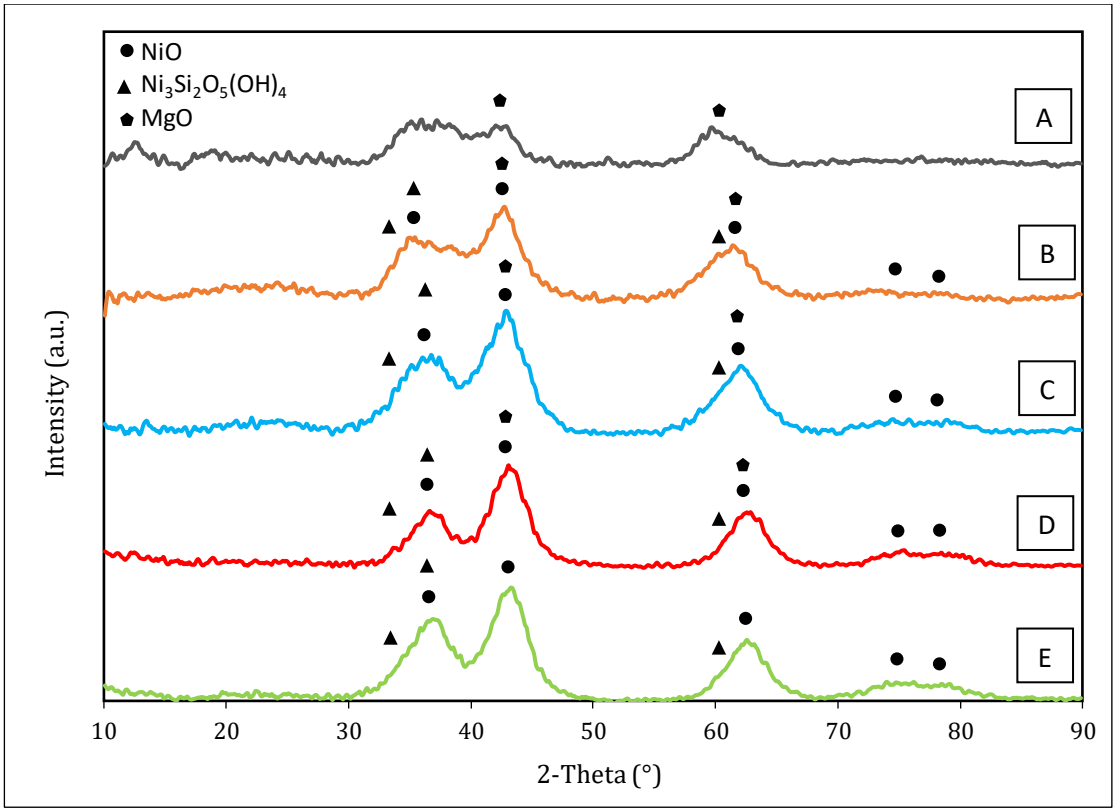


Figure 4.3: XRD diffractograms of the catalysts with their respective identified compounds, where samples A, B, C, D and E correspond to the Ni:Mg:Si ratio of 0:4:1, 1:3:1, 2:2:1, 3:1:1 and 4:0:1, respectively.

Based on the diffractograms in Figure 4.3, only the peak at 37 ° is exclusive to the presence of the NiO phase, whereas peaks at 43 and 63 ° can be attributed to the existence of both NiO and MgO (ICDD: 01-089-7746) compounds, hence explaining the absence of the 37 ° peak on the diffractogram of sample A. The observed amorphous and poorly crystallised patterns could be due to the interaction between the Ni salt and the silica support during the synthesis procedure, thus resulting in the formation of a supported layered Ni-phyllosilicate phase ($Ni_3Si_2O_5(OH)_4$), an imperfect antigorite-like structure (Gabrovska et al., 2011). Besides, it is also known that the usage of sodium silicate suppresses the degree of crystallinity of NiO (Liu et al., 2000). The formation of this less-ordered

structural feature stipulates that the different phases in the samples are well-mixed, as noted by other researchers as well (Ma et al., 1999; Wang and Zeng, 2005). The peak at 37 °, which contains the Ni silicate phase, seemed to have increased in intensity with the increase in the Ni to Mg ratio, suggesting said phase has increased in concentration. On the other hand, it can be observed that the diffractograms of the Mg-incorporated samples (B, C and D) appear to be similar to their pure NiO-Si counterpart (sample E). This can be justified by the partial substitution of the slightly smaller Ni^{2+} cations (ionic radius of 0.069 nm) by the slightly larger Mg^{2+} cations (ionic radius of 0.072 nm), with both having the same common oxidation state (2+) as well as the same bulk oxide structure (NaCl-type) (Bradford and Vannice, 1996). Subsequently, this leads to the partial amorphisation of the catalyst structure due to the formation of a NiO-MgO solid solution, resulting in more developed total surface areas as indicated by BET studies later (Babu et al., 1992; Gabrovska et al., 2015).

The XRD analysis was also used to obtain the crystallite sizes of the samples, presented in Table 4.3. Although there is no clear trend in the crystallite sizes of the samples based on their Ni to Mg molar ratio, it is noted that the sample doped with the lowest amount of Mg presented a comparably smallest crystallite size of 2.56 nm, marginally smaller than that of the undoped sample E (2.66 nm). The addition of Mg might have resulted in a 'spacing' effect towards the catalyst structure, whereby the relatively minor quantities of MgO acts as a physical spacer between NiO crystallites, subsequently averting the formation of bulky crystallites. When the Mg content increases as per sample C, the effect of MgO being a physical spacer becomes less conspicuous, as the crystallite size increased to 4.31 nm.

Lastly, when Ni is the minor constituent as per sample B, the crystallite size is a mere 3.46 nm, likely due to the significantly lower Ni content that resulted in a very limited crystallite growth. This finding resonates with that of Wong and associates (2018), whereby they noted a substantial decrease in Ni crystallite size when Zn was added in small quantities to their Ni/Al_2O_3 catalyst, while attributing this phenomenon to Zn playing a role as a barrier between Ni crystallites. Here, it is important to state that the crystallite size of a supported heterogeneous catalyst is an excellent indicator of its degree of metal-support interaction, in which catalysts possessing small crystallite sizes, such as that of sample D, would correspond to a stronger metal-support interaction (Słowik et al., 2016; Wang et al., 2019). For instance, as the crystallite size of CeO_2 in NiO/CeO_2 catalysts decreased, the interaction between NiO and CeO_2 increased, resulting in a higher active phase dispersion (Mahammadunnisa et al., 2013). Strong interactions between Ni and CZ (support phase), induced by the addition of Al_2O_3 into the catalyst matrix, also resulted in smaller Ni crystallite sizes in the NiK/CZ-A catalysts (Do et al., 2018).

It is noted that after the co-precipitation of Ni and Mg with sodium carbonate, NiO and MgO compounds are formed following the calcination of the precursors. Hence, the results presented here are pertaining to that of the NiO compound. As a comparison and verification to this present work, XRD results obtained from the literature for the analysis of pure NiO and pure Ni are shown in Figure 4.4. Here it can be clearly seen that NiO peaks occur at 37, 43 and 63 °, with weak reflections at 75 and 79 ° (Rifaya et al., 2012). Note that the peaks in Figure 4.4(A) are very sharp and distinct due to the high crystallinity (crystallite size = 12.2 nm) of the sample concerned, which is not the case regarding the samples in

this present work, which are highly amorphous. On the other hand, Figure 4.4(B) show pure Ni peaks at 44, 52 and 76 ° (Sahoo et al., 2005), which are all absent in the XRD diffractograms in this current study, further confirming that only the oxide phases are present post-calcination. The aforementioned findings are also confirmed in a study carried out by Richardson and colleagues (2003).

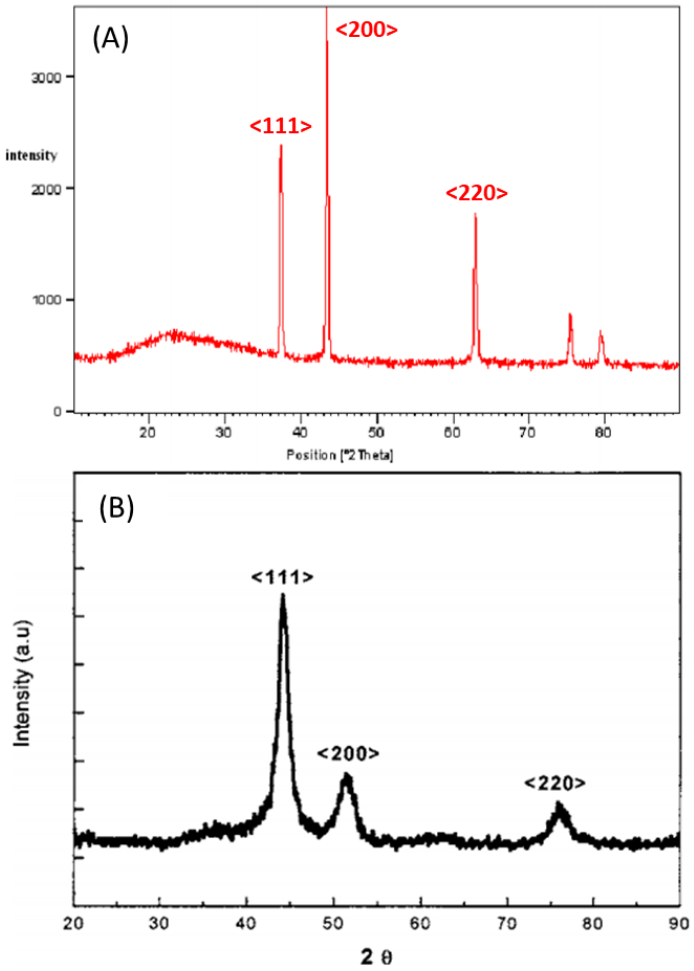


Figure 4.4: XRD diffractograms of (A) pure NiO sample; and (B) pure Ni sample.

Image (A) adapted from Rifaya et al. (2012) ; Image (B) adapted from Sahoo et al. (2005).

The FT-IR analysis was carried out to identify and verify the functional groups present in the samples, particularly that of Ni^{2+} species. The FT-IR transmission spectrum is shown in Figure 4.5. Starting from the highest

wavenumber, the peaks at the frequency 3360 cm^{-1} can be ascribed to the presence of O-H stretching bands due to water molecules intercalated between the catalyst structure (Kermarec et al., 1994; Tao et al., 2008; Yap et al., 2018). Furthermore, said band is also attributed to the existence of H_2O as bound water molecules in the structure (Yap et al., 2018). In addition to the band at 3360 cm^{-1}, the absorption band at ca. 1630 cm^{-1} is ascribed to the vibration and deformation of adsorbed water molecules (Stanković et al., 2017).

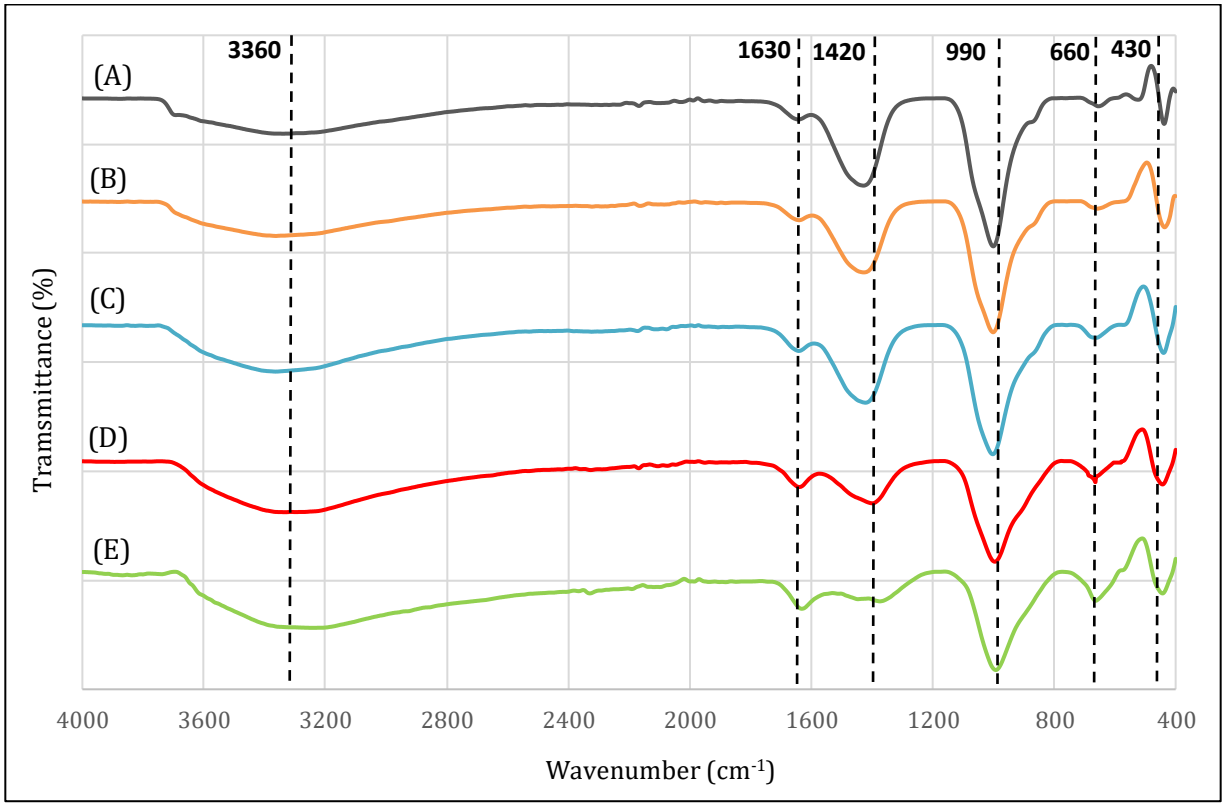


Figure 4.5: FT-IR spectrum for the catalysts, where samples A, B, C, D and E correspond to the Ni:Mg:Si ratio of 0:4:1, 1:3:1, 2:2:1, 3:1:1 and 4:0:1, respectively.

The absorption band around 1420 cm^{-1} in the IR spectrum can be allocated to the C-O stretching mode, as a result of the carbonate ions present on the surface, and in this case, particularly the adsorption of atmospheric carbon dioxide onto

the surface of MgO, in particular the adsorption of chelated bidentate carbonate species (Imani and Safaei, 2019; Jung et al., 2003; Wu et al., 2016). Transition metals, such as Ni, typically form repulsive forces with acidic carbon dioxide molecules (Kim et al., 2010), hence said peak is not attributed to carbon dioxide absorbed on NiO. On the contrary, the high basicity and favourable thermodynamics of MgO makes it extremely susceptible to carbon dioxide adsorption (Kumar and Saxena, 2014; Philipp and Fujimoto, 1992). Therefore, this phenomenon correlates well with the aforementioned bands shown in the figure. For instance, it can be observed that as the ratio of Ni to Mg decreases (i.e. increasing Mg content), the intensity of the bands increases due to the increased presence of carbon dioxide adsorbed on the surface of MgO.

Subsequently, the intense and apparent absorption band around 990 cm^{-1} is detected in all samples. This particular band has been commonly used to identify and characterise the incorporation of metal ions in the silica support framework, and in this case, the presence of Si-O-M bonds (M = Ni and/or Mg). This is caused by the anti-symmetric stretching Si-O vibration mode, disturbed by neighbouring metal ions (Cai et al., 2014; Stanković et al., 2017). However, it was reported that this band is originally observed at higher wavenumbers, i.e. 1050-1100 cm^{-1}, and this shift to a lower wavenumber such as 990 cm^{-1} is owed to the formation of phyllosilicate that is poorly crystallised (Blanco et al., 2014), which corroborates the XRD findings.

Moreover, it can be seen that the band at 660 cm^{-1} is absent in sample A, but its intensity appears to increase progressively as the ratio of Ni to Mg in the

samples increases (i.e. decrease in Mg content). This finding is well agreed with other researchers, as the band around 660 cm^{-1} is assigned to the formation of Ni hydrosilicates resulting from the interaction between Ni and the silica support (Hermida et al., 2019; Lehmann et al., 2012; Stanković et al., 2017). The co-precipitation synthesis technique tends to result in an extensive interaction between Ni ions and the silica support, as various characterisation studies have indicated that Ni^{2+} ions precipitate on silicate ions as layered Ni hydrosilicate (Coenen, 1989; Montes et al., 1984; van Eijk Van Voorthuijsen and Franzen, 2010). This phenomenon in turn leads to the generation of supported Ni hydrosilicates (Stanković et al., 2017). Hence, the increase in intensity of the bands at 660 cm^{-1} can be explained by the increase in the content of Ni hydrosilicates formed as the Ni content increases from sample B to E. Lastly, the absorption band around 430 cm^{-1} is attributed to the asymmetric bending of O-Si-O tetrahedra in silica, which is observed in all silica-containing samples (Almeida et al., 1990; Hermida et al., 2019; Kermarec et al., 1994; Stanković et al., 2017).

Furthermore, as the bands around 1420 cm^{-1} and 990 cm^{-1} are characteristic of both Ni and Mg, it is worth noting that as the concentration of Mg increases, the infrared bands are observed to shift to higher wavenumbers. For instance, as the Mg content increases, the wavenumber for basic carbonate vibrations shifted from 1373 cm^{-1} to 1428 cm^{-1}; while the wavenumber for hydroxy silicate vibrations shifted from 992 cm^{-1} to 1000 cm^{-1}. This is due to the fact that Mg is incorporated homogeneously and assumes the characteristics of basic Ni carbonate (Babu et al., 1992). Hitherto two factors can explain the observed shift towards higher wavenumbers for Mg-rich samples. On the one hand,

the bond lengths of the Mg species are shorter than that of the Ni species. On the other hand, the bond strengths of the Mg species are stronger than that of the Ni species, due to the higher charge/radius ratio for Mg compared to that of Ni (i.e. 3.030 vs. 2.898).

In summary, FT-IR results in Figure 4.5 indicate that during the co-precipitation reaction under alkaline conditions, the basic NiO generated during precipitation reacted with the silicate ion support. This subsequently led to the generation of new supported Ni hydrosilicate phase, which comprises Si-O-Ni linkages. Besides, the incorporation of Mg into the samples and its variation in concentration can also be observed through this analysis.

From the EDX analysis as indicated in Table 4.3, it is seen that the experimental molar ratios of the samples follow the theoretical molar ratios, thus representing apt synthesising methods. Furthermore, in all the samples involved, elements of Ni, Mg, Si and O are present, signifying that the metal-oxide compounds containing Ni, Mg and Si were formed during the synthesis.

Table 4.3: Elemental compositions and crystallite sizes for the catalysts prepared under different conditions.

Sample	Molar ratio			Atomic %				Crystallite size (nm)
	Ni	Mg	Si	Ni	Mg	Si	O	
A	-	4	1	-	25.9	5.5	68.5	5.65
B	1	3	1	5.7	20.2	6.3	67.8	3.46
C	2	2	1	14.3	14.1	6.8	64.8	4.31
D	3	1	1	24.9	8.2	8.3	58.6	2.56
E	4	-	1	28.5	-	7.9	63.6	2.66

Nitrogen adsorption-desorption studies were carried out to ascertain a more detailed picture of the effect of metal doping and preparation parameters on the textural properties of the samples. This characterisation method utilises the principle of physisorption to acquire adsorption and desorption isotherms and information regarding the surface area and porosity of heterogeneous catalysts.

The nitrogen sorption isotherms of the samples shown in Figure 4.6 resemble Type IV isotherms according to the International Union of Pure and Applied Chemistry (IUPAC) classification, which are associated with capillary condensation taking place in well-developed mesopores. It can be remarked that the isotherms of the samples exhibit hysteresis loops after $P/P^0 > 0.4$. To illustrate, for both Mg- and Ni-only silicate samples A and E, the isotherms resemble a Type H3 loop and a Type H2 loop, respectively. A Type H3 hysteresis loop is observed with aggregates of plate-like phases resulting in slit-shaped pores. On the other hand, a Type H2 loop is characterised by pore with narrow necks and wide bodies, often referred to as 'ink bottle' pores.

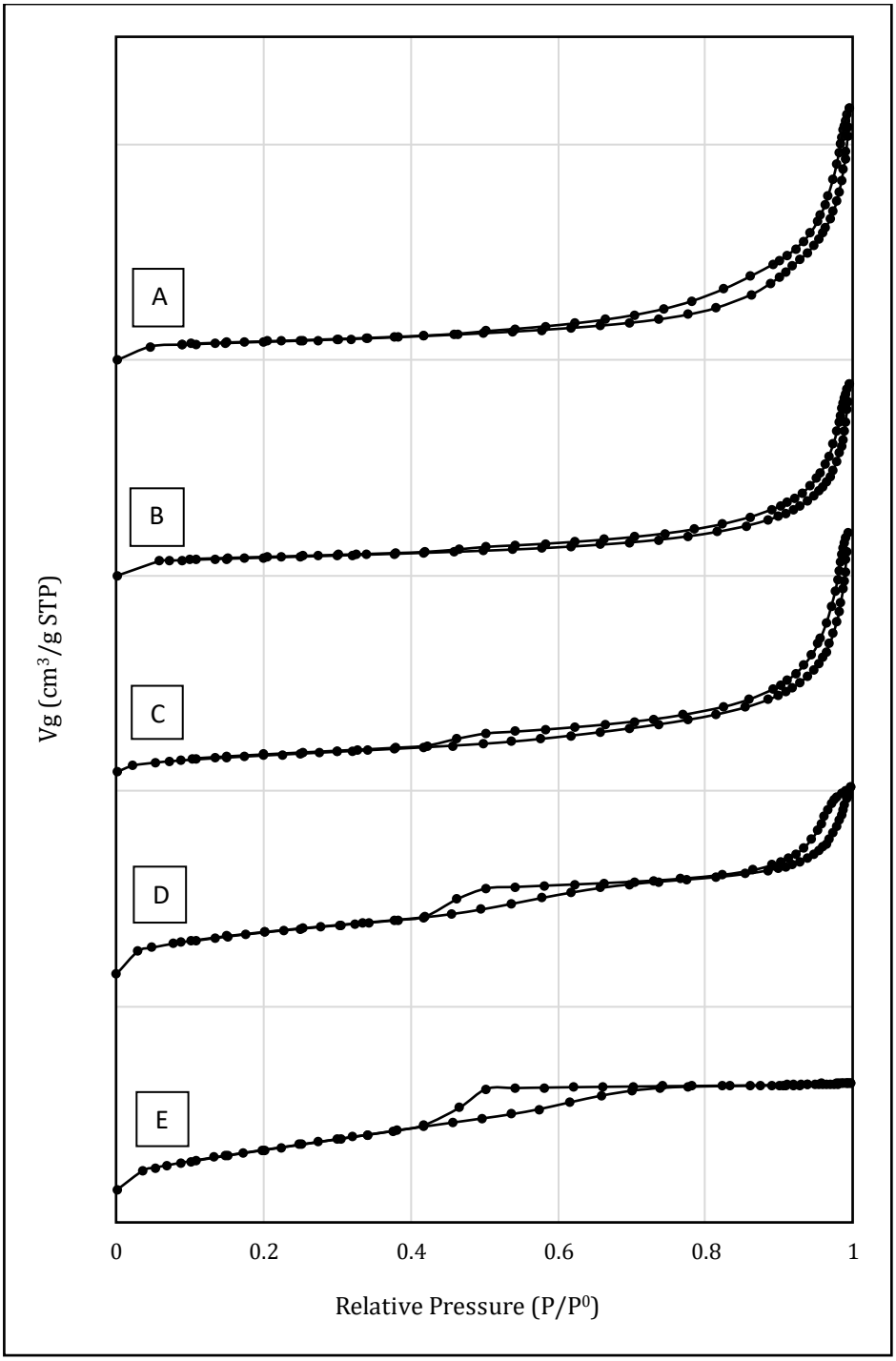


Figure 4.6: Nitrogen isotherms obtained for catalysts A – E.

Intriguingly, for the Mg-incorporated Ni samples, it can be seen that neither of those samples resemble hysteresis loops similar to that of the Ni-only silicate sample E, as the addition of Mg has obviously altered the pore characteristics of the catalyst. Nevertheless, it can be perceived that as the ratio of Ni to Mg increases

from samples B to D, the hysteresis loops presented evolve from a Type H1 loop, which is associated with porous materials known to comprise agglomerates, to a Type H3 loop. In this case, it is important to note that an aggregate (Type H3) is an assemblage of particles that are loosely coherent and as opposed to an agglomerate (Type H1), which is defined as an assemblage of particles rigidly joined together (Sing et al., 2008). This could also explain the dramatic increase in BET surface areas (Table 4.4) from 66.9 to 192.5 $m^2 g^{-1}$ for samples B to D when Mg is introduced, whereby particles in the samples form a more loosely packed structure, resulting in higher amounts of pores and hence, a higher total surface area. Babu and co-workers (1992) have noted that MgO acts as a spacer between Ni crystallites, thus enhancing the total surface area of the catalyst. Moreover, further evidence for the modification of textural properties due to Mg incorporation can be seen from the pore size distribution of the samples, as per Figure 4.7. Specifically, the addition of Mg resulted in a relatively broader pore size distribution, with more pores possessing pore widths larger than 5 nm. This subsequently resulted in the increase in total surface area (sample D), mean pore width (samples B, C and D) and total pore volume (samples B, C and D), as shown in Table 4.4. It is noted that catalysts that exhibit a high pore volume indicate the presence of well-developed mesopores (Jung et al., 2012). Among the Mg-containing samples, it should be made known that this effect is more apparent when Mg is added in smaller amounts, as per sample D. It is also discovered recently that by incorporating small amounts of Mg into catalysts, as previously reported by Dieuzeide et al. (2016) and Iriondo et al. (2010), has resulted in improved textural properties, stability and catalytic performance of their catalysts, which resonates with the results obtained in this study.

Table 4.4: Results obtained from BET analysis performed on the catalysts.

Sample	BET surface area ($m^2 g^{-1}$)	Pore volume [a] ($cm^3 g^{-1}$)	Average pore width [a] (nm)	Mesopore[b] (vol%)	Macropore[b] (vol%)
A	67.7	0.4260	19.57	62.09	37.91
B	66.9	0.3137	19.62	58.00	42.00
C	133.9	0.4136	15.58	64.35	35.65
D	192.5	0.2277	4.85	88.29	11.71
E	270.5	0.2404	3.57	99.98	0.02

[a] BJH desorption branch.
[b] Pore size distribution based on the BJH desorption branch.

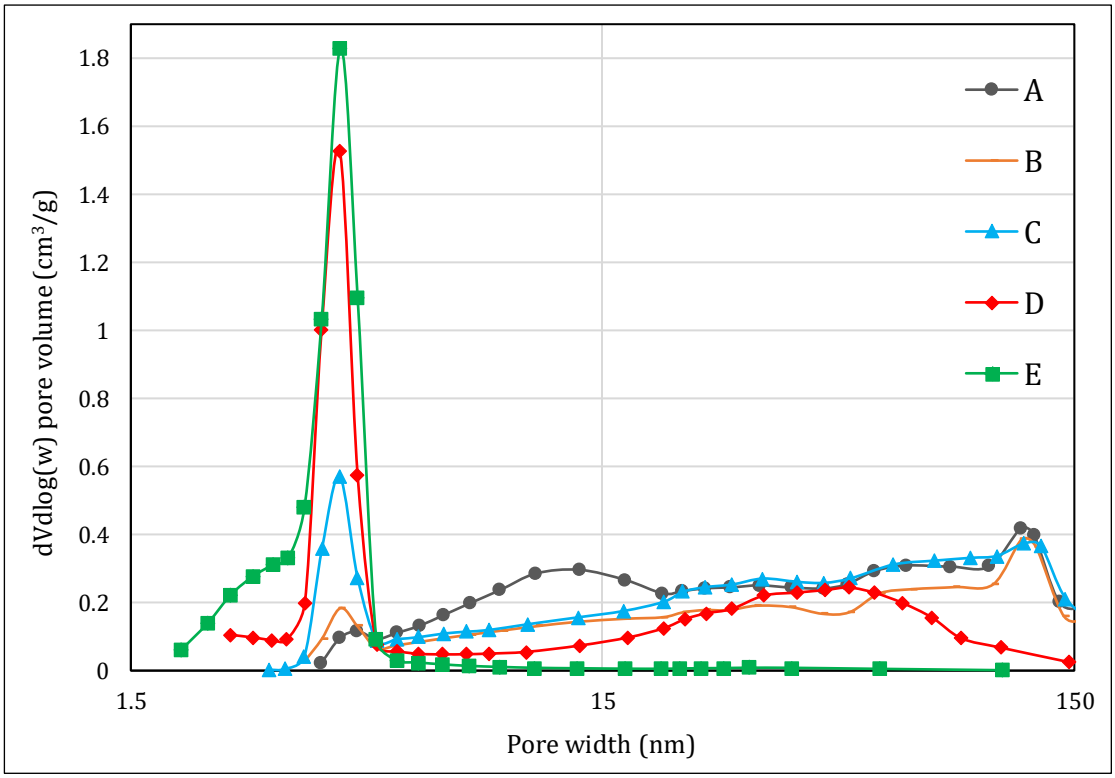


Figure 4.7: Pore size distributions obtained for the catalysts.

The H_2-TPR analysis was to determine the reducibility of the samples, as well as provide valuable insight into their optimum reduction temperatures. TPR

data is also useful in characterising the metal-support interaction (MSI) in supported heterogeneous catalysts.

A few observations can be drawn according to Figure 4.8. It can be seen that sample A has a stunted TPR profile as well as a relatively negligible hydrogen consumption, which is common for MgO as it does not undergo reduction at that temperature range (Kumar et al., 2004; Sulmonetti et al., 2016). The reduction profiles of the samples are characterised by multiple reduction peaks with poor resolution, thus denoting the presence of complex and intimate interactions between the basic Ni carbonate (during the co-precipitation step using sodium carbonate) and silica support, in accordance with other researchers (Coenen, 1989; Gabrovska et al., 2005; Ghuge et al., 1993). Nevertheless, the small reduction peaks in the curve ca. 150 – 200 °C (labelled as i) are ascribed unambiguously to the reduction of higher Ni(III) oxides in trace quantities (Ni_2O_3 to NiO), which is a common occurrence for precipitates calcined at temperatures 400 °C or lower, as per this present study (Ermakova and Ermakov, 2003; Mile et al., 1988). However, since the XRD results exhibited no obvious Ni_2O_3 signals, it is suggested that the Ni_2O_3 phase present was too sparse in amount and also highly dispersed on the support (Sidik et al., 2016). On the contrary, the broad reduction peaks at higher temperatures ca. 300 – 600 °C (labelled as ii) correspond to compounds of difficult reducibility, which can be justified by the formation of NiO and Ni hydrosilicates. Researchers have attributed this high temperature peak to the strong interaction between Ni and silica, resulting in a highly dispersed, antigorite-like ($Ni_3Si_2O_5(OH)_4$), Ni hydrosilicate (Ghuge et al., 1993; González-Marcos et al., 1997; Stanković et al., 2017), which is confirmed by previous XRD and FT-IR data.

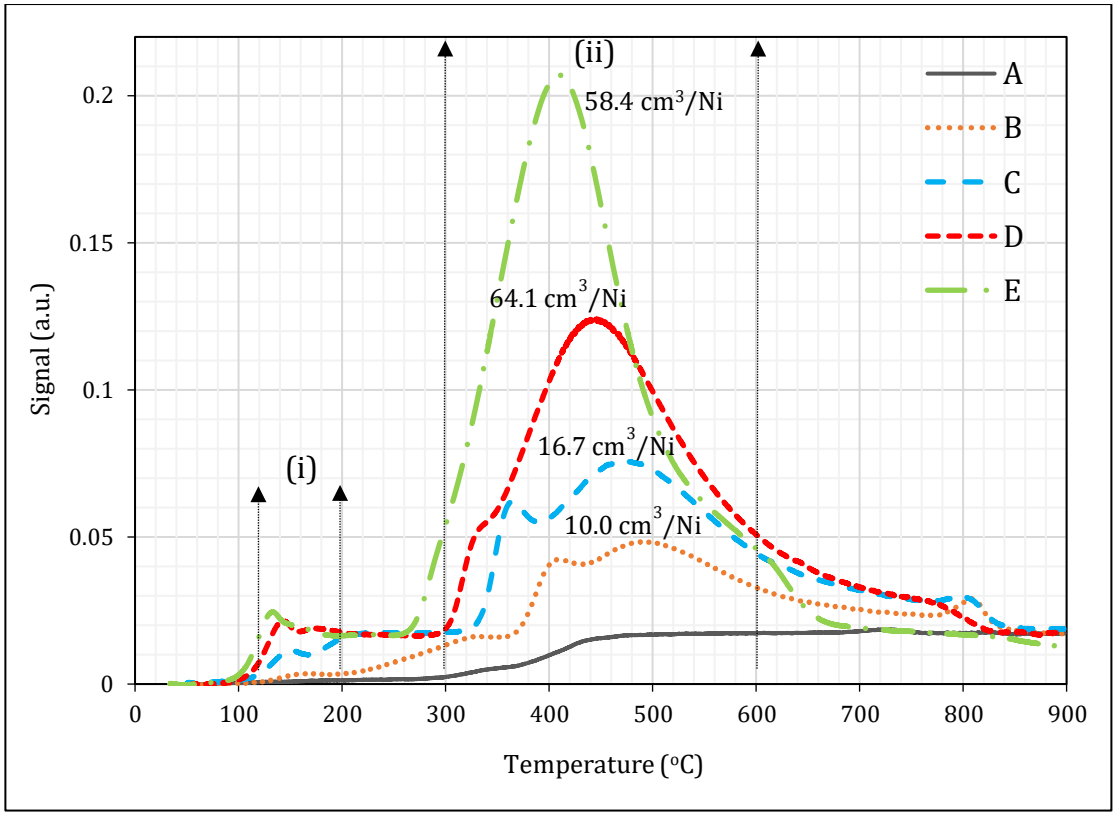


Figure 4.8: TPR profiles at temperatures 30 – 1000 °C obtained for the catalysts.

A general trend that can be discerned from Figure 4.8 is the decrease in Mg content results in the increase in hydrogen uptake for both low temperature (i) and high temperature (ii) peaks, increasing from 10.0 – 233.6 $cm^3\ g^{-1}$. As the Mg content decreases, more Ni forms Ni hydrosilicate with the silica support; hence, more Ni is available for reduction, thus increasing the intensity of the high temperature peak. However, when compared on a Ni molar basis, sample D consumed the most hydrogen (64.1 cm^3/Ni) per mole of nickel, higher than that of sample E (58.4 cm^3/Ni). This suggests that albeit having a lower nickel content, sample D was able to consume more hydrogen than sample E, presumably due to the presence of more active sites because of the incorporation of MgO as a catalyst promoter.

Furthermore, Mg seemed to have an apparent effect on the reducibility of the Ni-Mg samples. The incorporation of Mg decreased the reducibility, as noted by the shift of the high temperature (ii) peaks of samples B, C and D to higher temperatures, relative to that of sample E. Moreover, it is also observed that the shift in temperature is more obvious when the Mg content is increased, which is also reported in several other works (Bacariza et al., 2017; Guo and Lu, 2014; Hu et al., 2012). This displacement of the peak to higher temperatures could be ascribed to the stronger synergistic interactions between Ni, Mg and the Si support, which increases with the Mg content (Thyssen et al., 2017). Comparing the Mg-containing samples, it can be observed that samples B and C exhibit broad TPR profiles, which contains the reduction of several intermediate species in addition to the basic Ni carbonate and Ni hydrosilicate. The existence of these intermediate species points towards the possibility of complex physical and chemical interactions between Ni-Mg-Si, which could result in their relatively lower total surface area as presented in the textural analysis (BET). On the other hand, sample D exhibits a TPR profile that closely resembles that of sample E, albeit having a lower hydrogen uptake due to its lower Ni content and a lower reducibility. It is hence suggested that Mg has the ability to alter the metal-support interaction, consequently prompting a stronger interaction between Ni and the support, resulting in the stabilisation of the Ni species in the Ni-Mg structure that necessitates a higher reduction temperature (Bacariza et al., 2017; Nitta et al., 1985). In this case, electron density effects may have an important role in encouraging these alterations. In the basic Ni carbonate network, Mg as a promoter could effectively shift the electron density away from Ni in a -Ni-O-Mg- linkage, thus rendering the Ni species less reducible (Babu et al., 1992). This took into

consideration the large difference between Mg^{2+} and Si^{4+} in terms of their charge/radius ratio, whereby the former is 3.030 while the latter is 9.523. Thus, a Ni-O-Mg linkage instead of Ni-O-Si linkage would greatly affect the reducibility of the catalyst (Pfefferle et al., 2013). Ultimately, this leads to a stronger metal-support interaction (SMSI) in the catalyst, though hampering the reducibility of the catalyst, could bring about high catalyst stability and dispersion (Shalvoy and Reucroft, 1979). This decrease in reducibility is also said to be beneficial for some reactions and processes, as the Ni^0 crystallites would be less exposed on the surface when the strongly interacting Ni-Mg is reduced, thus lowering the probability of sintering from occurring (Choudhary et al., 1997). In addition, several other researchers have also noted the positive effect of Mg as a promoter, whereby the addition of Mg enhanced metal dispersion as well as strengthened the metal-support interaction of their catalysts, ergo improving the catalytic performance (Carrero et al., 2010; Vizcaíno et al., 2009).

Table 4.5 exhibits the results obtained from the hydrogen pulse chemisorption analysis. It should be noted as this analysis is specific for catalysts containing Ni, sample A was therefore rightfully omitted from this analysis, as it does not contain Ni. Based on the data obtained from the analysis, it can be seen that the samples generally possess high Ni dispersion and surface area, owing to the fact that the samples were synthesised via sequential precipitation, which results in catalytic materials containing highly developed surfaces (Lok, 2014).

Table 4.5: Hydrogen pulse chemisorption results obtained for the catalysts.

Sample	**H_2 adsorbed ($cm^3\ g^{-1}$ STP)**	**Ni dispersion [a], D_{Ni} (%)**	**Ni metal surface area [b], SA_{Ni} ($m^2\ g_{Ni}^{-1}$)**
A	-	-	-
B	2.017	5.28	35.18
C	3.710	5.86	39.00
D	8.116	8.79	58.55
E	7.428	7.45	49.63

[a] Calculated according to Eq. (2.9).
[b] Calculated according to Eq. (2.10).

According to Table 4.5, it is found that the hydrogen adsorbed, subsequently the Ni dispersion and surface area, decreased in the following order: D > E > C > B. Based on this observation, interestingly sample D, with a lower bulk Ni content than that of sample E, exhibits higher Ni dispersion (8.79 %) and Ni surface area (58.55 $m^2\ g_{Ni}^{-1}$), despite the fact that generally a higher bulk Ni content leads to higher Ni dispersion or Ni surface area, as more Ni is made available. Furthermore, samples B and C exhibit chemisorption properties comparable to that of sample E (within a 30 % range), although the former two possess lower Ni contents. Accordingly, this finding fortifies the fact that the presence of Mg induces a stronger metal-support interaction between the Ni crystallites and the silica support, ergo resulting in the enhancement of Ni dispersion and subsequently the Ni surface area, which is consistent with the previous TPR studies. This is also in agreement with the crystallite sizes obtained from the previous XRD results, whereby sample D, which has a smaller crystallite size, is expected to present better dispersion properties.

Furthermore, as elucidated by Babu and associates (1992a), Mg could potentially reduce the sintering of Ni crystallites through a migration mechanism by acting as a barrier or physical spacer for the Ni crystallites. In comparison with other researchers, it was discovered that Mg and Ce promoters had a positive influence on the metal-support interaction of Ni catalysts supported over γ-Alumina doped with titania (Al-Fatesh et al., 2019). In particular, the catalysts exhibited excellent Ni dispersion, Ni surface area and stability. In a separate work, Bacariza and co-workers (2017) further verified the role of Mg as a promoter in improving the Ni dispersion of their zeolite-based catalyst. Similarly, research carried out by Thyssen and associates (2017) have also exhibited optimistic results for the steam reforming of glycerol when they integrated MgO into their Ni catalyst, which was synthesised via an impregnation route. They noted that a possible interaction between Ni ions and MgO might have modified the synergy between the support and loaded metals, thus favouring the high dispersion of Ni and the increase in surface area of their samples. Nevertheless, the abovementioned researchers also noted that said benefits only manifested to a greater extent when Mg was incorporated in lower amounts, which is a finding that is in unison with this present work, as sample D exhibited the best properties. Therefore, for the silica-support-based samples containing Mg in this present study, albeit possessing lower reducibility, could have a lower extent of Ni crystallite sintering during the reduction step, which is due to the excellent dispersion of the Ni precursor phase within the silica matrix by Mg, thus diminishing the loss in metal surface area. This consequence could potentially signify that said samples could be more catalytically active, as more active metal centres are present.

Centred on the aforementioned characterisation techniques, it can be deduced that sample D is the best-performing sample amongst the rest. When a promoter metal such as Mg is incorporated into the nickel-silica catalyst structure in a relatively small amount, substantial improvements to the overall catalyst characteristics can be discerned. Firstly, physisorption analysis has shown that sample D possesses a high BET surface area and pore volume, as well as a uniform pore size distribution, which are quintessential qualities of an active catalyst as it is preferable to maximise the number of active sites available for reaction (Dumesic et al., 2008). Secondly, chemisorption analysis has demonstrated that sample D has a moderately strong metal-support interaction with a high metal dispersion and metal surface area. This could very well provide the catalyst with high stability and resistance against sintering during reduction or reactions, while allowing more reactants to attach to the active Ni sites, thus favouring catalytic activity. Therefore, sample D is hereafter employed as a base or benchmark sample for the following studies.

4.3.3. Effects of ultrasound irradiation during catalyst synthesis

4.3.3.1. Characterisation of synthesised catalysts

To ascertain the effects of incorporating ultrasonic irradiation into the catalyst synthesis, the subsequent sonicated catalysts were synthesised based on sample D, as it exhibited desirable characteristics as mentioned in the previous Section 4.3.2. These samples were then characterised accordingly as follows.

The morphology of the catalysts was interpreted via the SEM scans in Figure 4.9. While the non-sonicated catalyst D exhibited rough surfaces with the presence of conglomerates, the morphology of the sonicated catalysts all appeared to be smooth and uniform, which confirmed the capability of ultrasound to reduce the extent of particle aggregation (Raman and Abbas, 2008). As demonstrated later, the combination of ultrasound irradiation and co-precipitation generated a synergistic effect whereby a uniform environment was provided for the nucleation and growth of metal particles, while concurrently averting small particles from agglomerating (Mahboob et al., 2017), thus preventing the formation of aggregates such as those in the non-sonicated catalyst. In particular, the increased ultrasonic intensity instigated more violent micro-bubble implosions, hence inducing stronger shock waves and micro-jets with velocities of approximately 400 km/h. Consequently, vigorous inter-particle collisions and surface pitting could occur, simultaneously suppressing the aggregation of catalyst particles, thus producing particles with increased dispersion (Suslick and Doktycz, 1990). This observed phenomenon resonated with the work of other researchers, in which a lower degree of particle agglomeration was noticed with the use of ultrasound during synthesis (Mahboob et al., 2017; Sharifi et al., 2014).

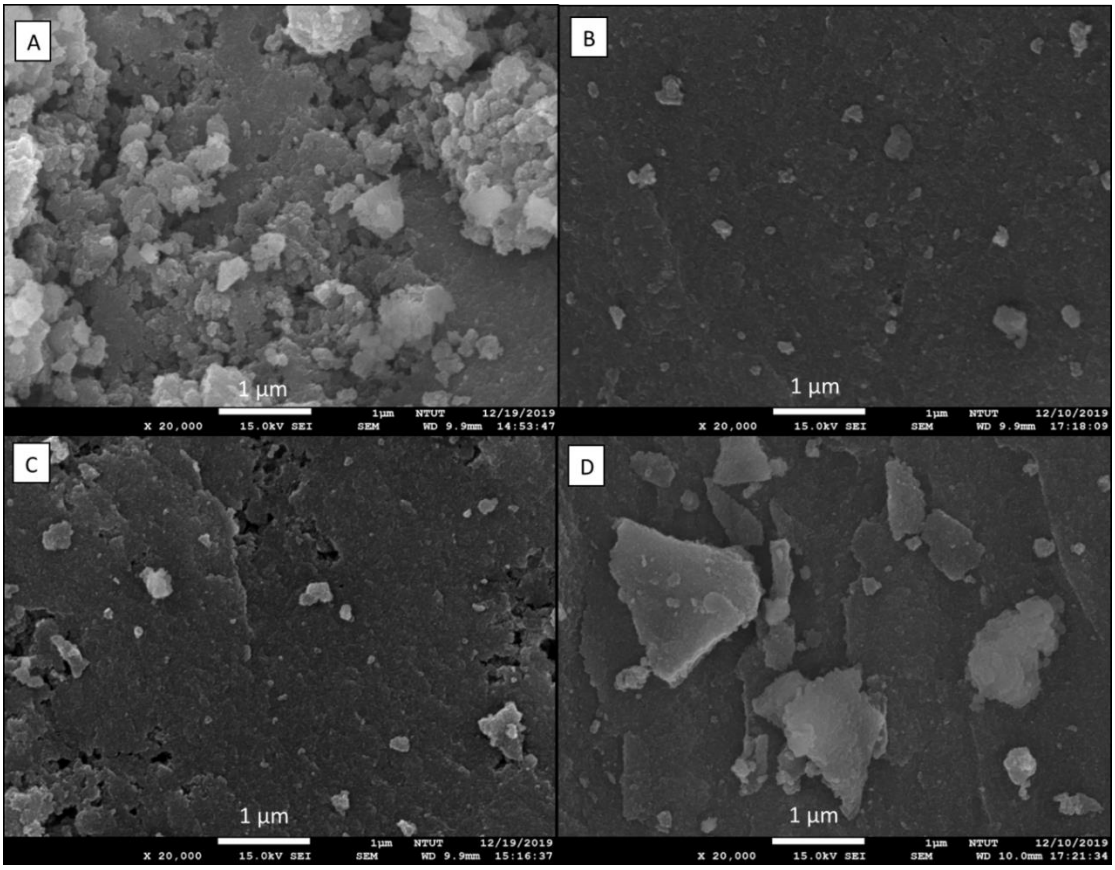


Figure 4.9: SEM scans for catalysts (A) D; (B) D_US20; (C) D_US30; and (D) D_US40.

Note: Micrographs are of 20,000x magnification and 1 µm scale.

From the EDX and XPS analysis of the synthesised catalysts in Table 4.6, it is apparent that they were constituted of the required elements for the formation of the catalysts, which indicates the efficacy of the synthesis procedure. With a typical approximated penetration depth of the EDX electron beam of 0.4 µm (Yang et al., 2020), the measured atomic percentage was considered to represent the bulk atomic percentage of the catalysts. On the other hand, characterisation by XPS detects the elemental composition of the samples at the surface layer, which corresponds to a penetration depth of approximately 1 – 12 nm, hence demonstrative of the superficial composition of the catalysts (Yang et al., 2020). As the catalysts investigated were all synthesised according to the same starting

materials, it will be useful to draw comparisons based on their bulk and surface atomic distributions to ascertain the changes due to the difference in synthesis conditions. As shown in Table 4.7, there were decreasing trends for the Mg/Ni and Si/Ni atomic ratios with the increase in ultrasound intensity during the ageing process from data obtained from both EDX and XPS analyses. It is worth noting that while the difference was small for the Mg/Ni ratios between the EDX and XPS methods, there was a substantial gap in the Si/Ni ratios between the two aforementioned methods. It is believed that the observed change in Mg/Ni and Si/Ni atomic ratios was mainly due to the effect of ultrasonic intensity (or lack thereof) on the sequentially co-precipitated Ni-Mg hydroxycarbonates and siliceous materials during the ageing process.

A conceptualisation demonstrating the action of ultrasound during the ageing process is presented in Figure 4.10. It is herein noted that, for the sake of accuracy, prefixes such as hydro- or hydroxy- are used to represent the actual phases of the precursors present during synthesis. After the synthesis process, the aforementioned phases were subjected to dehydration and calcination and subsequently transformed into their respective oxides or silicates, which were then used for characterisations mentioned in this present work. In conventional synthesis of sequentially precipitated catalysts without the presence of ultrasound, the formation of Ni silicate proceeded as the silica precursor was added during the ageing process, which occurs under an alkaline condition at elevated temperatures. Prior to the ageing process, co-precipitates of Ni-Mg hydroxycarbonates were present in the suspension. As the ageing process was initiated, silicate ions (in the form of Na_2SiO_3) were dosed into the ageing solution, which then: (i) attached

epitaxially to the co-precipitates (Lok, 2014), forming nickel hydrosilicates, in which Ni-Mg hydroxycarbonates would then be anchored; (ii) attached to existing hydrosilicates and underwent polymerisation to form silica clusters (Ghuge et al., 1993). This attachment of silicate ions is illustrated by Step 1 in Figure 4.10. In the presence of ultrasonic irradiation, the Ni-Mg hydroxycarbonate co-precipitates can experience erosion, causing the shrinkage of the size of the co-precipitates, which will eventually lead to higher Ni dispersion as seen in Table 4.8. The increase in ultrasound intensity also led to lower Mg/Ni ratios, beginning with sample D at 0.329 (theoretical ratio = 0.333 with Ni:Mg = 3:1) and down to 0.268 for sample D_US40. During the formation of Ni-Mg hydroxycarbonate nanoparticles, Mg has the tendency to migrate to surficial layers due to its lower surface energy compared to Ni. It is noted that Ni has a surface energy of 2.080 J/m^2, while Mg has a surface energy of 0.688 J m^{-2} (Tyson and Miller, 1977). As a result, it is quite likely that a significant amount of Mg was eroded away from the surface layers of Ni-Mg hydroxycarbonate co-precipitates when the ultrasonic intensity was increased. As shown in Table 4.7, the difference in the Mg/Ni ratio for the surface and bulk (XPS – EDX) decreased as the ultrasonic intensity increased from samples D to D_US30, indicating the increased extent of Mg erosion from the catalyst surface. However, sample D_US40 registered an increase in the Mg/Ni ratio difference between the surface and bulk, likely due to the re-attachment of the Mg ions at higher ultrasonic intensities, as similar investigations reported the inefficiency of ultrasonic irradiation at high powers causing the re-agglomeration of particles (Nguyen et al., 2011). In a similar manner, higher ultrasound intensity has also disrupted the formation of hydrosilicates and silica clusters and led to the drop in the bulk Si/Ni ratio, from 0.333 to 0.244.

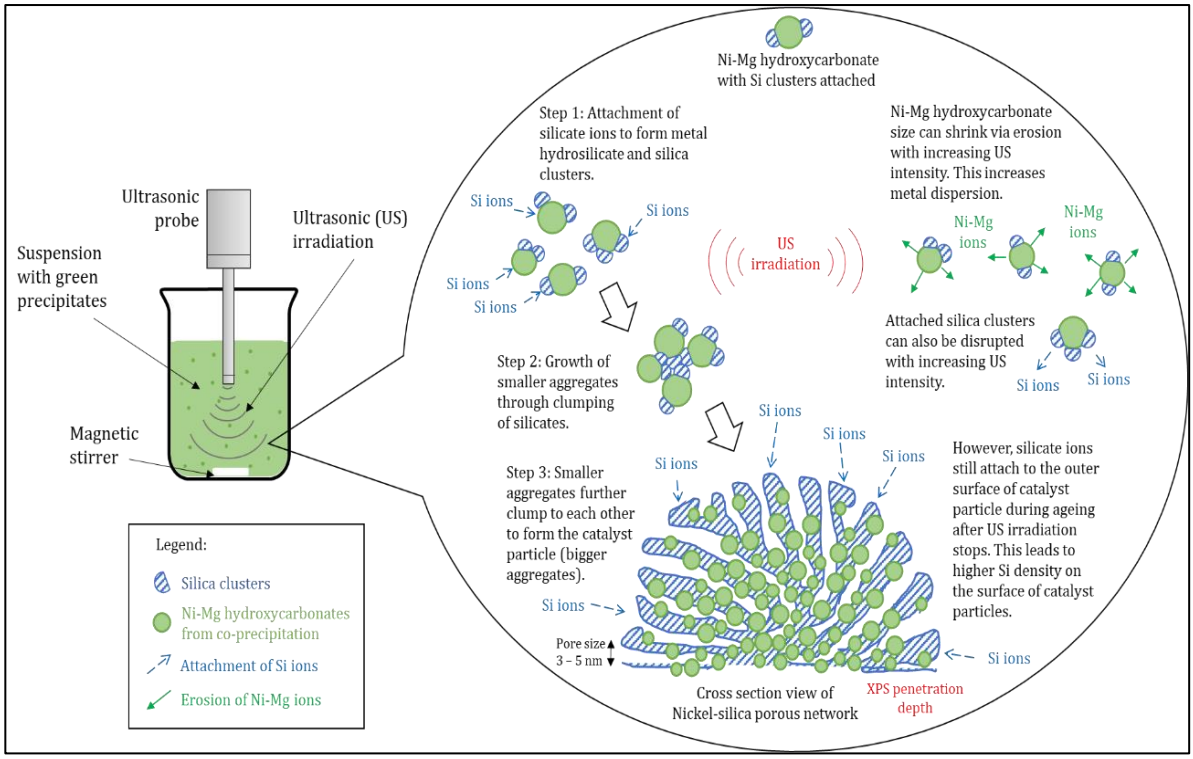


Figure 4.10: Conceptualisation of the formation of the nickel-silica porous network during the ultrasound-assisted synthesis of the catalysts.

Table 4.6: Elemental composition of the catalysts obtained from EDX and XPS.

Catalyst	**Ni (at%)**		**Mg (at%)**		**Si (at%)**		**O (at%)**	
	EDX	XPS	EDX	XPS	EDX	XPS	EDX	XPS
D	24.9	15.6	8.2	5.4	8.3	7.3	58.6	71.5
D_US20	26.0	15.5	9.0	5.5	8.0	7.2	57.0	71.7
D_US30	29.5	17.9	8.0	4.6	8.2	6.6	54.3	70.9
D_US40	35.3	18.3	9.5	5.3	8.6	6.1	46.6	70.3

Table 4.7: Molar ratio of the catalysts calculated using the EDX and XPS data.

Catalyst	Mg(at%)/Ni(at%)			Si(at%)/Ni(at%)		
	EDX	XPS	XPS-EDX	EDX	XPS	XPS-EDX
D	0.329	0.346	0.017	0.333	0.468	0.135
D_US20	0.346	0.354	0.008	0.308	0.464	0.156
D_US30	0.271	0.257	-0.014	0.278	0.369	0.091
D_US40	0.268	0.289	0.021	0.244	0.333	0.089

Following the attachment of silicate ions to form metal hydrosilicate and silica clusters, the individual silicate-attached Ni-Mg hydroxycarbonates would clump together through the -O-Si-O- bonding provided by silicate ions in the ageing solution (Ghuge et al., 1993; Jesionowski et al., 2002). Small aggregates begin to form from the clumping of nano-sized silicate-attached Ni-Mg hydroxycarbonates (Step 2 of Figure 4.10), while further clumping of small aggregates lead to bigger aggregates, eventually forming the catalyst particle network (Step 3 of Figure 4.10). The significantly higher Si/Ni ratios as observed by XPS (from 0.468 to 0.333) compared to EDX (from 0.333 to 0.244) was mainly a result of silicate ions attaching to and growing on the outer surface of the aggregated catalyst particles as silica clusters. Attachment of silicate ions within the pores of the catalyst particles is thought to be insignificant compared to the outer surface due to slower mass transfer in the narrow pores. In the present work, ultrasound irradiation was only active during the first 10 minutes of the ageing process for the sonicated samples, while the remaining ageing period was carried out without ultrasonic irradiation. As higher surface Si/Ni density was also observed for catalyst samples

sonicated with high intensity, it can be inferred that the growth of silicate ions on the surface of the catalyst particles took place predominantly following the termination of irradiation, since a high ultrasonic intensity can disrupt the formation of hydrosilicate and silica clusters. It should be noted that the discrepancy between the bulk and surface layer Si/Ni ratios in this present work was in stark contrast with the typical synthesis method of simultaneously co-precipitating the active and support phases. Compared to the sequential precipitation method used in this work, whereby the support phase was added after the co-precipitation of active phases, the simultaneous co-precipitation of both active and support phases could result in a more uniform and homogeneous distribution of the elements (Moulijn et al., 1993; Munnik et al., 2015), thus the clustering of the elements would be less drastic in that case.

The XRD diffractograms for the catalysts are shown in Figure 4.11. Peaks representing the phases of NiO (ICDD: 01-073-1523), MgO (ICDD: 01-089-7746) and nickel silicate ($Ni_3Si_2O_5(OH)_4$) (ICDD: 01-083-1648) were detected. Diffraction patterns of all samples exhibit reflections at the 2θ value of 36 °, 43 °, 63 °, 75 ° and 79 °, which correspond to NiO(111), NiO(200), NiO(220), NiO(222) and NiO(311) planes, respectively (Lovell et al., 2015; Sidik et al., 2016). These results agreed well with those of several other investigations (Cai et al., 2014; Cho et al., 2002). The SiO_2 support was amorphous, which did not contribute to any peaks on the diffractogram (McArdle et al., 2014; Pettiti et al., 2015). The NiO crystallite size was ascertained using the Scherrer equation, referencing the characteristic peak at 43 °, with the results presented in Figure 4.11. In general, the diffractograms registered reflections that appeared broad, which signified the poorly crystallised state of the

catalysts. This also indicated the presence of small and well-dispersed phases and highly developed surfaces (Echeverria and Andres, 1990; Gabrovska et al., 2005). In addition, the lack of sharp peaks also indicated the absence of large crystalline domains or metal oxide clusters, which could be of great advantage for metal dispersion during catalyst reduction (Sulmonetti et al., 2016). On the other hand, the presence of nickel silicate, formed by a strong interaction between Ni and Si, is also detected at the 37 ° peaks. Poorly crystallised nickel silicate compounds with imperfect nickel antigorite structures are commonly formed when the co-precipitating nickel salt and silicate solutions are at temperatures lower than 100 °C, with structures such as $Ni_3Si_2O_5(OH)_4$ (Gabrovska et al., 2006). Due to the incorporation of ultrasound during synthesis, the samples registered an increase in amorphicity, evidenced by the decrease in crystallite size of 2.56 nm for the unsonicated catalyst D, to a range of 2.28 – 2.41 nm, for the sonicated catalysts. Pertaining to the sonicated catalysts, the crystallite size decreased with the increase in ultrasonic intensity. This may be owed to the highly turbulent mixing induced by sonicating the suspension during synthesis, in which unique conditions due to acoustic cavitational bubble collapse were produced. This highly turbulent mixing is facilitated by the presence of acoustic streaming and high mass transfer (Cravotto et al., 2013) and subsequently resulted in a higher packing disorder in the samples, forming samples that were more amorphous (Suslick and Price, 1999). Furthermore, as the cavitation bubbles collapsed violently, localised regions of extremely high cooling rates, in the range of 10^{11} K s^{-1}, were generated, which could inhibit the growth of crystals (Suslick and Price, 1999).

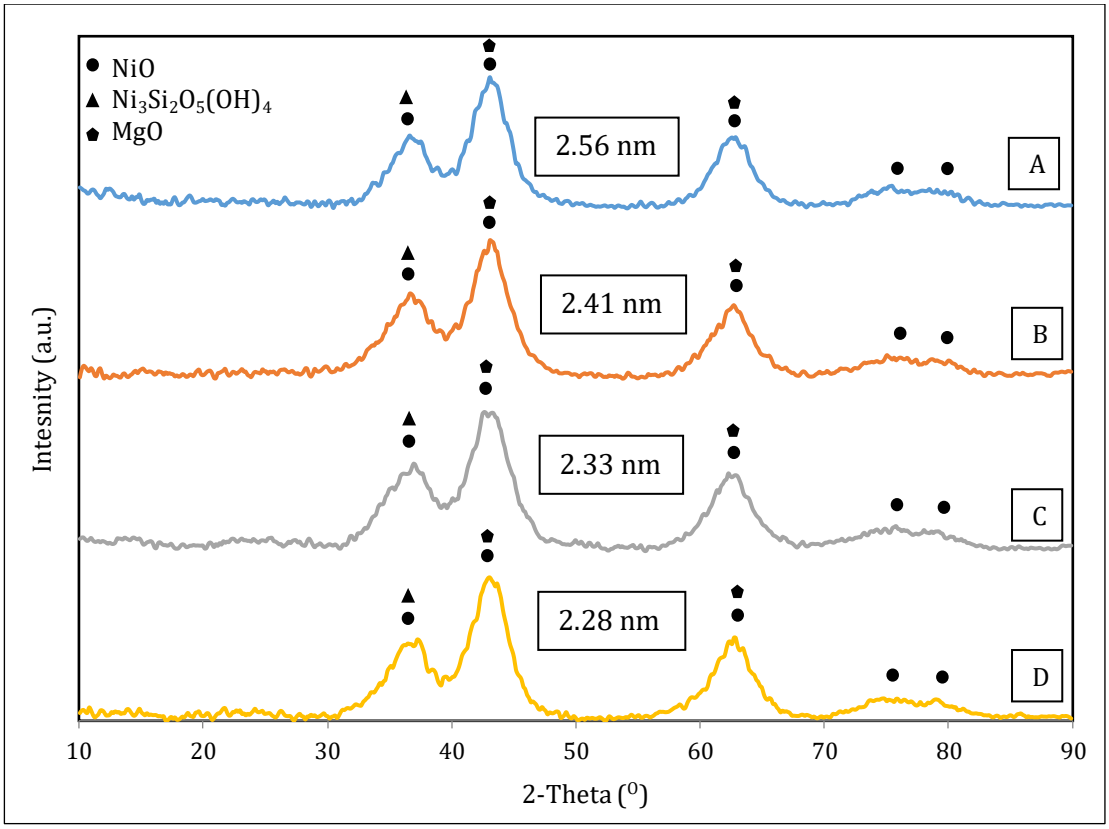


Figure 4.11: XRD diffractograms of catalysts (A) D; (B) D_US20; (C) D_US30; and (D) D_US40 and their respective identified compounds.

Note: Insets represent the crystallite size of NiO obtained using the Scherrer equation based on the XRD diffractograms.

H_2-TPR was used to probe the redox properties of the unsonicated and sonicated catalysts, with results presented in Figure 4.12. The reduction profiles of the catalysts are characterised by multiple reduction peaks fused together into a much broader reduction band from 100 – 800 °C, with a peak ca. 400 – 500 °C. This observation denotes the homogeneous distribution of small particles over the support, with the presence of complex and intimate interactions between the active phase and support, which supports the XRD diffractograms and is also in accordance with other researchers (Cepeda et al., 2016; Gabrovska et al., 2005;

Ghuge et al., 1993), as well as Ni catalysts prepared via other techniques such as sol-gel (Ermakova and Ermakov, 2003).

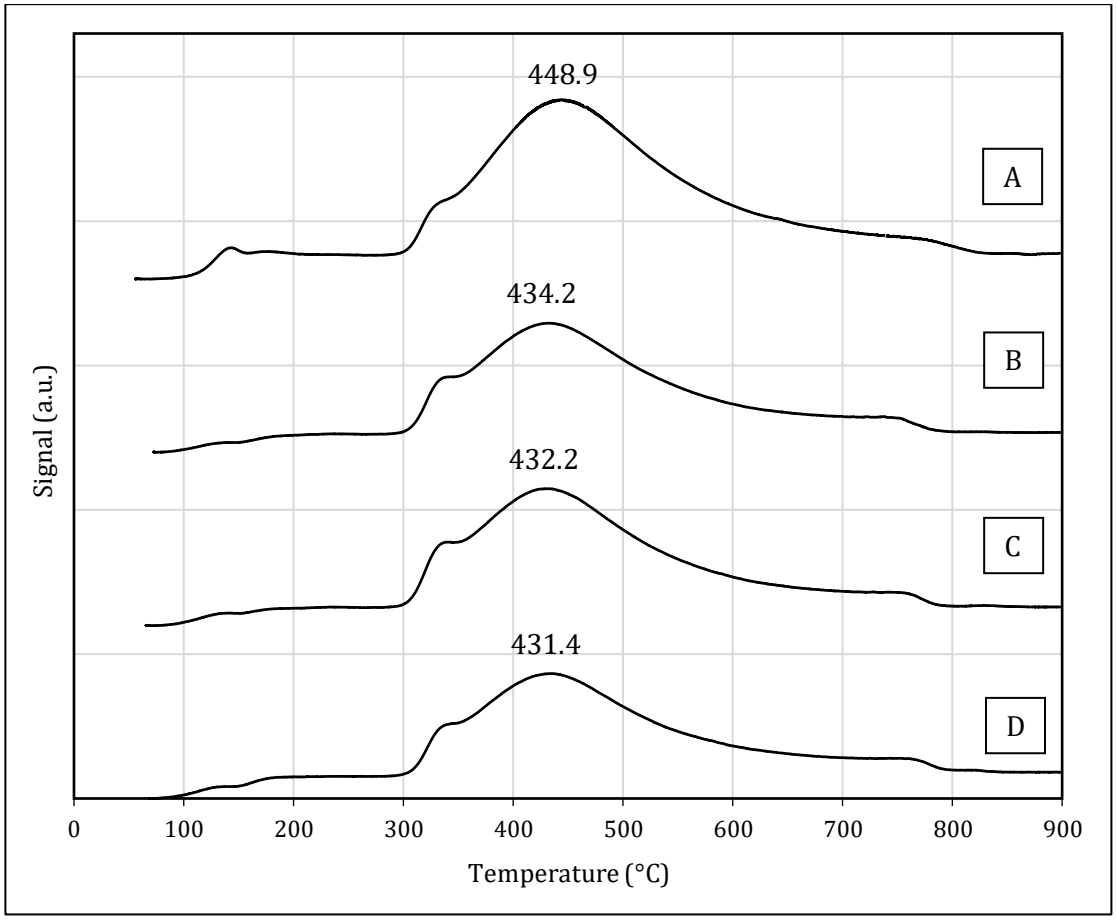


Figure 4.12: TPR profiles at temperatures 30 – 900 °C obtained for catalysts (A) D; (B) D_US20; (C) D_US30; and (D) D_US40.

From the figure, it is observed that the unsonicated catalyst D had the highest maxima of 448.9 °C, while the sonicated catalysts had maximum reduction peaks in the range of 431 – 435 °C. Moreover, sample D_US40, irradiated with the highest ultrasonic intensity presented the lowest reduction peak at 431.4 °C. The presence of ultrasound during synthesis has marginally increased the reducibility of the catalysts, which is also a finding supported by other relevant investigations concerning ultrasound-assisted catalysts synthesis (Ameen et al., 2019; Chu et al.,

2019). The increase in reducibility also signified the decrease in extent of metal-support interactions, in which phases with weaker interaction with the support (i.e. NiO) would be more readily reduced to Ni^0.

To gain more insight into the TPR results, the broad peaks were deconvoluted into symmetrical peaks via Gaussian multipeak curve-fitting to evaluate the relative percentage of the different reducible species, as well as their peak positions, presented in Figures S1-S4 (Appendix III). In total, three main peaks could be identified, which were labelled as α, β and γ. The reduction temperatures reported can be classified into different types of nickel species, which are directly associated with the degree of interaction with the silica support. This also indicates that Ni species of different extents of interaction coexist within a catalyst sample. Henceforth, the three peaks are classified based on their reducibility and explained based on their relative proportion and individual peak position. It is noted that no reduction peaks corresponded to the reduction of Mg species due to their extreme difficulty in reduction under the present conditions applied (Sulmonetti et al., 2016). The first low temperature peak (α) at ca. 181 – 198 °C represented a minor portion approximately 6 % or less of the total reduction profile. These are ascribed unambiguously to the reduction of higher Ni(III) oxides in trace quantities (Ni_2O_3 to NiO), which is a common occurrence for precipitates calcined at temperatures 400 °C or lower, as per this present study (Ermakova and Ermakov, 2003; Mile et al., 1988). However, since the XRD results exhibited no obvious Ni_2O_3 signals, it is suggested that the Ni_2O_3 phase present was too sparse in amount and also highly dispersed on the support (Sidik et al., 2016). On the other hand, the β peaks at ca. 411 – 422 °C were due to the NiO species

possessing weak interactions with the silica support (Moogi et al., 2019; Soghrati et al., 2018). Lastly, the γ peaks at ca. 495 – 514 °C were due to the Ni species having strong interactions with the silica support, hence forming Ni silicate, which presented difficulty in reduction (Moogi et al., 2019; Soghrati et al., 2018).

Based on Table 4.8, one can see that the composition of α for all samples remained in the range of approximately 3 - 6 %, representing their minor role in the catalysts. However, the percentages of β and γ varied significantly with the presence of ultrasound and its intensity. In general, the weaker NiO phase, β, observed an increase in proportion with the increase in ultrasound intensity, from 32.1 % in the unsonicated catalyst and up to 42.5 % in the sonicated counterparts. Accordingly, the Ni phase with stronger interactions, γ, also observed a declining trend with the increase in ultrasound intensity, registering 61.7 % in the unsonicated catalyst and down to 53.4 % for sample D_US40, which suggests the possibility of Ni silicate erosion or inhibition by ultrasonic irradiation. Interestingly, the increase in ultrasonic intensity from 20.78 to 27.72 W cm^{-2} did not lead to significant variations in the relative percentages of β and γ, which indicates that there is a limit to the extent of Ni silicate erosion caused by ultrasonic irradiation. Considering the bond linkages of -Si-O-Ni- present in Ni hydrosilicate species (Ghuge et al., 1993) and the bond dissociation energy of Ni-O as 391.6 kJ mol^{-1} (Dean, 1999), calculations have shown that it is in fact plausible for acoustic micro-bubble implosions to generate sufficient energy for the bond breakage of Ni-O (Nesterenko and Berlizov, 2007), which erodes away the Ni hydrosilicate structure. On the other hand, with a significantly higher bond dissociation energy at 440 kJ mol^{-1} for the Si-O bonds present in the bond linkages of -Si-O-Si-, it

became more difficult to instigate bond breakage once silicate ions were attached to the hydrosilicates to form silica. Consequently, this allowed the silica clusters to act as a protective layer, enclosing the Ni silicate phases to impede its erosion caused by ultrasonication. Instead of Ni silicate erosion, it appeared that the increasing ultrasonic intensity has caused considerable agitation that suppressed the build-up of silica clusters by deterring the polymerisation of silicic acid (Greenberg and Sinclair, 1955), leading to the decreasing trend of Si/Ni ratios as shown previously in Table 4.7.

Table 4.8: H_2-TPR and H_2-pulse chemisorption results for the catalysts.

Catalyst	**Peaks (Temperature, °C; Relative percentage, %)**			**Ni dispersion [a], D_{Ni} (%)**	**Ni surface area [b], SA_{Ni} ($m^2\ g_{Ni}^{-1}$)**	**Particle diameter [c] (nm)**
	α	β	γ			
D	181.4	422.2	501.7	8.79	58.55	11.51
	6.2	32.1	61.7			
D_US20	190.6	411.7	495.7	10.26	68.31	9.24
	3.9	35.8	60.3			
D_US30	198.1	418.3	498.7	14.26	94.95	7.10
	3.2	42.5	54.3			
D_US40	190.6	418.2	514.4	17.81	118.53	5.69
	5.2	41.4	53.4			

[a] Calculated according to Eq. (2.9).
[b] Calculated according to Eq. (2.10).
[c] Calculated according to Eq. (2.11).

Apart from the compositional change in Ni phases in the catalyst, the increase in ultrasonic intensity has also resulted in the shrinkage of Ni-Mg hydroxycarbonate nanoparticles, leading to higher Ni surface area and dispersion. In particular, Ni dispersion was increased from 8.79 % to 17.81 %, while the Ni surface area was increased from 58.55 $m^2\ g_{Ni}^{-1}$ to 118.53 $m^2\ g_{Ni}^{-1}$, as seen in Table

4.8. This suggested that Ni was more dispersed across the support due to the action of ultrasonic irradiation during synthesis, whereby the increase in intensity amplified this phenomenon. As discussed earlier, the improvement in Ni dispersion and surface area could be due to the erosion of Ni-Mg hydroxycarbonates caused by ultrasound irradiation, with higher intensity leading to more severe erosion. Given that the pH remains unchanged at 8.8 during the application of ultrasound irradiation, it is thought that the eroded Ni and Mg ions would re-precipitate and form smaller hydroxycarbonate nanoparticles, which in turn lead to higher Ni dispersion and Ni surface area. Generally, the increase in total metal surface area and dispersion are good indicators of enhanced catalytic activity, as more active sites equate to more area available for reaction to occur.

The chemical and electronic properties of the calcined catalysts were studied using XPS. As per Figure 4.13, the spectra show features associated with Ni $2p_{3/2}$. For all catalysts, the Ni $2p_{3/2}$ is accompanied by the presence of a satellite peak at 861 – 863 eV, congruous to the existence of Ni^{2+} instead of metallic Ni^{0} (Shalvoy et al., 1980). It is noted that these satellite peaks manifest due to the paramagnetic state of the Ni^{2+} species and electron shake-up. Notably, these peaks are typically ca. 6 eV higher than the main Ni $2p_{3/2}$ peak (Alvarez-Galvan et al., 2019), as noted by the ΔE_{sat} values in Table 4.9.

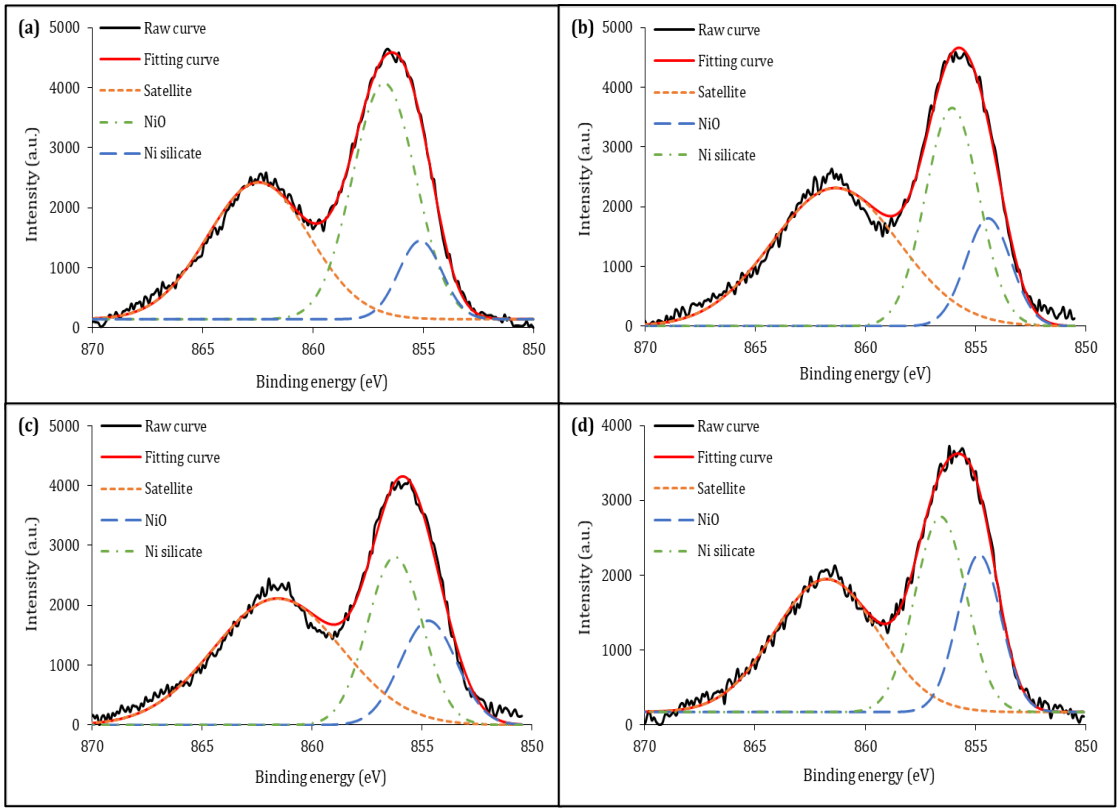


Figure 4.13: Ni 2p3/2 XPS spectra fitting for catalysts (a) D; (b) D_US20; (c) D_US30; and (d) D_US40.

Table 4.9: XPS analysis results for the calcined catalysts.

Sample	**Ni 2p3/2 (eV)**	**Ni 2p3/2 satellite (eV)**	**ΔEsat [a] (eV)**	**Fitted peaks (eV)**		**Relative proportion [b] (%)**		**Si 2p (eV)**	**ΔENi-Si [c] (eV)**
				NiO	Ni Silicate	NiO	Ni Silicate		
D	856.64	862.48	5.84	855.15	856.79	18.6	81.4	103.2	753.44
D_US20	855.78	861.37	5.59	854.44	856.08	29.5	70.5	103.6	752.18
D_US30	855.84	861.57	5.73	854.72	856.24	38.8	61.2	102.5	753.34
D_US40	855.83	861.76	5.93	854.83	856.58	40.7	59.3	102.1	753.73

[a] Separation of Ni 2p3/2 primary line to satellite.
[b] Ratio of integrated area of the two compounds via curve fitting.
[c] Difference between Ni 2p3/2 and Si 2p.

The Ni $2p_{3/2}$ binding energy of the unsonicated catalyst resonated well with reported values of 856.3 – 856.7 eV (Shalvoy and Reucroft, 1979; Vedrine et al., 1978). However, it is discovered that the Ni $2p_{3/2}$ binding energy of the sonicated catalysts experienced a shift to lower values at 855.7 – 855.9 eV. Since XPS analysis is surface sensitive, the discrepancies in binding energies indicated that the Ni species on the surface have been altered electronically (Stanković et al., 2017), in this case due to the incorporation of ultrasound into the synthesis procedure of the catalysts. Furthermore, a decrease in binding energy also indicated a lowered extent of metal-support interaction between the Ni phase and Si phase (Lu et al., 2020; Stanković et al., 2017). In this case, a shift to lower binding energies due to ultrasound has also been reported by other researchers (Li et al., 2006), which led to a change in electron density that may affect the bonding of chemical intermediates to the active sites, thus ultimately affecting the reaction pathways during hydrogenation (Bai et al., 2015, 2017; Wu et al., 2018). Furthermore, this indication of weakening in metal-support interactions is also corroborated with the TPR studies demonstrated earlier, noting the shift in main reduction peaks to lower temperatures in sonicated samples.

To gain more insight into the XPS results, the Ni $2p_{3/2}$ XPS core level region was deconvoluted via Gaussian multi-peak curve-fitting and fitted with three doublets assigned to NiO, Ni silicate and associated satellite features, as shown in Figure 4.13. As the NiO binding energies have been reported to be significantly lower at a range of 854 – 855 eV (Allen et al., 1989; Shalvoy and Reucroft, 1979; Vedrine et al., 1978), it is suggested that another Ni phase exists at a higher binding energy, which is assigned to the Ni silicate phase. Hence, this agreed well with the

two Ni phases detected in the XRD and TPR analyses. In addition, it is known that a relationship can be derived using the difference between Ni $2p_{3/2}$ and Si 2p binding energies, $\Delta E_{Ni\text{-}Si}$ (Coenen, 1991). The existence of Ni silicates in the catalyst sample would give $\Delta E_{Ni\text{-}Si}$ values of 753.2 – 753.8 eV (Lorenz et al., 1979; Occelli et al., 1986; Shalvoy and Reucroft, 1979). From Table 4.9, the $\Delta E_{Ni\text{-}Si}$ values of the catalysts synthesised agreed excellently with this, thus substantiating the presence of the aforementioned phases. Literature has also reported similar binding energy values of nickel silicates (Shalvoy and Reucroft, 1979).

The total area of respective signals, when averaged over the whole system, allows one to approximate the relative amount of species considered (Smith, 2009). In this case, the area under the curve of each deconvoluted peak in Figure 4.13 were used to estimate the relative surface proportion of each nickel species, which are presented in Table 4.9. Echoing the results from the TPR analysis, sonication has also imparted considerable discrepancies on the NiO and Ni silicate surface compositions. The proportion of NiO on the surface was increased from 18.6 % in the non-sonicated catalyst to 29.5 – 40.7 % in the sonicated catalysts, in which this proportion has also increased with higher ultrasonic intensities. Conversely, the Ni silicate phase has also seen a decrease in relative proportion when ultrasound was used during the synthesis, as it dropped from 81.4 % in the unsonicated catalyst D to a range of 59.3 – 70.5 % in its sonicated counterparts. This aforementioned trend observed in the XPS analysis was similar to those obtained from the TPR analysis, albeit with a greater magnitude of change. This was due to the fact that the XPS analysis presents details on the surface composition, which could vary slightly from those of the bulk provided by TPR measurements (Yang et al., 2016).

It was reported that the precipitation of silicates without the use of surface modifiers tend to clump to each other, which results in the formation of secondary aggregates (Jesionowski et al., 2002), hence in the case of no sonication (sample D) and low power sonication (sample D_US20), silicate ions would adhere to existing silicate networks in an unperturbed manner during suspension ageing, resulting in a higher degree of aggregation within a shorter period of time. With such a phenomenon, the relatively unhindered growth of the silicate network is more prominent, which brought about longer and more severe ageing conditions on the outer surface of the catalyst particles for sample D, as validated by the XPS analysis showing the high concentration of Ni silicates on the surface (81.4 %). As opposed to the above case, the inclusion of ultrasonic irradiation during support loading and the early stage of ageing could effectively disperse the aggregates and suppress the growth of the catalyst particles, mainly by delaying the growth of the silicate network. The erosion caused by high intensity ultrasonic irradiation coupled with the delayed growth of silica on the outer surficial layers eventually limited the extent of ageing, as exhibited by the lower Ni silicate concentration in samples D_US30 (61.2 %) and D_US40 (59.3 %). Such a delayed growth in particles could have also played a role in enhancing the Ni dispersion in sonicated catalysts, as smaller particles result in an increase in total exposure of Ni active sites. Herein, the conceptualisation of the two different states of ageing is shown in Figure 4.14.

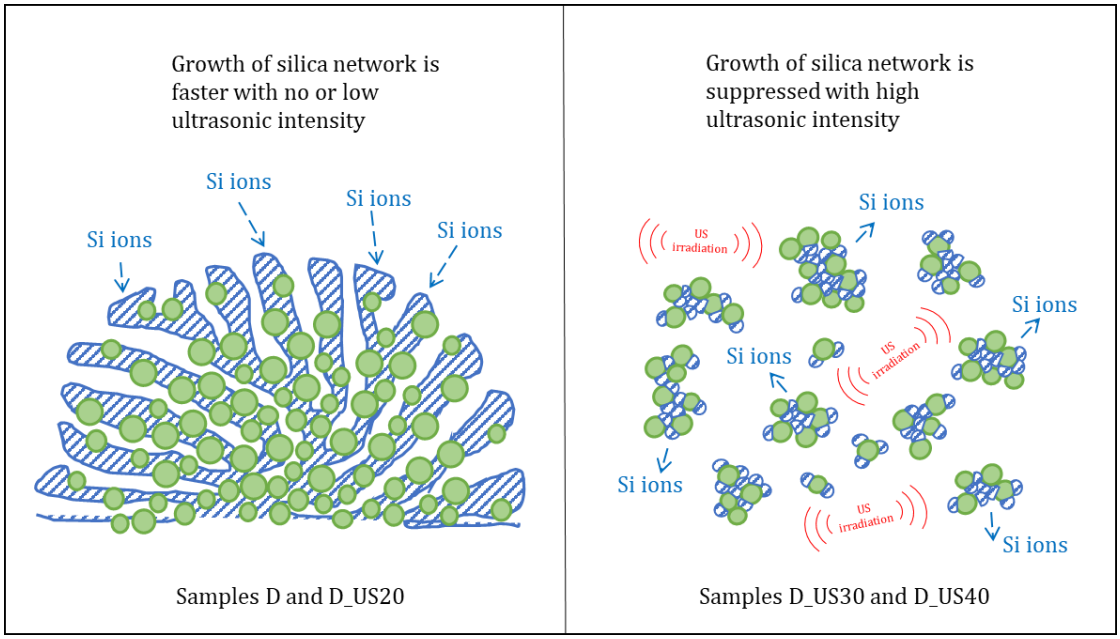


Figure 4.14: State of the nickel-silica network/particles upon first 10 min of ageing with and without ultrasonic irradiation.

The textural and structural properties of the calcined nickel catalysts were evaluated using N_2 physisorption, in which the adsorption-desorption isotherms for the catalysts can be seen in Figure 4.15. According to the IUPAC classification, the sonicated samples (D_US20 – D_US40) exhibited Type IV(a) isotherms, characteristic of mesoporous substances with capillary condensation accompanied by hysteresis. Contrariwise, the non-sonicated sample D exhibited a hybrid of the Type II and Type IV(a) isotherms, denoting the presence of mesopores and macropores, which was also accompanied by a hysteresis loop. Regarding the hysteresis loops exhibited by the catalysts, they can be ascribed to the Type H2(b) hysteresis loop, which signifies the presence of ink-bottle pores with a wider size distribution of neck widths, typical of mesoporous ordered silicas obtained after hydrothermal treatment (Thommes et al., 2015).

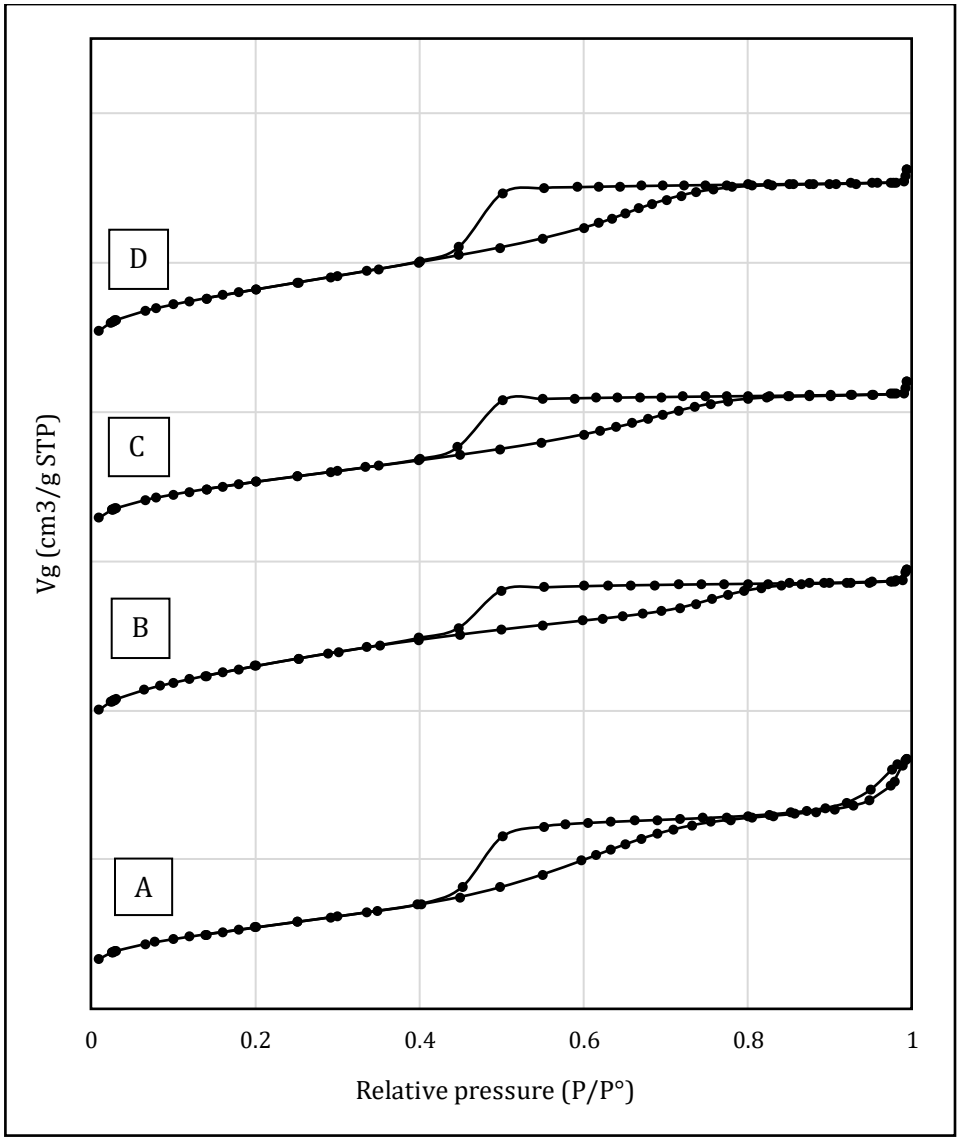


Figure 4.15: Nitrogen isotherms obtained for catalysts (a) D; (b) D_US20; (c) D_US30; and (d) D_US40.

The incorporation of ultrasound is said to have altered the textural properties of the catalyst, resulting in more uniform mesoporous structures with higher BET surface areas, as shown in Table 4.10. The increase in surface areas was also noted in other studies, in which ultrasound acted as a dispersant tool for catalyst phases, which might increase the total surface area available for reaction (Chu et al., 2019; Yap et al., 2018). The imploding micro-bubbles in the irradiated suspension as a result of acoustic cavitation facilitated the nucleation and fine

dispersion of particles, creating phases of more uniform and well-defined morphology that resulted in increased surface areas from 192.5 $m^2 g^{-1}$ to a range of 228.9 – 289.7 $m^2 g^{-1}$ (Dehghani and Haghighi, 2017). According to Coenen (1979) and Ghuge et al. (1993), it is the nickel antigorite (hydrosilicate) phase instead of the silica support that gives rise to a high BET surface area, with the former typically exhibiting > 300 $m^2 g^{-1}$ while the latter presenting surface areas in the range of 20 - 50 $m^2 g^{-1}$. If one is to refer to the results from the TPR studies (Table 4.8), it can be assumed that sample A with the highest Ni silicate percentage (61.7 %) would exhibit the highest BET surface area. However, Table 4.10 shows otherwise with sample D exhibiting a significantly lower BET surface area compared to the sonicated samples. As discussed earlier, the amount of silica clusters attached to the hydrosilicate declined with the usage of ultrasound, which in turn led to higher hydrosilicate to silica ratio in the samples synthesised with ultrasonic irradiation, thus giving rise to a higher BET surface area. In fact, this observation is also correlated with the increase in ultrasonic intensity from sample D_US20 – D_US40, whereby the formation of more silica clusters was suppressed, causing a further increase in hydrosilicate to silica ratio, thereby progressively increasing the BET surface area as per Table 4.10. As a result, sonicated catalysts exhibited higher range in the overall BET surface area than the unsonicated catalyst. Nevertheless, the pore volume and average pore width of the catalysts were similar in range, noting that the non-sonicated sample possessed a larger average pore width due to the presence of macropores, which can also be observed in the pore size distribution in Figure 4.16. One can see that all samples had a uniform pore size distribution in the mesoporous range, while the non-sonicated sample D also contained pores in the macroporous range. The presence of larger

macropores is likely due to the unperturbed and prolonged ageing (Meshkani and Rezaei, 2015; Takahashi et al., 2007) relative to that experienced by the sonicated catalyst, which contributed to the increase in average pore width for catalyst D. Overall, the presence of pores above 3.5 nm was a good indication that the catalysts were suitable for the hydrogenation of edible sunflower oil, which are approximately twice the size of the triglyceride molecules of 1.5 – 2 nm (Balakos and Hernandez, 1997; Lok, 2014). However, the presence of narrower pores with average width slightly below 3.5 nm in catalyst D_US20 might have posed significant diffusional and mass transport problems for the movement of triglycerides. Table 4.10 collates the relative pore flow rate for each catalyst, with catalyst D_US20 as the reference. Employing the flow continuity equation, it is inferred that the unsonicated catalyst D had a 96.4 % higher flow rate than sample D_US20. The smaller flow area due to smaller pores denote the increased hindrance in mass transfer, which results in the slower diffusion rate of reactants and products in and out of the pores, leading to decreased activity relative to samples possessing higher pore flow rates.

Table 4.10: Textural properties of calcined catalysts from N_2 physisorption.

Catalyst	**BET surface area ($m^2\ g^{-1}$)**	**Pore volume [a] ($cm^3\ g^{-1}$)**	**Average pore width [a] (nm)**	**Relative pore flow rate [b]**
D	192.5	0.2277	4.85	1.964
D_US20	228.9	0.2241	3.46	1
D_US30	258.6	0.2169	3.74	1.168
D_US40	289.7	0.2515	3.70	1.144

[a] BJH desorption branch.
[b] Calculated based on the $Q\ \alpha\ (\text{pore width})^2$ relationship from the flow continuity equation. It is assumed that all other parameters remain unchanged.

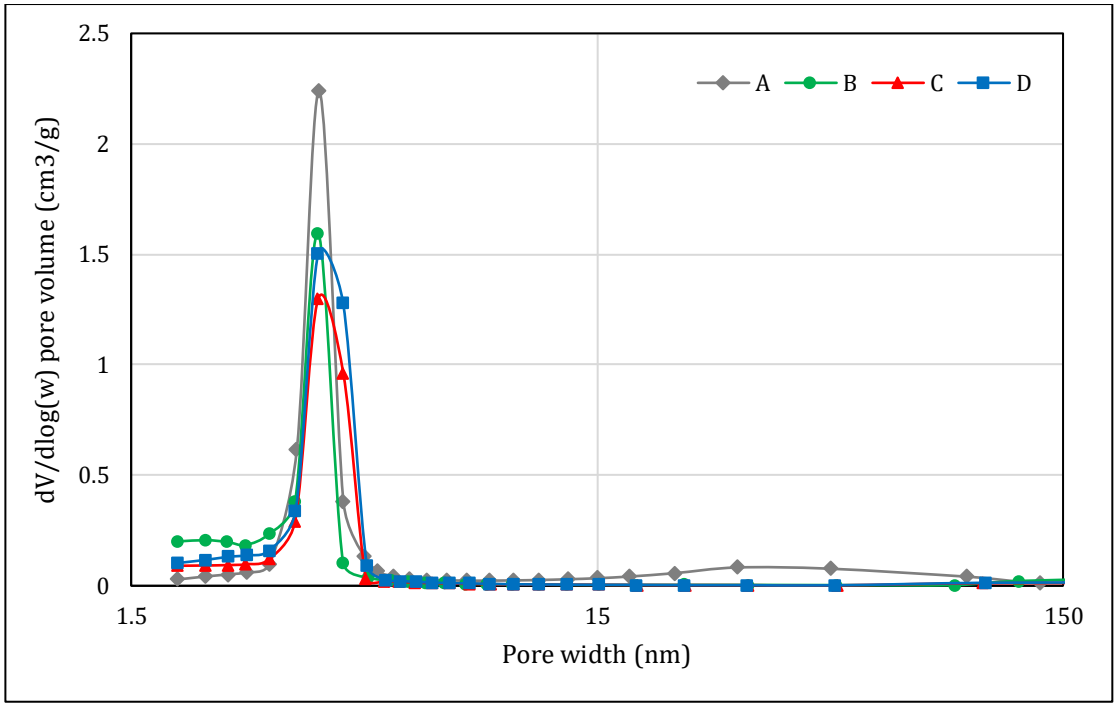


Figure 4.16: Pore size distributions obtained for catalysts (A) D; (B) D_US20; (C) D_US30; and (D) D_US40.

4.4. Concluding remarks

This current chapter has successfully demonstrated the positive influence of alkaline earth metals such as Mg on the characteristics of silica-supported Ni catalysts. In particular, Mg acts as a dopant or a promoter in relatively small amounts compared to the main active material that is Ni. Based on the characterisation tests, sample D, which has the lowest amount of Mg as a promoter at a Ni to Mg ratio of 3 to 1, exhibited superior properties as opposed to that of the pure Ni catalyst sample, which suggested that a small amount of promoter metal is sufficient to produce desirable characterisation properties. To illustrate, the amorphous sample D possesses a high BET surface area (192.5 m^2 g^{-1}) and pore volume (0.2277 cm^3 g^{-1}), as well as strong metal-support interactions via TPR experiments, hence resulting in the highest metal dispersion (8.79 %) and active

nickel surface area (58.55 $m^2 g_{Ni}^{-1}$) among all the samples synthesised. In this case, Mg is said to act as a spacer or barrier, decreasing the Ni crystallite size and consequently increasing the interaction between Ni and the silica support, which could improve the overall stability and activity of the catalyst.

On the other hand, this second part of this current chapter has also presented a novel investigation into the possibility of incorporating ultrasound into the catalyst synthesis of silica-supported Ni-Mg catalysts in order to impart appreciable effects on the catalyst structure and properties. It was successfully shown that the incorporation of ultrasonic irradiation into the ageing process of sequentially precipitated catalysts had led to benefits in terms of the catalyst characterisation properties. Further understanding into the proposed mechanisms indicated that the usage of ultrasonic irradiation, as well as variations in its intensity, had profound impacts on the overall characteristics and compositions (hydroxycarbonates, silicates and silica clusters) comprising the catalysts. It is noted that ultrasonic irradiation had a significant influence on the ageing properties of the catalysts, which directly affected the formation of silica clusters, followed by hydroxycarbonates and Ni silicates. For instance, ultrasonic irradiation led to the erosion of hydroxycarbonate phases and the suppression of silica clusters, which once formed, serve as protective enclosing to avert Ni silicate erosion. As the ultrasonic intensity was increased, greater Ni dispersion was achieved due to increasing extents in hydroxycarbonate erosion, while increase in BET surface areas was also noted due to the decrease in silica to hydrosilicate ratio as a result of the suppression of silica clusters. On the other hand, it was also observed that upon the termination of ultrasonic irradiation, the growth of the

silica network on the surface of the catalysts during ageing also led to a higher Si composition on the external layer of the catalyst particles. In general, these effects in turn imparted alterations to the geometrical and electronic properties of the catalysts, improving catalyst reducibility, surface area and dispersion of the material.

5. Catalytic Performance of Nickel-silica catalysts in the Partial Hydrogenation of Sunflower Oil

5.1. Introduction

The hydrogenation of fats and oils remains as one of the most versatile and effective methods to alter the thermal and oxidative stability, melting characteristics and colour. In addition, the process can also modify certain physical properties of the raw material such as its melting point, miscibility, surface tension, viscosity, etc.

Most natural oils possess C-C double bonds in the *cis* position. During the hydrogenation process, the saturation of the double bonds via the addition of hydrogen atoms take place, along with reactions of isomerisation (positional and geometrical), including the formation of *trans*-isomers. An increase in *trans*-isomer content in the oil or fat produces an increase in its melting point. This poses some advantages, as the fat with higher *trans* content will be able to attain higher melting points with a small amount of saturated fat, which is principally attractive. However, a series of medical papers published just a little more than two decades ago raised awareness that the presence of these *trans*-isomers in edible products have a detrimental effect on human health. Research suggested that a diet rich in elaidic acid (*trans* fats), compared to that rich in oleic acid, increases the total and low-density lipoprotein (LDL) cholesterol concentrations and subsequently decreases the high-density lipoprotein (HDL) cholesterol concentrations, hence

resulting in a less favourable total-cholesterol:HDL-cholesterol ratio in the human body. Further research has indicated that there is a dose-dependent relationship between *trans* fatty acid intake and the LDL:HDL ratio, when combining a number of studies, the magnitude of this effect is greater for *trans* fatty acids compared to saturated fatty acids. These *trans* fats are highly linked with the increased risk of coronary heart disease. As a result, in recent years there has been a growing shift in the industry to lower the levels of *trans*-isomers in fats to as low as possible.

Generally, the usage of hydrogenation catalysts is virtually constrained to nickel-based catalysts due their excellent activity, moderate selectivity, filterability, lower tendency to oxidise unsaturated fatty acids and economical value compared to precious metal catalysts such as those of Pt and Pd (Martin et al., 2007). Nevertheless, one common drawback of Ni catalysts is their substantial selectivity towards *trans* fatty acids (TFAs). Accordingly, this has prompted myriad investigations into not just the activity, but also the selectivity of nickel hydrogenation catalysts. This includes the usage of various metals and materials, the incorporation of promoter metals, the manipulation of catalyst structures and the interchanging of catalyst supports in order to enhance the selectivity toward *cis*-C18:1 fatty acids (Balakos and Hernandez, 1997; Cepeda et al., 2016; Konkol et al., 2016a; McArdle et al., 2014; Wong et al., 2018; Zhao et al., 2018).

As mentioned in previous chapters, ultrasound technology has found its niche in catalysis due to its multi-faceted benefits in accelerating or enhancing chemical processes, including during the synthesis of catalysts to bring about catalytic enhancements. In spite of this, most investigations focus on the

integration of ultrasound during the hydrogenation process itself (Čelková et al., 1989; Moulton et al., 1983; Sancheti and Gogate, 2017a). Contrariwise, there are no studies concerning the application of nickel catalysts synthesised via ultrasonic irradiation in the hydrogenation of edible oil. Therefore, the motivation of this current chapter is to investigate the catalytic performance of sonicated Ni-based catalysts from Chapter 4 (samples D_US20 – D_US40), relative to that of their non-sonicated counterpart (sample D). The hydrogenation activity and product selectivity of the catalysts are characterised and ascertained.

5.2. Experimental

The sunflower oil used for partial hydrogenation was O'life Sunflower Oil (Sime Darby and Marketing Sdn. Bhd., Malaysia). The sunflower oil has a tested initial iodine value (IV) of 124, while its chemical composition is listed in Table 5.1. All chemicals utilised were of analytical grade and obtained from Sigma Aldrich Malaysia, unless stated otherwise.

Table 5.1: Fatty acid composition of the sunflower oil used in this study.

Compounds	**Percentage (%)**
Palmitic acid (C16:0)	6.0
Stearic acid (C18:0)	3.3
Oleic acid (*cis*-C18:1)	42.0
Elaidic acid (*trans*-C18:1)	0.0
Linoleic acid (C18:2)	48.4

5.2.1. Catalyst reduction

Prior to carrying out the hydrogenation reaction tests, the catalyst samples used in this study (Samples D – D_US40 from Chapter 4) were reduced in pure hydrogen gas for activation. The samples were reduced in a tubular furnace. Before reduction, the samples were heated to 500 °C with a heating rate of 10 °C/min in N_2. Upon reaching 500 °C, the samples were subjected to a flow of H_2 and held for 2 h. Lastly, fully hydrogenated palm stearin (IV = 0) was used to coat the catalysts to prevent oxidation, thus forming fat-coated catalyst pellets of 22 wt% Ni. To ensure the catalyst pellets are of 22 wt% Ni, the Ni content of individual catalyst samples was first determined via AAS, and the respective masses of catalyst samples and hydrogenated palm stearin required to constitute 22 wt% Ni was calculated.

5.2.2. Partial hydrogenation

Partial hydrogenation was executed in a 1.5 L pressurised batch reactor (Buchiglasuster Eco-Clave). The temperature of the reactor was regulated by a high precision temperature regulatory system (Huber Unistat Tango Nuevo), with the use of a silicone oil jacket around the circular reactor and a temperature probe inside the reactor. Briefly, 750 ml of sunflower oil was added into the reactor with the aid of a vacuum pump and heated to a set-point temperature of 180 °C. Prior to dosing the catalyst, the reactor was vacuumed for 60 s to remove any air or moisture that will poison and deactivate the catalyst. Subsequently, a catalyst dosage of 2 g L^{-1} was used and hydrogen gas of 5 barg was charged into the reactor

to initiate the reaction, while the slurry was vigorously stirrer at 1500 rpm. Oil samples (4 – 5 ml) were taken from the bottom of the reactor for each time interval. The reaction was carried out for 90 min. Obtained samples were labelled and filtered using filter papers to remove the catalyst particles.

5.3. Results and discussion

The nickel-silica catalysts that were previously synthesised, as mentioned in Chapter 4, are further evaluated for their catalytic activity via the partial hydrogenation of edible oils, in which edible sunflower oil was utilised in this current chapter. From the correlations drawn between their characterisation data and catalytic performance, specific aspects that are beneficial for the enhancement of the catalyst performance could be distinguished and pin-pointed, which is extremely useful for the design and optimisation of the catalyst.

5.3.1. Hydrogenation activity

The hydrogenation pathway of triglycerides is generally represented by the reaction mechanism (Veldsink et al., 1997), as shown in Figure 5.1. The nomenclature used is depicted in the format of C*X*:*Y*, where *X* is the number of carbon atoms, while *Y* is the number of double bonds present in the fatty acid compound. The fatty acid tails in the triglycerides, through the catalytic addition of hydrogen atoms at an elevated temperature and pressure, are hydrogenated which results in the elimination of double bonds up to complete saturation. For instance, linolenic acid (C18:3) would undergo hydrogenation to form linoleic acid (C18:2), which has one less double bond.

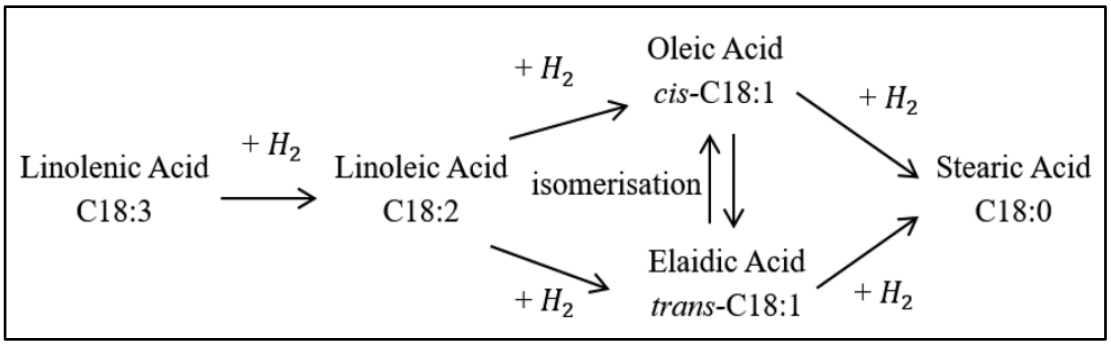


Figure 5.1: General reaction pathway for the hydrogenation of oils from linolenic acid (C18:3) to stearic acid (C18:0).

All synthesised catalysts were subjected to catalytic activity tests via the partial catalytic hydrogenation of sunflower oil. The decline in IV throughout the stipulated reaction time of 90 min for each catalyst sample was noted and presented in Figure 5.2. The hydrogenation performance was tracked by observing the decrease in the IV. The sunflower oil utilised as the reactant has an initial IV of 124, which was tested with the above-mentioned iodine value test. As anticipated, the IV for all sample sets decreased as the reactant was progressively saturated during hydrogenation. Furthermore, the gradient of the graph signified the rate of decline in the IV, whereby a sharper gradient represented an increase in hydrogenation activity. Catalyst D_US30, synthesised with an ultrasonic intensity of 20.78 W cm^{-2} registered the highest activity among the catalysts synthesised, attaining a final IV of 37.9 after a reaction time of 90 min. On the other hand, the unsonicated catalyst produced an IV drop to 53.8 in 90 min. The least active catalyst was catalyst D_US20, synthesised with an ultrasonic intensity of 7.07 W cm^{-2}. Although possessing higher Ni surface area and dispersion than its unsonicated counterpart, catalyst D_US20 presented a smaller pore size below 3.5 nm. Coenen (1986) postulated that while it is beneficial to possess a high Ni

dispersion and surface area, oil/fat hydrogenation is also structure-sensitive, whereby pores narrower than 3.5 nm would considerably impair the mass transport and pore diffusivity of bulky triglyceride molecules, hence causing pore congestion and affecting overall catalytic activity. The initial activity of catalyst D_US20 was higher than that of catalyst D due to its advantages in Ni dispersion and surface area. However, at IV = 90, the activity of catalysts D and D_US20 began to diverge as shown in Figure 5.2, the percentage of bulky triglyceride molecules (C18:2 and *cis*-C18:1) for sample D_US20 remained relatively high compared to that of sample D, as shown in Figure 5.3. As the narrower pores in sample D_US20 would effectively impede the diffusion of these molecules, the reaction and conversion of such molecules would be affected negatively, thus resulting in a slower drop in IV. In addition, as presented in Table 4.10 (Section 4.3.3.1) previously, the unsonicated catalyst A has a 96 % higher flow in the pores than that of catalyst D_US20, indicating that despite a higher intrinsic catalytic activity possessed by catalyst D_US20, its mass transfer at the pores was severely impacted thus affecting the overall catalytic activity.

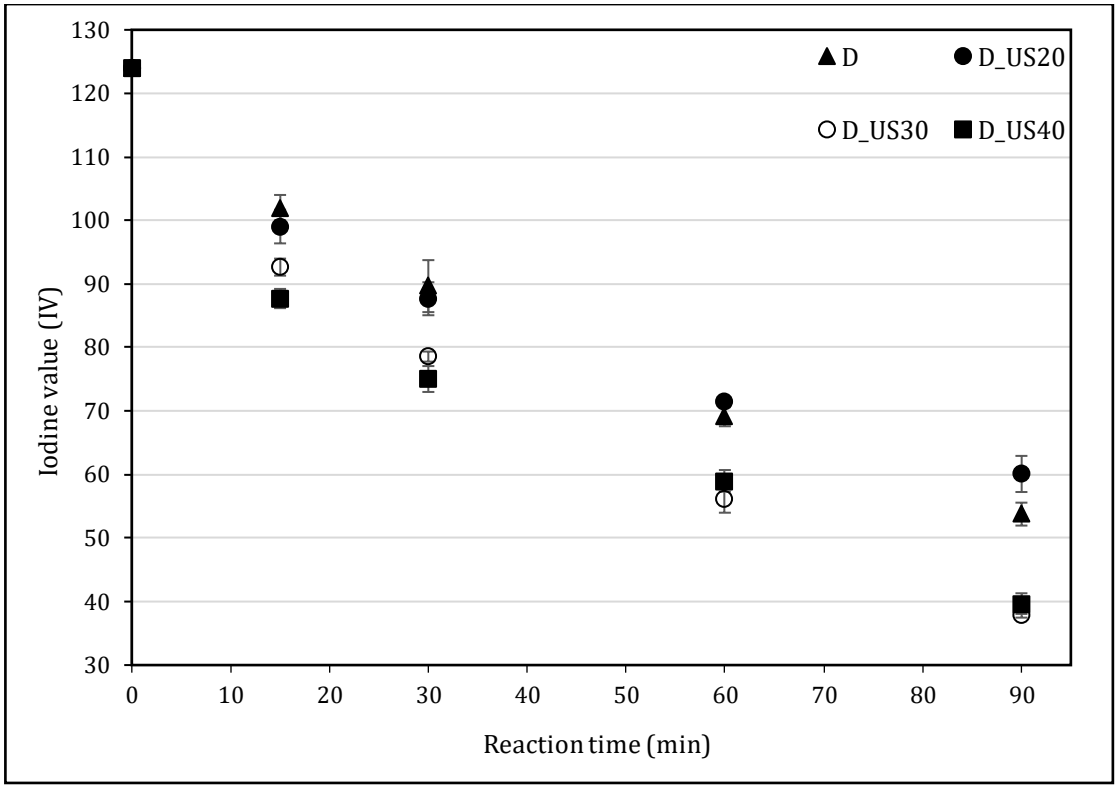


Figure 5.2: Change of iodine value (IV) over time using different catalysts over the course of partial hydrogenation using sunflower oil.

Based on the catalyst characterisation results presented in Section 4.3.3.1, the geometric effects imparted by ultrasonic irradiation have led to the sonicated catalysts possessing superior catalytic activity compared to their unsonicated counterpart, with the exception of the sonicated catalyst D_US20 due to its disadvantages in pore characteristics. The action of ultrasound during synthesis has induced the formation of more reducible Ni species available on the catalyst superficial layers, which on the other hand are composed of particles of lower agglomeration, thus leading to increased Ni surface area and dispersion after reduction. The presence of more well dispersed active sites ultimately allowed more reactants and intermediates to adsorb and react. Nevertheless, it was also discovered that catalyst D_US40, albeit sonicated with the highest ultrasonic

intensity, performed marginally poorer than catalyst D_US30, whereby the hydrogenation activity of the latter overtook the former during mid-hydrogenation. This could be due to the large Ni surface area exhibited by catalyst D_US40, allowing more surface area contact with the reacting medium, hence increasing the propensity of Ni lixiviation. Indeed, AAS analyses performed on the hydrogenation products of catalysts D_US30 and D_US40 confirmed that the concentration of Ni present in the hydrogenation product of catalyst D_US40 was ca. 30 % higher than that of catalyst D_US30 at 90 min (0.00294 $mg_{Ni}\ g_{oil}^{-1}$ vs. 0.00226 $mg_{Ni}\ g_{oil}^{-1}$), which caused the gradual deactivation of catalyst D_US40 over time.

5.3.2. Hydrogenation selectivity and product distribution

The hydrogenation activity of the synthesised catalysts was demonstrated via the IV tests, which is a direct representation of the number of carbon-carbon double bonds present in a sample, without any discrimination towards the product composition. Product analyses are also very crucial in distinguishing the behaviour of catalysts during edible oil hydrogenation. The synthesised catalysts were appraised by monitoring the evolution of saturated fat (C18:0), *trans*-C18:1 and *cis*-C18:1 at particular IV levels which represent a reaction time up to 90 min, as depicted in Figure 5.3. The respective yield and selectivity of the catalysts are shown in Table 5.2.

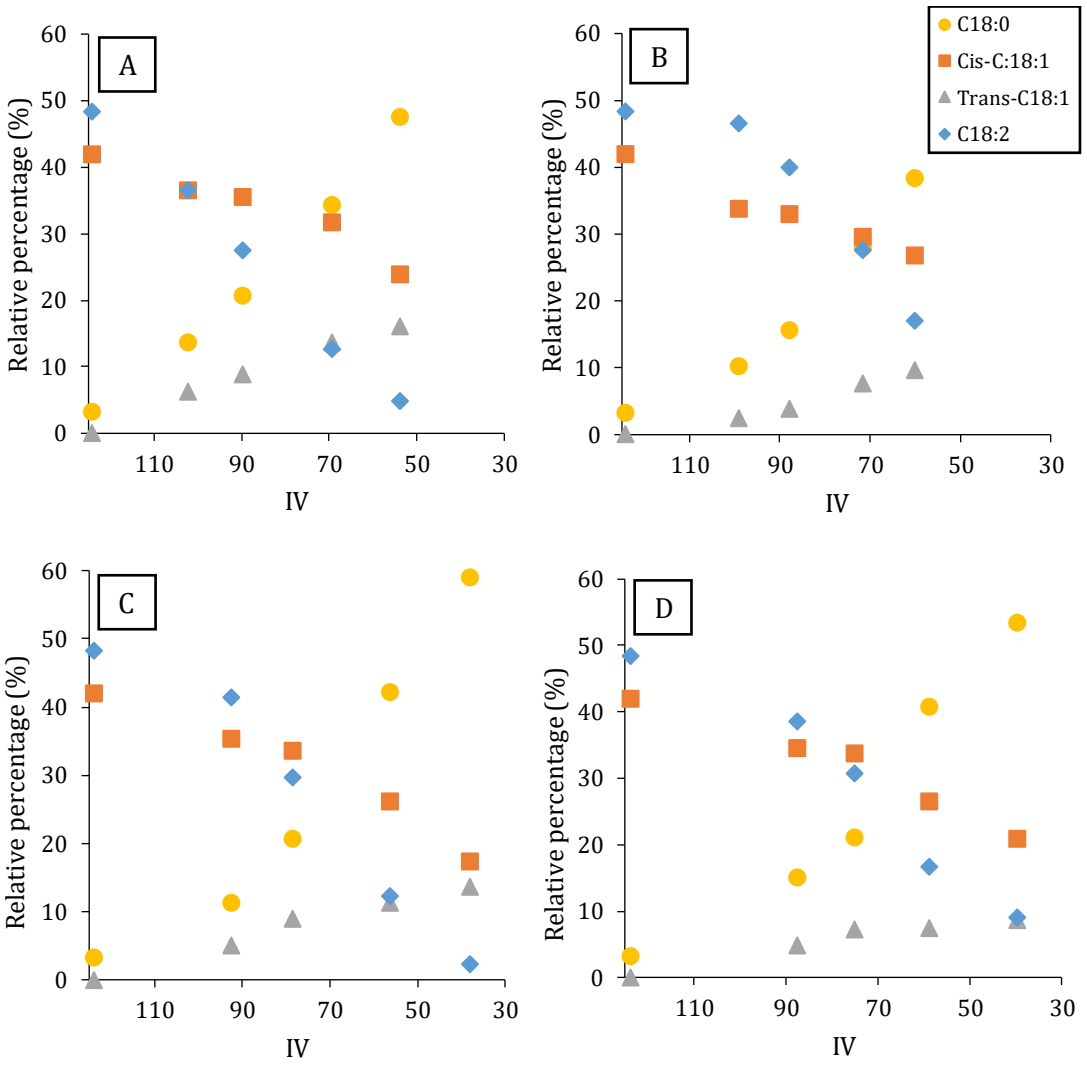


Figure 5.3: Evolution of fatty acid compositions with the iodine value (IV) during the partial hydrogenation reaction using catalysts (A) D; (B) D_US20; (C) D_US30; and (D) D_US40.

As seen in Figure 5.3 the composition profile of the hydrogenated fats depicted similar trends for all catalysts used. The elimination of carbon-carbon double bonds, as well as *cis-trans* isomerisation during hydrogenation can be tracked throughout the plots. Overall, a depletion of C18:2 and increase in C18:0 is observed, accompanied by a variation of *cis*-C18:1 and *trans*-C18:1 composition throughout the reaction. Another observation was the overall increase in *trans*-

C18:1 coupled with the overall decrease in *cis*-C18:1 for all hydrogenation runs. It has been documented that *trans*-C18:1 are preferentially formed during the initial phase of hydrogenation (Coenen, 1976). On the other hand, *cis*-C18:1 was either isomerised to *trans*-C18:1 or fully hydrogenated to C18:0. It can be seen that the formation of *trans*-C18:1 was generally less favoured in the hydrogenation runs using sonicated catalysts, whereby the selectivity of *trans*-C18:1/*cis*-C18:1 at IV 90 and 70 were at the lower range of 10 – 12.5 % and 18.42 – 24.39 %, respectively. Meanwhile, the unsonicated catalyst D presented higher *trans*-C18:1/*cis*-C18:1 selectivities of 20.46 % and 30.43 % at IV 90 and 70, respectively. It can be observed that while catalyst D_US20 presented a poorer hydrogenation activity, its selectivity appeared to be better than that of catalyst D_US30. While D_US30 presented better Ni dispersion and surface area compared to that of D_US20, which led to a better hydrogenation activity, the electronic properties of its active sites might have been less tuned toward a higher selectivity of *cis*-C18:1, which resulted in a slightly poorer selectivity compared to D_US20.

Table 5.2: Yield and selectivity of catalysts for the sunflower oil hydrogenation reaction.

	***trans*-C18:1 yield (%)**		**C18:0 yield (%)**		**C18:0/*trans*-C18:1 selectivity [a] (%)**		***trans*-C18:1/*cis*-C18:1 selectivity [b] (%)**	
IV	90	70	90	70	90	70	90	70
D	9.68	15.1	22.6	36.6	70.0	70.8	20.5	30.4
D_US20	4.30	8.70	16.1	31.5	79.0	78.4	10.8	21.6
D_US30	5.38	10.8	12.9	30.1	70.6	73.7	12.5	24.4
D_US40	4.26	7.61	13.8	31.5	76.5	80.6	10.0	18.4

[a] Calculated with $\frac{\text{C18:0 yield (\%)}}{\text{C18:0 yield (\%)} + \textit{trans}\ \text{C18:1 yield (\%)}} * 100$

[b] Calculated with $\frac{\textit{trans}\ \text{C18:1 yield (\%)}}{\textit{trans}\ \text{C18:1 yield (\%)} + \textit{cis}\ \text{C18:1 yield (\%)}} * 100$

While Figure 5.3 gives a useful outline of the catalytic performance of each sample over the course of the reaction, it is also highly crucial to analyse the product distribution correlated to a specific target IV. In particular, the concentrations of *trans*-C18:1 and C18:0 are of paramount significance in deciding the final oil quality. Figure 5.4 demonstrates the percentage of C18:0 and *trans*-C18:1 fatty acids at an IV of 70. In this case, this particular level was chosen for comparison as it is a common target IV for oleomargarine products and it also corresponds to the point where the formation of C18:0 starts to be significant (Cepeda et al., 2016). This extent of hydrogenation resembles to that in the manufacture of fatty acid components required for shortenings and margarine in the industry (Konkol et al., 2016b). Employing the sonicated catalysts, the

hydrogenation products obtained at an IV of 70 presented *trans*-C18:1 at equal to or less than 10 %, while the hydrogenation products of the unsonicated counterpart registered *trans*-C18:1 at 13.7 %, with the lowest *trans*-C18:1 level observed using catalyst D_US40. On the other hand, the sonicated catalysts had similar percentages at approximately 29 % in C18:0 production, while the unsonicated catalyst was slightly higher at 34 %.

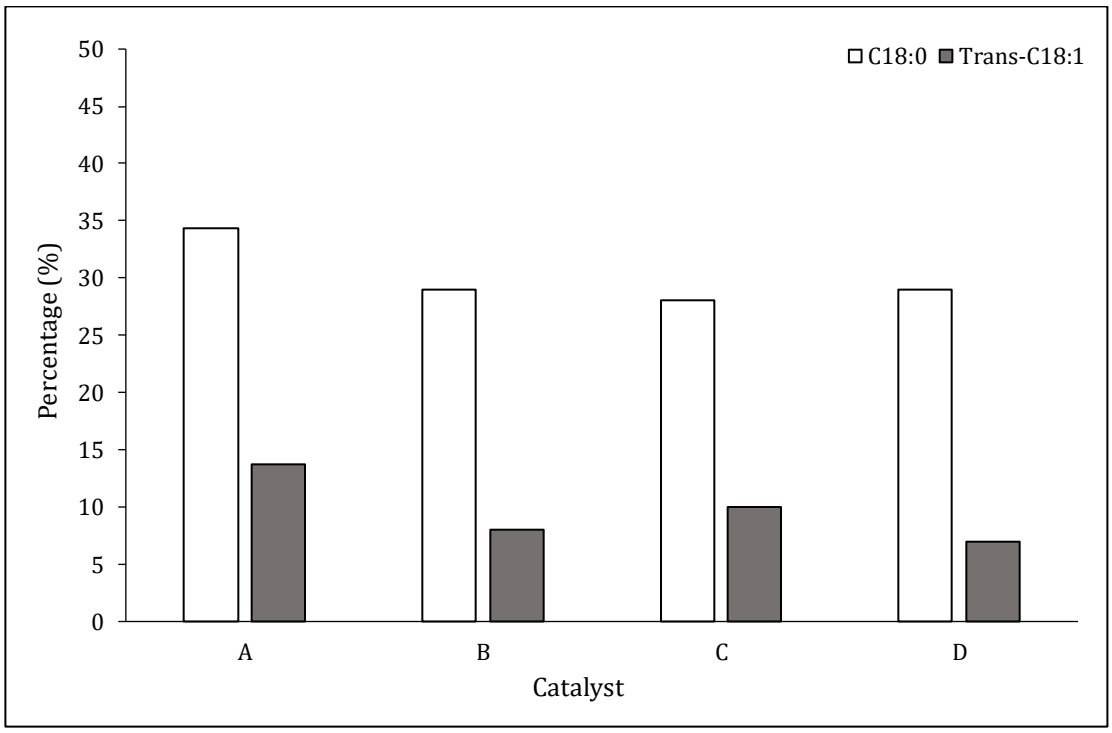


Figure 5.4: Percentage of trans fatty acids and saturated fatty acids formed at IV = 70 for catalysts (A) D; (B) D_US20; (C) D_US30; and (D) D_US40.

Generally, as the overall hydrogenation proceeded, the isomerisation of fatty acid products increased with conversion. However, it is noted that the mechanisms related to hydrogenation and *cis*/*trans* isomerisation are heavily interlinked. With regards to the formation of *trans* fatty acids (TFAs) during hydrogenation, the addition-elimination mechanism proposed by Horiuti and

Polanyi (1934) is commonly adopted to illustrate the process. The mechanism states that both the hydrogenation and isomerisation processes are governed by a half-hydrogenation state mechanism. Firstly, carbon-carbon double bonds of C18:2 or C18:1 molecules are adsorbed on active sites. It is noted that C18:2 bonds tend to adsorb to the surface to a stronger degree and are thus first hydrogenated. Therefore, this also explains the consecutive drop in linoleic content throughout the reaction as per Figure 5.3. After adsorption, one of the double bonds are half-hydrogenated by the addition of one hydrogen atom from the active sites. Further reaction resulting in the saturation of C-C bonds necessitates the addition of another hydrogen atom. Nevertheless, typically without the presence of a second hydrogen atom, the first hydrogen atom detaches from the half-hydrogenated intermediate, thus re-establishing the double bond with either a *cis*-C18:1 or *trans*-C18:1 configuration (McArdle et al., 2014). Particularly, the latter configuration is more thermodynamically favoured than the former (Wang, 2004). As hydrogenation is supplemented by isomerisation reactions, it is suggested that the change in the electronic characteristics of the sonicated Ni catalysts could also influence the isomerisation reactions. In this case, the enhanced removal of the chemisorbed half-hydrogenated intermediate from the active sites could prevent the further isomerisation to TFAs. This alteration in electronic properties may be used to explain the decrease in TFA formation for the sonicated catalysts, relative to the unsonicated counterpart (Stanković et al., 2017; Wong et al., 2018). Hence, one of the functions of ultrasound in this case of catalyst synthesis might be as a selectivity modifier for the Ni catalyst. Through sonication, the bonding strength of the adsorbates on the active sites were altered, which resulted in the increase of the energy barrier required for fatty acid isomerisation or the decrease of the

energy barrier for hydrogenation that hastens *cis*-C18:1 to C18:0 conversion (Wong et al., 2018). In particular, the shift from a higher to lower binding energy in the sonicated catalysts as observed in the XPS results (Table 4.9 in Chapter 4.3.3.1) complemented this finding. The changes in the electronic properties and electron densities of catalysts as observed by the shift in binding energies is known to alter the adsorption of reacting species and hence the selectivity towards the final products (Chen et al., 2020; Hoffer et al., 2003; Okamoto et al., 1980). In this case, the decrease in binding energy denotes the increase in electron density of Ni species on the catalyst surface, thus leading to weaker interactions between the adsorbed or hydrogenated intermediates and the active sites, allowing easier desorption thus diminishing the transformation of unsaturated fat molecules or *cis* isomers to *trans* isomers (Thunyaratchatanon et al., 2016), which was also a phenomenon reported by other researchers such as Iida et al. (2015). Similarly, Li et al. (2006) has noticed a negative shift in binding energy for Ru species in Ru-B catalysts after sonication, which facilitated the adsorption of the oxygen atom of carbonyl groups in the cinnamaldehyde molecule, ultimately enhancing the hydrogenation of the molecule.

To further assess the hydrogenation performance of the synthesised catalysts in this work, comparisons to novel catalysts obtained from recent literature were made, with a compilation presented in Table 5.3. Compared to most studies, it can be seen that catalyst C in this present work was able to achieve an IV drop to 70 in a shorter reaction time of 40 min, while containing a low amount of saturated fats and *trans*-fats, particularly the latter. Although noble metal (e.g. Pt and Pd) catalysts required milder reaction conditions (approximately 100 °C)

and produced lesser saturated fats, the present catalyst was able to achieve a relatively low *trans*-fats percentage of 10 %. It should also be noted that the saturated fats content for noble metal catalysts were comparatively lower due to their lower extent of reaction. Compared to the other Ni-based hydrogenation catalysts such as Ni/ZnO/Al_2O_3, Ni/SiO_2, Ni-Mg-Ag/D and Ni-Ce/Al_2O_3, the novel sonicated catalyst in this work has produced at least half the amount of *trans*-fats, while maintaining comparable if not better hydrogenation activity. Nevertheless, it should be noted that these studies obtained from the literature were executed with disparities in reaction conditions and oil variation, hence the overall activity and *trans*-fats and saturated fats contents would have also been affected. For instance, the Ni-Ce/Al_2O_3 catalyst although requiring only 33 min of reaction time for hydrogenation, was employed to hydrogenate a feed oil with the lowest initial IV of 115. Therefore, this present work has exemplified the potential of incorporating ultrasonic technology into the synthesis of such Ni hydrogenation catalysts, with positive and applicable end results, i.e. the enhancement of hydrogenation activity and the lowering of detrimental *trans*-fats for edible oil applications. For the latter application, edible oil manufacturers and catalyst developers who seek an alternative technique to lower their *trans*-fats production substantially could take the ultrasound-assisted catalyst synthesis procedure into consideration for their processes.

Table 5.3: Comparison of the present work to other studies in the literature.

Sample	**T & P**	**Initial IV**	**Final IV**	**React. time (min)**	***Trans*-fats (%)**	**Sat. fats (%)**	**Oil feed employed**	**Ref.**
Ni/ZnO /Al_2O_3	180 °C 5 bar	162	70	130	22.8	33.5	Sunflower	(Wong et al., 2018)
Ni/SiO_2	180 °C 4.5bar	138	70	44	26.1	33.6	Sunflower	(Emilio A. Cepeda et al., 2016)
Ni-Mg-Ag/D	160 °C 1.6bar	130	90	255	26.3	5.8	Soybean	(Stanković et al., 2015)
Ni-Ce/Al_2O_3	180 °C 6 bar	115	70	33	26.4	16.6	Canola	(Konkol et al., 2016a)
Pd-Ru /SBA-15	110 °C 5 bar	130	70	60	24.5	16.5	Sunflower	(Belkacemi et al., 2007)
Pd/γ- Al_2O_3	100 °C 4.2bar	125	90	20	19.9	5.6	Sunflower	(Fernández et al., 2009)
Pd/SBA-15	110 °C 5 bar	130	80	60	34	10	Sunflower	(Plourde et al., 2004)
Pt-Ni/SiO_2	170 °C 3 bar	130	70	180	16.8	23.2	Sunflower	(McArdle et al., 2014)
Ni-Mg/SiO_2 (non-sonicated)	180 °C 5 bar	124	70	59	13.7	34.4	Sunflower	Present work
Ni-Mg/SiO_2 (I_{US} = 7.07 W cm^{-2})	180 °C 5 bar	124	70	62	8.5	29	Sunflower	Present work
Ni-Mg/SiO_2 (I_{US} = 20.78 W cm^{-2})	180 °C 5 bar	124	70	40	10	28	Sunflower	Present work
Ni-Mg/SiO_2 (I_{US} = 27.72 W cm^{-2})	180 °C 5 bar	124	70	40	6.5	29	Sunflower	Present work

5.4. Concluding remarks

In this chapter, catalyst samples synthesised and characterised in Chapter 4 (Section 4.3.3) were further investigated and assessed for their catalytic reactivity. The partial hydrogenation of edible oil (sunflower oil) was carried out

to achieve this. It was successfully shown that the incorporation of ultrasonic irradiation into the co-precipitation synthesis of the catalyst has brought about discernible changes to the sunflower oil hydrogenation performance of the samples. The geometric and electronic alterations imparted by ultrasonic irradiation onto the nickel catalysts, as described in Chapter 4, have effectively enhanced both the activity and selectivity of silica-supported nickel catalysts. For instance, hydrogenation with the Ni catalyst synthesised with an ultrasonic intensity of 20.78 W cm^{-2} achieved the fastest decrease to IV = 70 in 40 min, compared to 58 min achieved by the non-sonicated counterpart. Furthermore, the usage of ultrasound prompted the modification of product selectivity by altering the electron density and subsequently the adsorption capability of the nickel species with hydrogenation intermediates. This led to a lower production of *trans* fats in the sonicated catalysts compared to the non-sonicated catalyst. To illustrate, at IV = 70, the sonicated and non-sonicated catalysts produced 7 – 10 % and 13.7 % of *trans* fats, respectively. Generally, the effects of sonication on nickel catalysts used for sunflower oil hydrogenation were positive and promising, which could potentially be extended to other oil types or catalyst systems, thus encouraging prospects for further research.

Overall, the current chapter has demonstrated the practical and beneficial usage of ultrasonic irradiation for the synthesis of hydrogenation catalysts, in which the activity and selectivity of the synthesised catalysts could be significantly modified by a brief exposure to ultrasonic waves. More importantly, this work has also highlighted the role of agitation during the catalyst ageing process, in which a high degree of agitation achieved through the incorporation of ultrasonic

irradiation can alter catalyst characteristics to significant extents. Consequently, this can be adapted and optimised to help engineer catalysts with desired properties.

6. Characterisation of Nickel-silica Composites Synthesised via Varied Ultrasonic Configurations

6.1. Introduction

Nickel nanocrystallites dispersed on porous silica materials, or nickel-silica composites, have various applications as drug carriers (Wang et al., 2018), adsorbents for heavy metals and toxins (Qu et al., 2012), lithium battery support anode materials (White et al., 2013), heterogeneous catalysts in reactions such as hydrogenation, reforming, water-gas-shift, benzylation, etc. (Kim et al., 2006; Laribi et al., 2012), as well as potential applications in optical and electronic devices and sensors (Ali et al., 2020; Kim et al., 2006). The versatility of the mesoporous material has instigated its relevance in many different scientific fields and in the chemical industry. Considering the importance of this class of functional materials, various efforts are currently being made to continuously improve their properties. Investigations may range from utilising different starting materials (Kowalewski et al., 2017; Kumar et al., 2019; Wang et al., 2018), incorporating promoter elements (Feng et al., 2019; Shimura and Fujitani, 2019), changing pre-treatment conditions (Gnanamani et al., 2020; Kaskow et al., 2020) and experimenting with various synthesis techniques and parameters (Aljishi et al., 2018; Badoga et al., 2017; Yao et al., 2018).

Common synthesis techniques include direct or incipient impregnation (Laribi et al., 2012), deposition-precipitation (Zhang et al., 2019), spray pyrolysis

(Kim et al., 2006), hydrothermal co-condensation (Kondrashova et al., 2016), sol-gel synthesis (Wu and Williams, 2010b) or co-precipitation (Lim et al., 2021). In co-precipitation, various synthesis steps such as precipitation, phase loading, ageing, drying, calcination are required to form the final composite precursor. Within these steps, multiple preparation or synthesis variables and parameters exist, e.g. operating temperature, reaction time, precipitant type and concentration, pH and the control of agitation (Jeong and Suh, 2016). These preparation conditions lead to a "chemical memory" effect, whereby changes in preparation variables can result in a chain effect in determining the final properties and application of the composites (Bems et al., 2003). One of the important parameters is the control of agitation during the procedure, whereby varying the non-chemical parameter can be highly influential towards the local micro-environment in the synthesis reaction and consequently the final composite properties and characteristics (Jiang et al., 2018a). For instance, the induction time, particle size distribution and the SiO_2/Al_2O_3 composite framework molar ratio of zeolite beta composites were significantly decreased by the presence of agitation (Ding et al., 2006), while a change in agitation intensity affected the phase distribution of Cu-ZnO nanocomposites (Jiang et al., 2018b).

Apart from agitation provided through mechanical means, the phenomenon of acoustic cavitation due to propagating ultrasonic waves in liquid media is also an effective method to generate high intensity agitation (Costa, 2020). The conditions generated under power ultrasound are responsible for myriad physicochemical effects such as the enhancement of chemical reaction kinetics, alterations in reaction mechanisms, emulsification effects, surface erosion,

crystallisation, precipitation, etc. (Cravotto and Cintas, 2007; Mason, 2003). Consequently, the structural and physicochemical properties of many functional materials could be significantly altered via the application of ultrasound.

Nonetheless, virtually all research concerning synthesis of these functional materials do not explore the effects of applying high intensity agitation via ultrasonic irradiation at different stages of the synthesis procedure. To illustrate, many studies from the literature demonstrate the application of sonication at specific stages during synthesis (i.e. co-precipitation or ageing) without considering the associated impacts (Ahmadi et al., 2016; Khoshbin and Haghighi, 2013; Pérez et al., 2011). In other words, the usage of ultrasound appeared to be rather random and unmethodical, which is further demonstrated by the fact that no justifications or explanations were provided as to why ultrasonic irradiation was applied at the aforementioned specific steps during the synthesis of the materials. Unfortunately, one can observe that this trend is in fact rather commonplace in this research area, whereby a brief literature search would lead to many studies of such nature. Consequently, this initiates further important uncertainties: what is the significance and consequence of incorporating ultrasonic irradiation at these different stages (i.e. co-precipitation, support loading, aging etc.) during material synthesis? Subsequently, will this result in the formation of final products with varying structures and properties? It is important to bear in mind that ultrasound is not just a simple tool for mixing, but a practical method to bring about results that are difficult to achieve via classical or conventional means. Hence, it is encouraged to further investigate these parameters as they could

potentially serve as more crucial factors in tuning material properties using ultrasonic irradiation.

Therefore, this chapter aims to bridge this knowledge, with objectives in twofold. Firstly, nickel-silica composites were synthesised through sequential precipitation, in which varying agitation intensity via sonication was introduced at two separate and different stages during the synthesis procedure, i.e. during the co-precipitation of the hydroxycarbonate precursors or the loading and ageing of the silica phase. The effects of agitation intensity could then be ascertained based on the composite characterisation properties, which are segmented into their: (i) textural and structural; (ii) morphological; (iii) composition and surface properties; (iv) reducibility and metal nanocrystallite characterisation. Secondly, this investigation would serve to delineate the impact of applying ultrasonic irradiation at different stages during the synthesis of functional materials, which demonstrates the non-randomness of this technology. Therefore, this allows material chemists to be more aware of the significance of applying ultrasonic irradiation at particular stages during their syntheses.

6.2. Experimental

6.2.1. Sample synthesis

Figure 6.1 below illustrates a schematic flow diagram to ease the understanding of the entire synthesis procedure of the unsonicated and sonicated composite samples. It should be noted that the synthesis procedure of the

unsonicated sample A in this chapter is akin to that of sample D in Chapter 4.2.1. The estimated power consumption of the unsonicated mechanical stirring at 500 rpm is 1 W, resulting in an agitation intensity of 0.005 W cm^{-3} with 200 ml of total reactant volume.

With sample A as a reference, samples B, C and D were subjected to ultrasonic irradiation during the co-precipitation step of the synthesis at ultrasonic amplitudes of 20, 30 and 40 %, corresponding to agitation intensities of 0.0283, 0.0831 and 0.111 W cm^{-3} respectively. On the other hand, samples E, F and G were subjected to ultrasonic irradiation during the silica loading and ageing steps of the synthesis at ultrasonic amplitudes of 20, 30 and 40 %, corresponding to agitation intensities of 0.0283, 0.0831 and 0.111 W cm^{-3} respectively. The ultrasonic probe was submerged 2 cm into the suspension, with a pulse setting at 2 s on/off, in temperature-controlled conditions.

It should also be noted that samples E, F and G in this chapter are synthesised in the same manner as that of samples D_US20, D_US30 and D_US40 in Chapter 4.2.1. The samples in this chapter will adopt a new naming system (samples A – F) for brevity.

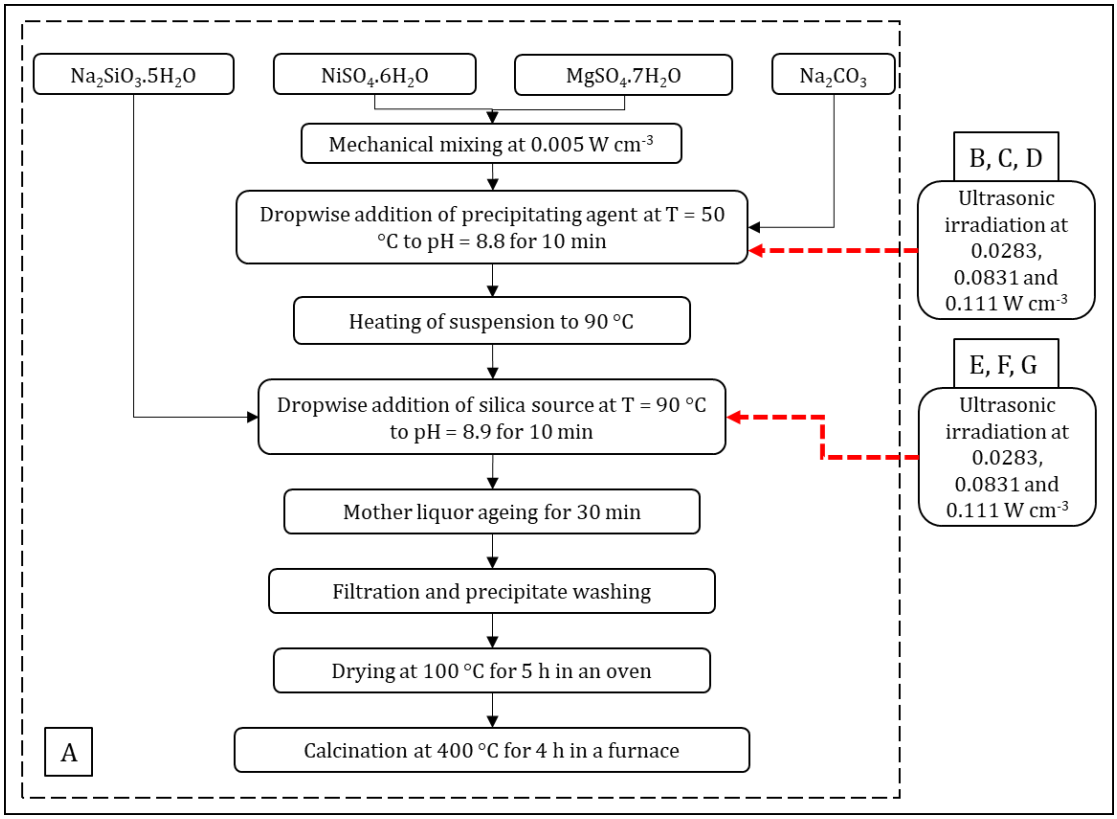


Figure 6.1: Schematic flow chart for the synthesis of samples A – G.

Note: Sample A is synthesised without sonication, while samples B – D and E – G are sonicated to achieve higher agitation intensity during co-precipitation and silica loading/ageing, respectively.

6.3. Results and discussion

6.3.1. Textural and structural characterisation

To ascertain the textural properties of the samples prepared, physisorption analysis was carried out. Figure 6.2 shows the N_2 adsorption-desorption isotherms for the calcined samples. It is important to note that the shape of the adsorption isotherm provides insight into the surface and pore structures of the composites.

From the isotherms, it is observed that there exists a vast difference between the pore structures of the two sample groups. Based on the IUPAC classification, the unsonicated sample A exhibited a hybrid of the Type II and Type IV(a) isotherms and leaned toward the latter, denoting the presence of mesopores and macropores. Similar to the unsonicated sample A, samples B, C and D also resemble a hybrid of Type II and Type IV(a) isotherms, nevertheless leaning towards the former, which stipulates the samples contain both mesopores and macropores as well. Meanwhile, the sonicated samples E, F and G resemble the Type IV(a) isotherm, characteristic of mesoporous materials. Hysteresis loops can also be observed on the isotherms at $0.4 < P/P^0 < 0.9$, due to the phenomenon of capillary condensation within the sample pores. In this case, the sample sets can be classified to two different types of hysteresis. On the one hand, samples B – D belong to Type H3 hysteresis loops. One the other hand, samples A, E – G belong to Type H2(b) hysteresis loops, indicating that the features of the pore structure of the samples differ from one another based on their synthesis procedures. Samples in the former group have non-rigid aggregates of plate-like phases, with pore networks consisting of macropores (Thommes et al., 2015). This type of hysteresis is common in porous materials with a wide distribution of pore sizes (Chang et al., 2009). Contrariwise, samples in the latter group have mesopores with complex structures, such as ink-bottle-shaped pore networks, whereby network effects are significant. In this case, the composites have a narrow distribution of pore bodies, but a wide neck size distribution.

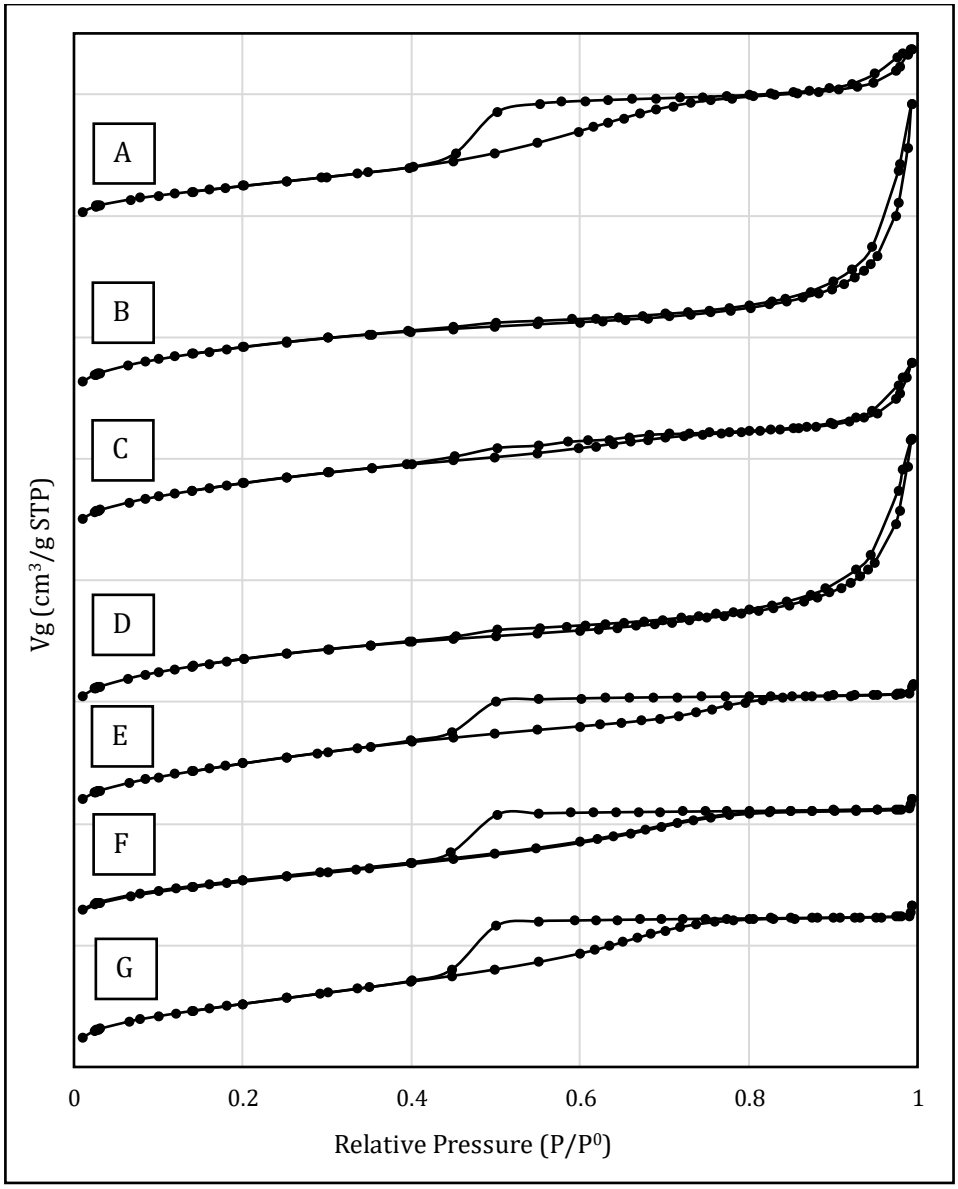


Figure 6.2: BET isotherms obtained for the samples via N_2 physisorption.

The pore size distributions shown in Figures 6.3 and 6.4 show good correlations to the isotherm plots. Sample A exhibited a slight bimodal pore size distribution, with a comparatively small proportion of pores located in the macroporous range (more than 50 nm), while the rest are in the mesoporous range (between 2 and 50 nm), denoting that sample A has a mixture of mesopores and a low amount of macropores. However as seen in Figure 6.3, samples B – D appeared to comprise of a more apparent bimodal pore size distribution, with a mixture of

mesopores and macropores, which justifies the hybridised isotherms. On the other hand, Figure 6.4 shows that pores in samples E – G are virtually all in the mesoporous range. Therefore, it can be inferred that applying ultrasound at different stages during the synthesis (i.e. during co-precipitation of active phase or during silica loading) had profound impacts on the composite pore structures and textural properties. In this case, the presence of high intensity agitation during co-precipitation further enhanced the density of pores in the macroporous range, producing both meso- and macropores; meanwhile, high intensity agitation during silica loading and ageing has resulted in the transformation of pores to the smaller mesoporous range.

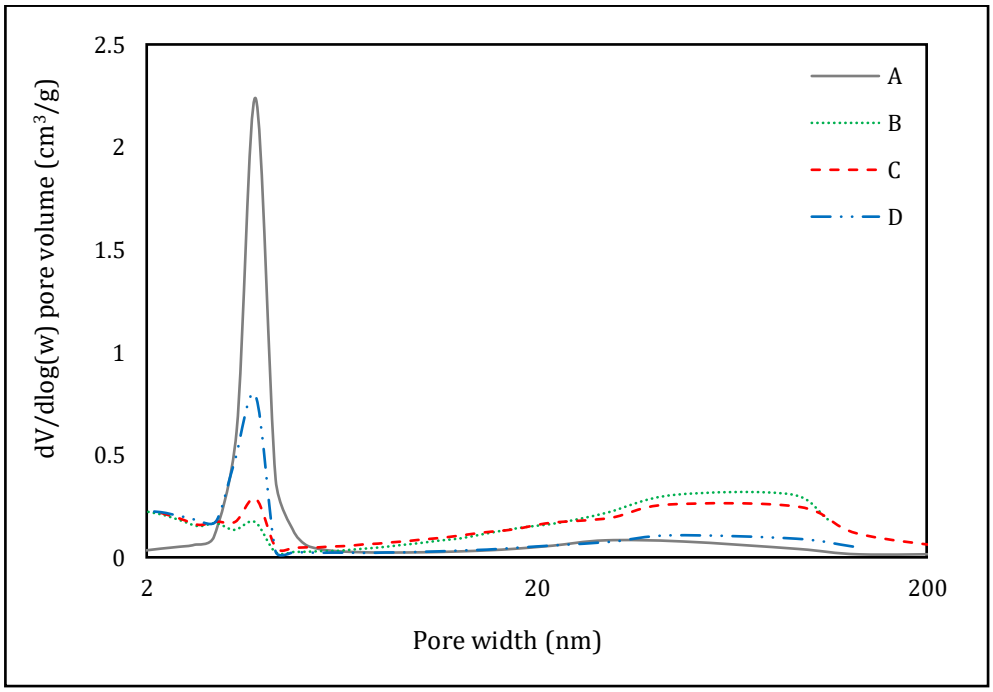


Figure 6.3: Pore size distribution plots for samples B – D with sample A as a reference.

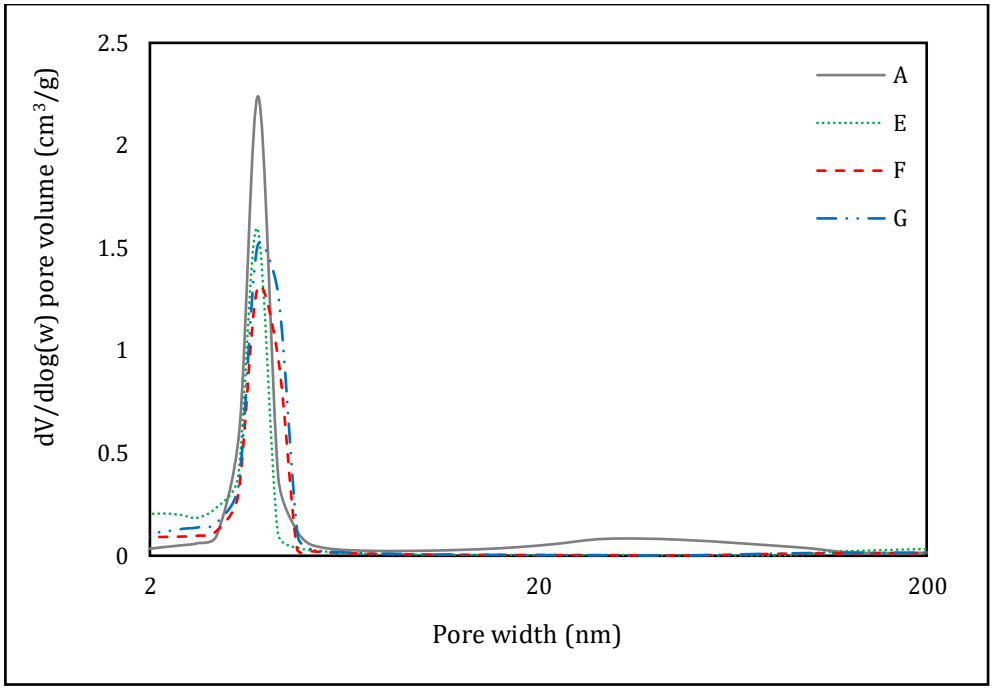


Figure 6.4: Pore size distribution plots for samples E – G with sample A as a reference.

Table 6.1 pertains to the structural properties of the samples synthesised. All samples possess high BET surface areas at a range of 192 – 298 m^2 g^{-1}. In both sets, the surface area of the samples increased as high intensity ultrasonic irradiation was used. The pore volume of the samples ranged from 0.22 – 0.28 cm^3 g^{-1}, with no significant variation between the samples or their synthesis procedures.

However, the average pore width of the samples varied significantly. With an average pore width of 4.85 nm, sample A had a pore size between the two different high intensity agitation procedures. Samples B – D comprise average pore widths of 4.9– 10.3 nm, while samples E – G had pore widths in the lower range of 3.4 – 3.7 nm. As denoted by the isotherm and pore size distribution data, samples

B – D contain a significant volume of macropores, which directly contributed to the increase in average pore widths of those samples. The disparity in pore sizes between the methods could be due to the difference in ageing time – expressed as 'effective ageing time' here – experienced by the sample precursors in the mother liquor during synthesis.

Table 6.1: Structural properties of the synthesised samples.

Sample	**BET area (m^2 g^{-1})**	**Pore volume [a] (cm^3 g^{-1})**	**Average pore width [a] (nm)**	**Isotherm type**	**Hysteresis type**	**Crystallite size [b] (nm)**
A	192.5	0.2277	4.85	II & IV(a)	H2(b)	2.56
B	284.4	0.2612	10.24	II & IV(a)	H3	3.50
C	297.6	0.2735	8.66	II & IV(a)	H3	2.46
D	281.7	0.2188	4.96	II & IV(a)	H3	2.43
E	228.9	0.2241	3.46	IV(a)	H2(b)	2.41
F	259.6	0.2169	3.74	IV(a)	H2(b)	2.33
G	289.7	0.2515	3.70	IV(a)	H2(b)	2.28

[a] BJH desorption branch.
[b] Crystallite size of NiO obtained from Scherrer equation based on the XRD diffractograms.

To illustrate, when left unperturbed (i.e. without the influence of high intensity agitation) during the ageing stage, such as those experienced by samples A – D, the effective ageing time of the samples is perceived to be longer. On the contrary, in of samples E – G the effective ageing time is perceived to be shorter as the process was perturbed by the presence of sonication. With a longer effective ageing period, the generation of interstitial pores in the crystallites becomes increasingly significant, allowing the voids formed between them to become more

diverse in size as the crystallites grow (Hussein et al., 2001). Consequently, a broader pore size distribution would arise, resulting in the bimodal pore size distribution observed by samples B – D. Notably, the effect of longer ageing periods in the mother liquor has also been observed by several other researchers, whereby an increase in ageing time would result in the enlargement of pores (Fulvio et al., 2005; Nares et al., 2009; Smitha et al., 2006). Hence, this suggests that the presence of high intensity agitation at these two different stages during synthesis could influence the pore characteristics of the composites substantially. However, it can also be observed that as the intensity of agitation increased from sample B – D, the pore sizes of the composites experienced a substantial decrease from 10.24 to 4.96 nm, indicating that the application of high intensity ultrasonic irradiation (0.111 W cm^{-3}) could result in the transformation of pores that revert to its unsonicated state, close to that of the unsonicated sample A of 4.85 nm. Shown in the pore size distribution of the samples (Figure 6.3), as the intensity of agitation was increased from samples B - D, the proportion of macropores decreased, which is followed by the increase in proportion of mesopores accordingly. In this case, the increase in agitation intensity caused by sonication has resulted in the transformation of more macropores to mesopores, likely due to the increase in localised hot-spot temperatures induced by acoustic cavitation, in which the macroporous framework will be more prone to collapsing (Xin et al., 2014). The collapse of macropores is also said to be caused by the frequent inter-particle collisions induced by high intensity agitation, whereby strong collisions favour the formation of new mesopores (Liu et al., 2019).

Particularly, the composite pores could be tailored to different size ranges, which caters to different applications. For instance when such materials are applied in catalysis, Lok (2014) demonstrated that the composites with narrow pores such as those of samples E – G are highly suitable for the hydrogenation of fatty acids. The narrower pores could hamper catalyst deactivation by blocking the larger nickel soap molecules from depositing within the pores, which results in the drop of catalytic activity. On the other hand, the hydrogenation of feedstock with much larger triglyceride molecules could benefit from wider pores such as those in samples B – D, in which molecular diffusion within the pores could be minimised effectively, hence preventing the case of complete hydrogenation of some molecules, which leads to undesirable product qualities such as fat grittiness (Lok, 2014). In particular, the formation of larger macropores may be more beneficial for the hydrogenation of comparatively larger triglyceride molecules, which are not restricted or even blocked from the usual movement in and out of the pores. Therefore, it is apparent that the usage of ultrasonic irradiation as a source of intense agitation at different stages of synthesis is highly influential towards the pore and textural characteristics of the composites, which is a parameter that could tune the formulation of related functional materials.

The XRD diffraction patterns of the samples are shown in Figure 6.5. The XRD analysis detected peaks representing the phases of NiO (ICDD: 01-073-1523), MgO (ICDD: 01-089-7746) and nickel silicate ($Ni_3Si_2O_5(OH)_4$) (ICDD: 01-083-1648). Diffraction patterns of all samples exhibit reflections at the 2θ value of 36 °, 43 °, 63 °, 75 ° and 79 °, which correspond to NiO(111), NiO(200), NiO(220), NiO(222) and Ni(311) planes, respectively (Lovell et al., 2015; Sidik et al., 2016).

This is in good agreement with the results of several other investigations (Cai et al., 2014; Cho et al., 2002; Thyssen et al., 2015). The SiO_2 phase was mesoporous and amorphous, which did not contribute to any peaks on the diffractogram (McArdle et al., 2014; Pettiti et al., 2015). The Scherrer equation was used to estimate the NiO crystal size by referencing the characteristic peak at 43 °, with the results presented in Table 6.1. In general, the diffractograms register reflections that appear broad, which signifies the poorly crystallised state of the samples, and indicates the presence of small and well-dispersed phases and highly developed surfaces (Echeverria and Andres, 1990; Gabrovska et al., 2005). In addition, the lack of sharp and narrow peaks also indicates the absence of large crystalline domains or metal oxide clusters, which could be of great advantage for metal dispersion for applications in catalyst reduction (Sulmonetti et al., 2016).

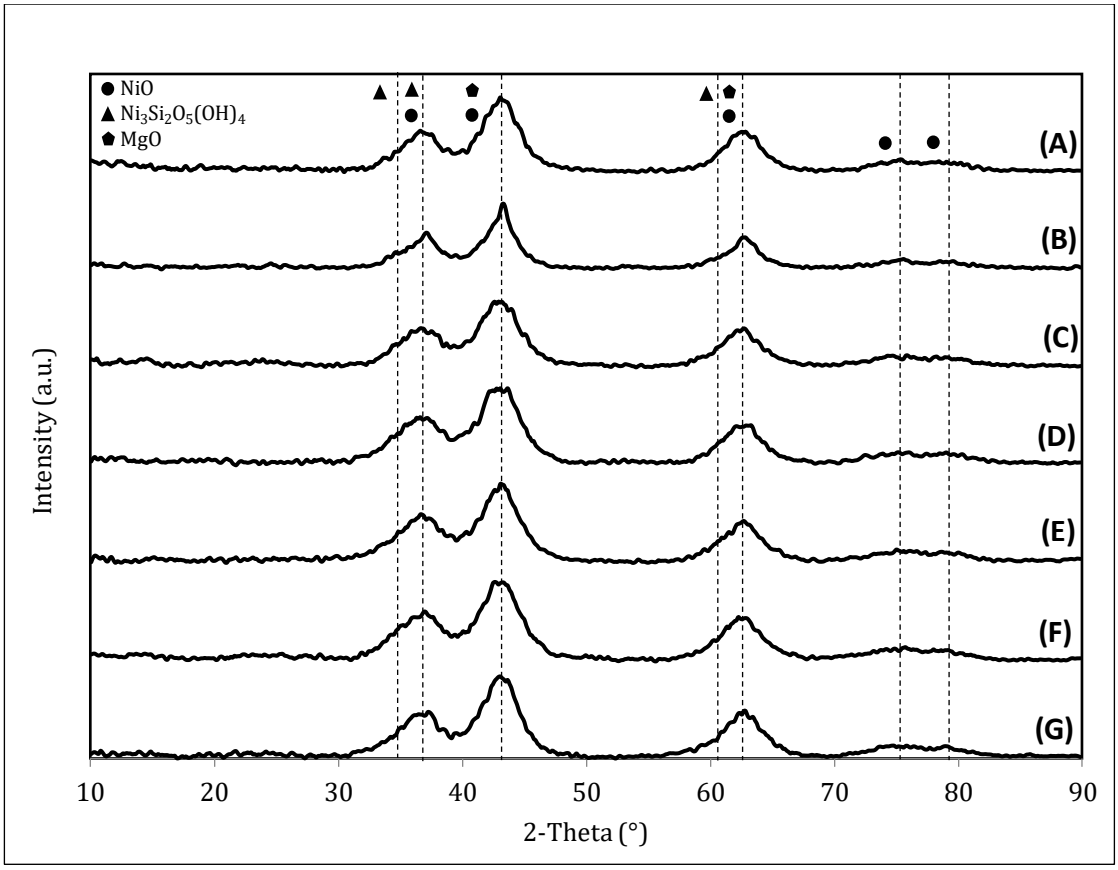


Figure 6.5: XRD diffractograms for samples A – G.

On the other hand, the presence of nickel silicate, formed by a strong interaction between Ni and Si, is also detected at the 35 °, 37 ° and 61 ° peaks. Poorly crystallised nickel silicate compounds with imperfect nickel antigorite structures are always formed for the co-precipitation of nickel and alkali silicate solutions under 100 °C, with structures such as $Ni_3Si_2O_5(OH)_4$ (Gabrovska et al., 2006; Liao et al., 2021; Zhang et al., 2017). This also evidences the interaction that occurs between nickel phases and silica during the precipitation process. When nickel salt is precipitated with sodium carbonate in the presence of silica, the resulting silica-supported basic nickel carbonate takes the composition of $Ni(OH)_x(CO_3)_y/SiO_2 \bullet zH_2O$. The strong interaction has been suggested to result in the formation of the aforementioned nickel silicate layers on the surface of the

silica phase (Ghuge et al., 1993). Furthermore, it was also reported that the $Ni_3Si_2O_5(OH)_4$ phase forms when the Ni/Si ratio is higher than 1.5 (Li et al., 2014), which is in agreement when the synthesis conditions used in this study.

As observed from the diffractograms, the diffraction patterns of the samples are similar regardless of synthesis methods with no significant changes. However, the group of samples sonicated during co-precipitation had a larger crystallite size range of 2.43 – 3.50 nm, compared to the samples sonicated during ageing, with a crystallite size range of 2.28 – 2.41 nm. During co-precipitation, the exposure of the mother liquor to high intensity agitation accelerates the recrystallisation process of the precipitates, thereby enhancing crystal growth and consequently increasing crystal size (Du and Qu, 2007). The generation of localised hot-spots due to acoustic cavitation results in adiabatic pockets of high temperature in the mother liquor, which accelerates the growth rate of the crystals (Costa and Almeida Neto, 2020; Pitto-Barry and Barry, 2019). Nevertheless, the decreasing trend in size from 3.50 – 2.43 nm in samples B – D suggest that the effect of inter-particle collision due to acoustic microstreaming and turbulent mixing became increasingly significant in causing crystal sonofragmentation as the ultrasonic intensity was increased, resulting in the decrease of crystal size as observed (Kim and Suslick, 2018). Therefore, it can be said that a moderately high agitation intensity could result in high local temperatures to enhance the supersaturation state, which lowers the nucleation energy barrier according to the nucleation theory and enhances the recrystallisation process (Madras and McCoy, 2003), causing the increase the crystal size as such in sample B. However, this level of agitation intensity was not high enough to instigate sufficient energy for crystal

fracture to occur, which was observed in samples C and D synthesised with high intensity agitation, thus causing their crystal size to decrease. On the other hand, sample E which was synthesised with an identical agitation intensity as sample B did not experience extensive crystal growth. This could be attributed to the stabilisation of crystal growth once the silica precursor was introduced to the synthesis system, thus forming nickel silicate and averting the further growth of crystals in the composite.

The FT-IR spectra of the calcined samples are shown in Figure 6.6, which can confirm the presence of certain structures in the composites. The broad bands around 3400 cm^{-1} are assigned to the stretching vibration of structural O-H groups of interlayer water molecules. Furthermore, the weak peaks observed ca. 1630 cm^{-1} are ascribed to the bending vibration of water molecules. The absorption band around 1420 cm^{-1} in the IR spectrum can be allocated to the C-O stretching mode, as a result of the carbonate ions present on the surface, and in this case, particularly the adsorption of atmospheric carbon dioxide onto the surface of MgO and SiO_2 (Tahari and Yarmo, 2014; Wu et al., 2016). The oxides of transition metals, such as NiO, typically form repulsive forces with acidic carbon dioxide molecules (Kim et al., 2010; Lee et al., 2015), hence the said peak is not attributed to carbon dioxide absorbed on NiO. On the contrary, the high basicity and favourable thermodynamics of MgO and SiO_2 makes it extremely susceptible to carbon dioxide adsorption (Kumar and Saxena, 2014; Philipp and Fujimoto, 1992). Typically observed at higher wavenumbers (i.e. 1100 – 1050 cm^{-1}), the most intense peaks in the spectra that were shifted to ca. 990 cm^{-1} can be owed to the stretching Si-O vibration mode, indicating the presence of poorly crystallised silicates (Blanco et

al., 2014). Furthermore, the presence of $Ni_3Si_2O_5(OH)_4$ is confirmed by the peaks at 700 – 600 cm^{-1}, which represent Si-O-Ni stretching vibrations (Korytkova et al., 2005), agreeing with those of the XRD analysis. The metal-oxide stretching vibration peaks for Mg-O are detected at around 650 – 600 cm^{-1} (Davar et al., 2017; Gandhi et al., 2011). Next, the Si-O rocking mode was also observed at peaks around 540 cm^{-1} (Capeletti and Zimnoch, 2016). Lastly, peaks at 450 – 400 cm^{-1} can be assigned to the vibration of Ni-O bonds (El-Kemary et al., 2013).

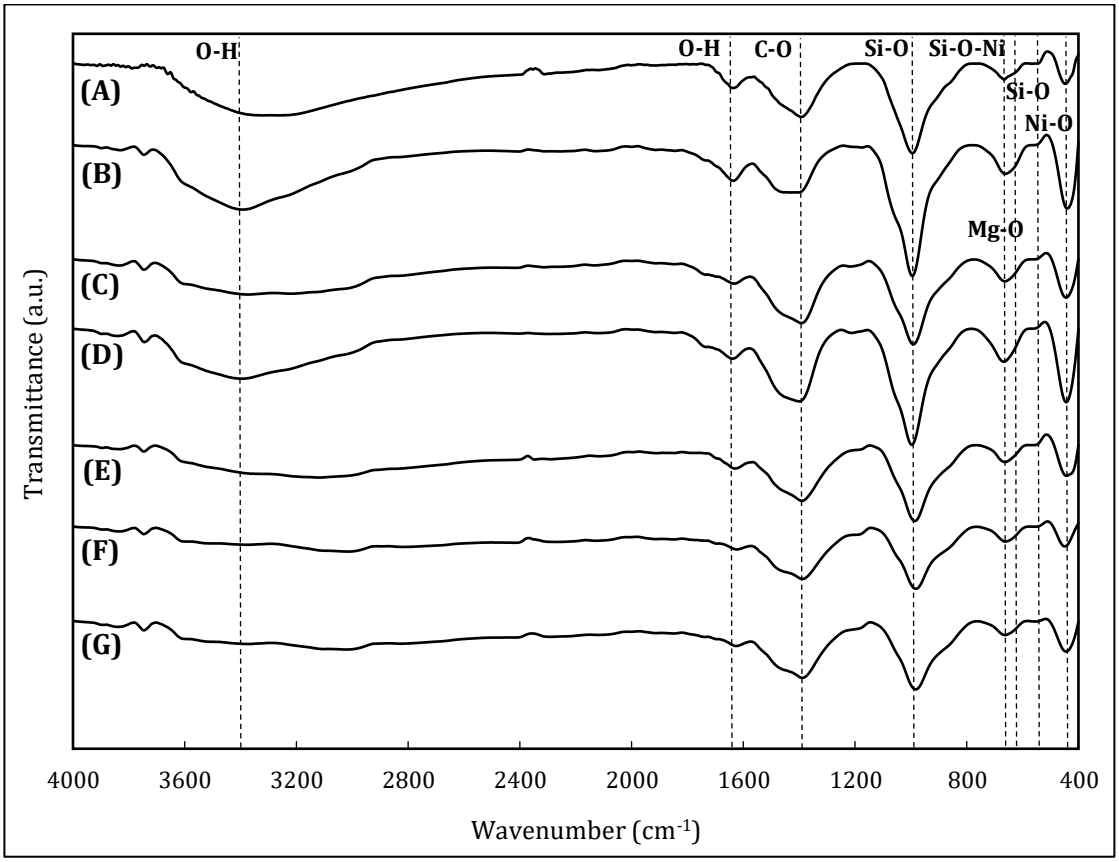


Figure 6.6: FT-IR spectra of samples A – G.

6.3.2. Morphological characterisation

SEM was used to appraise the morphology of the calcined samples. In Figure 6.7, the SEM images of samples A – G are presented. From the scans, sample A is characterised by rough morphologies and the appearance of conglomerates. Nevertheless, it can be observed that there are very apparent dissimilarities between the unsonicated and sonicated samples in terms of their morphology. Similar to the previous textural characterisation, the incorporation of ultrasound at different stages of the synthesis also has a profound impact on the composite morphology. In samples B – D, the morphology seemed to be vastly different from that of samples E – G, as well as sample A. Distinct particles and clumps are visible on the scans, as opposed to a smooth appearance as observed in samples E – G. Compared to the unsonicated sample A, the morphology of samples B – D appeared to be less aggregated, with more defined surface structures. This affirms the ability of ultrasonic irradiation to reduce particle aggregation (Rahbar Shamskar et al., 2017). Acoustic cavitation involves the formation, growth and collapse of numerous micro-bubbles formed in the solution due to ultrasonic irradiation. After attaining a critical bubble size, these bubbles collapse and generate unique environments of high temperature (5000 K) and high pressure (2000 atm), as well as high cooling rates in the magnitude of 10^{11} K s^{-1} (Suslick, 1989). Furthermore, violent shockwaves and turbulence are also generated. The combination of these events could effectively disperse the formation of nanocrystals, hence averting the existence of aggregates. In addition, these effects would be enhanced with the increase in ultrasonic power, thus explaining why the particles seem smaller and more defined. This observed phenomenon resonates with the work of other

researchers, in which a lower degree of particle aggregation was noticed with the use of ultrasound during synthesis (Mahboob et al., 2017; Rahbar Shamskar et al., 2017; Sharifi et al., 2014).

On the other hand, in samples E – G, the use of ultrasound during silica loading and ageing seemed to have smoothened the surface of the composites to a great extent, as evidenced by the scans in Figure 6.7. This observation is consistent with the effects anticipated from interparticle collisions driven by the turbulence and shock waves generated by an ultrasonic field in a solid suspension. In this case, it is theorised that when ultrasound is applied during silica loading to the co-precipitated Ni hydroxycarbonates, the nickel-on-silica particles collide with each other in a glancing manner, hence causing the smoothening of the surface, which results in smooth and even surfaces as shown in Figure 6.7. To illustrate, Suslick and colleagues (1989) noted that the surface of their Ni particles were greatly smoothened as a result of glancing collisions due to ultrasonic irradiation.

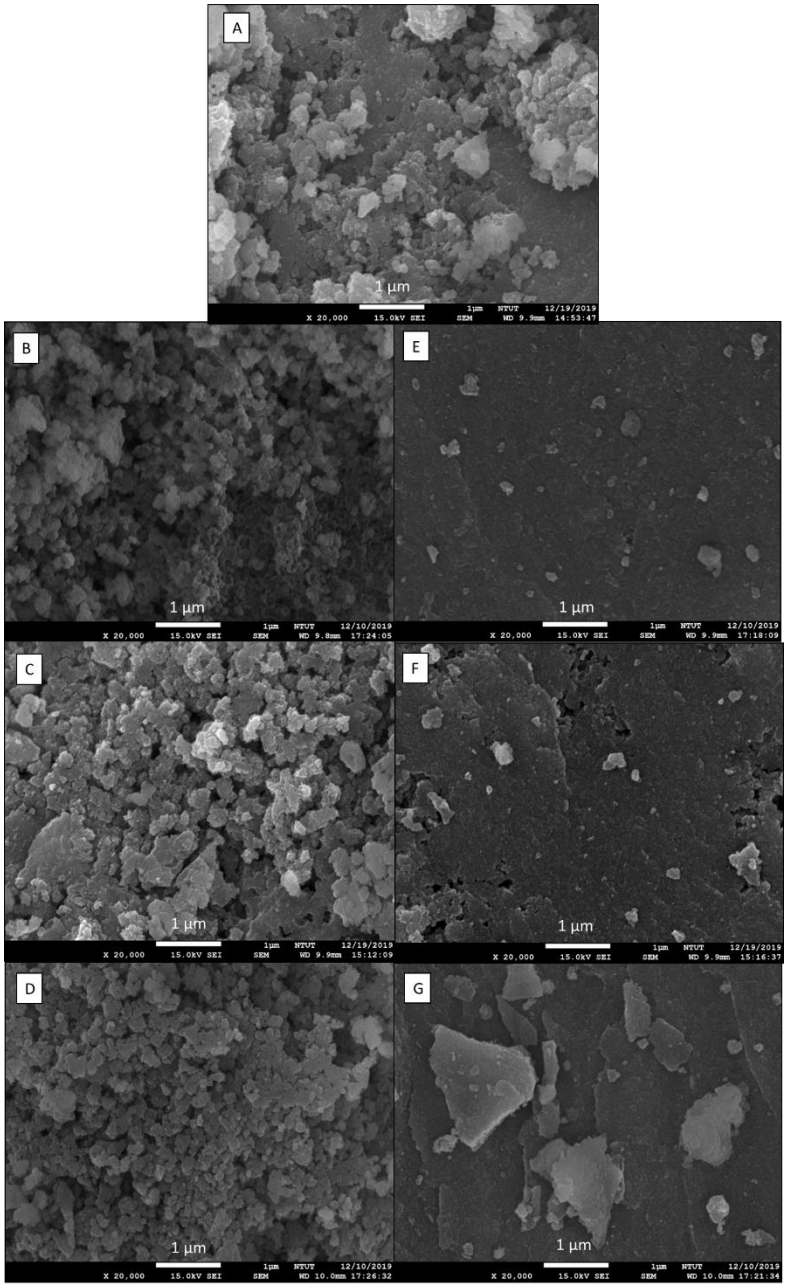


Figure 6.7: SEM images for samples A – G.

Note: Scans are of 20,000x magnification with a 1 µm scale provided.

6.3.3. Composition and surface properties characterisation

Table 6.2 shows the composition of the prepared samples acquired via EDX and XPS analyses. The samples constitute the required elements for the formation of the composites, which confirms the efficacy of the synthesis procedures.

As the typical approximated penetration depth of EDX electron beams is 0.4 μm (Yang et al., 2020), the measured atomic percentage reflects the bulk atomic percentage of the composites. On the contrary, XPS analysis probes the elemental composition of the samples at the surface, corresponding to a penetration depth of approximately 1 – 12 nm, hence demonstrative of the superficial composition of the samples (Yang et al., 2020). While in EDX electrons are directed at the powdered sample and X-ray photos are generated and then detected to determine the elemental composition, in XPS X-rays are directed at the samples and ejected electrons are detected instead. As the samples were all synthesised using identical starting materials, it will be meaningful to draw comparisons based on their bulk and surface atomic distributions to ascertain any changes imparted by the difference in synthesis conditions, as both characterisation techniques present a different depth of information, where the EDX analysis will probe into the deeper layers of the samples, while the XPS analysis will probe the surface layers of the samples.

Table 6.2: Sample compositions obtained from EDX and XPS.

Sample			Sonicated @ co-precipitation			Sonicated @ ageing		
		A	B	C	D	E	F	G
EDX (at %)	Ni	24.9	27.2	26.9	24.7	26	29.5	35.3
	Mg	8.2	9.6	9.1	8.7	9	8	9.5
	Si	8.3	9.7	8.4	7.6	8	8.2	8.6
	O	58.6	53.5	55.6	59	57	54.3	46.6
EDX Mg/Ni		0.329	0.353	0.338	0.352	0.346	0.271	0.268
Δ [a]			0.024	0.009	0.023	0.017	-0.058	**-0.061**
%Δ [b]			7.29	2.74	6.99	5.17	-17.63	**-18.54**
EDX Si/Ni		0.333	0.357	0.312	0.308	0.308	0.278	0.244
Δ [a]			0.024	-0.021	-0.025	-0.025	-0.055	**-0.089**
%Δ [b]			7.21	-6.31	-7.51	-7.51	-16.52	**-26.73**
XPS (at %)	Ni $2p_{3/2}$	15.6	13.2	15.2	15.49	15.5	17.9	18.3
	Mg $2p_{3/2}$	5.4	6.4	6.4	6.25	5.5	4.6	5.3
	Si 2p	7.3	7.9	8	7.03	7.2	6.6	6.1
	O 1s	71.5	71.8	70.4	71.23	71.7	70.9	70.3
XPS Mg/Ni		0.346	0.488	0.421	0.403	0.353	0.257	0.289
Δ [a]			**0.142**	0.075	0.057	0.007	-0.089	-0.057
%Δ [b]			**41.04**	21.68	16.47	2.02	-25.72	-16.47
XPS Si/Ni		0.468	0.598	0.526	0.454	0.465	0.369	0.333
Δ [a]			0.13	0.058	-0.014	-0.003	-0.099	**-0.135**
%Δ [b]			27.78	12.39	-2.99	-0.64	-21.15	**-28.85**

[a] Deviation of value from that of sample A.
[b] Percentage of deviation of value from that of sample A.

Table 6.2 also details the Mg/Ni and Si/Ni ratios and their deviations from sample A, which can be used to compare how much the samples differ from the unsonicated sample and between the ultrasonic treatments. According to the results for both EDX and XPS analyses, the unsonicated sample A registered Mg/Ni ratios close to the experimental stoichiometry ratio introduced during the co-precipitation step. On the other hand, the Si/Ni ratio for sample A was higher at the surface level measured by XPS (0.468) compared to that of EDX (0.333). The higher Si/Ni ratio was mainly due to the growth of the silica network on the outer

surface of the composite during the ageing step under normal conditions. However, comparing the elemental composition obtained from EDX to those of XPS, one can observe an interesting difference between the results obtained for the two sonicated sample sets (B – D vs. E – G).

Table 6.3 presents a summary of the observed change in elemental atomic ratios based on data presented on Table 6.2 with regards to the ultrasound synthesis method and the ultrasonic intensity. For the samples synthesised with ultrasonic irradiation during co-precipitation (i.e. samples B – D), the Mg/Ni ratio from the EDX analysis did not show a significant variation from the parent sample A. This indicates that the bulk Mg/Ni composition of the sonicated samples remained similar to that of sample A despite ultrasonication during the co-precipitation step. Furthermore, the increase in ultrasonic intensity also did not affect the distribution of elements in the bulk to a great extent.

Table 6.3: Summary of the observed change in elemental atomic ratios with increasing ultrasonic intensity.

	Sonication during co-precipitation (Samples B – D)	**Sonication during silica loading/ageing (Samples E – G)**
EDX Mg/Ni	No significant deviation from sample A. Ratio closely followed the stoichiometric ratio of metal precursor during synthesis.	Mg/Ni ratio decreased with increasing ultrasound intensity, which can be attributed to the erosion of Mg from the Ni-Mg hydroxycarbonate precipitates during ageing.
EDX Si/Ni	No significant deviation from sample A. This was due to the absence of ultrasonic irradiation the ageing period when the silica precursor was introduced. Therefore, ageing was allowed to proceed undisturbed.	Si/Ni ratio decreased with increasing ultrasonic intensity. This was mainly due to the suppression of silica cluster formation by ultrasound during the ageing period.
XPS Mg/Ni	Mg/Ni ratio was in a higher range than sample A, with sample B significantly higher than sample A, while the ratio decreased with increasing ultrasound intensity and eventually the Mg/Ni ratio of sample D approached that of sample A. This can be attributed to the migration of Mg to the outer surface of the composite, leading to a Mg-rich surface.	Mg/Ni ratio decreased with increasing ultrasonic intensity following the trend of samples B – D. However, the ratios are lower than samples B – D due to the suppression of silica clusters when ultrasound was activated during ageing. This led to a higher Ni ratio on the surface, resulting in Mg/Ni ratios in a lower range.
XPS Si/Ni	Si/Ni ratio decreased with increasing ultrasonic intensity. The high ratios were mainly due to higher tendency of Si ions attaching on the outer surface during ageing. The decreasing trend from B to D followed that of XPS Mg/Ni, due to the migration of Mg to the surface. With a lower Ni content on the Ni-Mg hydroxycarbonate surface, the XPS Si/Ni ratio became significantly higher.	Si/Ni ratio decreased with increasing ultrasonic intensity following the trend of EDX Si/Ni ratio. However, the ratios were lower than samples B – D primarily due to the application of ultrasound during ageing. Overall, the ratios are higher than that of EDX Si/Ni, which validates the tendency of silica clusters to form on the outer surface of the composite.

On the other hand, it can be observed that the bulk Mg/Ni ratio for the samples synthesised with ultrasonic irradiation during silica loading/ageing (i.e. samples E – G) experienced significant changes. A decreasing trend is also seen as the ultrasonic intensity was increased. This can be attributed to the erosion of Mg during the ultrasound-assisted ageing step from the Mg-rich surface of Ni-Mg hydroxycarbonate precipitates, formed during the preceding co-precipitation step (Lim et al., 2021). It has been reported that elements with a lower surface free energy are inclined to migrate to the surfacial layers of a composite material, in response to being in a mixture with other elements with higher surface free energies (Behrens et al., 2012). With respect to that, Mg (0.688 J m^{-2}) tends to migrate to surface layers as its surface energy is lower than that of Ni (2.080 J m^{-2}) (Tyson and Miller, 1977), which is a phenomenon noted by other researchers as well (Behrens et al., 2012; Wong et al., 2018; Yang et al., 2012). Consequently, the severity of Mg erosion from the surficial layers of the samples increased as the ultrasonic intensity was increased from 0.0283 – 0.111 W cm^{-3}, resulting in the decrease in Mg/Ni ratio from 0.329 in sample A to 0.268 in sample G.

The Si/Ni ratio obtained from the EDX analysis for samples B – D also showed no significant deviation from that of the unsonicated sample A. Similarly, an increase in ultrasonic intensity did not affect the distribution. This is due to the absence of ultrasonic irradiation when the silica phase was loaded and aged, hence the Si network formation of the samples was not disrupted and closely mirrors that of sample A.

On the contrary, the application of sonication during silica loading/ageing effectively reduced the Si/Ni ratio from 0.333 for sample A to a range of 0.244 – 0.308 for samples E – G. The samples sonicated during silica addition and ageing are said to possess a shorter effective ageing time due to the action of ultrasonic irradiation, which perturbs the ageing process. Compared to an undisturbed ageing process, the presence of acoustic waves leads to cavitation phenomena in the mother liquor, which causes violent conditions such as asymmetric micro-bubble implosions at the solid-liquid boundaries, could generate high velocity micro-jets towards the Ni-Si or Si-Si interface. The resulting consequence would be the decrease in extent of polymerisation and crystallisation of the silicate phases (Nares et al., 2009), leading to the disruption and suppression of the formation of silica clusters and hydrosilicates, thus leading to a lower Si content in the samples. With the increase in ultrasonic intensity, the Si/Ni ratio decreases from 0.308 – 0.244, indicating the effectiveness of high intensity ultrasound in suppressing the Si network to a greater extent.

In the surface analysis provided by XPS, samples B – D noted a significant increase in the Mg/Ni ratio compared to that of sample A, from 0.346 to the range of 0.403 – 0.488. This range was also much higher than that of samples E – G, which were at 0.257 – 0.353. In this case, it can be said that the incorporation of ultrasonic irradiation during the co-precipitation of the Ni-Mg hydroxycarbonates has augmented the presence of Mg on the sample surface. As mentioned previously, Mg tends to migrate to the surfacial layers of a composite due to its surface energy properties. The action of ultrasound in accelerating mass transfer likely resulted in the intensification of Mg migration to the surface of the samples during the

nucleation and crystallisation process of precursor co-precipitation (Sadeghpour et al., 2021). Studies have shown that the usage of ultrasound during co-precipitation allowed the constant exposure of precursor particles to the salt cations in the mother liquor, thus enhancing the access of the cationic species to the interlayer and surfacial spaces of the precursors, which increases their incorporation into the material structure (Kooli et al., 1997; Macedo Neto et al., 2010). Therefore, ultrasonic irradiation during co-precipitation was likely to result in the apparent enrichment of Mg on the surface of samples B – D. This ratio, however, decreased with the increase in ultrasonic intensity, with the ratio of sample D (0.403) approaching the ratio of sample A (0.346). In this case, it is speculated that the usage of ultrasonication in the higher intensity range (0.0831 – 0.111 W cm^{-3}) might have caused the over-intensification of Mg migration to the sample surface, thus concurrently leading to a higher degree of Mg erosion from the samples, resulting in the decrease of the surface ratio of Mg/Ni.

Similarly, samples E – G experienced a decreasing Mg/Ni ratio with the increase in ultrasonic intensity, following the trend of samples B – D. Nevertheless, it is noted that the Mg/Ni ratios for samples E – G are comparatively lower than those in the unsonicated sample A and samples B – D. This is likely due to the erosion of Mg from the Mg-rich Ni-Mg hydroxycarbonates as a result of sonication during ageing.

The surfacial Si/Ni ratio for samples B – D were in the higher range of 0.454 – 0.598. The increased presence of Si could be attributed to the higher tendency of Si ion attachment onto the outer surface of the samples during ageing. As samples

B – D were synthesised without ultrasonic irradiation during ageing, the continual and uninterrupted attachment of Si ions has also resulted in the formation of more silica clusters on the outer surface of the composites, which led to the high Si/Ni ratio reported. It is also noted that the decreasing trend of the Si/Ni ratio with the increase in ultrasonic intensity follows that of the XPS Mg/Ni ratio, due to the migration of Mg to the surface. With a lower Ni content of the Ni-Mg hydroxycarbonate surface, the XPS Si/Ni ratio becomes significantly higher.

Contrariwise, samples E – G experienced a dramatic decrease in surfacial Si/Ni ratio when sonicated during silica loading and ageing, in which the ratio decreased from 0.465 – 0.333 as the ultrasonic intensity was increased. This trend also follows the decreasing Si/Ni ratio obtained from EDX for the samples. It is noted that the overall Si/Ni ratio for samples E – G were lower than that of samples B – D primarily due to the application of ultrasonic irradiation during the ageing step, which suppresses the formation of the silica network on the surface of the samples. In addition, it is noted that the Si/Ni ratios obtained from XPS were higher than that obtained from EDX for samples E – G. This was predominantly due to the attachment of silicate ions on the outer surface of the silica clusters and their subsequent growth (Lim et al., 2021). As the application of ultrasound was only during the initial 10 minutes of the ageing step, the remaining unsonicated ageing period allowed the growth of silica clusters, which further validates that silica clusters tend to form on the outer surface of the composite.

In terms of predicted catalytic activity, the increased presence of the Mg species on the surface of the samples, such as those in samples B – D may affect the

product selectivity during hydrogenation (Meshkani and Rezaei, 2011). For instance, the migration of Mg to the surface of samples B – D might positively or negatively affect the production of *trans*-C18:1. On the other hand, the formation of surfacial silica clusters in samples B – D might also affect the accessibility of the nickel active sites, which might affect overall hydrogenation activity.

It should be highlighted that since applying ultrasonic irradiation during the ageing stage would disrupt the ageing process due to the perturbation of the mother liquor by ultrasonic waves and result in a shorter effective ageing time, thus a probable way to counter this would be to increase the overall ageing time for materials aged under sonication to achieve the equal ageing effect as materials aged with sonication. However, these results fulfil one of the aims of this chapter to demonstrate that ultrasonic irradiation produces different results when applied at different stages of material synthesis.

The chemical nature and electronic properties of the calcined samples were studied by XPS. Figure 6.8 shows the Ni 2p photoelectron spectrum of the composites synthesised. From the figure, the Ni 2p core level is similar in pattern for all samples. The respective Ni binding energies of the composites are tabulated in Table 6.4. For all samples, the Ni $2p_{3/2}$ is accompanied by the presence of a satellite peak at 861 – 863 eV, congruous to the existence of Ni^{2+} instead of metallic Ni^{0} (Shalvoy et al., 1980). It is noted that these satellite peaks manifest due to the paramagnetic state of the Ni^{2+} species and electron shake-up. Notably, these peaks are typically ca. 6 eV higher than the main Ni $2p_{3/2}$ peak (Alvarez-Galvan et al., 2019), as noted by the ΔE_{sat} values in Table 6.4.

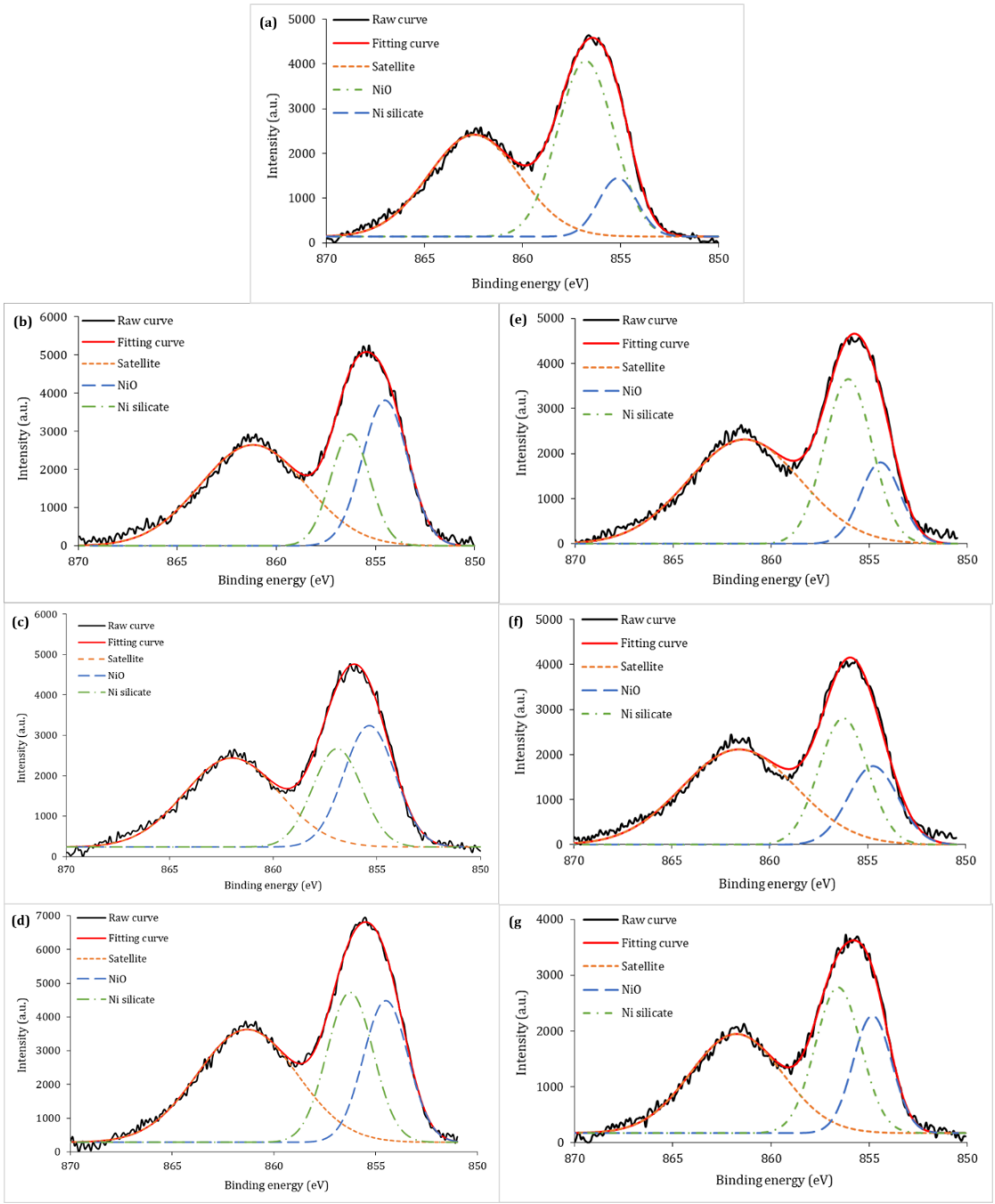


Figure 6.8: Ni 2p3/2 XPS spectra fitting for samples A – G.

The XPS peak for Ni 2p3/2 of the non-sonicated sample A was detected at a binding energy of 856.64 eV, which resonated well with reported values of 856.3 – 856.7 eV (Shalvoy and Reucroft, 1979; Vedrine et al., 1978). Since the XPS analysis is surface sensitive, the discrepancies in binding energies indicate that the Ni species on the surface have been altered electronically due to the ultrasound-

augmented synthesis procedure (Stanković et al., 2017). In this case, the binding energies of the sonicated samples shifted to a lower range of 855.45 – 855.84 eV. This indicates that the application of ultrasound in the synthesis procedures altered the electronic properties of the Ni surface species in the sonicated nickel-silica composites (Wong et al., 2018). This shift in binding energy denotes the change in strength of interaction between the NiO species and the silica phase (Xu et al., 2012), which is consistent with the results obtained from the TPR analysis later, noting the shift in main reduction peaks to lower temperatures in the sonicated samples. In this case, the shift to lower binding energies indicated a decrease in nickel-silica interactions (Stanković et al., 2017). Nevertheless, it is noted that the technique of ultrasonic incorporation did not have an apparent effect on the binding energies of the nickel-silica composites, in which the values reported for samples in all samples B – G remained at ca. 855 eV. This shift to lower binding energies due to the application of ultrasound was also reported by other researchers (Li et al., 2006). Perhaps most importantly this interesting finding could entail probable changes in the functionality of the composites. As a case in point, in certain applications such as catalytic hydrogenation reactions, the change in electron density of catalyst composites could affect the bonding of chemical intermediates to the active sites, ultimately influencing changes in reaction pathways and hence the selectivities during the reaction (Bai et al., 2017; Lim et al., 2021; Wu et al., 2018).

Table 6.4: Results for the XPS analysis of samples A – G.

Sample	**Ni $2p_{3/2}$ (eV)**	**Ni $2p_{3/2}$ satellite (eV)**	**ΔE_{sat} [a] (eV)**	**Fitted peaks (eV)**		**Relative proportion [b] (%)**		**Si 2p (eV)**	**$\Delta E_{Ni\text{-}Si}$ [c] (eV)**
				NiO	Ni Silicate	NiO	Ni Silicate		
A	856.64	862.48	5.84	855.15	856.79	18.64	81.36	103.2	753.44
B	855.45	861.18	5.73	854.52	856.28	60.08	39.92	101.9	753.53
C	855.70	862.00	6.30	855.37	856.92	56.24	43.76	102.4	753.30
D	855.47	861.29	5.82	854.71	856.29	47.82	52.18	102.0	753.47
E	855.78	861.37	5.59	854.44	856.08	29.52	70.48	102.7	753.08
F	855.84	861.57	5.73	854.72	856.24	38.80	61.20	102.5	753.34
G	855.83	861.76	5.93	854.83	856.58	40.65	59.35	102.1	753.73

[a] Separation of Ni $2p_{3/2}$ primary line to satellite.
[b] Ratio of integrated area of the two compounds via curve fitting.
[c] Difference between Ni $2p_{3/2}$ and Si 2p.

To gain more insight into the XPS results, the Ni $2p_{3/2}$ XPS core level region was deconvoluted via Gaussian multi-peak curve-fitting and fitted with three doublets assigned to NiO, Ni silicate and the associated satellite features, as shown in Figure 6.8. As the NiO binding energies have been reported to be significantly lower at a range of 854 – 855 eV (Allen et al., 1989; Shalvoy and Reucroft, 1979; Vedrine et al., 1978), it is suggested that another Ni phase exists at a higher binding energy, which can be attributed to the Ni silicate phase. Hence, this agreed well with the two Ni phases detected in the XRD, FT-IR and following TPR analyses. In addition, it was reported the difference between Ni $2p_{3/2}$ and Si 2p binding energies, $\Delta E_{Ni\text{-}Si}$, can be used to verify the presence of nickel silicates (Coenen, 1991). Several studies have established that should nickel silicates exist, the

typical values for $\Delta E_{Ni\text{-}Si}$ would lie between 753.2 – 753.8 eV (Lorenz et al., 1979; Occelli et al., 1986; Shalvoy and Reucroft, 1979). From Table 6.4, the $\Delta E_{Ni\text{-}Si}$ values of the samples synthesised agreed excellently with this, thus substantiating the presence of the said phases. In this study, the binding energy of the nickel silicate phases are reported at 856.08 – 856.92 eV, similar to those reported in the literature (Shalvoy and Reucroft, 1979).

The deconvoluted peaks obtained for the XPS curves could provide additional insight into the composition of the phases present in the samples. The area under each of the individual deconvoluted peaks in Figure 6.8 represent the relative proportion of the corresponding phase, when averaged over the total area of the curves (Smith, 2009). In this case, the area under the curve of each deconvoluted peak in Figure 6.8 were used to estimate the relative surface proportion of each nickel species. Corroborating the results from the TPR analysis, as will be shown in next section, the presence and absence of ultrasound and the stage when it was activated during synthesis also imparted considerable discrepancies on the NiO and Ni silicate surface compositions. The unsonicated sample A recorded the lowest percentage of NiO at 18.64 % and the highest percentage of Ni silicate at 81.36 %, among all the samples. The samples subjected to sonication during co-precipitation, however, contains NiO in the higher range of 47.82 – 60.08 %, while the Ni silicate content is in the lower range of 39.92 – 52.18 %. With the increase in ultrasonic intensity from 0.0283 – 0.111 W cm^{-3}, samples B – D experienced a decrease in NiO from 60.08 – 47.82 %, while the Ni silicate phase was increased from 39.92 – 52.18 %. Contrariwise, the samples subjected to sonication during silica loading and ageing presented the opposite

trend, with lower NiO content at 29.52 – 40.65 % and a higher Ni silicate content at 59.35 – 70.48 %. In this case, the increase in ultrasonic intensity resulted in the corresponding increase in the NiO phase from 29.52 – 40.65 % and the decrease in the Ni silicate phase from 70.48 – 59.35 % for samples E – G.

6.3.4. Reducibility and active site characterisation

H_2-TPR profiles of the samples are shown in Figure 6.9. The reduction profiles of the samples are characterised by multiple reduction peaks fused together into a broader reduction band from 100 – 800 °C, with a peak ca. 400 – 500 °C. This observation denotes the homogeneous distribution of Ni phases over the Si phase, with the presence of complex and intimate interactions between the phases, which supports the XRD reflections and is also in accordance with other researchers (Gabrovska et al., 2005; Ghuge et al., 1993).

Based on the main reduction peaks, it can be observed that the unsonicated sample A has the highest reduction temperature at 448.9 °C. Furthermore, the incorporation of ultrasonic irradiation has resulted in the decrease of reduction temperatures for all samples B – G. Nevertheless, it is interesting to note that the two different strategies of ultrasound-assisted synthesis also resulted in a discernible difference between the reduction properties and reducibility of the nickel-silica composites.

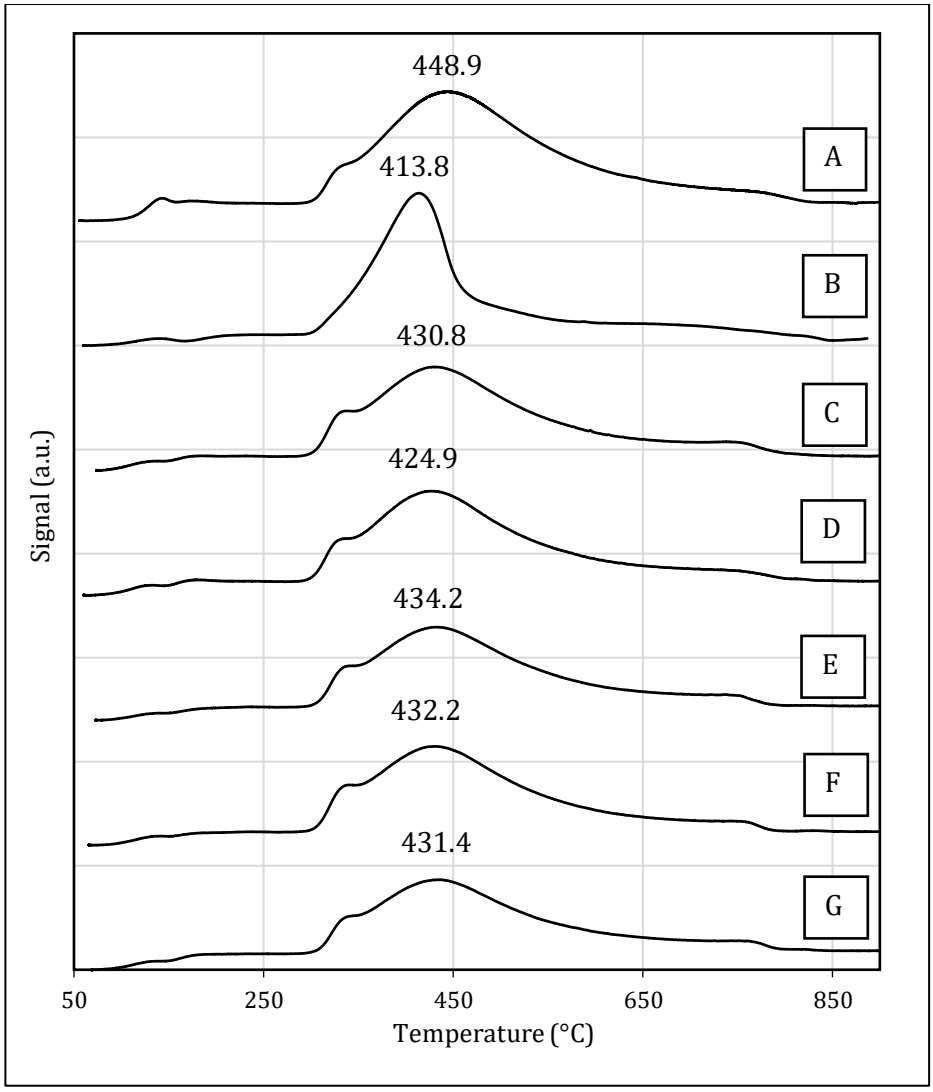


Figure 6.9: Reduction profiles obtained for the samples A – G via H_2-TPR.

Samples B – D, which were sonicated during the co-precipitation stage have reduction temperatures in the lower temperature range of 413.8 – 430.8 °C. On the other hand, samples E – G, which were sonicated during silica loading and ageing step have reduction temperatures in a higher range of 431.4 – 434.2 °C. A higher reduction temperature for samples E – G denotes the increase in difficulty of reducing the Ni^{2+} species to Ni^0, and vice versa for samples B – D. In this case, the usage of ultrasound during the co-precipitation of the active phases would result in samples possessing a higher ease of reducibility, due to lower nickel-silica

interactions. Meanwhile, sonication during the silica loading and ageing phase resulted in samples with lower reducibility, thereby possessing higher nickel-silica interactions.

As reported by Mile et al. (1988), the existence of these low and high temperature peaks, which correspond to phases of varying reducibility, are often highly sensitive to preparation conditions. In this case, the usage of ultrasound at the two distinct stages of the synthesis in this study seemed to have an apparent effect on the reduction properties of the samples. During precipitation, liquid mixing, nucleation and crystal growth take place to form primary crystallites, and aggregation of the primary crystallites occur. The nucleation process could be highly influenced by the presence of ultrasonic irradiation, whereby a homogeneous environment allows the fast nucleation and controlled growth of metal crystallites, concurrently averting the formation of large agglomerates during precipitation, thus improving the dispersion of the nanocrystallites. Furthermore, •OH radicals produced from the sonolysis of water molecules could also convert the metal salts to metal hydroxides without the influence of the precipitant, thereby increasing the formation of active site precursors (Allahyari et al., 2014a).

In this case, this might have led to the increase in reducibility of the samples B – D, which was also observed by other researchers for their catalysts (Ameen et al., 2016; Kruatim et al., 2017; Panahi et al., 2015). However, with increasing ultrasonic intensity, more intense cavitation leads to increased nucleation during co-precipitation, producing smaller crystallites with higher interaction with the

silica phase (Allahyari et al., 2014a), thus forming more Ni silicates with increased ultrasonic intensity.

On the other hand, the decreased reducibility caused by higher nickel-silica interactions in samples E – G might be due to the anchoring effect imparted by ultrasonic irradiation as the silica phase was added to the co-precipitated precursors in the mother liquor during silica loading and ageing stage (Gedanken, 2004). In the simultaneous presence of a silica phase, the cavitational implosion of micro-bubbles near solid boundaries (i.e. solid metal particle surfaces) generates micro-jets, which propels the co-precipitated precursors onto the silica phase surfaces, thereby effectively immobilising the Ni phases and increasing the chemical interaction between the Ni phases and the silica phase (Allahyari et al., 2014a; Lim et al., 2009; Ramesh et al., 1997). This would result in the decrease in reducibility of the nickel phases for samples E – G as shown in Figure 6.9, compared to that of samples B – D, but does not supersede that of sample A.

To gain further insight into the TPR results, the broad peaks observed were deconvoluted into symmetrical peaks to evaluate the relative percentage of the different reducible species, as well as their peak positions, presented in Table 6.5. The deconvolution was carried out using the OriginPro software via Gaussian multipeak curve-fitting. In total, three main peaks could be identified, and are labelled as α, β and γ. The deconvoluted TPR profiles are presented in Figures S5-S7 (Appendix III). The reduction temperatures reported can be classified into different types of nickel species, which are directly associated with the degree of interaction with the silica phase. This also indicates that Ni species of different

extents of interaction coexist within the nickel-silica composites. Henceforth, the three peaks are classified based on their reducibility and explained based on their relative proportions. It is noted that no reduction peaks corresponded to the reduction of MgO species due to their extreme difficulty in reduction under the present conditions applied (Sulmonetti et al., 2016).

Table 6.5: Further insight into the reduction properties of the samples and results for the H_2-pulse chemisorption analysis.

Sample	**Peaks (Temperature, °C; Relative percentage, %)**			**Ni dispersion [a], D_{Ni} (%)**	**Ni surface area [b], SA_{Ni} ($m^2\ g_{Ni}^{-1}$)**
	α	β	γ		
A	181.4	422.2	501.7	8.79	58.55
	6.2	32.1	61.7		
B	227	412.1	608.7	15.95	106.24
	10.8	60.3	28.9		
C	174.8	423.1	608.4	16.54	110.17
	8.18	59.2	32.7		
D	175.6	422.4	541.1	13.61	90.63
	5.1	54.4	40.5		
E	190.6	411.7	495.7	10.26	68.31
	3.9	35.8	60.3		
F	198.1	418.3	498.7	14.26	94.95
	3.2	42.5	54.3		
G	190.6	418.2	514.4	17.81	118.53
	5.2	41.4	53.4		

[a] Calculated according to Eq. (2.9).
[b] Calculated according to Eq. (2.10).

The first low temperature peaks (α) represent a minor portion approximately 10 % or less of the total reduction profile. These peaks can be ascribed unambiguously to the reduction of higher Ni(III) oxide in trace quantities (Ni_2O_3 to NiO), which is a common occurrence for precipitates calcined at

temperatures ≤ 400 °C (Ermakova and Ermakov, 2003; Mile et al., 1988). However, since the XRD results exhibited no obvious Ni_2O_3 signals, it is suggested that the Ni_2O_3 phase present is too sparse in amount and also highly dispersed on the silica phase (Sidik et al., 2016). Next, the β peaks at ca. 411 – 423 °C are due to the Ni phases possessing weak interactions with the silica phase (Moogi et al., 2019; Soghrati et al., 2018). On the other hand, the γ peaks at ca. 495 – 609 °C are due to the Ni species having strong interactions with the silica phase, hence forming nickel silicate, which has a higher difficulty to reduce (Moogi et al., 2019; Soghrati et al., 2018).

Based on Table 6.5, the composition of α for all samples remain in the same range of approximately 3 – 11 %, irrespective of synthesis strategy or ultrasonic intensity, thus representing their minor role in the samples. It is observed that samples B – D possessed a higher percentage of α at an upper range of 5 – 11 %, which aided in their higher reducibility. Nonetheless, the impact of this phase is considered minor due to their low percentage in the sample composition. The unsonicated sample A registered the lowest percentage of β at 32.1 % and the highest percentage of γ at 61.7 %, indicating that the sample has a higher difficulty in reduction compared to the sonicated samples, in line with the XPS results and TPR profiles. On the other hand, the percentages of β and γ for the sonicated samples B – G vary significantly with the manipulation of synthesis techniques and the respective ultrasonic intensities. Comparing both the ultrasonic synthesis strategies, similar to the previous XPS analysis, it can be seen that sonication during the co-precipitation stage for samples B – D resulted in a higher proportion of β at 54.4 – 60.3 %. Contrariwise, a lower proportion of γ for said samples was

also registered at 28.9 – 40.5 %. With regards to the change in ultrasonic intensity, when the parameter for said samples were increased from 0.0283 – 0.111 W cm^{-3}, the β phase for samples B – D decreased from 60.3 – 54.4 %, while the γ phase increased from 28.9 – 40.5 %. The application of ultrasound during co-precipitation seemed to have reduced the ability of the hydroxycarbonates to bind and react with the Si phase dosed at the later stage, resulting in the presence of more NiO phases with lower interaction with the Si phase.

On the other hand, sonication during silica loading and ageing achieved results opposite to that of samples B – D, in which the percentages of β and γ for samples E – G recorded lower and higher ranges of 35.8 – 42.5 % and 53.4 – 60.3 %, respectively. It is also noted that with the increase in ultrasonic intensity, the β phase increased from 35.8 – 42.5 %, while the γ phase decreased from 60.3 – 53.4 %. The decreased proportion of Ni phases with stronger interactions indicate that ultrasound during ageing inhibited the formation of Ni hydrosilicates, possibly through erosion (Lim et al., 2021). However, it is observed that a raise in ultrasonic intensity failed to instigate any appreciable change in the β and γ phases from sample F to G, signifying the erosion of Ni silicate due to ultrasonic irradiation has reached a plateau (Lim et al., 2021). Bond linkages of -Si-O-Ni- exist in Ni hydrosilicate compounds (Ghuge et al., 1993), with the corresponding Ni-O bonds possessing dissociation energies of 391.6 kJ mol^{-1} (Dean, 1999). In the presence of ultrasonic waves, the collapse of acoustic bubbles is capable of supplying ample energy to instigate Ni-O bond breakage (Nesterenko and Berlizov, 2007), hence eroding the Ni hydrosilicate structure. Meanwhile, Si-O bonds in the bond linkages of -O-Si-O- found in silica clusters possess higher bond energies of 440 kJ mol^{-1},

making it tougher for bond breakage via acoustic cavitation after the attachment of silicate ions onto hydrosilicates, which subsequently form more silica clusters (Lim et al., 2021). As a consequence, Ni silicate phases were enclosed by the silica clusters that serve as a protective enclosing, thus effectively averting them from being eroded severely by ultrasonic irradiation. During ageing, the increase in ultrasonic intensity increased the suppression of the silica cluster build-up, as the polymerisation of silicic acid was restrained (Greenberg and Sinclair, 1955). This resulted in the decrease of Si/Ni ratios, as demonstrated in Table 6.2.

These above results infer that when sonication was carried out during the co-precipitation stage, more Ni phases with weak interaction with the Si phase was formed, resulting in a lower temperature reduction peak. Inversely, when sonication was carried out during the addition of silica and subsequent ageing, a stronger interaction occurred between the Ni phases and the Si phase. Thus, forming more nickel silicate, resulting in the shift of the main reduction peak to higher temperatures. These findings echo those of the XPS analysis, whereby the samples also presented similar trends in their surface compositions with regards to the NiO and Ni silicate phases. Nevertheless, despite the mirroring trends from XPS and TPR, it is also noted that there exist some discrepancies in results between the two analysis techniques. To illustrate, the NiO phase detected by XPS for each sample was at a lower value compared to the corresponding results obtained from TPR. Conversely, the Ni silicate phase detected by XPS for each sample was at a higher value compared to that of TPR. In other words, it can be said that the XPS analysis detected the presence of more Ni silicates and less NiO compared to the TPR analysis. As mentioned previously, XPS is a surface sensitive analysis,

conversely TPR represents the bulk of the samples. During the undisturbed ageing step, the build-up of silica clusters occurred on the surface of the samples, allowing the polymerisation and crystallisation of the silicate phases, therefore the detection of a higher proportion of Ni silicates via XPS could be justified. Hence, for sequentially precipitated composites of nickel-on-silica, the introduction of ultrasonic irradiation during active metal co-precipitation instigated weaker nickel-silica interactions, while applying ultrasonic irradiation during the loading of silica and ageing strengthened the nickel-silica interactions.

H_2-pulse chemisorption analysis was carried out to probe the active metal dispersion properties of the composites, with results displayed in Table 6.5. According to the results, the application of ultrasonic irradiation either during co-precipitation or silica loading/ageing has effectively increased the metal dispersion of the nickel-silica composite from 8.79 to 17.81 % and metal surface area from 58.55 to 118.53 $m^2\ g_{Ni}^{-1}$. The increase in both properties indicates the better dispersion of Ni across the silica phase due to the incorporation of ultrasonic irradiation during the synthesis. The dispersing action of ultrasound during the co-precipitation of the Ni-Mg hydroxycarbonate precursors resulted in smaller precursor aggregates, allowing the increase in dispersion and surface area of Ni even with a high Si coverage for samples B – D. On the other hand, for samples E – G, the severe erosion of the Ni-Mg hydroxycarbonates due to ultrasonic irradiation could be the main driving factor behind the enhancement of dispersion and surface area properties (Lim et al., 2021). Throughout the synthesis of the composites, the pH of the mother liquor remained ca. 8.8, including during the application of ultrasonic irradiation. It is likely that the eroded Ni and Mg ions re-precipitated to

become finer hydroxycarbonate nanoparticles, resulting in greater dispersion and Ni surface area (Lim et al., 2021).

6.3.5. Summary of the effects of ultrasonic irradiation on the mechanisms of composite formation

Based on the data analysed so far, the underlying mechanisms behind these ultrasound-driven synthesis processes are suggested. Figure 6.10 illustrates the disparities in composite formation mechanisms ensuing the conventional unsonicated synthesis pathway and the ultrasound-assisted synthesis pathways, with either sonication during co-precipitation or during silica loading/ageing. As illustrated, a time scale of 50 min is depicted, which represents the entire synthesis pathway of the composites from beginning to end. In particular, the represented synthesis segments in Figure 6.10 are the Ni-Mg hydroxycarbonate co-precipitation step (10 min), addition of Si ions (10 min) and subsequent ageing step (30 min), followed by the termination of the ageing period. Pathway A represents the synthesis pathway for the conventional precipitation technique without sonication (i.e. sample A), while in pathways B and C sonication was applied at the co-precipitation step (i.e. samples B – D) and the silica loading/ageing step (i.e. samples E – G), respectively.

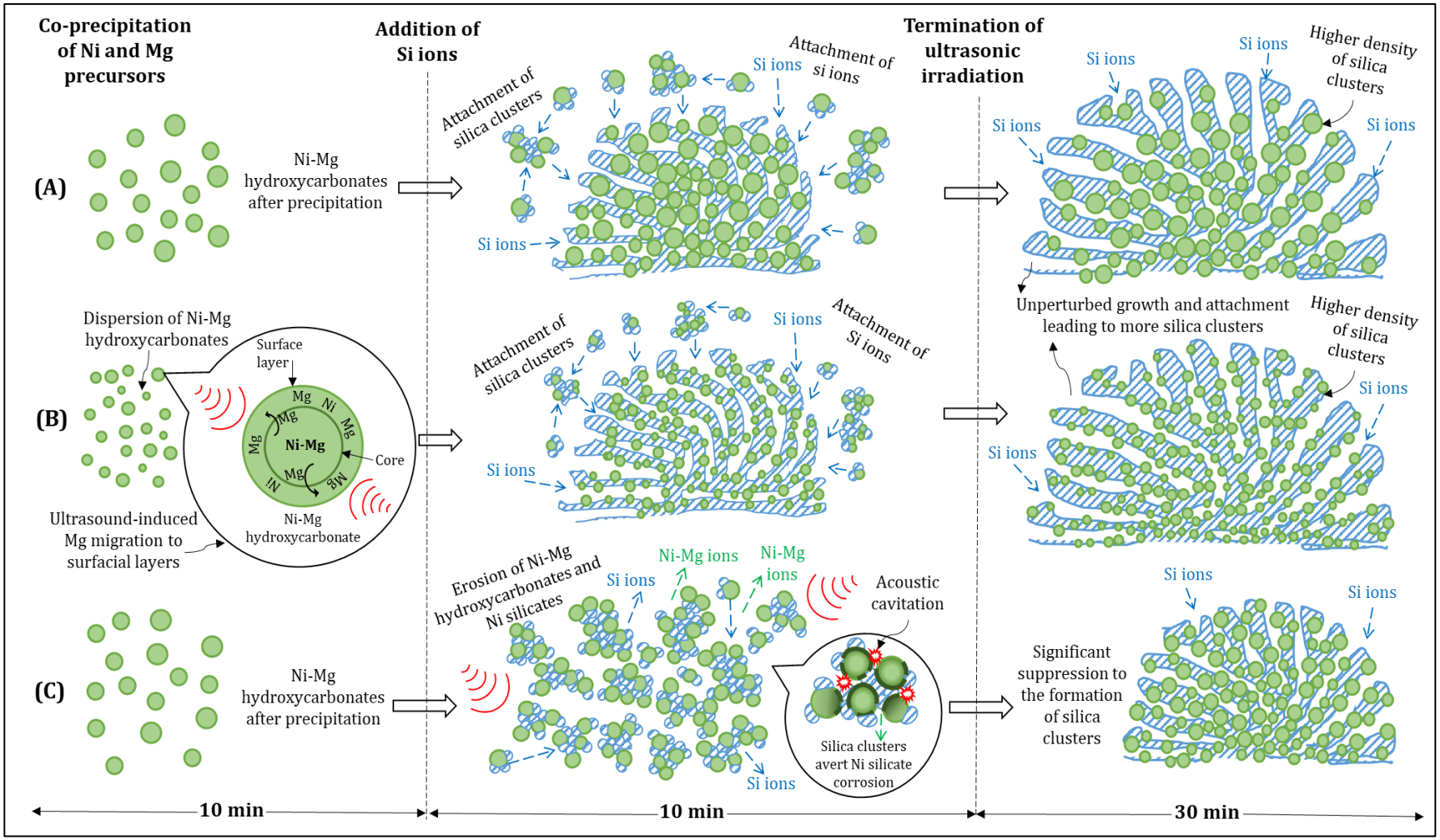


Figure 6.10: Mechanisms of nickel-silica composite formation at varied synthesis configurations for (A) Sample A; (B) Samples B – D; and (C) Sample E – G.

In the absence of ultrasound during both co-precipitation and silica loading/ageing for sample A (synthesis pathway A in Figure 6.10), the precursors could form without disturbance via insonation. Therefore, any erosion towards Ni-Mg hydroxycarbonates during co-precipitation was averted, resulting in composite particles with lower dispersion. In addition, erosion towards the Si clusters and hydrosilicates during silica loading and ageing was also avoided, with a longer effective ageing period compared to those of samples E – G. As a result, the growth of the composite particles was unperturbed, permitting a higher extent of polymerisation and crystallisation of the silicate phases (Nares et al., 2009). Consequently, this uninterrupted attachment of Si ions onto the outer surface during ageing led to the build-up of silica clusters as well as the formation of more Ni silicate phases. As a result, stronger nickel-silica interactions ensued, as noted by the characterisation tests discussed previously. This phenomenon is also noted by other researchers, whereby longer ageing durations resulted in higher reduction temperatures, which represents stronger Ni interactions with the Si phase, thus evincing the formation of a higher proportion of Ni silicates (Lim et al., 2021; Liu et al., 2008).

For samples B – D (synthesis pathway B in Figure 6.10) synthesised with ultrasonic irradiation during the co-precipitation stage, it is apparent that the action of ultrasonic irradiation effectively hastened the migration of Mg to the composite surface through the acceleration of mass transfer during precursor nucleation and crystallisation, resulting in a surface enrichment of Mg as shown in the XPS studies (pathway B figure callout). However, the high Si surface content as demonstrated in the XPS analysis indicate that much of the Si might still be in the

form of Si-O that are predominantly unattached to the Ni hydroxycarbonates, thus unable to react extensively to form more Ni hydrosilicates. Consequently, a higher NiO percentage and a lower Ni silicate percentage in the composites were observed, as indicated by the XPS and TPR analyses, resulting in composites with lower reduction temperatures. Similar to the unsonicated sample A, the build-up of silica clusters on the surface of the composites was more pronounced due to the unperturbed attachment of Si ions during the ageing step, forming more Si-O clusters on the outer surface of the composites, resulting in higher Si/Ni ratios as reported. The effective dispersion of precursors during the ultrasound-assisted co-precipitation stage has also resulted in the enhancement of the dispersion and surface area properties of the samples.

In the presence of ultrasonic irradiation during silica loading/ageing for samples E – G (synthesis pathway C in Figure 6.10), the precursors in this process are speculated to experience severe perturbation due to the action of acoustic cavitation. In the presence of solid particles, acoustic cavitation ensuing from sonication results in asymmetric implosions at the solid-liquid boundaries, such as the precipitates present in the composite suspension, which generates high velocity micro-jets towards the material surface, rupturing the chemical bonds present in the composite structure (Suslick, 1989). It is suggested that this phenomenon could cause erosion to the Ni-Mg hydroxycarbonate phases, as well as effectively disrupt and suppress the formation of weak nickel hydrosilicates (dark green in pathway C figure callout). Furthermore, the build-up of silica clusters can also be averted, thus resulting in a higher percentage of Ni-Mg hydroxycarbonate phases (light green in pathway C figure callout) in the material

composition, leading to lower reduction temperatures than the unsonicated sample A, although not lower than those of samples B – D. The suppression of large aggregates is also ensued from ultrasonic irradiation, resulting in smaller particle sizes after ageing, thus enhancing the metal dispersion and surface area.

A succinct overview and breakdown of the resulting composite properties due to the mechanisms involved in the synthesis of the composites, with or without ultrasonic irradiation and the variation in ultrasonic intensity and ultrasonic synthesis configuration, are highlighted in Table 6.6 below.

Table 6.6: Summary of composite properties as a result of the mechanisms involved in the synthesis of the composite.

Ultrasonic intensity	**Synthesis technique**	
	Sonication during co-precipitation	**Sonication during silica loading/ageing**
N/A (unsonicated composite sample)	- No erosion on hydroxycarbonate, hydrosilicate and silica clusters, allowing the unperturbed growth of composite particles, thus resulting in high Si content on the superficial layers of the composite in the majority form of silica clusters. - A longer effective ageing time resulted in larger pore sizes.	
Low ultrasonic intensity = 0.0283 W cm^{-3}	- High movement of Mg to the outer surface of the Ni-Mg hydroxycarbonates due to ultrasound-induced mass transfer acceleration. - Formation of high-density silica cluster on surface due to uninhibited attachment of Si ions during ageing.	- Negligible erosion to Ni-Mg hydroxycarbonates. - Minimal erosion of Ni silicates due to low ultrasonic intensity. - Disruption of polymerisation to form silica clusters.

Table 6.6 (continued): Summary of composite properties as a result of the mechanisms involved in the synthesis of the composite.

Medium ultrasonic intensity = 0.0831 W cm^{-3}	- Enhanced migration of Mg to the surface due to higher acceleration of mass transfer by sonication. - Erosion of Mg from Ni-Mg hydroxycarbonates due to higher density of Mg resulted in decreased Mg surface concentration. The erosion may affect electronic properties, which may alter product selectivity during catalytic hydrogenation. - High density silica cluster on composite surface due to Si ion attachment.	- Significant erosion to the Ni-Mg hydroxycarbonates, resulting in increased dispersion of phases. - Increased ultrasonic intensity resulted in erosion of Ni silicates. - Increased ultrasonic intensity further suppressed the formation of silica clusters.
High ultrasonic intensity = 0.111 W cm^{-3}	- Further enhancement of Mg migration to the surface due to the extreme acceleration of mass transfer by higher ultrasonic intensity. - Severe erosion of Mg from Ni-Mg hydroxycarbonates due to the presence of more Mg resulted in the further decrease in Mg surface concentration. The erosion may affect electronic properties, which may alter product selectivity during catalytic hydrogenation. - High density of silica cluster due to Si ion attachment.	- Increased ultrasonic intensity compared to sample C did not significantly increase the erosion of Ni-Mg hydroxycarbonates. - Increased dispersion of Ni in the composite. - Concentration of Ni silicate did not decrease significantly, as a result of the enclosing of Ni silicate by silica clusters, thus resisting erosion. - Further increase in ultrasonic intensity suppressed the formation of silica clusters more significantly.

6.4. Concluding remarks

This present work has successfully addressed the initial problem statements, in which it is determined that there will be major transformations to the composite material if sonication were applied at different stages during the synthesis procedure. To demonstrate, it was ascertained that the application of ultrasound at the co-precipitation step and the silica loading/ageing step during the synthesis of nickel-silica composites resulted in differing material properties and characteristics.

The characterisation techniques employed in this study provided evidence that various textural, structural, morphological, reduction and surface composition characteristics could be influenced by the presence of ultrasonic irradiation during synthesis, as well as the configuration of ultrasonication in the synthesis procedure. For instance, sonication during co-precipitation resulted in samples possessing wider pores with Type II and IV(a) isotherms, rough morphology, enriched superficial Mg and Si contents due to enhanced Mg migration to the surface and the clustering of surfacial Si, higher reducibility and a higher concentration of NiO. Contrariwise, samples sonicated during silica loading/ageing led to samples with narrower pores with Type IV(a) isotherms, smooth morphology, lower superficial Mg and Si contents due to erosion to Ni-Mg hydroxycarbonate phases and silica clusters, lower reducibility and a higher concentration of Ni silicates.

Aside from ascertaining the disparity in the nickel-silica composite properties when synthesised with different ultrasound-assisted procedures or the lack thereof, this chapter also serves to highlight the significance of how ultrasound is incorporated into material synthesis and one should bear in mind that the mechanisms and subsequent effects of ultrasonic irradiation is inherently complex and not as straight-forward as perceived. To illustrate, applying ultrasound during the silica loading/ageing stage of the synthesis might not bring about the same effects as to when ultrasound is applied during the precipitation stage of the same synthesis.

Overall, it is recommended that the ultrasound-assisted technique, when incorporated in either the co-precipitation or support loading/ageing stage of nickel-silica composite synthesis, is recommended for adoption in order to tune and optimise the properties and subsequently the catalytic performance of the composite.

7. Recovery of Nickel from Spent Catalysts via Ultrasound-assisted Hydrometallurgy

7.1. Introduction

Heterogeneous, supported nickel catalysts are often employed for a wide range of industrial processes, namely methanation, catalytic steam reforming, hydrotreating, hydrodesulphurisation and vegetable oil hydrogenation (Oza et al., 2011, 2010; Singh, 2009). While being economical and highly active, nickel catalysts decline in activity over time until it drops below a particular satisfactory threshold (Argyle and Bartholomew, 2015). In this case, the catalyst undergoes regeneration to be recycled until it is no longer economically feasible due to the severe loss in activity after prolonged usage, which is often ascribed to catalyst sintering, poisoning, fouling or mechanical attrition (Oza and Patel, 2012). Nonetheless, the deactivated catalyst is typically disposed of as solid waste and such wastes are generated in significant quantities (Dufresne, 2007; Marafi and Stanislaus, 2008). These wastes comprise metals that are leachable by water, and if not handled aptly, could consequently instigate alarming environmental concerns, as well as health risks as nickel is a known carcinogen (Marafi et al., 2010; Rapaport, 2000). To avert the disposal of such hazardous waste to landfills or to the environmental, the Malaysian government has enacted the Environmental Quality Act (EQA) in 1974 (*Environmental Quality Act*, 1974) and the Environmental Quality (Schedules Wastes) Regulations in 2007 (Artika et al., 2019). In particular, it was suggested to render all scheduled waste harmless by enacting policies for wastes to be treated at the point of waste generation or at

specially designed treatment plants. On the other hand, the Basel Convention was also designed to minimise the generation of hazardous wastes on a global scale, which also directly elicited various industries to treat, recycle and reuse part of their waste materials, preferably at the point of generation (Aja et al., 2016; Hackett, 1990).

In general, two different methods are employed in the extraction and recovery of nickel from ores or spent catalysts: pyrometallurgical and hydrometallurgical. The pyrometallurgical technique describes the extraction of ferronickel from various sources with the use of high temperatures (Oza and Patel, 2012). For instance, Llanos et al (1997) carried out high temperature alkali roasting to recover valuable metals (e.g. molybdenum, vanadium, nickel, cobalt and alumina) from spent catalysts, whilst others explored the recovery of spent Ni-Mo/Al_2O_3 catalysts using low temperature sulphuric acid baking process (Kim et al., 2009). On the other hand, the hydrometallurgical technique involves the leaching of metals from their sources using mineral acids (i.e. sulphuric or nitric acid) or solutions of ammonia and ammonium salts (Kolosnitsyn et al., 2006). Juxtaposing both pyrometallurgical and hydrometallurgical processes, the latter is more favourable and vastly applied in the recovery of metals from industrial wastes due to their process versatility, eco-friendliness and high energy-efficiency (Kinoshita et al., 2003; Lai et al., 2008).

Various parameters and conditions have been studied and manipulated to execute the leaching process of nickel as efficient and cost-effective as possible. For example, parameters such as leaching time, acid concentration (Khalid and Athraa,

2017), solid to liquid ratio (Lee et al., 2010), leaching temperature and pressure, average spent catalyst particle size and agitation speed (Sahu et al., 2005) were studied. In particular, ultrasonic energy generates unique and extreme environment in a liquid medium that leads to various chemical and physical consequences. The phenomena of ultrasonic cavitation in liquid-solid systems are reportedly responsible for several chemical and physical effects. Physical effects include (*a*) the improvement of mass transport from rigorous mixing and acoustic streaming; (*b*) the initiation of superficial damage at liquid-solid interfaces through micro jets and shock waves; (*c*) the manifestation of high-velocity interparticle collisions in suspensions; and (*d*) the fragmentation of friable solids and deagglomeration of aggregates to increase surface area (Suslick and Price, 1999). On the other hand, chemical effects due to sonication, also known as sonochemistry, include (*a*) the formation of H• and •OH primary radicals due to high temperatures inside an imploding bubble; (*b*) the generation of secondary radicals due to reactions between primary radicals and solute molecules; (*c*) the enhancement of redox reactions (Kentish and Ashokkumar, 2011; Mason and Lorimer, 2002). All of the above effects could be beneficial for the intensification of leaching processes, whereby ultrasonic agitation decreases the activation energy for metal dissolution compared to conventional agitation methods, thereby increasing the leaching rate of nickel by manifold (Wei et al., 2015).

Oza et al. (2011) recovered almost 95 % Ni from spent Ni/Al catalysts using harsh reaction conditions such as high temperatures and acid concentrations as well as a high-power ultrasonic probe, which poses safety issues due to probe corrosion from direct contact with strong acids. However, Si as a support is more

commonly employed than Al for Ni-based catalysts for the hydrogenation of edible oils due to its stronger metal-support interaction, higher activity, better selectivity and lower production of *trans* fats (Cepeda et al., 2016). Nevertheless, studies regarding the recovery of Ni from such supports are limited, which are important due to their prevalent usage and the subsequent demand in recovery. Furthermore, milder operating conditions for optimal ultrasonic leaching processes are not documented. Motivated by this gap in knowledge, this present work is prompted to establish the effects of an ultrasonic bath on leaching processes involving silica-supported nickel catalysts by comparing sonicated and unsonicated leaching experiments under various operating parameters such as time, temperature, ultrasonic density and acids. Furthermore, the effectiveness of various mineral acids including nitric acid and sulphuric acid as leaching reagents was also investigated. This chapter attempts to further intensify and optimise the recovery using optimised conditions at lower temperatures and acid concentrations with an ultrasonic bath, which is more feasible for industrial scale-up than probes. The optimisation of this process intensification technique was carried out by adopting response surface methodology (RSM) with a central composite design (CCD) in order to ascertain the optimum leaching parameters and the interactive effects of the leaching conditions (ultrasonic density, leaching temperature, acid concentration and pulp density).

7.2. Experimental

7.2.1. Pre-treatment of spent catalysts

The spent catalyst was provided by a local vegetable oil hydrogenation company, which had a nickel content of 65 wt% and was grinded prior to calcination. A suitable calcination temperature for the spent catalysts was determined through thermogravimetric analysis (TGA, Mettler Toledo TGA/DSC 1), at a ramp of 10 °C/min until it reached 995 °C. Spent catalysts were subjected to calcination at 400 °C for 3 h to remove all coated fats and carbonaceous matter. Lastly, calcined spent catalysts were sieved using a 500 μm sieve (Fieldmaster, 35 mesh) to obtain particles below 500 μm.

7.2.2. Acid leaching under conventional mechanical stirring

2 g of the spent catalyst sample in its powdered form was added to the selected acid in a conical flask to constitute a solid to liquid ratio of 1:10 (pulp density of 10 %). Experiments were conducted using 10 vol% HNO_3, with a total volume of 20 ml. The slurry was then heated on a hot plate stirrer (Cole-Parmer, StableTemp) to their respective leaching temperatures and mechanically stirred using a magnetic stirrer for 2 h, except for time dependent studies. Finally, the slurry was centrifuged to separate the leachate from the leach residue after the leaching process was terminated. The concentration of nickel was determined *via* UV-Visible spectroscopy (Perkin Elmer, Lambda 35), which was detected at a wavelength of 394 nm. Next, the recovery percentage was determined according to the formula:

$$\text{Recovery percentage (\%)} = \frac{\text{Recovered nickel concentration}}{\text{Initial nickel concentration}} \text{ x } 100 \qquad \text{Eq. (7.1)}$$

Experiments were repeated with a similar molarity for H_2SO_4. For time-based experiments, 20 g of spent catalyst were added to 200 ml of 10 vol% nitric acid to form the leaching slurry at 70 °C, in which it should be noted that the working volume of this experimental set is ten times of the non-time-based experiments. This was done in order to ensure the mass loss during the entire experimental duration was kept to a minimum (10 % difference). Accordingly, 2.5 ml of the slurry were extracted at 1 h intervals and subsequently sent for nickel concentration analysis. To ascertain the effects of temperature on leaching, temperature dependent studies were conducted at leaching temperatures of 40, 50, 60 and 70 °C for 2 h.

7.2.3. Acid leaching under ultrasonic irradiation

Leaching experiments subjected to ultrasonic irradiation were conducted using an ultrasonic bath, with temperature controlled at ca. 40 – 70 °C ± 2 °C. All experimental and reagent conditions remained similar to those described in Chapter 7.2.2, without the usage of a magnetic stirrer.

7.2.4. Sample characterisation

7.2.4.1. UV-Visible spectroscopy (UV-Vis)

The spectra and absorbance of nickel in solution were determined by a Perkin Elmer Lambda 35 double beam UV-Vis spectrophotometer, along with a

pair of 1-cm optical path length quartz cuvette. The spectrophotometer was equipped with a tungsten lamp as the source and a deuterium lamp as the background corrector. The standard addition method was used to eliminate matrix interferences (Grinshtein et al., 1999). The Ni calibration curve was obtained by progressively adding standard solutions to an unknown leach solution and acquiring their solution absorbance. A known quantity of analyte was added to subsequent experiment leach solutions of unknown concentrations and their absorbance measured. The Ni concentration of the unknown leach solutions can then be determined from the difference in absorbance of known and unknown concentration samples using the calibration curve.

7.2.4.2. Analysis of variance (ANOVA)

The statistical significance of the data acquired were examined based on the single factor analysis of variance (ANOVA). The statistical significance was employed at a 95 % confidence level, whereby a significance level below 0.05 would deem the data as statistically significant, vice versa.

7.2.4.3. Experimental design and model development

In this study, the Design Expert software (Stat-Ease Inc., Version 12) was utilised to optimise the ultrasonic leaching parameters. The response surface methodology (RSM) is a statistical technique widely used to enhance, analyse and optimise various processes, and is thus applied to the design of the tests in this present work. The Central Composite Design (CCD) was used to study the effects of four main chosen parameters, i.e. ultrasonic amplitude (A, %), leaching

temperature (B, °C), acid concentration (C, vol%) and pulp density (D, %). These factors are coded and listed in Table 7.1. The CCD applying the four factors mentioned involved an experimental set of 30 generated runs, whose details are shown in Table 7.2. Accordingly, the experimental response for this study was the percentage recovery of Ni. The behaviour of the ultrasonic leaching system was interpreted using the empirical polynomial model described by the following second-order polynomial equation:

$$Y = \beta_0 + \sum_{i=1}^{k} \beta_i X_i + \sum_{i=1}^{k} \beta_{ii} X_i^2 + \sum_{i=1}^{k-1} \sum_{j=1}^{k} \beta_{ij} X_i X_j + \varepsilon \qquad \text{Eq. (7.2)}$$

where:

Y is the model predicted response for Ni percentage recovery (%), β_0 is the model constant. β_i, β_{ii} and β_{ij} are linear, quadratic and interaction coefficients, respectively. X_i, X_j,..., X_k are the individual factors, X_i^2, X_j^2,..., X_k^2 are the quadratic effects, X_iX_j, X_iX_k and X_jX_k are the interaction relationships of the individual parameters. ε is the random error.

Furthermore, analysis of variance (ANOVA) was used to ascertain the significance of the models and parameters. The results include the probability value (p-value) and Fischer's test value (F-value) at a 95 % confidence level. In efforts to substantiate the precision and foresight of the model applied, supplementary diagnostic analyses, i.e. R^2, adjusted R^2, predicted R^2, normalised residual plots and adequate precision were also obtained. Final validation experiments were executed thrice to obtain an average Ni percentage recovery in order to authenticate the model predictions.

Table 7.1: Experimental factors at different levels for the ultrasonic leaching and recovery of Ni from spent catalysts for 2 h.

Factor	**Code**	**Unit**	**Low axial (-2)**	**Low factorial (-1)**	**Centre point (0)**	**High factorial (+1)**	**High axial (+2)**
Ultrasonic amplitude	A	%	20	40	60	80	100
Leaching temperature	B	°C	30	40	50	60	70
Acid concentration	C	Vol%	5	7.50	10	12.50	15
Pulp density	D	%	5	7.50	10	12.50	15

Table 7.2: Experimental plan based on CCD and the results of nickel recovery.

Run	US amp., A (%)	Temp., B (°C)	Acid conc., C (vol%)	Pulp density, D (%)	Actual Ni recovery (%)	Predicted Ni recovery (%)	Residue
1	40	40	7.5	12.5	20.6	22.2	-1.56
2	60	50	5	10	28.7	28.0	0.65
3	20	50	10	10	41.6	35.5	6.10
4	80	60	12.5	7.5	95.0	87.0	7.31
5	60	50	10	10	56.1	53.2	2.97
6	60	50	10	10	52.9	53.2	-0.22
7	80	60	7.5	12.5	44.2	41.2	3.01
8	40	60	12.5	7.5	92.8	90.4	2.39
9	100	50	10	10	38.3	43.7	-5.35
10	40	40	7.5	7.5	22.2	27.4	-5.12
11	80	40	12.5	12.5	35.4	35.0	0.51
12	60	50	10	10	61.7	53.2	8.55
13	80	60	12.5	12.5	79.0	72.0	7.10
14	80	60	7.5	7.5	67.3	63.5	3.83
15	40	60	7.5	7.5	54.9	57.9	-2.96
16	80	40	7.5	7.5	28.0	29.5	-1.42
17	60	50	10	5	76.5	71.3	5.18
18	60	50	10	15	37.8	42.3	-4.47
19	80	40	12.5	7.5	39.9	41.1	-1.10
20	60	70	10	10	73.8	81.3	-7.43
21	40	60	12.5	12.5	64.9	65.9	-0.99
22	80	40	7.5	12.5	24.4	24.9	-0.46
23	60	50	10	10	53.0	53.2	-0.15
24	60	30	10	10	22.0	13.8	14.14
25	60	50	15	10	70.6	70.6	0.03
26	60	50	10	10	52.4	53.2	-0.76
27	40	40	12.5	12.5	30.5	32.4	-1.93
28	60	50	10	10	42.9	53.2	-10.20
29	40	60	7.5	12.5	38.0	35.0	3.02
30	40	40	12.5	7.5	33.6	39.1	-5.47

7.3. Results and discussion

7.3.1. Pre-treatment of spent catalysts

From the information obtained from Figure 7.1, ca. 60 % of the spent catalyst mass is lost between 30 – 400 °C, denoting the removal of volatile compounds, with the onset of the plateau beginning at 400 °C. Nonetheless, in a TGA study carried out by Hermida and colleagues (2019), they have attributed the weight loss of their silica-supported nickel catalyst at high temperatures to the decomposition of nickel compounds, which can very well explain the observable weight loss of ca. 10 % from 400 – 1000 °C, as seen in Figure 7.1. Hence, a calcination temperature of 400 °C was applied for all the spent catalyst samples.

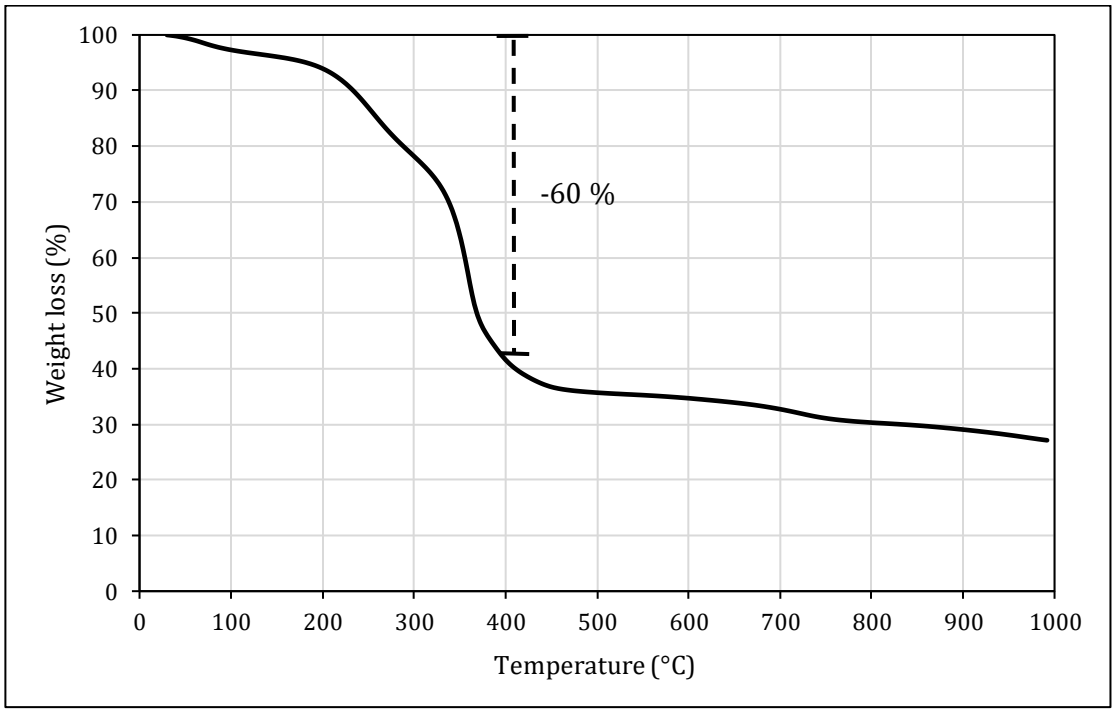


Figure 7.1: Thermogravimetric analysis (TGA) performed on spent catalysts, in flowing air.

7.3.2. Ultrasonic bath calorimetry

The area of highest energy output was determined and used for all experiments. Results from the calibration experiment was obtained and shown in Table 7.3, whereby the ultrasonic densities were calculated with respect to the working volume used for the experiments. The ultrasonic power is the amount of energy dissipated by the transducers into the leach solution due to change in temperature induced, while the ultrasonic density takes into account the amount of ultrasonic energy experienced by a particular volume of liquid. Accordingly, both aforementioned parameters increased as the ultrasonic amplitude was increased, caused by the rise in energy dissipated by the ultrasonic transducers.

Table 7.3: Ultrasonic densities acquired for the ultrasonic bath operating at different amplitudes.

Amplitude, (%)	**Temperature rise per unit time, (°C s^{-1})**	**Ultrasonic power, (W)**	**Ultrasonic density [a], (W cm^{-3})**	**Ultrasonic density [b], (W cm^{-3})**
20	0.002	0.467	0.0225	0.00225
40	0.003	0.700	0.0350	0.00350
60	0.005	1.050	0.0525	0.00525
80	0.007	1.517	0.0750	0.00750
100	0.008	1.633	0.0825	0.00825

[a] Calculated for the working volume of 20 ml in non-time-based experiments.
[b] Calculated for the working volume of 200 ml in the time-based experiment.

7.3.3. Comparison of ultrasonic and conventional mechanical stirring techniques for nickel leaching from spent catalysts

Results presented in Figure 7.2 shows the relationship of the nickel percentage recovery with the stirring speeds of 300, 400, 500 and 600 rpm at 70 °C for 2 h. With the significant increase in stirring speed, the percentage recovery, however, only experienced a marginal improvement throughout the whole study. Here, it is noted that Ni concentrations were obtained after performing a Ni concentration calibration via UV-Vis spectroscopy. A calibration curve of a linear regression line with a regression coefficient (R^2) of 0.9994 was acquired to determine subsequent Ni concentration in samples. The most considerable improvement in the nickel percentage recovery was from stirring speeds of 400 rpm (33.9 wt%) to 500 rpm (39.4 wt%), representing over 15 % increase in recovery. Further increase from 500 to 600 rpm resulted in nickel recoveries of 40.17 ± 0.6771 % and 41.62 ± 0.9774 %, respectively. Hence, it can be said that the increase from 500 to 600 rpm did not provide significant improvement to leaching, in which *p*-value of the two data sets recorded 0.1035 at a confidence level of 0.95. It is noted that at a *p*-value of more than 0.05, the data are statistically insiginificant. Analogous results were obtained by several other researchers, whereby the stirring speed did little or nothing to enhance the leaching rate of metals from the waste catalysts (Aras and Agacayak, 2017; Khalid and Athraa, 2017). This denotes that (i) the diffusion of HNO_3 from the leaching solution towards the surface of the spent catalyst particles and (ii) the reaction products away from the catalyst particles were rapid. Hence, external diffusion does not have a significant control over the leaching rate within the range of the stirring speeds investigated (David,

2007; Khalid and Athraa, 2017). Therefore, all subsequent studies were conducted at a stirring speed of 500 rpm to ensure the invariance of this reaction parameter.

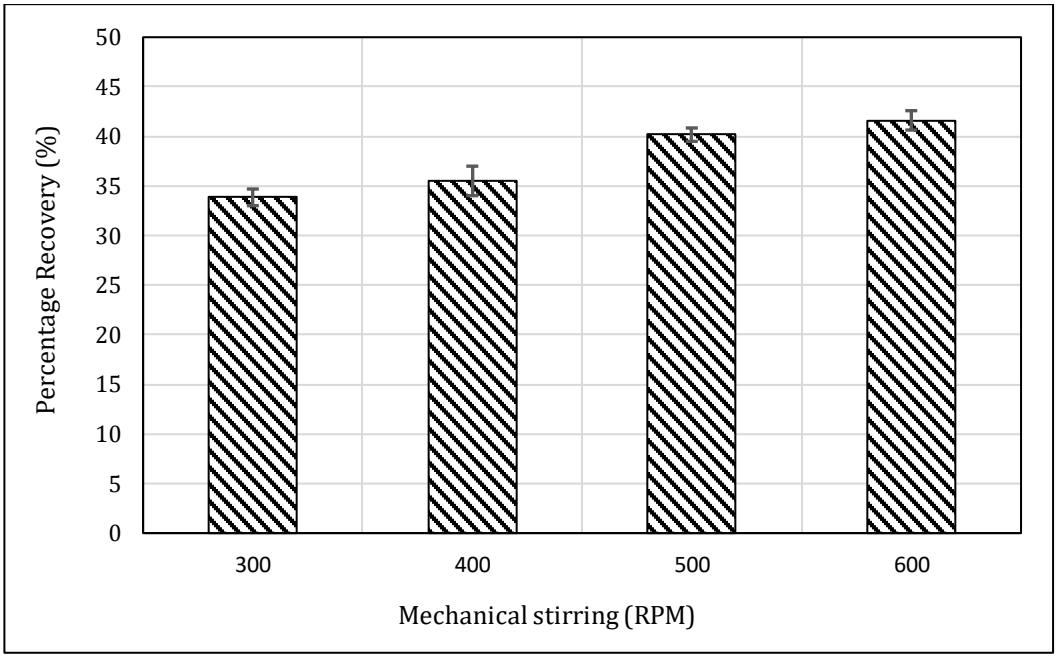


Figure 7.2: Effect of mechanical stirring speed on the recovery on nickel recovery via nitric acid leaching.

Figure 7.3 shows the comparison of nickel recovery upon mechanical and ultrasonic treatment. It should be noted that as the time-based experimental set for Figure 7.3 was scaled up ten times compared to the non-time-based experiments in order to account for sample collections at different time intervals, as mentioned in the Experimental section. Hence, there would be discrepancies in nickel recovery rates due to the difference in working volumes of the experiments. As indicated in Table 7.3, the increased working volume of the time-based experiment has resulted in lower ultrasonic densities experienced by the leaching system, which is 0.00825 W cm^{-3} at a 100 % ultrasonic amplitude compared to 0.0825 W cm^{-3} experienced by the non-time-based experiments. Therefore, the

lower nickel recovery obtained at 2 h for this experimental set compared to that of the subsequent sections would be justified due to the decrease in cavitation events ensuing a lower ultrasonic density.

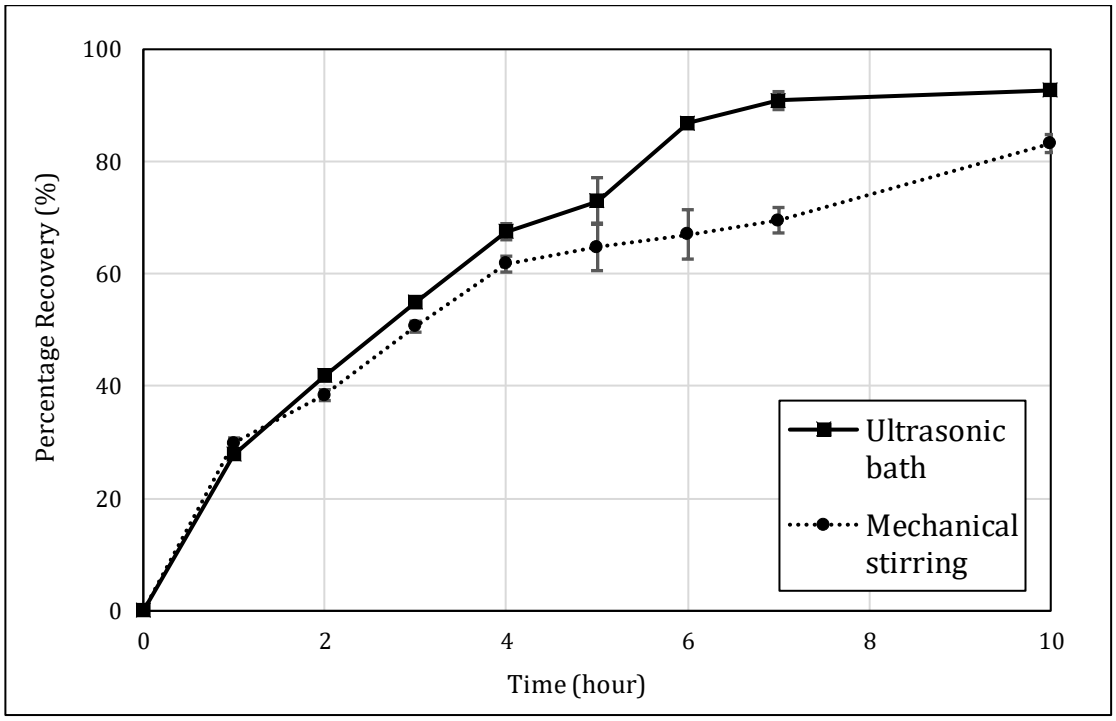


Figure 7.3: Effect of time on nickel recovery via ultrasound-assisted nitric acid leaching (Ultrasonic density = 0.00825 W cm^{-3}, 70 °C) and conventional mechanical stirring nitric acid leaching (500 rpm, 70 °C).

According to the time-based experiment (Figure 7.3), it is noted that the extent of nickel extraction from conventional leaching (29.8 wt%) was only marginally higher than that of ultrasonic leaching (27.8 wt%) in the first hour. Standard deviation calculations showed that the difference between the upper bound of ultrasonic leaching (28.7 wt%) and the lower bound of conventional leaching (28.9 wt%) was marginal, which was statistically insignificant ($p > 0.05$). However, for all successive intervals, the recovery via ultrasonic leaching exceeded

conventional leaching and escalated after the 5 h mark. After 10 h, the percentage recovery for the conventional and ultrasonic leaching techniques was 83.2 and 92.7 wt%, respectively. This proves a significant increase in the amount of nickel extracted under ultrasonic treatment, as well as indicating that applying ultrasonic irradiation could accelerate the leaching process, allowing nickel recovery to plateau at a faster rate. It is also interesting to note that with the incorporation of ultrasonic treatment, the same extent of nickel was recovered in 4 h as compared to that of the conventional stirring method in 6 h, hence showing a 2 h, or ca. 30 % of enhancement in nickel recovery using the ultrasonic treatment. This infers that ultrasonic irradiation facilitates and accelerates the solubility and diffusivity action of the acid (Marafi and Stanislaus, 2011), ergo increasing the leaching rate. Moreover, the usage of ultrasound also hastens the reaction kinetics involved in acid leaching, thus minimising the reaction time required (Chang et al., 2017; Oza et al., 2011). Ultrasonic irradiation induces acoustic cavitation in the leaching acid medium, which generates numerous micro-bubbles that collapse in a violent manner, releasing remarkable amounts of energy (Suslick et al., 1999a). In this unique environment, not only does ultrasonic energy result in the intense shear, mixing and distribution of the acid medium, it induces particle fragmentation through inter-particle collisions that effectively breaks apart aggregates and reveals fresh and exposed surfaces. Figure 7.4 illustrates the action and effects of ultrasonic irradiation in the presence of spent catalyst particle surfaces.

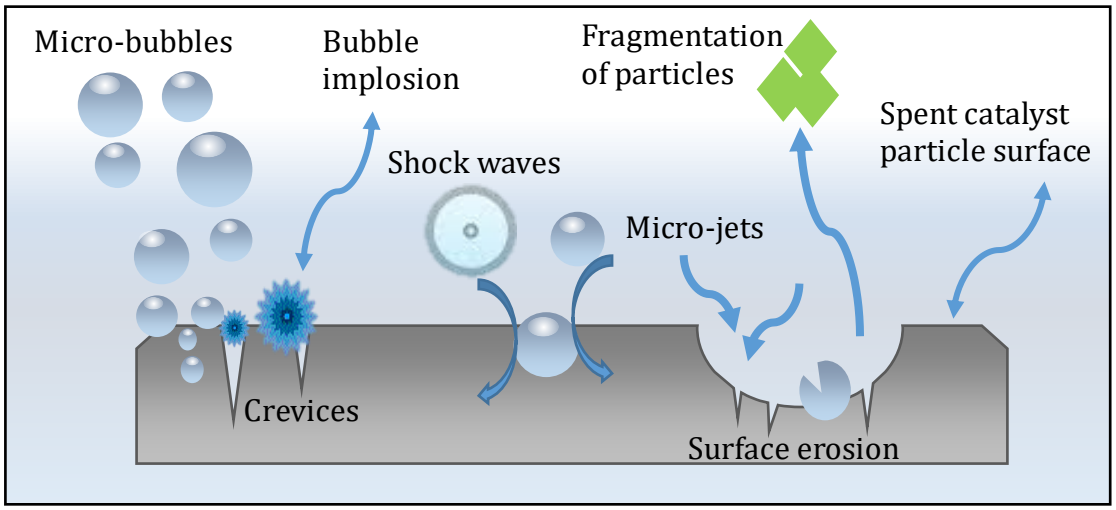


Figure 7.4: Schematic diagram of cavitation events near the surface of spent catalyst particle.

This consequently increases the total contact area between the spent catalyst particles and the leaching reagent (de Castro and Priego Capote, 2007; Kentish and Ashokkumar, 2011). These effects are essential in improving the convective diffusivity of the leaching reagent into the pores of the spent catalyst particles (Marafi and Stanislaus, 2011), thus further allowing the reagent to access porous regions that might be inaccessible via conventional circumstances (Kolosnitsyn et al., 2006). On the other hand, another key feature that enhances the efficiency of ultrasound-assisted leaching is the generation of free-radicals as a result of acoustic cavitation. The generation of free radicals or oxidising species during sonolysis of aqueous solutions is initiated by the thermolysis of water as follows:

$$H_2O \rightarrow_{)))} \cdot OH + \cdot H \qquad \text{Eq. (7.3)}$$

The • OH radicals can react with each other to form hydrogen peroxide:

$$2 \cdot OH \rightarrow H_2O_2 \quad \text{Eq. (7.4)}$$

Both H_2O_2 and •OH radicals are strong oxidants. It is noted that the oxidative energy of these species produced by the sonolysis of the acid solvent drastically improves the efficiency of leaching (de Castro and Priego Capote, 2007). Furthermore, H_2O_2 has been added as a leaching promoter for the recovery of some metals (Ding et al., 2019; Petrovic et al., 2018). In this study, H_2O_2 could be generated as a consequence of acoustic cavitation without the need for an external dosage of the chemical. On the other hand, the sonolysis of HNO_3 in aqueous solutions could occur in the gas phase of cavitation microbubbles and in the liquid shell surrounding the bubbles (Shimizu et al., 2005; Venault et al., 1997), which results in the formation of nitrous acid (HNO_2) as follows:

$$\cdot OH + HNO_3 \rightarrow \cdot NO_3 + H_2O \quad \text{Eq. (7.5)}$$

$$\cdot NO_3 + H_2O \rightarrow NO_2 + H_2O_2 \quad \text{Eq. (7.6)}$$

$$2NO_2 + H_2O \rightarrow HNO_2 + HNO_3 \quad \text{Eq. (7.7)}$$

HNO_2 was investigated by researchers as a by-product in the sonication of nitric acid in aqueous solutions, in which this phenomenon enabled the acceleration of many redox reactions (Nikitenko and Seliverstov, 2000). This could also be the case for this present study, whereby the presence of ultrasound initiated the formation of HNO_2 radicals that facilitated the leaching of Ni. This suggestively demonstrates that ultrasound played both physical and chemical

roles in hastening the leaching process of nickel, permitting the extraction of a higher proportion of nickel in a shorter amount of time.

7.3.4. Effects of temperature on leaching

To assess the effects of temperature on the leaching performance, a series of experiments were conducted at various temperatures with and without sonication, as illustrated in Figure 7.5. Here, the percentage recovery increases with temperature for both leaching methods. Higher temperatures led to greater rates of reaction between the value mineral and the solvent (i.e. spent catalyst and nitric acid). A higher leaching temperature also stipulates that a higher proportion of particles in the medium possess more kinetic energy, hence inter-particle collisions occur at a higher frequency, which consequently accelerates the reactions involved in leaching (Khalid and Athraa, 2017). Nevertheless, it is apparent that incorporating ultrasound into leaching has an appreciable effect on the extent of extraction, in which more nickel is extracted at each temperature investigated, relative to the conventional stirring technique. To illustrate, the ultrasound-assisted technique was able to recover 60.2 wt% of nickel at 70 °C, while the conventional stirring method recovered a mere 39.8 wt% of nickel in 2 h. Calorimetry performed on the ultrasonic bath and hot plate stirring showed that heating power dissipated into the system was 0.0329 W cm^{-3} and 0.0418 W cm^{-3}, respectively. This signifies that more energy was supplied by the hot plate in heating, which denotes that the ultrasonic system was able to extract more Ni at a higher energy efficiency.

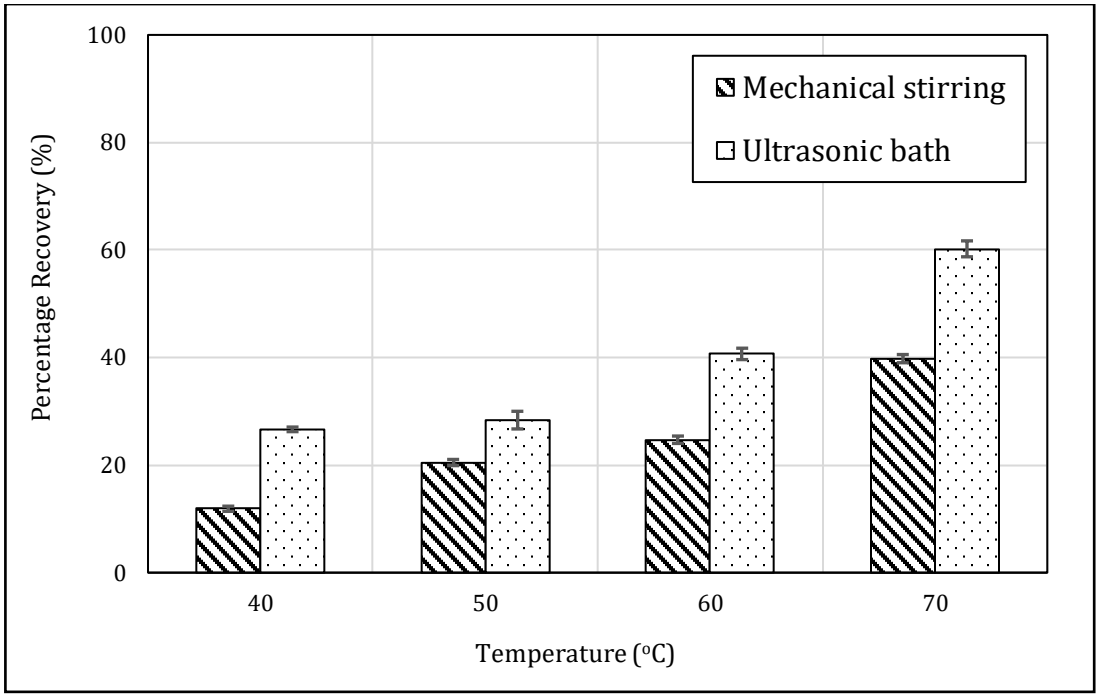


Figure 7.5: Effect of temperature on nickel recovery via ultrasound-assisted nitric acid leaching and conventional mechanical stirring nitric acid leaching (Ultrasonic density = 0.0825 W cm^{-3}).

Over and above that, it is also interesting to note that ultrasound allows a higher nickel recovery at a lower temperature compared to conventional leaching. It is suggested that the additional energy provided by ultrasonic vibrations (Legay et al., 2011; Marshall and Wu, 2015) is sufficient to compensate the difference in kinetic energy possessed by the spent catalyst particles when a lower leaching temperature is concerned. The physical effects (i.e. shock waves and micro-jets) prompted by ultrasonic irradiation led to high-velocity collisions among the solid particles and severe turbulence in the liquid medium on a microscopic level during the leaching process, hence strengthening eddy diffusion (Hou et al., 2015). Chemical effects, i.e. the formation of radicals as mentioned earlier has also facilitated the redox reactions in Ni leaching. The combination of these physical

and chemical effects of ultrasound are said to play a great role in accelerating the leaching process, thus allowing a higher or equal amount of nickel to be extracted while using a lower leaching temperature compared to conventional leaching.

7.3.5. Effects of ultrasonic amplitudes on leaching

Another set of results were acquired to study the extent of extraction by varying the ultrasonic amplitudes from 20 – 100 %, which correspond to the ultrasonic densities in the range of 0.0225 – 0.0825 W cm^{-3}, as indicated in Table 7.3. Figure 7.6 depicts the percentage recovery of each leaching experiment after 2 h at 70 °C, with an extra set obtained via conventional mechanical stirring under the same conditions for comparative purposes. As exhibited in Figure 7.6, it can be confirmed that the increase in ultrasonic density had resulted in an increase in nickel recovery. Nevertheless, it can be seen from Figure 7.6 that the percentage recovery of nickel did not increase linearly with ultrasonic density and only marked differences were observed at higher ultrasonic amplitudes of 80 and 100 %, which correspond to ultrasonic densities of 0.0750 and 0.0825 W cm^{-3}, respectively. It should be noted that a high ultrasonic amplitude does not necessarily correlate to a high ultrasonic efficiency (Kojima et al., 2010; Zisu et al., 2010), which could explain why the increase in ultrasonic density from 0.0750 to 0.0825 W cm^{-3} failed to produce any appreciable enhancement in nickel recovery. While an optimum acoustic power dissipation exists depending on the reactor configuration and application concerned, beyond this optimal point the cavitational activity would be negatively affected due to shielding effects and decoupling losses (Gogate et al., 2011). Meanwhile, the percentage recovery at

lower amplitudes of 40 and 60 % (0.0350 and 0.0525 W cm^{-3}) were only slightly higher if not comparable to that of mechanical stirring. Moreover, an ultrasonic amplitude of 20 % (0.0225 W cm^{-3}) resulted in a lower percentage recovery than that of the mechanical stirring technique.

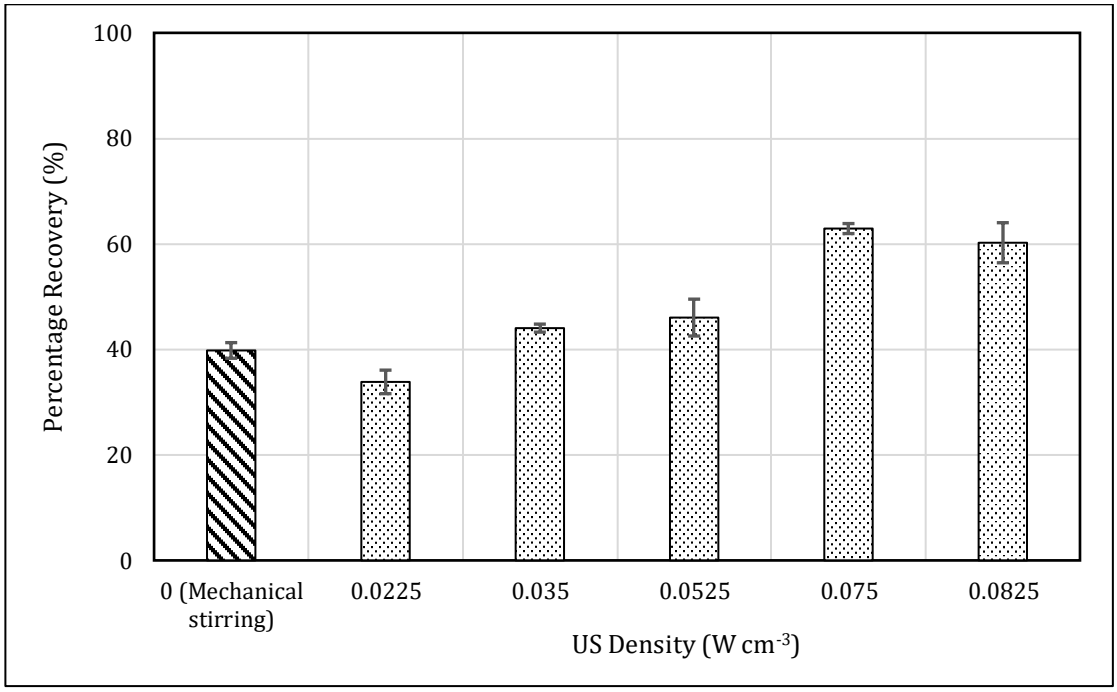


Figure 7.6: Effect of ultrasonic amplitude on nickel recovery via ultrasound-assisted nitric acid leaching with conventional mechanical stirring (500 rpm) nitric acid leaching as a reference (Temperature = 70 °C).

Accordingly, the bubble collapse time, temperature and pressure during bubble collapse are all dependent on acoustic amplitude. Hence, the implosion of each cavitation bubble will be progressively violent with the rise in acoustic intensity, which in most cases bring about enhanced physical consequences in and surrounding the imploding bubble (Adewuyi, 2001; Luche, 1998). However, it is postulated that at low ultrasonic densities of 0.0225 – 0.0525 W cm^{-3} such as those described previously, the cavitation and physical consequences produced by the

ultrasonic transducer were not sufficient to bring about any enhanced leaching effects, relative to the effects caused by mechanical stirring (Cabrera-Trujillo et al., 2016; Merouani et al., 2013). Particularly, this observed phenomenon may be due to the limitations of acoustic streaming when the acoustic waves produced at low amplitudes were below the Blake's threshold, as the bubbles generated were more quasistatically stable (Harkin et al., 1999). Similarly, this could also result in a lower extent of chemical effects, in which the formation of radicals was more limited, leading to lower leaching efficiencies. On the other hand, the noticeable improvement in percentage recovery was observed at higher ultrasonic density range of 0.0750 – 0.0825 W cm^{-3} may indicate the violent sonochemical effects in the ultrasonic bath catered by the formation of transient cavitation. Similarly, radical formation and chain reactions were enhanced due to the intensified chemical effects produced at higher ultrasonic densities. This was also supplemented by the violent collapse of micro-bubbles, production of micro-jets and shockwaves, which all led to elevated magnitudes of physical disruption to the diffusion layer on the particle surface (de Castro and Priego Capote, 2007). Subsequently, a larger amount of leaching reagent was propelled further into the tiny crevices of the spent catalyst particles, hence ejecting confined Ni phases more effectively. Likewise, with the combination of increased pressure, temperature and velocity ensuing from increased ultrasonic intensity, the micro-jets were more efficient in dislodging the nickel crystallites from their substrate in a way that reattachment to the silica support will not arise (Oza et al., 2011), ultimately increasing the percentage recovery of nickel in a more pronounced manner.

7.3.6. Comparison of nitric acid and sulphuric acid for nickel leaching from spent catalyst

Sulphuric acid was used in place of nitric acid to compare their effectiveness as leaching reagents, with remaining experimental conditions unaltered (leaching temperature = 70 °C; leaching time = 2 h; ultrasonic density = 0.0825 W cm^{-3}). Figure 7.7 depicts the percentage recovery of nickel for both conventional and ultrasonic leaching using sulphuric acid at different temperatures. In accord with predictions based on experiments in the previous sections, results from Figure 7.7 further validated the hypothesis that ultrasound has indeed played role in enhancing the leaching of nickel from spent catalysts, notwithstanding the fact that nitric acid was substituted by sulphuric acid as the leaching reagent. In all three different leaching temperatures, the ultrasonic leaching technique exhibited significantly improved nickel recovery in 2 h, as compared to that of the conventional mechanical stirring method.

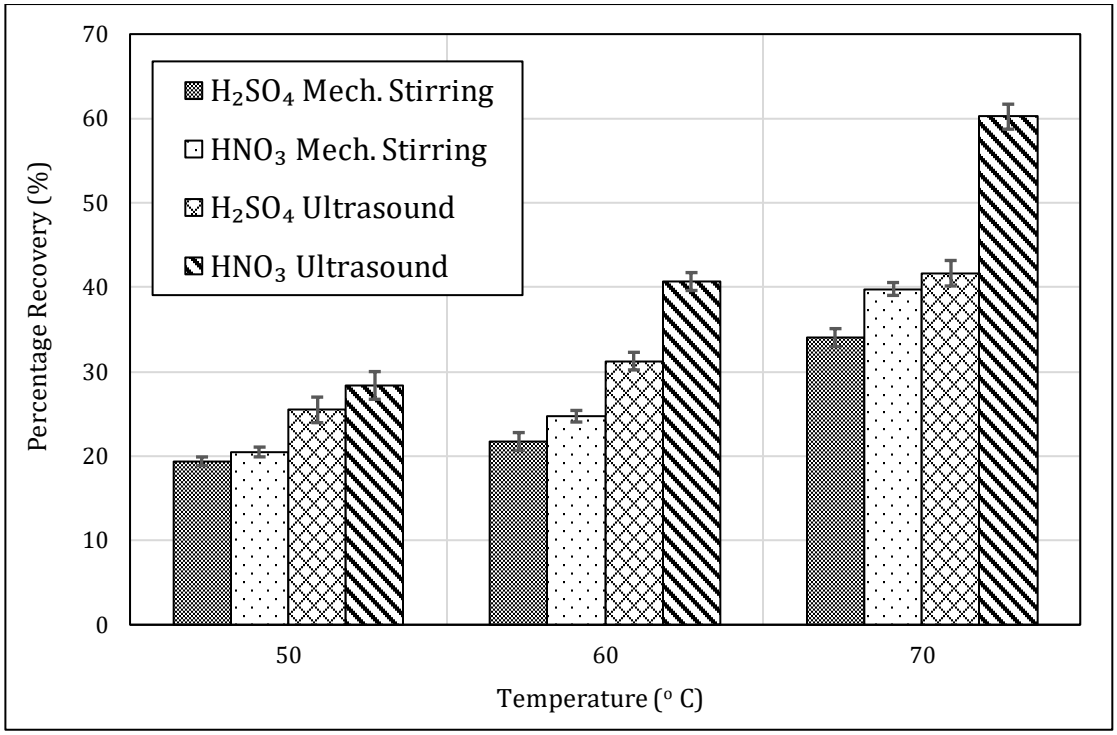


Figure 7.7: Percentage recovery of nickel via ultrasound-assisted leaching (ultrasonic density = 0.0825 W cm^{-3}) and conventional mechanical stirring leaching (500 rpm) with nitric acid and sulphuric acid as the leaching reagents.

Figure 7.7 also showed the difference in percentage recovery for nickel when sulphuric acid and nitric acid were used as leaching reagents in both ultrasonic irradiation and conventional mechanical stirring techniques. Sulphuric acid, being a diprotic acid, dissociates into two moles of hydrogen ions and one mole of sulphate ion in an aqueous solution, in comparison to the dissociation of nitric acid to form a mole of hydrogen and nitrate. It was discovered that, however, sulphuric acid had a weaker performance as a leaching reagent compared to nitric acid, in which experiments employing sulphuric acid had a significantly weaker effect on nickel extraction. It is deduced that sulphuric acid, albeit a diprotic acid that supplies twice as many hydrogen ions as nitric acid, generates sulphate ions that are weaker than nitrate ions in terms of their oxidising ability (Wulfsberg,

2000). In addition, investigations carried out by researchers have indicated that the nitrate ion is indeed a relatively stronger oxidising agent than the sulphate ion. In particular, rate of reactions were accelerated in the presence of nitrate ions and on the other hand, sulphate ions prominently diminished the efficiency of certain oxidation processes (De Laat et al., 2004; El-Naggar, 2006; Lipczynska-Kochany et al., 1995). To further illustrate, the nitrate ion (+0.80 V) is located far below the sulphate ion (+0.17 V) on the standard electrode potential series, which represents the stronger oxidising ability of the former compared to that of the latter. On the other hand, sonicating aqueous nitric acid results in the sonochemical formation of nitrous acid due to the degradation of nitrate ions in the liquid reaction zone surrounding the cavitation bubbles, as mentioned previously (Dalodière et al., 2016; Venault et al., 1997). Studies have also shown that the presence of nitrous acid in a low concentration acted as a catalyst in oxidation reactions, which helped in the extraction of metals (Nikitenko et al., 1999). As nickel leaching is an oxidation process, the synergistic effect between ultrasound and nitric acid resulted in the enhanced recovery of nickel. Hence, in this case, it is suggested that the nitrate ions are in fact far more effective in oxidising nickel from the spent catalyst, forming the nickel nitrate, $Ni(NO_3)_2$, leach solution.

One other contributing factor to the desirable performance of nitric acid upon sonication may be its lower cavitation threshold due to the differences in viscosity between the two acids involved (Santos et al., 2009). Under the same conditions of 20 °C and at 60 wt% concentration, nitric acid and sulphuric acid have viscosities of 2.5 and 6 cP, respectively (Liley et al., 1999). This suggests that sulphuric acid possesses higher acoustic cavitation threshold as compared to nitric

acid, which in turn lowers the extent of acoustic cavitation in sulphuric acid under the same operating conditions. In other words, the viscosity of the solvent in question has a substantial influence on the cavitation phenomenon – the stronger the cohesive forces between the molecules in a solvent, the tougher it is for the acoustic waves to instigate cavitation in the solvent (Ali et al., 2014). The equation below shows the relationship between the acoustic cavitation threshold and the fluid viscosity (Louisnard, 2012):

$$\frac{\partial}{\partial t}(K_l + 4\pi R^2\sigma) = -16\pi\mu_l\dot{R}R^2 - p\frac{\partial V}{\partial t} + p_g\frac{\partial V}{\partial t} \qquad \text{Eq. (7.8)}$$

In this equation, the term on the LHS represents the sum of kinetic energy and potential energy of the radially moving liquid, or the energy dissipated per acoustic bubble. The first term of the RHS of the equation represent the acoustic power irreversibly lost due to the viscous friction forces within the solvent (note the negative sign of the term). Therefore, this signifies that more acoustic energy is lost as a result of the solvent possessing a higher viscosity.

With this, it is safe to deduce that, under the influence of power ultrasound, the nitric acid solution is more capable of producing more transient cavitation, which subsequently collapses to form micro-jets onto the surface of the catalyst samples, resulting in improved nickel recovery.

7.3.7. Characterisation of spent catalyst and leach residues

Characterisation (XRD, FE-SEM, EDX and FT-IR) of the spent catalyst and leach residues for both ultrasound-assisted leaching and conventional mechanical stirring were carried out to assess and compare their characteristics before and after leaching. The XRD patterns (Figure 7.8) of the spent catalyst and leaching residues for ultrasound-assisted leaching and conventional leaching display no major differences in their compositions. The increase in intensity of the peak at 22 ^{o} observed in the XRD plots (b) and (c) indicated that the proportion of SiO_2 in the leach residues had increased after leaching, which in turn confirms the loss of nickel due to the leaching process. Furthermore, the broadness of peaks at 37, 43 and 63 ^{o} decreased after leaching for both leaching methods, representing the increase in crystallite size (Jian and Hejing, 2003) as shown in the insets of Figure 7.8.

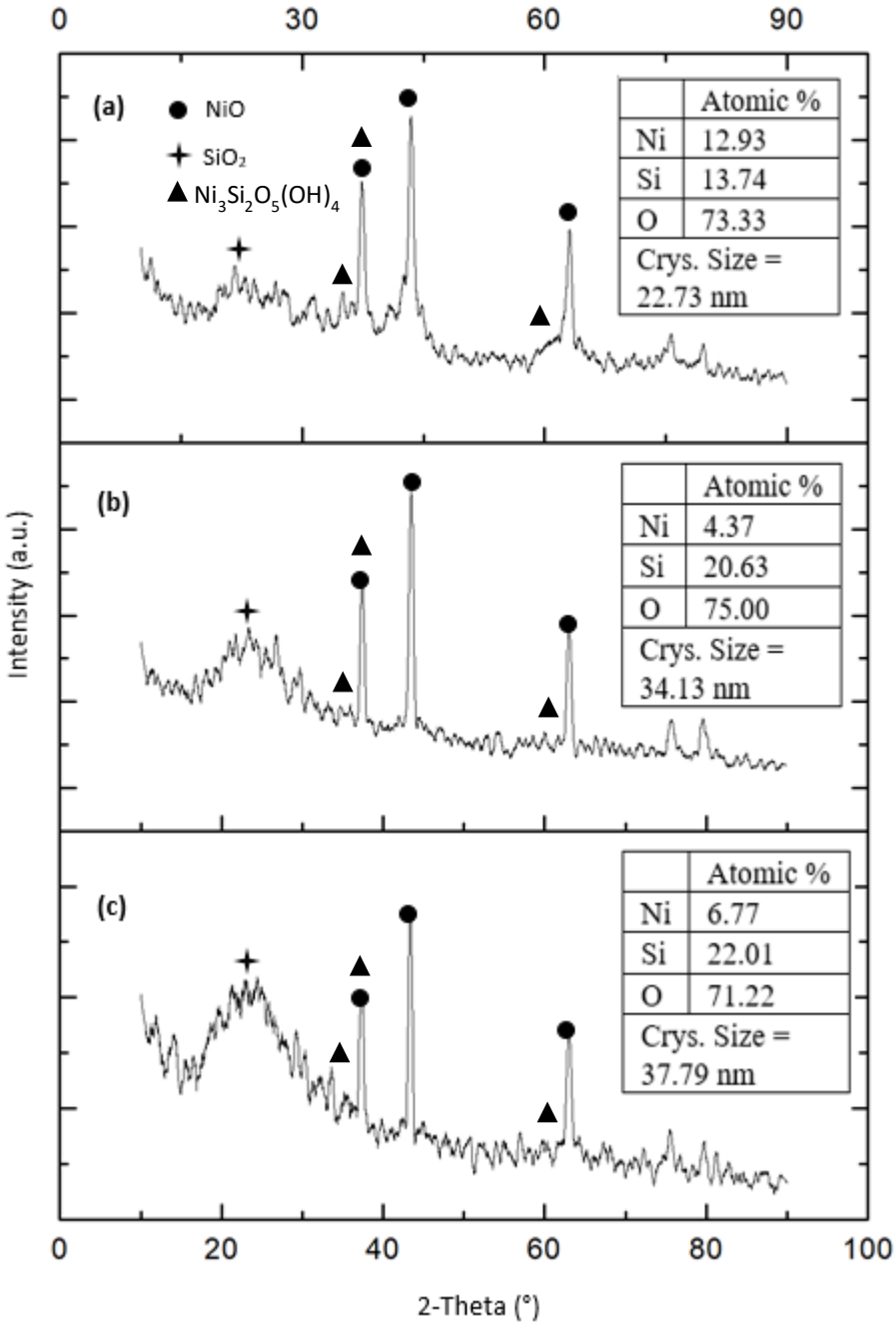


Figure 7.8: XRD diffractograms for (a) spent catalyst; (b) ultrasonic leaching residue at US density = 0.0825 W cm^{-3}; and (c) conventional leaching residue, with their corresponding compounds at specific peaks.

Note: Insets contain elemental composition and crystallite size.

The increase in crystallite size from 22.73 nm to 34.13 nm for the ultrasonic leaching residue and to 37.79 nm for the conventional leaching residue could be

attributed to the acidic environment during leaching. The dissolution of silica would occur, followed by the growth of larger phases at the expense of silica monomers through condensation (Otterstedt and Brandreth, 1998) to form larger silicate species, which may also simultaneously contribute to the enlargement of the Ni phase crystallites. The first step involves the protonation of the dissolved silica species:

$$2 \equiv \mathrm{Si} - \mathrm{O}^- + 2\,\mathrm{H}^+ \rightarrow 2 \equiv \mathrm{Si} - \mathrm{OH} \qquad \text{Eq. (7.9)}$$

Followed by condensation to form larger silicate species:

$$2 \equiv \mathrm{Si} - \mathrm{OH} \rightarrow \equiv \mathrm{Si} - \mathrm{O} - \mathrm{Si} \equiv + \mathrm{H_2O} \qquad \text{Eq. (7.10)}$$

where ≡ Si represents a silicon atom that is bound to four oxygen atoms.

At lower pH conditions such as the acidic environment in this study, the species carry little or no charge and are not stabilised by electric repulsion. Therefore, growth of the siliceous network is dominated by larger units connecting to one another (Hanefeld and Lefferts, 2017). This leads to events of silica polymerisation and the subsequent aggregation of silica phases, resulting in the structural growth of amorphous silica, which can be observed by the increased presence of the 22 ° peak in the XRD plots of Figures 7.8(b) and (c), thus leading to increased sizes after leaching was terminated (Gorrepati et al., 2010; Lunevich, 2020).

To verify this, the IR spectra of the spent catalyst and leach residues are depicted in Figure 7.9. The wavelength range of 1200 – 800 cm^{-1} is shown as it represents the fingerprint region for the different states of silicate, in which the extent of silicate connectivity is represented by the notation Q^x (Jansson et al., 2015). In this terminology, X ranges from 0 – 4 and signifies the number of neighbouring Si atom(s) connected to a SiO_4^{4-} tetrahedron via the oxygen atom. It can be seen that the spent catalyst has a prominent band ca. 1050 cm^{-1}, which is attributed to the silica species of the Q^3 silica environment, denoting large silicate structures with three Si-O-Si bridges (Vidal et al., 2016). In the leaching residues for both ultrasonic and conventional leaching, it can be observed that the main Q^3 absorbance band experienced a shift to higher wavenumbers of ca. 1075 cm^{-1} and an increase in intensity, indicating the increase in polymerisation and the size of structural silica units (Jansson et al., 2015), congruent with the increase in crystallite sizes obtained. Furthermore, absorbance bands at the wavenumbers of ca. 800 and 950 cm^{-1} have also appeared to increase in intensity, which represents silica species of the Q^0 and Q^1 configurations, respectively. The presence of such bands indicates the formation of smaller silicate structures, most likely from the dissolution of the silica support, which subsequently undergo condensation to form larger silicate structures, as mentioned previously. In addition, this also suggests that the ultrasonic treatment did not affect the restructuring of the silica support, whereby both ultrasonic and conventional leaching methods lead to similar residue structural properties.

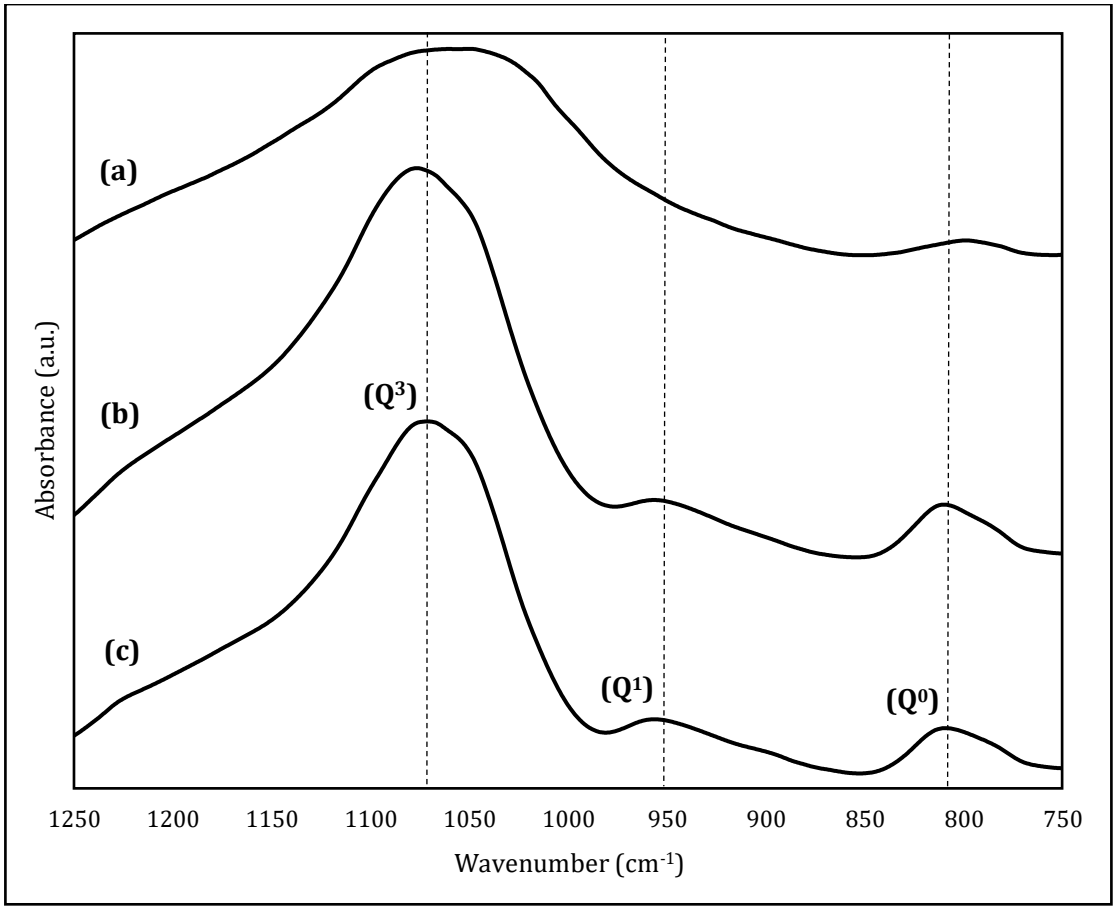


Figure 7.9: FT-IR spectra of (a) spent catalyst; (b) ultrasonic leaching residue at US density = 0.0825 W cm^{-3} and (c) conventional leaching.

Nevertheless, it was revealed that the crystallite size for the ultrasound-assisted leaching residue (34.13 nm) was comparatively smaller than that of the conventional leaching residue (37.79 nm), which vindicated the role of ultrasound in initiating the de-aggregation of the spent catalyst with a higher total specific surface area through surface pitting (Jiang et al., 2018). This phenomenon corresponded to a higher contact area between the spent catalyst and leaching reagent, which consequently enhanced the leaching of nickel, corroborating with the results obtained in Figures 7.3, 7.5, 7.6 and 7.7.

SEM scans exhibited in Figure 7.10 evidently depict the aforementioned effects of ultrasound, whereby particles in scan (C), leached in a conventional method, presented a higher degree of agglomeration as compared to that of the particles in scan (B), which were leached in the presence of ultrasound. Moreover, particles in scan (B) demonstrated a higher degree of uniformity, which is a direct result of ultrasonic irradiation. Furthermore, elemental compositions obtained through EDX analysis (see insets of Figure 7.8) denoted that the decrease in nickel content of the leach residues after ultrasonic leaching was more substantial than that of conventional leaching, which further vindicated the enhancement of nickel leaching via ultrasonic irradiation.

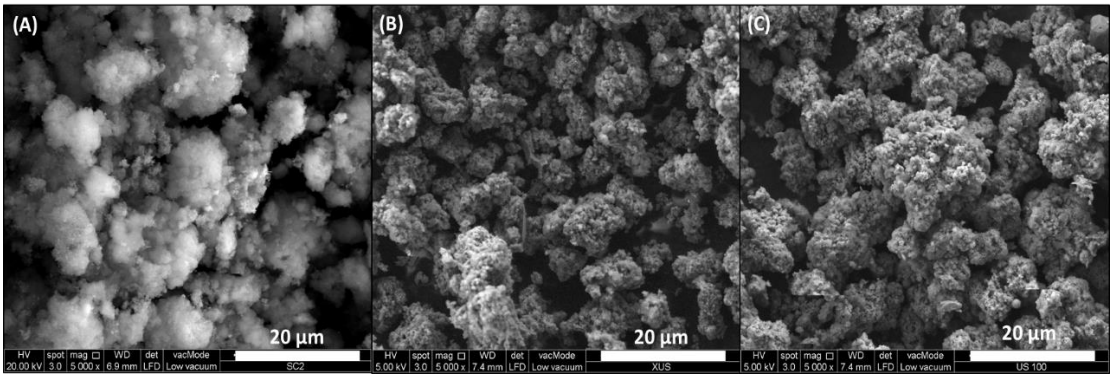


Figure 7.10: SEM images for (A) spent catalyst; (B) ultrasonic leaching residue at US density = 0.0825 W cm^{-3}; and (C) conventional leaching residue.

Note: Scans are of 5,000x magnification with a 20 µm scale provided.

7.3.8. Model validation and statistical analysis

As evidenced by the previous sections, the application of ultrasound to the acid leaching of Ni from spent catalysts has brought about profound and positive impacts on the recovery. Moving forward, the process optimisation for ultrasonic

leaching was attempted using the response surface methodology in order to achieve the maximum recovery attainable. The analysis of variance (ANOVA) was carried out and the results are presented in Table 7.4. In this case, a reduced cubic model was utilised for the response (Ni percentage recovery). The correlation between the four defined parameters and the Ni recovery percentage can be expressed by fitting the experimental data shown in Table 7.2 to Eq. (7.11). Here, a second-order polynomial model representing the relationship between the independent variables and the process response is established as follows:

$$Y = +94 + 0.8779A + 2.5225B - 2.3733C + 3.52D + 0.004406AB - 0.000875AC + 0.002875AD + 0.2078BC - 0.1778BD - 0.063CD - 0.008466A^2 - 0.01399B^2 - 0.1538C^2 + 0.1462D^2 \quad \text{Eq. (7.11)}$$

where:

A, B, C and D are ultrasonic amplitude, leaching temperature, acid concentration and pulp density, respectively.

Predicted Ni percentage recovery for each set was calculated using Eq. (7.11) above and presented in Table 7.2. The formulated model correlated well with the experimental values obtained, in which the residues range from 0.03 – 14.14 %. Here it is noted that the residue is the difference between the predicted and actual data. Furthermore, as evidenced in Figure 7.11(a), the predicted response was in reasonable approximation to the actual response with high correlation.

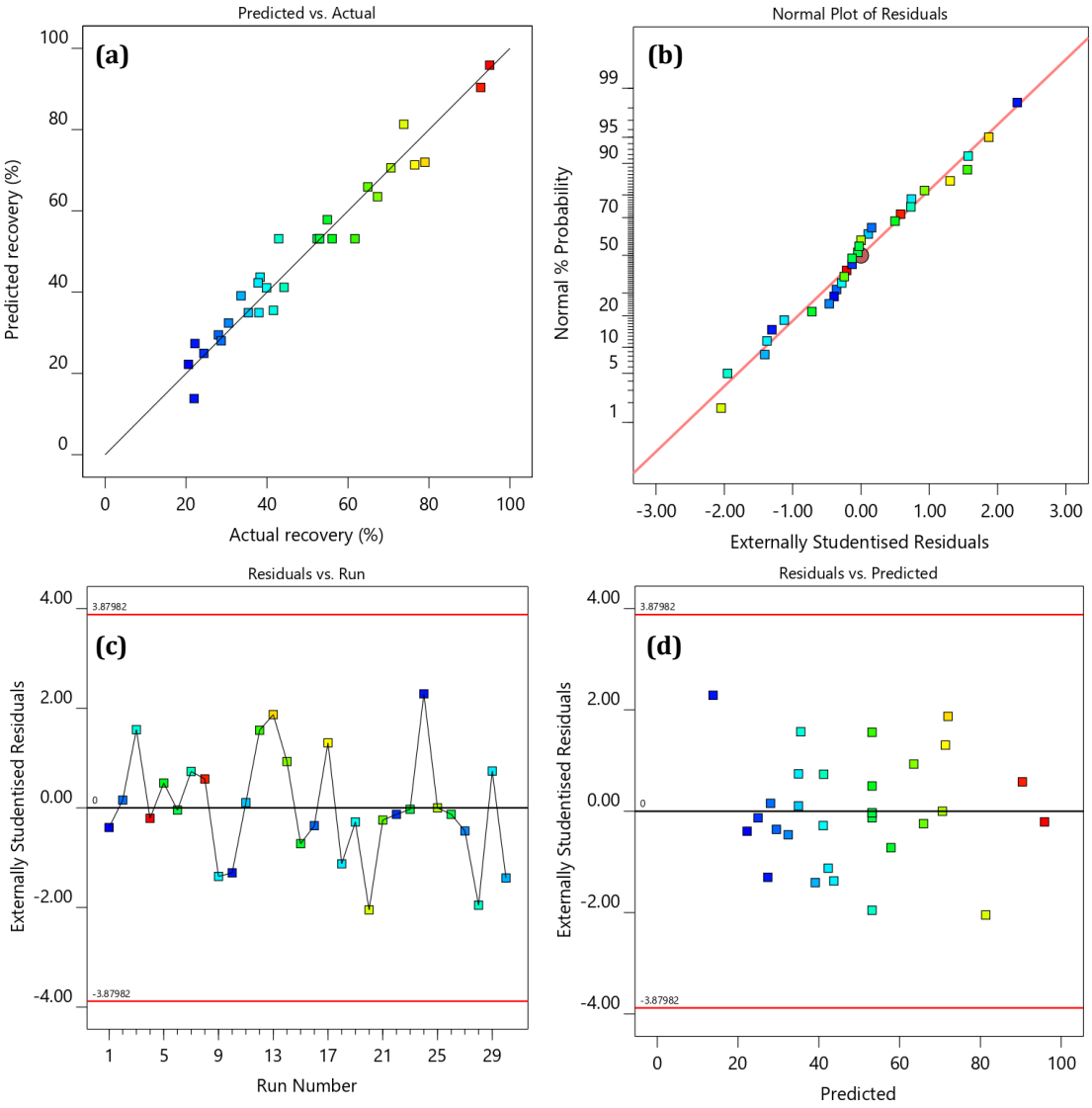


Figure 7.11: Diagnostic plots obtained from Design Expert: (a) predicted vs. actual Ni recovery; (b) internally studentised graph; (c) internally studentised outlier t *plot; (d) studentised residuals and predicted response plot.*

The high R^2 (0.9534) and adjusted R^2 (0.9099) values registered in Table 7.4 show that the model was a positive fit with the experimental results (Esmaeili et al., 2020). In particular, a R^2 value of 0.9534 for the model denotes that 95.34 % of the total variations in the results was caused by the investigated experimental factors (Chauhan et al., 2013b). In theory, the R^2 and adjusted R^2 values should ideally be close to each other to justify the significance of the included terms in the

model, which were also demonstrated in the results of this analysis. A general rule of thumb suggests that the adjusted and predicted R^2 values should be within 0.2 of each other, which was also adequately achieved by this study (0.9099 vs. 0.7955). It is also worth noting that the "lack-of-fit" was statistically not significant, indicating a good model fit (Asfaram et al., 2015). Therefore, this authenticated the applicability of the model used as per Eq. (7.11) for the ultrasonic leaching of Ni. On the other hand, the statistical significance of the model is set at 95 % confidence level as indexed by its p-value ($p < 0.05.$) (Arabi et al., 2016; Ghaedi et al., 2015). It should be noted that a decrease in p-value signifies the increase in significance of the corresponding model term. Moreover, the adequate precision, stipulated by the signal to noise (S/N) ratio, is highly recommended to be higher than 4. This current study presented a S/N ratio of 18.49, which was far higher than the typical threshold of 4. Hence, this characterised an adequate response signal and that the proposed model was highly appropriate in navigating the design space (Sharahi and Shahbazi, 2017).

To further validate the accuracy and predictability of the model, the diagnostic plots acquired were studied. In particular, the distribution of the residuals was investigated via ascertaining the normal distribution. Residues are projected to adhere to the normal distribution line if the experimental errors were random. In brief, with respect to the standard deviation, residuals were first normalised. This was followed by fitting the studentised residuals to a normal distribution function. Lastly, the studentised residual predicted by the best fit normal distribution was plotted against the studentised residual acquired from the experiments, as shown in Figure 7.11(b). It can be observed that the plot exhibited

a good linear fit without any significant deviations from the line, which further substantiated the accuracy of the predicted model and that the error terms followed a normal distribution (Karri and Sahu, 2018; Mallaiah and Reddy, 2016a).

In Figure 7.11(c), the outlier *t* plot is displayed for all 30 experimental sets carried out in this study. These findings allow an experimentalist to identify the occurrence of residuals with a large magnitude, if any. Generally, provided that the residuals are situated within the interval of ± 3.0 %, it can be said that the model and experimental data are free from potential or operational errors (Mallaiah and Reddy, 2016b). In this case, all the experimental data obtained fell within the range of ± 2.0 %, which indicated that the model was congruous with all data.

Figure 7.11(d) plots the internally studentised residuals against the predicted Ni percentage recovery. In the case whereby the residuals are not dependent on the response value, the plot will be randomly scattered around zero deviation, as acquired in this study, thus confirming the assumption of linearity (Chauhan et al., 2013b). Furthermore, all points lie within the satisfactory range of ± 3.0 %, ruling out the presence of systematic errors. Hence, this evidenced the alteration of response variables was not required and that the model proposed was highly reliable (Beiramzadeh et al., 2019).

Therefore, through the ANOVA results and diagnostic plots acquired, the developed model in this present study could be satisfactorily utilised to describe the ultrasonic leaching and recovery of Ni from spent catalysts, with a 95 % confidence interval.

Table 7.4: ANOVA results for the model developed for the ultrasonic leaching of Ni from spent catalysts.

Source	**Sum of squares**	**df**	**Mean square**	**F-value**	**p-value**	**Remark**
Model	12090.86	14	863.63	21.92	< 0.0001	**Significant**
A	100.45	1	100.45	2.55	0.1311	
B	6837.75	1	6837.75	173.58	< 0.0001	
C	2715.75	1	2715.75	68.94	< 0.0001	
D	1262.95	1	1262.95	32.06	< 0.0001	
AB	12.43	1	12.43	0.3154	0.5827	
AC	0.0306	1	0.0306	0.0008	0.9781	
AD	0.3306	1	0.3306	0.0084	0.9282	
BC	431.60	1	431.60	10.96	0.0048	
BD	315.95	1	315.95	8.02	0.0126	
CD	2.48	1	2.48	0.0630	0.8053	
A^2	314.55	1	314.55	7.99	0.0128	
B^2	53.68	1	53.68	1.36	0.2613	
C^2	25.36	1	25.36	0.6437	0.4349	
D^2	22.89	1	22.89	0.5811	0.4577	
Residual	590.88	15	39.39			
Lack of fit	403.37	10	40.34	1.08	0.4988	**Not significant**
Pure error	187.51	5	37.50			
Std. dev.	6.28			**R^2**	0.9535	
Mean	49.30			**Adjusted R^2**	0.9099	
				Predicted R^2	0.7955	
				Adequate precision	18.49	

7.3.9. Response surface analysis plots and leaching optimisation

Three-dimensional response surface plots of the analysis are depicted in Figure 7.12. Herein, this study could be used to investigate the concurrent interaction between two manipulated factors on Y (Ni percentage recovery), in which the other two factors were controlled at optimal conditions. The interactive impacts of A with B, C and D are depicted in Figures 7.12(a), (b) and (c), respectively. Across all three plots, the ultrasonic amplitude had a relatively subtle

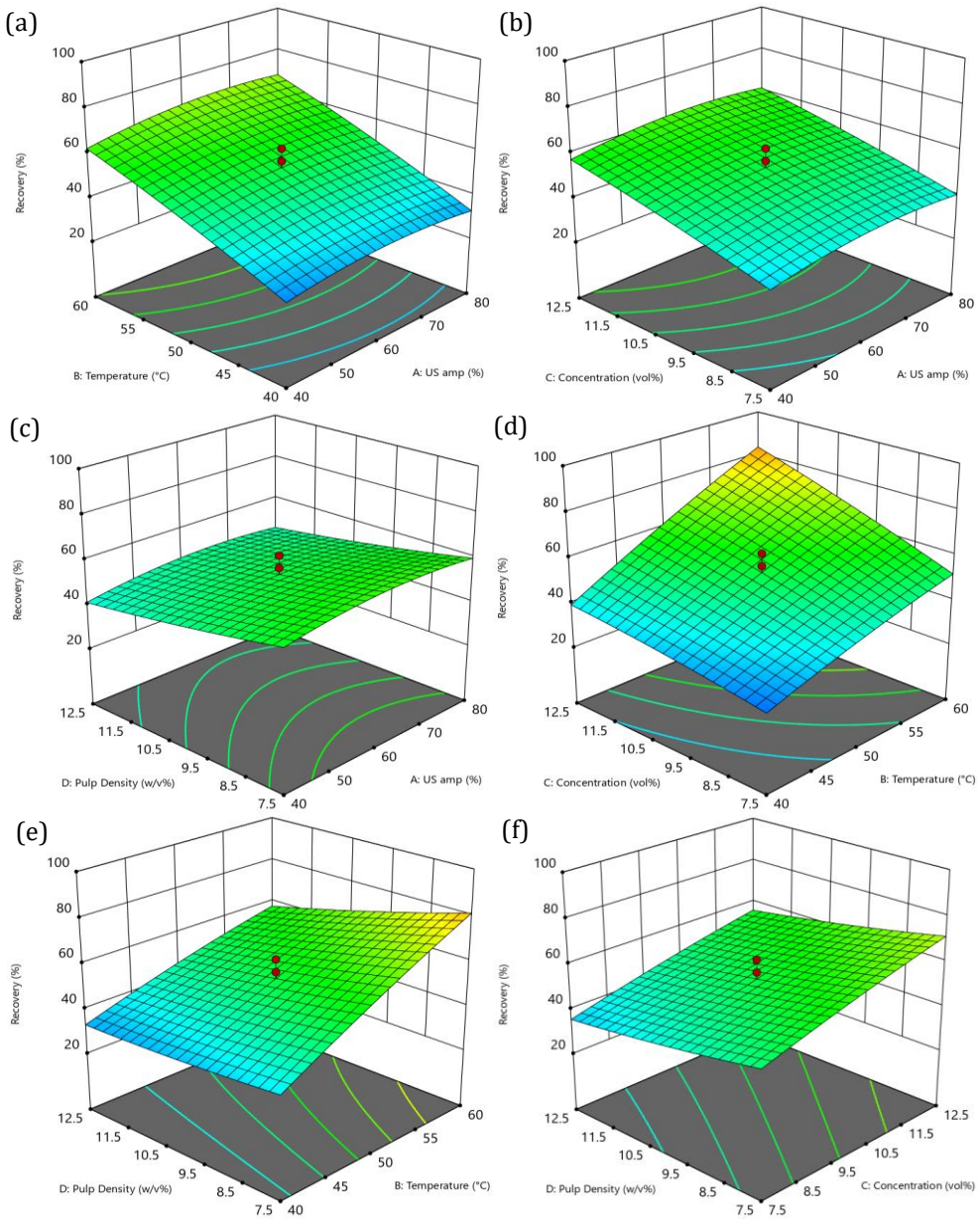


Figure 7.12: Combined effects of (a) ultrasonic amplitude and temperature (acid concentration 10 vol%, pulp density 10 %); (b) ultrasonic amplitude and acid concentration (temperature 50 °C, pulp density 10 %); (c) ultrasonic amplitude and pulp density (temperature 50 °C, acid concentration 10 vol%); (d) temperature and acid concentration (ultrasonic amplitude 60 %, pulp density 10 %); (e) temperature and pulp density (ultrasonic amplitude 60 %, acid concentration 10 vol%); and (f) acid concentration and pulp density (ultrasonic amplitude 60 %, temperature 50 °C) on the Ni percentage recovery.

influence on the Ni recovery, which increases with the amplitude due to the intensified cavitational effects provided by the ultrasonic waves. Maximum recovery can be attained when A > 60 %, B > 50 °C, C > 10 vol% and D < 10 %.

Figures 7.12(a), (d) and (e) demonstrate the influences of B with A, C and D, respectively. Generally, it can be observed that the increase in leaching temperature had a relatively significant influence on the improvement in leaching efficiency, which was also evidenced by the high F-value of B in Table 7.4. Higher temperatures increased the kinetic energy of particles in the leaching solution, effectively enhancing the rate of mass transfer between the leaching acid and particle surface, thus resulting in more Ni recovered. Hence, in this case the most efficient conditions in recovering Ni were A > 60 %, B > 55 °C, C > 11 vol% and D < 8 %.

Figures 7.12(b), (d) and (f) portray the interactions between C with A, B and D, respectively. Generally, the acid concentration had the second largest influence on the overall leaching efficiency, after leaching temperature. In particular, higher acid concentrations resulted in more Ni being recovered due to the increased availability of H^+ ions, which are the oxidising agent in acid leaching. Best recovery was obtained when A > 60 %, B > 55 °C, C > 11 vol% and D < 8 %.

Lastly, Figures 7.12(c), (e) and (f) represent the interaction between D with A, B and C, respectively. With the decrease in pulp density, a lower solid concentration and hence a lower suspension viscosity is achieved. This consequently enabled the improvement in diffusional mass transfer and thus more

leaching acid would be available per unit mass of spent catalyst for reactions to occur, which led to more Ni leached (Esmaeili et al., 2020). Consequently, efficient conditions for highest Ni recovery were A > 60 %, B > 55 °C, C > 12 vol% and D < 8 %.

The Design Expert software is used to establish the optimal ultrasonic leaching parameters to extract the highest possible percentage of Ni from the spent catalysts. The process optimisation was governed by the Derringer's desirability function with the Ni percentage recovery as a response parameter. At the highest desirability number of 0.963 obtained, it was predicted that a Ni percentage recovery of 97.08 % could be attained with the following optimum conditions: ultrasonic amplitude (A) 67 %, temperature (B) 60 °C, acid concentration (C) 12.5 vol% and pulp density (D) 7.5 %. Table 7.5 shows the results of the experimental leaching runs using the aforementioned conditions. It can be seen that the model excellently predicted the Ni percentage recovery with an error margin of 2.29 %. Based on the optimal parameters, the increase in acid concentration to 12.5 vol% and the decrease in pulp density to 7.5 % have also aided in the enhancement of nickel leaching, with the plots of correlation between the parameters highlighted in Figure 7.12. The higher acid concentration resulted in the increased availability of H^+ ions, leading to increased oxidising ability of the leaching agent. On the other hand, the decrease in pulp density enabled improvement in diffusional mass transfer and hence more leaching agent was available per unit mass of spent catalyst for reactions to occur (Esmaeili et al., 2020).

Table 7.5: Optimisation of leaching parameters and results from model validation.

Parameters	**US amplitude (%)**	**Leaching temp. (°C)**	**Acid conc. (vol%)**	**Pulp density (%)**	**Ni percentage recovery (%)**			
					Predicted	Experimental		
						1	2	3
Optimal conditions	67	60	12.5	7.5	97.08	100	98.1	100
						Average: ***99.37***		

7.3.10.Leaching kinetics study

The leaching process can be represented by a heterogeneous system consisting of a leaching reagent (acid) and solid particles (spent catalysts). The reactants in the solid body dissolve into the liquid phase during the leaching process. Any event that occurs between the solid and liquid phases can be ascertained by examining the reaction kinetics and the relationship between various parameters (Çetintaş and Bingöl, 2016). To illustrate, the two most commonly applied models to elucidate the heterogeneous phase reaction are the "shrinking core model" and the "shrinking particle model". The kinetic parameters of the process were analysed using the shrinking core model, which has been vastly studied for solid-liquid systems such as those in this present study (Gharabaghi et al., 2013; He et al., 2011; Parhi et al., 2013). The aforesaid model elucidates the solid-liquid reaction kinetics of dense particles in the most practical manner (Çetintaş and Bingöl, 2016). The rate of reaction for a liquid-solid system is typically governed by either: (1) diffusion through the product layer or (2) chemical reaction at the surface of the particle. The former and latter are otherwise known as diffusion-control and reaction-control, respectively (Rahimi et al., 2020). With respect to the shrinking core model, the leaching process is governed by

either of these two mentioned steps. Steps (1) and (2) can be represented by the following Eqs. (7.12) and (7.13), respectively:

$$1 - 3(1 - X)^{\frac{2}{3}} + 2(1 - X) = k_d t \qquad \text{Eq. (7.12)}$$

$$1 - (1 - X)^{\frac{1}{3}} = k_r t \qquad \text{Eq. (7.13)}$$

where:

X is the percentage recovery (%); k_d is the diffusion-controlled reaction rate constant (min^{-1}); k_r is the reaction-controlled reaction rate constant (min^{-1}); t is the reaction time (min).

In order to classify the fitting governing mechanism, plots of the left-hand side of the equations against time are required to be linear. Experiments were carried out in 360 min and the data were fitted according to the Eqs. (7.12) and (7.13) as demonstrated in Figures 7.13(a) and 7.13(b), respectively. Interestingly, both ultrasonic and non-ultrasonic leaching showed differing kinetic mechanisms, with the former fitting the reaction-controlled mechanism better, whereas the latter fit the diffusion-controlled mechanism well. Therefore, it can be established that chemical reaction is the limiting step for ultrasonic leaching. On the other hand, diffusion is the limiting step for conventional leaching, which is also evidenced by other researchers (Çetintaş and Bingöl, 2016; El-Okazy et al., 2018). One possible explanation for this dissimilarity is the ability of ultrasound to enhance the diffusion of the acid reactant into the spent catalyst pores, thus effectively reducing diffusion-related limitations to a pronounced extent.

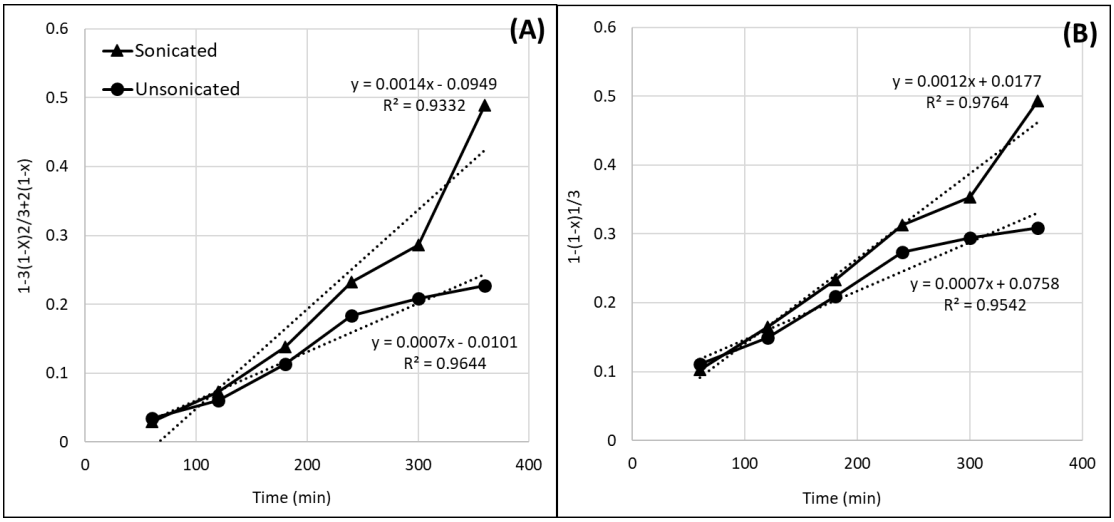


Figure 7.13: Shrinking core model with (a) diffusion control and (b) reaction control.

Table 7.6 includes the comparison of Ni percentage recovery obtained in this present work to those from the literature, with relevant process parameters stated. In comparison to other techniques including those utilising ultrasonic technology, this work presents enhanced Ni leaching efficiency. In addition, mild operating conditions such as low temperature and acid concentration were successfully applied in this work. Leaching studies obtained from the literature required longer reaction times compared to the present study, excluding those of Oza et. al (2011), which was achieved in 50 min. Nevertheless, it should be noted that the leaching conditions used in the aforesaid study were extremely rigorous. In particular, the combined usage of an energy-intensive ultrasonic probe with high reaction temperatures of 90 °C and high acid concentrations of 40 vol% is generally unfavourable for large scale industrial operations. These conditions would be less cost effective while posing serious safety issues. Furthermore, a concentrated acidic solution will severely corrode the ultrasonic probe due to direct contact, thus necessitating periodic replacements as well as complicating

the leaching process due to metal contamination from the probe (Retamal Marín et al., 2018; Santos et al., 2009). Contrariwise, these issues could be eliminated by using an ultrasonic bath as per this present study, which provides indirect contact between the ultrasonic source and the target solution, which is more suited for large-scale operations (Sancheti and Gogate, 2017b). Therefore, nickel recovery employing an ultrasonic bath proves to be an effective technique for the near-total recovery of useful metals, which could potentially be extended to an industrial scale.

Table 7.6: Comparison of Ni recoveries of this present work with relevant investigations from the literature.

No.	Usage of ultrasound and/or technique	Leaching temp. (°C)	Leaching agent and conc.	Pulp density (%)	Leaching duration (min)	Ni recovery (%)	Reference
1	Yes (ultrasonic probe, 30 kHz)	90	HNO_3, 40 vol%	10	50	95	(Oza et al., 2011)
2	Yes (ultrasonic bath, 43 kHz)	60	Citric acid, 10 vol%	2.5	360	95	(Marafi and Stanislaus, 2011)
3	No (conventional stirring)	65	HNO_3, 50 vol%	33	120	85	(Ramos-Cano et al., 2016)
4	No (conventional stirring)	80	Formic acid, 0.6 M	10	90	94	(Arslanoğlu and Yaraş, 2019)
5	No (conventional stirring)	80	HNO_3, 40 vol%	2	240	94	(Khalid and Athraa, 2017)
6	No (sequential NaOH-HCl leaching)	91.1	NaOH 1.06 M; HCl, 4.0 M	6.67	180	95.4	(Moosakazemi et al., 2020)
7	No (chelation with EDTA [a])	150	EDTA, 0.8 M	5	240	95	(Vuyyuru et al., 2010)
8	No (chelation with EDDS [b])	90	EDDS, molar ratio: 3.6	5	360	84	(Chauhan et al., 2012)
9	Yes (ultrasonic bath)	60	HNO_3, 12.5 vol%	7.5	120	99.4	This work

[a] Ethylenediaminetetraacetic acid
[b] Ethylenediamine-*N*,*N*'-disuccinic acid

7.3.11.Process analysis

An economic analysis was carried out to evaluate the overall and approximate cost of nickel recovery in this study. The spent catalysts can be obtained from Malaysian governmental sources of scheduled wastes (SW 204) or industrial sources such as nickel hydrogenation process plants. According to Table

7.7, the cost of processing and recovering 1 kg of spent catalysts is calculated to be USD 141.1. However, it should be noted that this is an approximate for lab-scale operations, without taking into account the difficulty of scaling up ultrasonic reactors and the subsequent complex purification steps required before the crystals can be sold for further utilisation. Nevertheless, the base commercial price for nickel nitrate hexahydrate crystals is included in Table 7.7 for comparison purposes.

As the nickel nitrate discussed in this thesis is not purified, therefore its pricing could be estimated at ca. USD 60 per kg. The recovered and purified nickel nitrate crystals can be used in various applications such as the synthesis of nickel-based catalysts or as catalyst dopants and promoters, the manufacture of nickel plates for nickel-cadmium batteries or for general laboratory usage.

Table 7.7: Economic analysis for recycling 1 kg of spent Ni hydrogenation catalysts.

Note: Calculated based on the price in March 2021.

	Reagents	Dosage [a] (L)	Price [b] (USD/L)	Cost (USD)
Reagent cost	HNO_3	1.97	4.56	-8.98
	H_2O	11.4	0.000553	-0.00630
	Total			**-8.986**
	Procedure	Energy consumption [a] (kWh)	Price [b] (USD/kWh^{-1})	Cost (USD)
Energy cost	Ultrasonic leaching	1601	0.082	-131.3
	Calcination	8.10	0.082	-0.664
	Evaporation	1.2	0.082	-0.0984
	Total			**-132.1**
	Product	Mass [c] (kg)	Commercial price (USD/kg)	Cost (USD)
Revenue	$Ni(NO_3)_2.6H_2O$ (Nickel nitrate hexahydrate crystals)	3.20	60	192
	Total			
Total profit				**USD 50.9**

[a] Scaled up to process 1 kg of spent catalyst.
[b] Prices were calculated based on commercial/industrial tariffs in Malaysia.
[c] Assuming total crystallisation of nickel nitrate crystals calculated with nickel recovery rate of 99.4 %.

7.4. Concluding remarks

In this current chapter, the positive effects of incorporating ultrasound into acid leaching for the recovery of nickel from spent silica-supported nickel hydrogenation catalysts were identified and presented. Compared to the

conventional mechanical stirring acid leaching technique, the ultrasonic leaching method was more effective for the extraction of nickel in all experiments conducted. The extent of agglomeration of the spent catalyst particles was greatly diminished under sonicated conditions, resulting in new exposed surfaces, hence increasing the total contact area for leaching to occur. Furthermore, HNO_3 was found to be more effective than H_2SO_4 in terms of its leaching and oxidising ability.

Overall, this work has successfully demonstrated the role of ultrasound in the recovery of spent nickel catalysts, as well as successfully formed nickel salt crystals for further applications, which is beneficial for relevant industries that are keen on process sustainability. In addition, the optimum conditions for ultrasonic leaching proposed via CCD are ultrasonic bath amplitude = 67 %, temperature = 60 °C, acid concentration = 12.5 vol% and pulp density = 7.5 %. The proposed model with a high value of regression coefficient (R^2 > 0.95) excellently demonstrated the interactive influences of ultrasonic density, temperature, acid concentration and pulp density on the Ni recovery percentage, leading to an optimal Ni recovery of 99.37 % in 2 h. Lastly, an economic analysis was performed to approximate the overall recovery cost of recovering nickel via the ultrasonic method introduced in this study.

These results could potentially provide useful insights and incentives into future developments concerning the employment of ultrasonic technology to intensify leaching processes on an industrial scale. As nickel catalysts are high in demand for certain critical industries such as the oleochemical sector, the amount of solid waste generated from such sources would also be substantial, which

necessitate appropriate and efficient waste processing techniques. One of the potential applications of this study could be the incorporation of an ultrasound-assisted nickel salt recovery process into chemical processing plants that involve nickel-based catalysts. For instance, a nickel recovery unit could be designed and fitted into a nickel catalyst manufacturing plant, whereby after further purification the nickel salts recovered from solid wastes (i.e. spent nickel catalysts) could then be recycled and reused as raw materials for the subsequent production of fresh nickel catalysts, thus posing an attractive waste-to-resource initiative.

8. Conclusions and Recommendations for Future Work

8.1. Conclusions

The investigations detailed in this thesis pertained to the development of nickel-based heterogeneous hydrogenation catalysts as a central theme. For the breakdown and brief description of the individual chapters, please refer to Section 1.11.

In *Chapter 3*, the deactivation of nickel catalysts in the hydrogenation of various liquid organic media was studied. The results have indicated that the principal deactivation mechanisms involved in the hydrogenation of palm-based liquid organic media are lixiviation and poisoning. In acidic feeds such as the S-RBD-PS and distilled fatty acid blend, the dissociated fatty acid molecules in the reactant had a greater tendency to form nickel soap with the active nickel phases present in the catalysts. Therefore, the concentration of dissolved nickel in the reactant was prominent, with up to 8-fold increase in dissolved nickel concentration in S-RBD-PS products as determined by AAS, thus increasing the extent of catalyst deactivation due to the loss of active sites. On the other hand, catalyst poisoning also played a substantial role in dictating catalytic activity. Dirtier feeds such as the S-RBD-PS and RBD-PS contained much higher levels of catalyst poisons such as S, N, P and Cl compared to the cleaner distilled fatty acid blend feed. Such poisons chemisorb and bind with the catalyst active sites, consequently eliminating effective active sites and lowering the catalytic activity.

Silica-supported nickel catalysts were synthesised and characterised in *Chapter 4*. The introduction of an alkali metal, Mg, as a catalyst promoter improved the catalyst properties by increasing the BET surface area, pore volume and metal-support interaction via TPR experiments, thus the increase in metal surface area and dispersion were also observed. In this chapter, the incorporation of ultrasonic irradiation into the sequential precipitation of the catalysts was also studied. Mechanistic studies indicated that ultrasonic irradiation during ageing had profound influences on the catalyst compositions, directly affecting the formation of silica clusters, hydroxycarbonates and Ni silicates. Observed changes were the erosion of hydroxycarbonates phases and the suppression of silica clusters, resulting in greater Ni dispersion, surface area and reducibility, as well as alterations to the geometrical and electronic properties of the catalysts.

Chapter 5 presents a further continuation of the study described in *Chapter 4*, in which the sonicated catalysts were employed in the partial hydrogenation of sunflower oil to ascertain their catalytic performance. The partial hydrogenation experiments determined that the presence of ultrasonic irradiation during catalyst ageing enhanced the catalytic activity and selectivity. An ultrasonic intensity of 20.78 W cm^{-2} resulted in a 22.6 % increase in hydrogenation activity, along with a 28.5 % decrease in *trans*-C18:1 yield at IV = 70. In particular, the usage of ultrasonic irradiation prompted the modification of product selectivity by shifting the electron density and subsequently the adsorption capability of the active nickel species with hydrogenation intermediates, thus leading to a lower production of *trans*-fats using the sonicated nickel catalysts.

Chapter 6 presents a characterisation study of nickel-silica composites synthesised via two different ultrasonic synthesis configurations. Particularly, ultrasonic irradiation was incorporated into two different stages of the synthesis: the co-precipitation stage or the support loading/ageing stage. It was determined that sonication during the co-precipitation stage resulted in composites with wide pores of Type II and IV(a) isotherms, rough morphology, enriched superficial Mg and Si contents due to enhanced Mg migration to the surface and the clustering of surfacial Si and increased reducibility. On the other hand, composites synthesised with sonication during silica loading/ageing had narrower pores of Type IV(a) isotherms, smooth morphology, lower superficial Mg and Si contents due to the erosion of Ni-Mg hydroxycarbonate phases and silica clusters and decreased reducibility. Through this chapter, the usage of ultrasound at the two different stages of the synthesis is found to have profound impacts on the final properties of materials. This established that the configuration of sono-syntheses is also a significant and non-random parameter in synthesising materials with differing characteristics.

The recovery of nickel from industrial spent hydrogenation catalysts was carried out using ultrasonic irradiation and is described in *Chapter 7*. Ultrasound proved to be successful in enhancing the recovery of nickel, compared to the mechanical stirring method, whereby the ultrasonic leaching method was more effective for the extraction of nickel in all experiments conducted. The extent of agglomeration of the spent catalyst particles was greatly diminished under sonicated conditions, resulting in new exposed surfaces, hence increasing the total contact area for leaching to occur. Furthermore, nitric acid was found to be more

effective than sulphuric acid in terms of its leaching and oxidising ability, thus allowing the former to achieve greater nickel recovery than the latter. Lastly, an approximate economic analysis was carried out for the ultrasound-assisted leaching process. An approximate economic analysis was performed to determine the overall recovery cost of recovering nickel via the ultrasonic method.

8.2. Recommendations for future work

Overall, this project was able to provide insights into several research areas with regards to nickel-based heterogenous catalysts, bridging the knowledge gaps present in current literature. While the benefits of this research work are acknowledged, several limitations can be identified, which could serve as foundations for future investigations.

Considering the ubiquity of palm-based products and their associated chemical reactions, further extending catalyst deactivation studies to a wider range of organic liquid reactants could be of research and commercial significance.

In this thesis, the development of nickel-silica catalysts was carried out using a high-power ultrasonic probe as the ultrasonic source. Nevertheless, it will be interesting to further explore the possibility of employing the low-power ultrasonic bath instead of the high-power ultrasonic probe during material synthesis. The usage of an ultrasonic bath system with a much lower energy input will be economically attractive should it bring about similar positive enhancements in the material properties akin to its ultrasonic probe counterpart.

In addition, through this work the multifaceted benefits of ultrasonic irradiation in chemical processes were demonstrated. While applicable on a laboratory scale, this current study lacks thorough and extensive investigations into the scalability and economic feasibility of employing ultrasound technology on an industrial scale in the techniques described. Therefore, future work could be geared towards investigating and optimising the upscaling process as it is inherently complex with multi-dimensional considerations such as reactor design, acoustic pressure field distribution, energy dissipation in bulk volume and the optimisation of operating and geometric parameters.

Bibliography

Abramov, O.V., 1998. High-Intensity Ultrasonics. Gordon and Breach Science Publishers.

Adewuyi, Y.G., 2001. Sonochemistry: environmental science and engineering applications. Ind. Eng. Chem. Res. 40, 4681–4715. https://doi.org/10.1021/IE010096L

Adibi, P.T.Z., 2014. Studies of catalyst sintering during operating conditions. Chalmers University of Technology.

Adu-Mensah, D., Mei, D., Zuo, L., Zhang, Q., Wang, J., 2019. A review on partial hydrogenation of biodiesel and its influence on fuel properties. Fuel 251, 660–668. https://doi.org/10.1016/j.fuel.2019.04.036

Ahmadi, F., Haghighi, M., Ajamein, H., 2016. Sonochemically coprecipitation synthesis of $CuO/ZnO/ZrO_2/Al_2O_3$ nanocatalyst for fuel cell grade hydrogen production via steam methanol reforming. J. Mol. Catal. A Chem. 421, 196–208. https://doi.org/10.1016/j.molcata.2016.05.027

Ahmadova, R., Ibragimov, H., Kondratenko, E., Rodemerc, U., 2018. Synthesis of SAPO-34 catalysts via sonochemically prepared method and its catalytic performance in methanol conversion to light olefins. Appl. Petrochemical Res. 8, 13–20. https://doi.org/10.1007/s13203-018-0193-x

Aja, O.C., Al-Kayiem, H.H., Zewge, M.G., Joo, M.S., 2016. Overview of Hazardous Waste Management Status in Malaysia, in: Management of Hazardous Wastes. InTech, pp. 69–87. https://doi.org/10.5772/63682

Akcil, A., Vegliò, F., Ferella, F., Okudan, M.D., Tuncuk, A., 2015. A review of metal recovery from spent petroleum catalysts and ash. Waste Manag. 45, 420–433. https://doi.org/10.1016/j.wasman.2015.07.007

Al-Fatesh, A.S., Olajide Kasim, S., Aidid Ibrahim, A., Hamza Fakeeha, A., Elhag Abasaeed, A., Alrasheed, R., Ashamari, R., Bagabas, A., 2019. Combined Magnesia, Ceria and Nickel catalyst supported over γ-Alumina Doped with Titania for Dry Reforming of Methane. Catalysts 9, 188. https://doi.org/10.3390/catal9020188

Al-Swai, B.M., Osman, N.B., Abdullah, B., 2017. Catalytic performance of Ni/MgO

catalyst in methane dry reforming. AIP Conf. Proc. 1891, 020028. https://doi.org/10.1063/1.5005361

Ali, F., Reinert, L., Levêque, J.-M., Duclaux, L., Muller, F., Saeed, S., Shah, S.S., 2014. Effect of sonication conditions: Solvent, time, temperature and reactor type on the preparation of micron sized vermiculite particles. Ultrason. Sonochem. 21, 1002–1009. https://doi.org/10.1016/j.ultsonch.2013.10.010

Ali, Z., Mehmood, M., Ahmad, J., Malik, T.S., 2020. Catalytic growth of CNTs and carbon onions by chemical vapor deposition on nickel-silica nanocomposite and its electrochemical catalytic study towards OER. J. Porous Mater. https://doi.org/10.1007/s10934-020-00934-9

Aljishi, A., Veilleux, G., Lalinde, J.A.H., Kopyscinski, J., 2018. The effect of synthesis parameters on ordered mesoporous nickel alumina catalyst for CO_2 methanation. Appl. Catal. A Gen. 549, 263–272. https://doi.org/10.1016/j.apcata.2017.10.012

Allahyari, S., Haghighi, M., Ebadi, A., Hosseinzadeh, S., 2014a. Ultrasound assisted co-precipitation of nanostructured CuO–ZnO–Al_2O_3 over HZSM-5: Effect of precursor and irradiation power on nanocatalyst properties and catalytic performance for direct syngas to DME. Ultrason. Sonochem. 21, 663–673. https://doi.org/10.1016/j.ultsonch.2013.09.014

Allahyari, S., Haghighi, M., Ebadi, A., Hosseinzadeh, S., Gavam Saeedi, H., 2014b. The beneficial use of ultrasound irradiation and nitrate/acetate metal precursors in the co-precipitation synthesis and characterization of nanostructured CuO–ZnO–Al_2O_3 catalyst for methanol synthesis. React. Kinet. Mech. Catal. 112, 101–116. https://doi.org/10.1007/s11144-014-0677-3

Allen, G.C., Harris, S.J., Jutson, J.A., Dyke, J.M., 1989. A study of a number of mixed transition metal oxide spinels using X-ray photoelectron spectroscopy. Appl. Surf. Sci. 37, 111–134. https://doi.org/10.1016/0169-4332(89)90977-X

Allen, R.R., 1978. Principles and catalysts for hydrogenation of fats and oils. J. Am. Oil Chem. Soc. 55, 792–795. https://doi.org/10.1007/BF02682650

Almeida, R.M., Guiton, T.A., Pantano, C.G., 1990. Characterization of silica gels by infrared reflection spectroscopy. J. Non. Cryst. Solids 121, 193–197. https://doi.org/10.1016/0022-3093(90)90130-E

Alsobaai, A.M., Shaibani, A.M. Al, Moustafa, T., Derhem, A., 2012. Effect of

hydrogenation temperature on the palm mid-fraction fatty acids composition and conversion. J. King Saud Univ. - Eng. Sci. 24, 45–51. https://doi.org/10.1016/j.jksues.2011.02.004

Alvarez-Galvan, C., Melian, M., Ruiz-Matas, L., Eslava, J.L., Navarro, R.M., Ahmadi, M., Roldan Cuenya, B., Fierro, J.L.G., 2019. Partial Oxidation of Methane to Syngas Over Nickel-Based Catalysts: Influence of Support Type, Addition of Rhodium, and Preparation Method. Front. Chem. 7. https://doi.org/10.3389/fchem.2019.00104

Ambati, R., Gogate, P.R., 2018. Ultrasound assisted synthesis of iron doped TiO_2 catalyst. Ultrason. Sonochem. 40, 91–100. https://doi.org/10.1016/j.ultsonch.2017.07.002

Ameen, M., Azizan, M.T., Ramli, A., Yusup, S., Alnarabiji, M.S., 2019. Catalytic hydrodeoxygenation of rubber seed oil over sonochemically synthesized Ni-Mo/γ-Al_2O_3 catalyst for green diesel production. Ultrason. Sonochem. 51, 90–102. https://doi.org/10.1016/j.ultsonch.2018.10.011

Ameen, M., Azizan, M.T., Ramli, A., Yusup, S., Yasir, M., 2016. Physicochemical Properties of Ni-Mo/γ-Al_2O_3 Catalysts Synthesized via Sonochemical Method. Procedia Eng. 148, 64–71. https://doi.org/10.1016/j.proeng.2016.06.496

Amora, M.R., Pacheco, M.E., Azevedo, D.C.S., Cavalcante, C.L., Luna, F.M.T., 2019. Deactivation Analysis of Industrial Spent Catalysts Applied to Lube Oil Hydrotreating in a Pilot Plant. Chem. Eng. Technol. 42, 1018–1026. https://doi.org/10.1002/ceat.201800252

Ananikov, V.P., 2015. Nickel: The "Spirited Horse" of Transition Metal Catalysis. ACS Catal. 5, 1964–1971. https://doi.org/10.1021/acscatal.5b00072

Arabi, M., Ostovan, A., Ghaedi, M., Purkait, M.K., 2016. Novel strategy for synthesis of magnetic dummy molecularly imprinted nanoparticles based on functionalized silica as an efficient sorbent for the determination of acrylamide in potato chips: Optimization by experimental design methodology. Talanta 154, 526–532. https://doi.org/10.1016/j.talanta.2016.04.010

Aras, A., Agacayak, T., 2017. Optimization of nickel extraction from lateritic ore in hydrochloric acid solution with hydrogen peroxide by taguchi method. Selcuk Univ. J. Eng. ,Science Technol. 5, 341–352. https://doi.org/10.15317/Scitech.2017.94

Argyle, M., Bartholomew, C., 2015. Heterogeneous Catalyst Deactivation and Regeneration: A Review. Catalysts 5, 145–269. https://doi.org/10.3390/catal5010145

Ariaansz, R.F., 1993. Hydrogenation Theory, in: Applewhite, T.H. (Ed.), Proceedings of the World Conference on Oilseed Technology and Utilization. AOCS Press, pp. 165–172.

Arslanoğlu, H., Yaraş, A., 2019. Recovery of precious metals from spent Mo–Co–Ni/Al_2O_3 catalyst in organic acid medium: Process optimization and kinetic studies. Pet. Sci. Technol. 37, 2081–2093. https://doi.org/10.1080/10916466.2019.1618867

Artika, N.H., MZ, Y., MT, N.F., 2019. An overview of schedules wastes management in Malaysia. J. Wastes Biomass Manag. 1, 01–04. https://doi.org/10.26480/jwbm.02.2019.01.04

Asfaram, A., Ghaedi, M., Agarwal, S., Tyagi, I., Kumar Gupta, V., 2015. Removal of basic dye Auramine-O by ZnS:Cu nanoparticles loaded on activated carbon: optimization of parameters using response surface methodology with central composite design. RSC Adv. 5, 18438–18450. https://doi.org/10.1039/C4RA15637D

Ashokkumar, M., 2016. Ultrasonic Synthesis of Functional Materials, SpringerBriefs in Molecular Science. Springer International Publishing, Cham. https://doi.org/10.1007/978-3-319-28974-8

Babu, G.P., Ghuge, K.D., Rammohan, S. V., Krishnan, V., Bhat, A.N., 1992. Characterization of silica supported Ni and Mg basic carbonate catalyst precursors. Catal. Letters 15, 95–103. https://doi.org/10.1007/BF00770902

Bacariza, M.C., Graça, I., Bebiano, S.S., Lopes, J.M., Henriques, C., 2017. Magnesium as Promoter of CO_2 Methanation on Ni-Based USY Zeolites. Energy & Fuels 31, 9776–9789. https://doi.org/10.1021/acs.energyfuels.7b01553

Badoga, S., Ganesan, A., Dalai, A.K., Chand, S., 2017. Effect of synthesis technique on the activity of CoNiMo tri-metallic catalyst for hydrotreating of heavy gas oil. Catal. Today 291, 160–171. https://doi.org/10.1016/j.cattod.2017.01.005

Bai, S., Yang, L., Wang, C., Lin, Y., Lu, J., Jiang, J., Xiong, Y., 2015. Boosting Photocatalytic Water Splitting: Interfacial Charge Polarization in Atomically Controlled Core-Shell Cocatalysts. Angew. Chemie Int. Ed. 54, 14810–14814.

https://doi.org/10.1002/anie.201508024

Bai, Y., Huang, H., Wang, C., Long, R., Xiong, Y., 2017. Engineering the surface charge states of nanostructures for enhanced catalytic performance. Mater. Chem. Front. 1, 1951–1964. https://doi.org/10.1039/C7QM00020K

Balakos, M.W., Hernandez, E.E., 1997. Catalyst characteristics and performance in edible oil hydrogenation. Catal. Today 35, 415–425. https://doi.org/10.1016/S0920-5861(96)00212-X

Ball, P., 1996. Designing the Molecular World: Chemistry at the Frontier. Princeton University Press, NJ.

Bartholomew, C., 2003. Catalyst Deactivation and Regeneration, in: Kirk-Othmer Encyclopedia of Chemical Technology. John Wiley & Sons, Inc., Hoboken, NJ, USA. https://doi.org/10.1002/0471238961.1415021218150209.a01.pub2

Bartholomew, C.H., 2001. Mechanisms of catalyst deactivation. Appl. Catal. A Gen. 212, 17–60. https://doi.org/10.1016/S0926-860X(00)00843-7

Bartholomew, C.H., 1987. Mechanisms of Nickel Catalyst Poisoning, in: Catalyst Deactivation 1987, Proceedings of the 4th International Symposium. pp. 81–104. https://doi.org/10.1016/S0167-2991(09)60352-9

Barzureau, J.-P., Draye, M., 2011. Ultrasound and Microwaves: Recent Advances in Organic Chemistry. Transworld Research Network, Kerala.

Behrens, M., Studt, F., Kasatkin, I., Kuhl, S., Havecker, M., Abild-Pedersen, F., Zander, S., Girgsdies, F., Kurr, P., Kniep, B.-L., Tovar, M., Fischer, R.W., Norskov, J.K., Schlogl, R., 2012. The Active Site of Methanol Synthesis over $Cu/ZnO/Al_2O_3$ Industrial Catalysts. Science (80-.). 336, 893–897. https://doi.org/10.1126/science.1219831

Beiramzadeh, Z., Baqersad, M., Aghababaei, M., 2019. Application of the response surface methodology (RSM) in heavy metal removal from real power plant wastewater using electrocoagulation. Eur. J. Environ. Civ. Eng. 1–19. https://doi.org/10.1080/19648189.2019.1640139

Belkacemi, K., Kemache, N., Hamoudi, S., Arul, J., 2007. Hydrogenation of Sunflower Oil over Bimetallic Supported Catalysts on Mesostructured Silica Material. Int. J. Chem. React. Eng. 5. https://doi.org/10.2202/1542-6580.1528

Bems, B., Schur, M., Dassenoy, A., Junkes, H., Herein, D., Schlögl, R., 2003. Relations between Synthesis and Microstructural Properties of Copper/Zinc Hydroxycarbonates. Chem. - A Eur. J. 9, 2039–2052. https://doi.org/10.1002/chem.200204122

Bergeret, G., Gallezot, P., 2008. Particle Size and Dispersion Measurements, in: Handbook of Heterogeneous Catalysis. Wiley-VCH Verlag GmbH & Co. KGaA, Weinheim, Germany, pp. 738–764. https://doi.org/10.1002/9783527610044.hetcat0038

Besson, M., Gallezot, P., 2003. Deactivation of metal catalysts in liquid phase organic reactions. Catal. Today 81, 547–559. https://doi.org/10.1016/S0920-5861(03)00153-6

Bhering, D.L., Nele, M., Pinto, J.C., Salim, V.M.., 2002. Preparation of high loading silica-supported nickel catalyst: analysis of the reduction step. Appl. Catal. A Gen. 234, 55–64. https://doi.org/10.1016/S0926-860X(02)00198-9

Blanco, P.H., Wu, C., Williams, P.T., 2014. Influence of Ni/SiO_2 catalyst preparation methods on hydrogen production from the pyrolysis/reforming of refuse derived fuel. Int. J. Hydrogen Energy 39, 5723–5732. https://doi.org/10.1016/j.ijhydene.2014.01.150

Bond, G.C., Louis, C., Thompson, D.T., 2006. Catalysis by gold. Imperial College Press, London.

Bradford, M.C.J., Vannice, M.A., 1996. Catalytic reforming of methane with carbon dioxide over nickel catalysts I. Catalyst characterization and activity. Appl. Catal. A Gen. 142, 73–96. https://doi.org/10.1016/0926-860X(96)00065-8

Bremner, D., 1990. Historical introduction to sonochemistry. Adv. Sonochemistry 1, 1–38.

Burattin, P., Che, M., Louis, C., 1999. Metal Particle Size in Ni/SiO_2 Materials Prepared by Deposition−Precipitation: Influence of the Nature of the Ni(II) Phase and of Its Interaction with the Support. J. Phys. Chem. B 103, 6171–6178. https://doi.org/10.1021/jp990115t

Burattin, P., Che, M., Louis, C., 1998. Molecular Approach to the Mechanism of Deposition−Precipitation of the Ni(II) Phase on Silica. J. Phys. Chem. B 102, 2722–2732. https://doi.org/10.1021/jp980018k

Cabrera-Trujillo, M.A., Sotelo-Díaz, L.I., Quintanilla-Carvajal, M.X., 2016. Effect of amplitude and pulse in low frequency ultrasound on oil/water emulsions. DYNA 83, 63. https://doi.org/10.15446/dyna.v83n199.56192

Cai, W., Ye, L., Zhang, L., Ren, Y., Yue, B., Chen, X., He, H., 2014. Highly Dispersed Nickel-Containing Mesoporous Silica with Superior Stability in Carbon Dioxide Reforming of Methane: The Effect of Anchoring. Materials (Basel). 7, 2340–2355. https://doi.org/10.3390/ma7032340

Campbell, C.T., 2012. Electronic perturbations. Nat. Chem. 4, 597–598. https://doi.org/10.1038/nchem.1412

Campos, A.F., Cassella, R.J., 2018. Development of an extraction method for the determination of inorganic anions (chloride, sulfate and phosphate) in edible oils from different origins by ion chromatography. J. Food Sci. Technol. 55, 3922–3929. https://doi.org/10.1007/s13197-018-3317-5

Capeletti, L.B., Zimnoch, J.H., 2016. Fourier Transform Infrared and Raman Characterization of Silica-Based Materials, in: Stauffer, M.T. (Ed.), Applications of Molecular Spectroscopy to Current Research in the Chemical and Biological Sciences. IntechOpen Limited, London. https://doi.org/10.5772/64477

Carrero, A., Calles, J.A., Vizcaíno, A.J., 2010. Effect of Mg and Ca addition on coke deposition over Cu–Ni/SiO_2 catalysts for ethanol steam reforming. Chem. Eng. J. 163, 395–402. https://doi.org/10.1016/j.cej.2010.07.029

Cavalieri, F., Zhou, M., Ashokkumar, M., 2010. The Design of Multifunctional Microbubbles for Ultrasound Image-Guided Cancer Therapy. Curr. Top. Med. Chem. 10, 1198–1210. https://doi.org/10.2174/156802610791384180

Čelková, A., Schmidt, Š., Zajíc, J., 1989. Effect of Ultrasound on Hydrogenation of Sunflower Oil. Fett Wiss. Technol. Sci. Technol. 91, 62–65. https://doi.org/10.1002/lipi.19890910204

Cepeda, E. A., Calvo, B., Sierra, I., Iriarte-Velasco, U., 2016. Selective hydrogenation of sunflower oil over Ni catalysts. Korean J. Chem. Eng. 33, 80–89. https://doi.org/10.1007/s11814-015-0095-x

Cepeda, Emilio A., Iriarte-Velasco, U., Calvo, B., Sierra, I., 2016. Hydrogenation of Sunflower Oil over M/SiO_2 and M/Al_2O_3 (M = Ni, Pd, Pt, Co, Cu) Catalysts. J. Am. Oil Chem. Soc. 93, 731–741. https://doi.org/10.1007/s11746-016-2815-8

Çetintaş, S., Bingöl, D., 2016. Response surface methodology approach to leaching of nickel laterite and evaluation of different analytical techniques used for the analysis of leached solutions. Anal. Methods 8, 3075–3087. https://doi.org/10.1039/C6AY00457A

Chang, J., Zhang, E., Zhang, L., Peng, J., Zhou, J., Srinivasakannan, C., Yang, C., 2017. A comparison of ultrasound-augmented and conventional leaching of silver from sintering dust using acidic thiourea. Ultrason. Sonochem. 34, 222–231. https://doi.org/10.1016/j.ultsonch.2016.05.038

Chang, S.-S., Clair, B., Ruelle, J., Beauchene, J., Di Renzo, F., Quignard, F., Zhao, G.-J., Yamamoto, H., Gril, J., 2009. Mesoporosity as a new parameter for understanding tension stress generation in trees. J. Exp. Bot. 60, 3023–3030. https://doi.org/10.1093/jxb/erp133

Chatel, G., 2019. Sonochemistry in nanocatalysis: The use of ultrasound from the catalyst synthesis to the catalytic reaction. Curr. Opin. Green Sustain. Chem. 15, 1–6. https://doi.org/10.1016/j.cogsc.2018.07.004

Chauhan, G., Pant, K.K., Nigam, K.D.P., 2013a. Metal Recovery from Hydroprocessing Spent Catalyst: A Green Chemical Engineering Approach. Ind. Eng. Chem. Res. 52, 16724–16736. https://doi.org/10.1021/ie4024484

Chauhan, G., Pant, K.K., Nigam, K.D.P., 2013b. Development of green technology for extraction of nickel from spent catalyst and its optimization using response surface methodology. Green Process. Synth. 2. https://doi.org/10.1515/gps-2013-0016

Chauhan, G., Pant, K.K., Nigam, K.D.P., 2012. Extraction of Nickel from Spent Catalyst Using Biodegradable Chelating Agent EDDS. Ind. Eng. Chem. Res. 51, 10354–10363. https://doi.org/10.1021/ie300580v

Che, M., Clause, O., Marcilly, C.H., 1997. Supported catalysts: impregnation and ion exchange, in: Ertl, G., Knözinger, H., Weitkamp, J. (Eds.), Handbook of Heterogeneous Catalysis. Wiley-VCH, Weinheim.

Che Man, Y.B., Setiowaty, G., van de Voort, F.R., 1999. Determination of iodine value of palm oil by fourier transform infrared spectroscopy. J. Am. Oil Chem. Soc. 76, 693–699. https://doi.org/10.1007/s11746-999-0161-9

Chen, J.Z., Gao, J., Probus, P.R., Liu, W., Wu, X., Wegener, E.C., Kropf, A.J., Zemlyanov, D., Zhang, G., Yang, X., Miller, J.T., 2020. The effect of strong metal–support

interaction (SMSI) on Pt–Ti/SiO_2 and Pt–Nb/SiO_2 catalysts for propane dehydrogenation. Catal. Sci. Technol. https://doi.org/10.1039/D0CY00897D

Chheda, J.N., Dumesic, J.A., 2007. An overview of dehydration, aldol-condensation and hydrogenation processes for production of liquid alkanes from biomass-derived carbohydrates. Catal. Today 123, 59–70. https://doi.org/10.1016/j.cattod.2006.12.006

Cho, Y.S., Park, J.C., Lee, B., Kim, Y., Yi, J., 2002. Preparation of Mesoporous Catalyst Supported on Silica with Finely Dispersed Ni Particles. Catal. Letters 81, 89–96.

Chorkendorff, I., Niemantsverdriet, J.W., 2003. Concepts of Modern Catalysis and Kinetics. Wiley-VCH, Weinheim.

Choudhary, V.R., Uphade, B.S., Mamman, A.S., 1997. Oxidative Conversion of Methane to Syngas over Nickel Supported on Commercial Low Surface Area Porous Catalyst Carriers Precoated with Alkaline and Rare Earth Oxides. J. Catal. 172, 281–293. https://doi.org/10.1006/jcat.1997.1838

Chu, J.K., Lim, M.S.W., Tiong, T.J., Yap, Y.H., Lim, L.Y., Yeoh, P.S.J., Kumar, K., Chong, S., Chan, Y.J., Pan, G.-T., Yang, T.C.K., 2019. One-pot co-precipitation of copper–manganese–zinc oxide catalysts for the oxidation of CO and SO_2 in the presence of ultrasonic irradiation. Res. Chem. Intermed. https://doi.org/10.1007/s11164-019-04016-7

Coenen, J.W.E., 1991. Characterization of the standard nickel/silica catalyst EuroNi-1. Appl. Catal. 75, 193–223. https://doi.org/10.1016/S0166-9834(00)83132-2

Coenen, J.W.E., 1989. Characterization of the standard nickel/silica catalyst EuroNi-1. Appl. Catal. 54, 65–78. https://doi.org/10.1016/S0166-9834(00)82355-6

Coenen, J.W.E., 1986. Catalytic hydrogenation of fatty oils. Ind. Eng. Chem. Fundam. 25, 43–52. https://doi.org/10.1021/i100021a006

Coenen, J.W.E., 1979. Reduction of Silica Supported Nickel Catalysts, in: Preparation of Catalysts II, Proceedings of the Second International Symposium. pp. 89–111. https://doi.org/10.1016/S0167-2991(09)60207-X

Coenen, J.W.E., 1976. Hydrogenation of Edible oils. J. Am. Oil Chem. Soc. 53, 382–

389. https://doi.org/10.1007/BF02605727

Coşkuner, B., Kantürk Figen, A., Pişkin, S., 2014. Sonochemical Approach to Synthesis of Co-B Catalysts and Hydrolysis of Alkaline $NaBH_4$ Solutions. J. Chem. 2014, 1–9. https://doi.org/10.1155/2014/185957

Costa, J.M., Almeida Neto, A.F. de, 2020. Ultrasound-assisted electrodeposition and synthesis of alloys and composite materials: A review. Ultrason. Sonochem. 68, 105193. https://doi.org/10.1016/j.ultsonch.2020.105193

Courty, P., Marcilly, C., 1983. A Scientific Approach To The Preparation Of Bulk Mixed Oxide Catalysts, in: Poncelet, G., Grange, P., Jacobs, P. (Eds.), Preparation of Catalysts III. Elsevier, Amsterdam, pp. 485–519. https://doi.org/10.1016/S0167-2991(09)60044-6

Cravotto, G., Cintas, P., 2007. Forcing and Controlling Chemical Reactions with Ultrasound. Angew. Chemie Int. Ed. 46, 5476–5478. https://doi.org/10.1002/anie.200701567

Cravotto, G., Gaudino, E.C., Cintas, P., 2013. On the mechanochemical activation by ultrasound. Chem. Soc. Rev. 42, 7521. https://doi.org/10.1039/c2cs35456j

Crum, L.A., 1984. Acoustic cavitation series: part five rectified diffusion. Ultrasonics 22, 215–223. https://doi.org/10.1016/0041-624X(84)90016-7

Dalodière, E., Virot, M., Moisy, P., Nikitenko, S.I., 2016. Effect of ultrasonic frequency on H_2O_2 sonochemical formation rate in aqueous nitric acid solutions in the presence of oxygen. Ultrason. Sonochem. 29, 198–204. https://doi.org/10.1016/j.ultsonch.2015.09.014

Daniel, J.S., Solomon, S., Portmann, R.W., Garcia, R.R., 1999. Stratospheric ozone destruction: The importance of bromine relative to chlorine. J. Geophys. Res. Atmos. 104, 23871–23880. https://doi.org/10.1029/1999JD900381

Daroughegi, R., Meshkani, F., Rezaei, M., 2017. Enhanced activity of CO_2 methanation over mesoporous nanocrystalline Ni–Al_2O_3 catalysts prepared by ultrasound-assisted co-precipitation method. Int. J. Hydrogen Energy 42, 15115–15125. https://doi.org/10.1016/j.ijhydene.2017.04.244

Davar, F., Shayan, N., Hojjati-Najafabadi, A., Sabaghi, V., Hasani, S., 2017. Development of ZrO_2 -MgO nanocomposite powders by the modified sol-gel method. Int. J. Appl. Ceram. Technol. 14, 211–219.

https://doi.org/10.1111/ijac.12624

David, E., 2007. Extraction of valuable metals from amorphous solid wastes. J. Achiev. Mater. Manuf. Eng. 25, 15–18.

Davis, B.H., Ertl, G., Knozinger, H., Weitkamp, J., 1997. Handbook of Heterogeneous Catalysis; Vol. 1. VCH, Weinheim.

de Castro, L., Priego Capote, F., 2007. Ultrasound-assisted leaching, in: Analytical Applications of Ultrasound. Elsevier Science, pp. 99–142. https://doi.org/10.1016/S0167-9244(07)80020-5

De Laat, J., Truong Le, G., Legube, B., 2004. A comparative study of the effects of chloride, sulfate and nitrate ions on the rates of decomposition of H_2O_2 and organic compounds by Fe(II)/H_2O_2 and Fe(III)/H_2O_2. Chemosphere 55, 715–723. https://doi.org/10.1016/j.chemosphere.2003.11.021

Dean, J.A., 1999. Properties of Atoms, Radicals and Bonds, in: Dean, J.A. (Ed.), Lange's Handbook of Chemistry. McGraw-Hill, Inc., New York.

Dehghani, S., Haghighi, M., 2017. Sono-sulfated zirconia nanocatalyst supported on MCM-41 for biodiesel production from sunflower oil: Influence of ultrasound irradiation power on catalytic properties and performance. Ultrason. Sonochem. 35, 142–151. https://doi.org/10.1016/j.ultsonch.2016.09.012

Deutschmann, O., Knözinger, H., Kochloefl, K., Turek, T., 2009. Heterogeneous Catalysis and Solid Catalysts, in: Ullmann's Encyclopedia of Industrial Chemistry. Wiley-VCH Verlag GmbH & Co. KGaA, Weinheim, Germany. https://doi.org/10.1002/14356007.a05_313.pub2

Dieuzeide, M.L., Laborde, M., Amadeo, N., Cannilla, C., Bonura, G., Frusteri, F., 2016. Hydrogen production by glycerol steam reforming: How Mg doping affects the catalytic behaviour of Ni/Al_2O_3 catalysts. Int. J. Hydrogen Energy 41, 157–166. https://doi.org/10.1016/j.ijhydene.2015.12.009

Dijkstra, A.J., 2012. Kinetics and mechanism of the hydrogenation process - the state of the art. Eur. J. Lipid Sci. Technol. 114, 985–998. https://doi.org/10.1002/ejlt.201100405

Dijkstra, A.J., 2006. Revisiting the formation oftrans isomers during partial hydrogenation of triacylglycerol oils. Eur. J. Lipid Sci. Technol. 108, 249–264. https://doi.org/10.1002/ejlt.200500335

Ding, L., Zheng, Y., Zhang, Z., Ring, Z., Chen, J., 2006. Effect of agitation on the synthesis of zeolite beta and its synthesis mechanism in absence of alkali cations. Microporous Mesoporous Mater. 94, 1–8. https://doi.org/10.1016/j.micromeso.2006.03.010

Ding, Y., Zheng, H., Li, J., Zhang, S., Liu, B., Ekberg, C., Jian, Z., 2019. Recovery of Platinum from Spent Petroleum Catalysts: Optimization Using Response Surface Methodology. Metals (Basel). 9, 354. https://doi.org/10.3390/met9030354

Do, L.T., Nguyen-Huy, C., Shin, E.W., 2018. Different Metal Support Interactions over NiK/Mixed Oxide Catalysts and Their Effects on Catalytic Routes in Steam Catalytic Cracking of Vacuum Residue. ChemistrySelect 3, 1827–1835. https://doi.org/10.1002/slct.201702819

Dong, H., Zhao, J., Chen, J., Wu, Y., Li, B., 2015. Recovery of platinum group metals from spent catalysts: A review. Int. J. Miner. Process. 145, 108–113. https://doi.org/10.1016/j.minpro.2015.06.009

Du, L., Qu, B., 2007. Effects of synthesis conditions on crystal morphological structures and thermal degradation behavior of hydrotalcites and flame retardant and mechanical properties of EVA/hydrotalcite blends. Polym. Compos. 28, 131–138. https://doi.org/10.1002/pc.20279

Dufresne, P., 2007. Hydroprocessing catalysts regeneration and recycling. Appl. Catal. A Gen. 322, 67–75. https://doi.org/10.1016/j.apcata.2007.01.013

Dumesic, J.A., Huber, G.W., Boudart, M., 2008. Principles of Heterogeneous Catalysis, in: Handbook of Heterogeneous Catalysis. Wiley-VCH Verlag GmbH & Co. KGaA, Weinheim, Germany. https://doi.org/10.1002/9783527610044.hetcat0001

Echeverria, S.M., Andres, V.M., 1990. Effect of the method of preparation on the activity of nickel—Kieselguhr catalyst for vegetable oil hydrogenation. Appl. Catal. 66, 73–90. https://doi.org/10.1016/S0166-9834(00)81628-0

Edmund, D., 1820. On Some Combinations of Platinum. Philos. Trans. R. Soc. London 110, 108–125.

Edvardsson, J., Rautanen, P., Littorin, A., Larsson, M., 2001. Deactivation and coke formation on palladium and platinum catalysts in vegetable oil hydrogenation. J. Am. Oil Chem. Soc. 78, 319–327. https://doi.org/10.1007/s11746-001-

0263-6

El-Kemary, M., Nagy, N., El-Mehasseb, I., 2013. Nickel oxide nanoparticles: Synthesis and spectral studies of interactions with glucose. Mater. Sci. Semicond. Process. 16, 1747–1752. https://doi.org/10.1016/j.mssp.2013.05.018

El-Naggar, M.M., 2006. Effects of Cl−, NO_3^- and SO_4^{2-} anions on the anodic behavior of carbon steel in deaerated 0.50M $NaHCO_3$ solutions. Appl. Surf. Sci. 252, 6179–6194. https://doi.org/10.1016/j.apsusc.2005.08.025

El-Okazy, M.A., Zewail, T.M., Farag, H.A.-M., 2018. Recovery of copper from spent catalyst using acid leaching followed by electrodeposition on square rotating cylinder. Alexandria Eng. J. 57, 3117–3126. https://doi.org/10.1016/j.aej.2017.12.001

Elbaba, I.F., Williams, P.T., 2014. Deactivation of Nickel Catalysts by Sulfur and Carbon for the Pyrolysis–Catalytic Gasification/Reforming of Waste Tires for Hydrogen Production. Energy & Fuels 28, 2104–2113. https://doi.org/10.1021/ef4023477

Environmental Quality Act, 1974. . Parliament of Malaysia.

Ermakova, M.A., Ermakov, D.Y., 2003. High-loaded nickel–silica catalysts for hydrogenation, prepared by sol–gel. Appl. Catal. A Gen. 245, 277–288. https://doi.org/10.1016/S0926-860X(02)00648-8

Esmaeili, M., Rastegar, S.O., Beigzadeh, R., Gu, T., 2020. Ultrasound-assisted leaching of spent lithium ion batteries by natural organic acids and H_2O_2. Chemosphere 254, 126670. https://doi.org/10.1016/j.chemosphere.2020.126670

Estifaee, P., Haghighi, M., Mohammadi, N., Rahmani, F., 2014. CO oxidation over sonochemically synthesized Pd–Cu/Al_2O_3 nanocatalyst used in hydrogen purification: Effect of Pd loading and ultrasound irradiation time. Ultrason. Sonochem. 21, 1155–1165. https://doi.org/10.1016/j.ultsonch.2013.11.019

Farnetti, E., Di Monte, R., Kaspar, J., 2009. Homogeneous and Heterogeneous Catalysis, in: Bertini, I. (Ed.), Inorganic and Bio-Inorganic Chemistry. EOLSS Publications, Oxford.

Feng, X., Liu, J., Zhang, P., Zhang, Q., Xu, L., Zhao, L., Song, X., Gao, L., 2019. Highly

coke resistant Mg–Ni/Al_2O_3 catalyst prepared via a novel magnesiothermic reduction for methane reforming catalysis with CO_2 : the unique role of Al–Ni intermetallics. Nanoscale 11, 1262–1272. https://doi.org/10.1039/C8NR08447E

Feng, Y.-Y., Song, G.-H., Zhang, Q., Lv, J.-N., Hu, X.-Y., He, Y.-L., Shen, X., 2019. Morphology effect of MnO_2 promoter to the catalytic performance of Pt toward methanol electrooxidation reaction. Int. J. Hydrogen Energy 44, 3744–3750. https://doi.org/10.1016/j.ijhydene.2018.12.108

Fernández, M.B., Sánchez M., J.F., Tonetto, G.M., Damiani, D.E., 2009. Hydrogenation of sunflower oil over different palladium supported catalysts: Activity and selectivity. Chem. Eng. J. 155, 941–949. https://doi.org/10.1016/j.cej.2009.09.037

Fernández, M.B., Tonetto, G.M., Crapiste, G.H., Damiani, D.E., 2007. Revisiting the hydrogenation of sunflower oil over a Ni catalyst. J. Food Eng. 82, 199–208. https://doi.org/10.1016/j.jfoodeng.2007.02.010

Flowers, P., Robinson, W.R., Langley, R., Theopold, K., 2015. Chemistry, OpenStax. Houston, Texas.

Fulvio, P.F., Pikus, S., Jaroniec, M., 2005. Tailoring properties of SBA-15 materials by controlling conditions of hydrothermal synthesis. J. Mater. Chem. 15, 5049. https://doi.org/10.1039/b511346f

Gabrovska, M., Krstić, J., Edreva-Kardjieva, R., Stanković, M., Jovanović, D., 2006. The influence of the support on the properties of nickel catalysts for edible oil hydrogenation. Appl. Catal. A Gen. 299, 73–83. https://doi.org/10.1016/j.apcata.2005.10.011

Gabrovska, M., Krstić, J., Tzvetkov, P., Tenchev, K., Shopska, M., Vukelić, N., Jovanović, D., 2011. Effect of the support and the reduction temperature on the formation of metallic nickel phase in Ni/silica gel precursors of vegetable oil hydrogenation catalysts. Russ. J. Phys. Chem. A 85, 2392–2398. https://doi.org/10.1134/S0036024411130073

Gabrovska, M.V., Edreva-Kardjieva, R.M., Shopska, M.G., Nikolova, D.A., Bilyarska, L.P., Crisan, D., Crisan, M., 2015. Purification of hydrogen-rich streams from CO2 by methanation. Bulg. Chem. Commun. 47, 66–72.

Gabrovska, M.V., Shopska, M., Shtereva, I., Kardjieva, R., Tzvetkov, P., Krstić, J.,

Jovanović, D., 2005. Effect of the preparation method on the reducibility and the crystal size of the Ni-Mg/SiO_2 precursors as catalysts for edible oil hydrogenation, in: 1st International Workshop on Nanoscience & Nanotechnology IWON 2005. Belgrade, Serbia and Montenegro, pp. 56–59.

Gandhi, S., Abiramipriya, P., Pooja, N., Jeyakumari, J.J.L., Arasi, A.Y., Dhanalakshmi, V., Nair, M.R.G., Anbarasan, R., 2011. Synthesis and characterizations of nano sized MgO and its nano composite with poly(vinyl alcohol). J. Non. Cryst. Solids 357, 181–185. https://doi.org/10.1016/j.jnoncrysol.2010.09.050

Gates, B.C., 1992. Catalytic Chemistry. Wiley, London.

Gayubo, A.G., Arandes, J.M., Aguayo, A.T., Olazar, M., Bilbao, J., 1993. Deactivation and acidity deterioration of a silica/alumina catalyst in the isomerization of cis-butene. Ind. Eng. Chem. Res. 32, 588–593. https://doi.org/10.1021/ie00016a003

Gedanken, A., 2004. Using sonochemistry for the fabrication of nanomaterials. Ultrason. Sonochem. 11, 47–55. https://doi.org/10.1016/j.ultsonch.2004.01.037

Geus, J.W., van Dillen, J., 1997. Preparation of Supported Catalysts by Deposition-Precipitation, in: Ertl, G., Knözinger, H., Weitkamp, J. (Eds.), Handbook of Heterogeneous Catalysis. Wiley-VCH, Weinheim.

Ghaedi, M., Hajjati, S., Mahmudi, Z., Tyagi, I., Agarwal, S., Maity, A., Gupta, V.K., 2015. Modeling of competitive ultrasonic assisted removal of the dyes – Methylene blue and Safranin-O using Fe_3O_4 nanoparticles. Chem. Eng. J. 268, 28–37. https://doi.org/10.1016/j.cej.2014.12.090

Gharabaghi, M., Irannajad, M., Azadmehr, A.R., 2013. Leaching kinetics of nickel extraction from hazardous waste by sulphuric acid and optimization dissolution conditions. Chem. Eng. Res. Des. 91, 325–331. https://doi.org/10.1016/j.cherd.2012.11.016

Ghuge, K.D., Babu, G.P., 1995. Infrared Investigations on Metal-Support Interactions in Ni-SiO_2 Catalyst Precursors: Role of Silica. J. Catal. 151, 453–455. https://doi.org/10.1006/jcat.1995.1047

Ghuge, K.D., Bhat, A.N., Babu, G.P., 1993. Identification of nickel species and their interaction with the support in Ni-silica catalyst precursor. Appl. Catal. A Gen. 103, 183–204. https://doi.org/10.1016/0926-860X(93)85051-P

Gnanamani, M.K., Garcia, R., Jacobs, G., Góra-Marek, K., Cronauer, D.C., Kropf, A.J., Marshall, C.L., 2020. Effect of pretreatment conditions on acidity and dehydration activity of CeO_2-MeO_x catalysts. Appl. Catal. A Gen. 117722. https://doi.org/10.1016/j.apcata.2020.117722

Gogate, P.R., Pandit, A.B., 2011. Sonocrystallization and its Application in Food and Bioprocesing, in: Ultrasound Technologies for Food and Bioprocessing. Food Engineering Series, pp. 467–493. https://doi.org/10.1007/978-1-4419-7472-3_17

Gogate, P.R., Sutkar, V.S., Pandit, A.B., 2011. Sonochemical reactors: Important design and scale up considerations with a special emphasis on heterogeneous systems. Chem. Eng. J. 166, 1066–1082. https://doi.org/10.1016/j.cej.2010.11.069

González-Marcos, M.P., Gutiérrez-Ortiz, J., González-Ortiz^de Elguea, C., González-Velasco, J.R., 1997. Effect of thermal treatments on surface chemical distribution and catalyst activity in nickel on silica systems. J. Mol. Catal. A Chem. 120, 185–196. https://doi.org/10.1016/S1381-1169(96)00443-8

Gorrepati, E.A., Wongthahan, P., Raha, S., Fogler, H.S., 2010. Silica Precipitation in Acidic Solutions: Mechanism, pH Effect, and Salt Effect. Langmuir 26, 10467–10474. https://doi.org/10.1021/la904685x

Greenberg, S.A., Sinclair, D., 1955. The Polymerization of Silicic Acid. J. Phys. Chem. 59, 435–440. https://doi.org/10.1021/j150527a014

Grinshtein, I.L., Vilpan, Y.A., Vasilieva, L.A., Kopeikin, V.A., 1999. Reduction of matrix interference during the atomic absorption determination of lead and cadmium in strongly interfering matrix samples using a two-step atomizer with vaporizer purging. Spectrochim. Acta Part B At. Spectrosc. 54, 745–752. https://doi.org/10.1016/S0584-8547(99)00024-5

Guo, M., Lu, G., 2014. The effect of impregnation strategy on structural characters and CO_2 methanation properties over MgO modified Ni/SiO_2 catalysts. Catal. Commun. 54, 55–60. https://doi.org/10.1016/j.catcom.2014.05.022

Haber, F., 1905. Thermodynamik technischer Gasreaktionen (in German) (1st ed.). Salzwasser Verlag, Paderborn.

Hackett, D.P., 1990. An Assessment of the Basecl Convention on the Control of Transboundary Movements of Hazardous Wastes and Their Disposal. Am.

Univ. Int. Law Rev. 5, 219–323.

Hanefeld, U., Lefferts, L., 2017. Synthesis of solid supports and catalysts, in: Catalysis: An Integrated Textbook for Students. John Wiley & Sons, p. 321.

Hansen, T.W., DeLaRiva, A.T., Challa, S.R., Datye, A.K., 2013. Sintering of Catalytic Nanoparticles: Particle Migration or Ostwald Ripening? Acc. Chem. Res. 46, 1720–1730. https://doi.org/10.1021/ar3002427

Harkin, A., Nadim, A., Kaper, T.J., 1999. On acoustic cavitation of slightly subcritical bubbles. Phys. Fluids 11, 274–287. https://doi.org/10.1063/1.869878

Harrhy, J.H., Wang, A., Jarvis, J.S., He, P., Meng, S., Yung, M., Liu, L., Song, H., 2019. Understanding zeolite deactivation by sulfur poisoning during direct olefin upgrading. Commun. Chem. 2, 37. https://doi.org/10.1038/s42004-019-0141-4

Hastert, R.C., 1979. Hydrogenation of fatty acids. J. Am. Oil Chem. Soc. 56, 732A-739A. https://doi.org/10.1007/BF02667431

Hayeemasae, N., Sensem, Z., Surya, I., Sahakaro, K., Ismail, H., 2020. Synergistic Effect of Maleated Natural Rubber and Modified Palm Stearin as Dual Compatibilizers in Composites based on Natural Rubber and Halloysite Nanotubes. Polymers (Basel). 12, 766. https://doi.org/10.3390/polym12040766

He, S., Wang, J., Yan, J., 2011. Pressure leaching of synthetic zinc silicate in sulfuric acid medium. Hydrometallurgy 108, 171–176. https://doi.org/10.1016/j.hydromet.2011.04.004

Hermida, L., Abdullah, A.Z., Mohamed, A.R., 2019. FT-IR and TGA of MCF Silica-Supported Nickel Catalyst. J. Mater. Environ. Sci. 9, 2328–2333.

Hoffer, B.W., Crezee, E., Devred, F., Mooijman, P.R.M., Sloof, W.G., Kooyman, P.J., van Langeveld, A.D., Kapteijn, F., Moulijn, J.., 2003. The role of the active phase of Raney-type Ni catalysts in the selective hydrogenation of D-glucose to D-sorbitol. Appl. Catal. A Gen. 253, 437–452. https://doi.org/10.1016/S0926-860X(03)00553-2

Horiuti, I., Polanyi, M., 1934. Exchange reactions of hydrogen on metallic catalysts. Trans. Faraday Soc. 30, 1164. https://doi.org/10.1039/tf9343001164

Hou, D., Zhang, L., Wang, Z., Fan, H., Wang, J., Huang, H., 2015. Humic acid fouling mitigation by ultrasonic irradiation in membrane distillation process. Sep. Purif. Technol. 154, 328–337. https://doi.org/10.1016/j.seppur.2015.09.073

Hu, D., Gao, J., Ping, Y., Jia, L., Gunawan, P., Zhong, Z., Xu, G., Gu, F., Su, F., 2012. Enhanced Investigation of CO Methanation over Ni/Al_2O_3 Catalysts for Synthetic Natural Gas Production. Ind. Eng. Chem. Res. 51, 4875–4886. https://doi.org/10.1021/ie300049f

Hunicke, R.L., 1990. Industrial applications of high power ultrasound for chemical reactions. Ultrasonics 28, 291–294. https://doi.org/10.1016/0041-624X(90)90034-L

Hussein, M.Z. Bin, Taufiq-Yap, Y.H., Shahadan, R., Abd Rashid, N.Y., 2001. The Effect of Aging Time on the Properties of Nickel-Aluminium-Carbonate Layered Double Hydroxide Synthesized by Hydrothermal Method. Chem. Pap. 55, 273–278.

Idris, J., Musa, M., Yin, C.-Y., Hamid, K.H.K., 2010. Recovery of nickel from spent catalyst from palm oil hydrogenation process using acidic solutions. J. Ind. Eng. Chem. 16, 251–255. https://doi.org/10.1016/j.jiec.2010.01.044

Iida, H., Itoh, D., Minowa, S., Yanagisawa, A., Igarashi, A., 2015. Hydrogenation of soybean oil over various platinum catalysts: Effects of support materials on trans fatty acid levels. Catal. Commun. 62, 1–5. https://doi.org/10.1016/j.catcom.2014.12.025

Imani, M.M., Safaei, M., 2019. Optimized Synthesis of Magnesium Oxide Nanoparticles as Bactericidal Agents. J. Nanotechnol. 2019, 1–6. https://doi.org/10.1155/2019/6063832

Irandoust, S., Edvardsson, J., 1993. Poisoning of nickel-based catalysts in fat hydrogenation. J. Am. Oil Chem. Soc. 70, 1149–1156. https://doi.org/10.1007/BF02632158

Iriondo, A., Güemez, M.B., Barrio, V.L., Cambra, J.F., Arias, P.L., Sánchez-Sánchez, M.C., Navarro, R.M., Fierro, J.L.G., 2010. Glycerol conversion into H_2 by steam reforming over Ni and PtNi catalysts supported on MgO modified γ-Al_2O_3, in: Gaigneaux, E.M., Devillers, M., Hermans, S., Jacobs, P., Martens, J., Ruiz, P. (Eds.), Scientific Bases for the Preparation of Heterogeneous Catalysts. Elsevier B.V., pp. 449–452. https://doi.org/10.1016/S0167-2991(10)75082-5

Jansson, H., Bernin, D., Ramser, K., 2015. Silicate species of water glass and insights for alkali-activated green cement. AIP Adv. 5, 067167. https://doi.org/10.1063/1.4923371

Jeong, C., Suh, Y.-W., 2016. Preparation of Active Cu/ZnO-based Catalysts for Methanol Synthesis. Appl. Chem. Eng. 27, 555–564. https://doi.org/10.14478/ace.2016.1109

Jesionowski, T., Zurawska, J., Krysztafkiewicz, A., 2002. Surface properties and dispersion behaviour of precipitated silicas. J. Mater. Sci. 37, 1621–1633. https://doi.org/10.1023/A:1014936428636

Jham, G.N., Teles, F.F.F., Campos, L.G., 1982. Use of aqueous HCI/MeOH as esterification reagent for analysis of fatty acids derived from soybean lipids. J. Am. Oil Chem. Soc. 59, 132–133. https://doi.org/10.1007/BF02662261

Jian, Z., Hejing, W., 2003. The physical meanings of 5 basic parameters for an X-ray diffraction peak and their application. Chinese J. Geochemistry 22, 38–44. https://doi.org/10.1007/BF02831544

Jiang, F., Chen, Y., Ju, S., Zhu, Q., Zhang, L., Peng, J., Wang, X., Miller, J.D., 2018. Ultrasound-assisted leaching of cobalt and lithium from spent lithium-ion batteries. Ultrason. Sonochem. 48, 88–95. https://doi.org/10.1016/j.ultsonch.2018.05.019

Jiang, X., Qin, X., Ling, C., Wang, Z., Lu, J., 2018. The effect of mixing on Co-precipitation and evolution of microstructure of Cu-ZnO catalyst. AIChE J. 64, 2647–2654. https://doi.org/10.1002/aic.16168

Jones, M., Forero-Hernandez, H., Zubov, A., Sarup, B., Sin, G., 2019. Splitting Triglycerides with a Counter-Current Liquid–Liquid Spray Column: Modeling, Global Sensitivity Analysis, Parameter Estimation and Optimization. Processes 7, 881. https://doi.org/10.3390/pr7120881

Jung, H.S., Lee, J.-K., Kim, J.-Y., Hong, K.S., 2003. Crystallization behaviors of nanosized MgO particles from magnesium alkoxides. J. Colloid Interface Sci. 259, 127–132. https://doi.org/10.1016/S0021-9797(03)00034-1

Jung, Y.-S., Yoon, W.-L., Seo, Y.-S., Rhee, Y.-W., 2012. The effect of precipitants on Ni-Al2O3 catalysts prepared by a co-precipitation method for internal reforming in molten carbonate fuel cells. Catal. Commun. 26, 103–111. https://doi.org/10.1016/j.catcom.2012.04.029

Kanicky, J.R., Shah, D.O., 2002. Effect of Degree, Type, and Position of Unsaturation on the pKa of Long-Chain Fatty Acids. J. Colloid Interface Sci. 256, 201–207. https://doi.org/10.1006/jcis.2001.8009

Karri, R.R., Sahu, J.N., 2018. Process optimization and adsorption modeling using activated carbon derived from palm oil kernel shell for Zn (II) disposal from the aqueous environment using differential evolution embedded neural network. J. Mol. Liq. 265, 592–602. https://doi.org/10.1016/j.molliq.2018.06.040

Kaskow, I., Wojtaszek-Gurdak, A., Sobczak, I., 2020. Methanol oxidation on AuAg-Zn/MCM-36 – The effect of catalyst components and pretreatment. Catal. Today 354, 123–132. https://doi.org/10.1016/j.cattod.2019.04.010

Kentish, S., Ashokkumar, M., 2011. The Physical and Chemical Effects of Ultrasound, in: Hao, F., Barbosa-Canovas, G. V., Weiss, J. (Eds.), Ultrasound Technologies for Food and Bioprocessing. Springer, New York, pp. 1–12. https://doi.org/10.1007/978-1-4419-7472-3_1

Kermarec, M., Carriat, J.Y., Burattin, P., Che, M., Decarreau, A., 1994. FTIR Identification of the Supported Phases Produced in the Preparation of Silica-Supported Nickel Catalysts. J. Phys. Chem. 98, 12008–12017. https://doi.org/10.1021/j100097a029

Khairudin, N.F., Sukri, M.F.F., Khavarian, M., Mohamed, A.R., 2018. Understanding the performance and mechanism of Mg-containing oxides as support catalysts in the thermal dry reforming of methane. Beilstein J. Nanotechnol. 9, 1162–1183. https://doi.org/10.3762/bjnano.9.108

Khalid, M.M., Athraa, B.A., 2017. Experimental Study on Factors Affecting the Recovery of Nickel from Spent Catalyst. J. Powder Metall. Min. 06. https://doi.org/10.4172/2168-9806.1000146

Khoshbin, R., Haghighi, M., 2013. Direct syngas to DME as a clean fuel: The beneficial use of ultrasound for the preparation of CuO–ZnO–Al_2O_3/HZSM-5 nanocatalyst. Chem. Eng. Res. Des. 91, 1111–1122. https://doi.org/10.1016/j.cherd.2012.11.017

Kim, B.-J., Cho, K.-S., Park, S.-J., 2010. Copper oxide-decorated porous carbons for carbon dioxide adsorption behaviors. J. Colloid Interface Sci. 342, 575–578. https://doi.org/10.1016/j.jcis.2009.10.045

Kim, H.-I., Park, K.-H., Mishra, D., 2009. Influence of sulfuric acid baking on leaching of spent Ni–Mo/Al_2O_3 hydro-processing catalyst. Hydrometallurgy 98, 192–195. https://doi.org/10.1016/j.hydromet.2009.04.002

Kim, H.-S., Kim, C.S., Kim, S.-G., 2006. Preparation of nickel oxide– and nickel–silica nanocomposites by spray pyrolysis. J. Non. Cryst. Solids 352, 2204–2212. https://doi.org/10.1016/j.jnoncrysol.2006.02.040

Kim, H., Suslick, K., 2018. The Effects of Ultrasound on Crystals: Sonocrystallization and Sonofragmentation. Crystals 8, 280. https://doi.org/10.3390/cryst8070280

Kinoshita, T., Akita, S., Kobayashi, N., Nii, S., Kawaizumi, F., Takahashi, K., 2003. Metal recovery from non-mounted printed wiring boards via hydrometallurgical processing. Hydrometallurgy 69, 73–79. https://doi.org/10.1016/S0304-386X(03)00031-8

Kinsler, L.E., Frey, A.R., Coppens, A.B., Sanders, J.V., 1999. Fundamentals of acoustics. Wiley, New York.

Klimmek, H., 1984. Influence of various catalyst poisons and other impurities on fatty acid hydrogenation. J. Am. Oil Chem. Soc. 61, 200–204. https://doi.org/10.1007/BF02678769

Ko, E.I., 1997. Sol-gel process, in: Ertl, G., Knözinger, H., Weitkamp, J. (Eds.), Handbook of Heterogeneous Catalysis. Wiley-VCH, Weinheim.

Koda, S., Kimura, T., Kondo, T., Mitome, H., 2003. A standard method to calibrate sonochemical efficiency of an individual reaction system. Ultrason. Sonochem. 10, 149–156. https://doi.org/10.1016/S1350-4177(03)00084-1

Kohli, K., Prajapati, R., Maity, S.K., Sau, M., Garg, M.O., 2016. Deactivation of hydrotreating catalyst by metals in resin and asphaltene parts of heavy oil and residues. Fuel 175, 264–273. https://doi.org/10.1016/j.fuel.2016.02.036

Kohli, K., Prajapati, R., Maity, S.K., Sau, M., Sharma, B.K., 2019. Deactivation of a hydrotreating catalyst during hydroprocessing of synthetic crude by metal bearing compounds. Fuel 243, 579–589. https://doi.org/10.1016/j.fuel.2019.01.153

Kojima, Y., Yamaguchi, K., Nishimiya, N., 2010. Effect of amplitude and frequency of ultrasonic irradiation on morphological characteristics control of calcium

carbonate. Ultrason. Sonochem. 17, 617–620. https://doi.org/10.1016/j.ultsonch.2009.10.020

Kolosnitsyn, V.S., Kosternova, S.P., Yapryntseva, O.A., Ivashchenko, A.A., Alekseev, S. V., 2006. Recovery of nickel with sulfuric acid solutions from spent catalysts for steam conversion of methane. Russ. J. Appl. Chem. 79, 539–543. https://doi.org/10.1134/S1070427206040069

Kondrashova, N.B., Val'tsifer, I. V., Strel'nikov, V.N., Mitrofanov, V.Y., Uporov, S.A., 2016. Preparation and magnetic characteristics of mesoporous nickel oxide–silica composites. Inorg. Mater. 52, 909–914. https://doi.org/10.1134/S0020168516090089

Konkol, M., Bicki, R., Kondracka, M., Antoniak-Jurak, K., Wiercioch, P., Próchniak, W., 2016a. Characteristics and catalytic behavior of NiAlCe catalysts in the hydrogenation of canola oil: the effect of cerium on cis/trans selectivity. React. Kinet. Mech. Catal. 119, 595–613. https://doi.org/10.1007/s11144-016-1080-z

Konkol, M., Wróbel, W., Bicki, R., Gołębiowski, A., 2016b. The Influence of the Hydrogen Pressure on Kinetics of the Canola Oil Hydrogenation on Industrial Nickel Catalyst. Catalysts 6, 55. https://doi.org/10.3390/catal6040055

Kooli, F., Jones, W., Rives, V., Ulibarri, M.A., 1997. An alternative route to polyoxometalate-exchanged layered double hydroxides: the use of ultrasound. J. Mater. Sci. Lett. 16, 27–29. https://doi.org/10.1023/A:1018580229611

Korytkova, E.N., Maslov, A. V., Pivovarova, L.N., Polegotchenkova, Y. V., Povinich, V.F., Gusarov, V. V., 2005. Synthesis of Nanotubular $Mg_3Si_2O_5(OH)_4$-$Ni_3Si_2O_5(OH)_4$ Silicates at Elevated Temperatures and Pressures. Inorg. Mater. 41, 743–749. https://doi.org/10.1007/s10789-005-0202-1

Kowalewski, E., Kamińska, I.I., Słowik, G., Lisovytskiy, D., Śrębowata, A., 2017. Effect of metal precursor and pretreatment conditions on the catalytic activity of Ni/C in the aqueous phase hydrodechlorination of 1,1,2-trichloroethene. React. Kinet. Mech. Catal. 121, 3–16. https://doi.org/10.1007/s11144-017-1148-4

Kremkau, F., 1975. Basic physical principles of ultrasound. DC Conf. X. https://doi.org/10.1002/9783527610174.ch1b

Krstić, J., Vukelić, N., Nedić, Z., Milutinović-Nikolić, A., Šućurović, A., Jovanović, D.,

2005. Nickel/Silica Precursor from Sodium Silicate Solution - Synthesis and Characterization. Mater. Sci. Forum 494, 333–338. https://doi.org/10.4028/www.scientific.net/MSF.494.333

Kruatim, J., Jantasee, S., Jongsomjit, B., 2017. Improvement of Cobalt Dispersion on Co/SBA-15 and Co/SBA-16 Catalysts by Ultrasound and Vacuum Treatments during Post-Impregnation Step. Eng. J. 21, 17–28. https://doi.org/10.4186/ej.2017.21.1.17

Kumar, M., Aberuagba, F., Gupta, J.., Rawat, K.., Sharma, L.., Murali Dhar, G., 2004. Temperature-programmed reduction and acidic properties of molybdenum supported on $MgO–Al_2O_3$ and their correlation with catalytic activity. J. Mol. Catal. A Chem. 213, 217–223. https://doi.org/10.1016/j.molcata.2003.12.005

Kumar, R., Kumar, K., Choudary, N.V., Pant, K.K., 2019. Effect of support materials on the performance of Ni-based catalysts in tri-reforming of methane. Fuel Process. Technol. 186, 40–52. https://doi.org/10.1016/j.fuproc.2018.12.018

Kumar, S., Saxena, S.K., 2014. A comparative study of CO_2 sorption properties for different oxides. Mater. Renew. Sustain. Energy 3, 30. https://doi.org/10.1007/s40243-014-0030-9

Kunz, U., Binder, C., Hoffmann, U., 1995. Preparation of fine particles as catalysts and catalyst precursors by the use of ultrasound during precipitation. Stud. Surf. Sci. Catal. 91, 869–878. https://doi.org/10.1016/S0167-2991(06)81829-X

Kusserow, B., Schimpf, S., Claus, P., 2003. Hydrogenation of Glucose to Sorbitol over Nickel and Ruthenium Catalysts. Adv. Synth. Catal. 345, 289–299. https://doi.org/10.1002/adsc.200390024

Lai, Y.-C., Lee, W.-J., Huang, K.-L., Wu, C.-M., 2008. Metal recovery from spent hydrodesulfurization catalysts using a combined acid-leaching and electrolysis process. J. Hazard. Mater. 154, 588–594. https://doi.org/10.1016/j.jhazmat.2007.10.061

Landau, M. V., 2008. Sol-Gel Process, in: Handbook of Heterogeneous Catalysis. Wiley-VCH Verlag GmbH & Co. KGaA, Weinheim, Germany. https://doi.org/10.1002/9783527610044.hetcat0009

Lange, J., 2015. Renewable Feedstocks: The Problem of Catalyst Deactivation and its Mitigation. Angew. Chemie Int. Ed. 54, 13186–13197.

https://doi.org/10.1002/anie.201503595

Laribi, M., Bachari, K., Chebout, R., Touati, M., 2012. Synthesis, characterization and catalytic application of the nickel containing mesoporous silica. J. Assoc. Arab Univ. Basic Appl. Sci. 12, 42–47. https://doi.org/10.1016/j.jaubas.2012.03.001

Lee, J.Y., Rao, S.V., Kumar, B.N., Kang, D.J., Reddy, B.R., 2010. Nickel recovery from spent Raneynickel catalyst through dilute sulfuric acid leaching and soda ash precipitation. J. Hazard. Mater. 176, 1122–1125. https://doi.org/10.1016/j.jhazmat.2009.11.137

Lee, Z.H., Ichikawa, S., Lee, K.T., Mohamed, A.R., 2015. The role of nickel oxide additive in lowering the carbon dioxide sorption temperature of CaO. J. Energy Chem. 24, 225–231. https://doi.org/10.1016/S2095-4956(15)60305-9

Legay, M., Gondrexon, N., Le Person, S., Boldo, P., Bontemps, A., 2011. Enhancement of Heat Transfer by Ultrasound: Review and Recent Advances. Int. J. Chem. Eng. 2011, 1–17. https://doi.org/10.1155/2011/670108

Lehmann, T., Wolff, T., Hamel, C., Veit, P., Garke, B., Seidel-Morgenstern, A., 2012. Physico-chemical characterization of Ni/MCM-41 synthesized by a template ion exchange approach. Microporous Mesoporous Mater. 151, 113–125. https://doi.org/10.1016/j.micromeso.2011.11.006

Leong, T., Ashokkumar, M., Kentish, S., 2011. The fundamentals of ultrasound - A review. Acoust. Aust. 39, 54–63.

Li, H., Ma, C.-J., Li, H.-X., 2006. Ultrasound-assisted Cinnamaldehyde Hydrogenation to Cinnamyl Alcohol at Atmospheric Pressure over Ru-B Amorphous Catalyst. Chinese J. Chem. 24, 613–619. https://doi.org/10.1002/cjoc.200690118

Li, Z., Mo, L., Kathiraser, Y., Kawi, S., 2014. Yolk–Satellite–Shell Structured Ni–Yolk@Ni@SiO_2 Nanocomposite: Superb Catalyst toward Methane CO_2 Reforming Reaction. ACS Catal. 4, 1526–1536. https://doi.org/10.1021/cs401027p

Liao, L., Chen, L., Ye, R., Tang, X., Liu, J., 2021. Robust nickel silicate catalysts with high Ni loading for CO_2 methanation. Chem. – An Asian J. 16, 678–689. https://doi.org/10.1002/asia.202001384

Liley, P.E., Thomson, G.H., Friend, D.G., Daubert, T.E., Buck, E., 1999. Physical and

Chemical Data, in: Green, D.W., Perry, R.H. (Eds.), Perry's Chemical Engineers' Handbook. The McGraw-Hill Companies, Inc., pp. 322–323.

Lim, M.S.W., Yang, T.C.-K., Tiong, T.J., Pan, G.-T., Chong, S., Yap, Y.H., 2021. Ultrasound-assisted sequentially precipitated nickel-silica catalysts and its application in the partial hydrogenation of edible oil. Ultrason. Sonochem. 73, 105490. https://doi.org/10.1016/j.ultsonch.2021.105490

Lim, W.T.L., Zhong, Z., Borgna, A., 2009. An effective sonication-assisted reduction approach to synthesize highly dispersed Co nanoparticles on SiO_2. Chem. Phys. Lett. 471, 122–127. https://doi.org/10.1016/j.cplett.2009.02.041

Lima, S., Chadwick, D., Hellgardt, K., 2017. Towards sustainable hydrogenation of 5-(hydroxymethyl)furfural: a two-stage continuous process in aqueous media over RANEY® catalysts. RSC Adv. 7, 31401–31407. https://doi.org/10.1039/C7RA03318D

Lindley, J., Mason, T.J., Lorimer, J.P., 1987. Sonochemically enhanced Ullmann reactions. Ultrasonics 25, 45–48. https://doi.org/10.1016/0041-624X(87)90011-4

Lindström, B., Pettersson, L.J., 2003. A Brief History of Catalysis. CATTECH 7, 130–138. https://doi.org/10.1023/A:1025001809516

Lipczynska-Kochany, E., Sprah, G., Harms, S., 1995. Influence of some groundwater and surface waters constituents on the degradation of 4-chlorophenol by the Fenton reaction. Chemosphere 30, 9–20. https://doi.org/10.1016/0045-6535(94)00371-Z

Liu, D., Hao, Z., Zhao, X., Su, R., Feng, W., Li, S., Jia, B., 2019. Effect of Physical and Mechanical Activation on the Physicochemical Structure of Coal-Based Activated Carbons for SO_2 Adsorption. Processes 7, 707. https://doi.org/10.3390/pr7100707

Liu, H., Wang, H., Shen, J., Sun, Y., Liu, Z., 2008. Preparation, characterization and activities of the nano-sized Ni/SBA-15 catalyst for producing CO_x-free hydrogen from ammonia. Appl. Catal. A Gen. 337, 138–147. https://doi.org/10.1016/j.apcata.2007.12.006

Liu, X., Chun, C.-M., Aksay, I.A., Shih, W.-H., 2000. Synthesis of Mesostructured Nickel Oxide with Silica. Ind. Eng. Chem. Res. 39, 684–692. https://doi.org/10.1021/ie990129l

Llanos, Z.R., Provoost, G.F., Deering, W.G., Debaene, F.J., 1997. Integrated process for the recovery of metals and fused alumina from spent catalysts. US Patent 5,702,500.

Lok, C.M., 2018. Structure and performance of selective hydrogenation catalysts, in: Jackson, S.D. (Ed.), Hydrogenation: Catalysts and Processes. De Gruyter, pp. 1–18.

Lok, C.M., 2014. The 2014 Murray Raney Award Lecture: Architecture and Preparation of Supported Nickel Catalysts. Top. Catal. 57, 1318–1324. https://doi.org/10.1007/s11244-014-0298-0

Lorenz, P., Finster, J., Wendt, G., Salyn, J.V., Žumadilov, E.K., Nefedov, V.I., 1979. Esca investigations of some NiO/SiO_2 and $NiO—Al_2O_3/SiO_2$ catalysts. J. Electron Spectros. Relat. Phenomena 16, 267–276. https://doi.org/10.1016/0368-2048(79)80023-7

Louisnard, O., 2012. A simple model of ultrasound propagation in a cavitating liquid. Part I: Theory, nonlinear attenuation and traveling wave generation. Ultrason. Sonochem. 19, 56–65. https://doi.org/10.1016/j.ultsonch.2011.06.007

Lovell, E., Scott, J., Amal, R., 2015. $Ni\text{-}SiO_2$ Catalysts for the Carbon Dioxide Reforming of Methane: Varying Support Properties by Flame Spray Pyrolysis. Molecules 20, 4594–4609. https://doi.org/10.3390/molecules20034594

Lu, J., Lei, Y., Wan, G., Mei, Z., Yu, J., Zhao, Y., He, S., Luo, Y., 2020. Weakening the metal-support strong interaction to enhance catalytic performances of alumina supported Ni-based catalysts for producing hydrogen. Appl. Catal. B Environ. 263, 118177. https://doi.org/10.1016/j.apcatb.2019.118177

Lu, P., Huang, Q., Bourtsalas, A.C., Chi, Y., Yan, J., 2019. Effect of Operating Conditions on the Coke Formation and Nickel Catalyst Performance During Cracking of Tar. Waste and Biomass Valorization 10, 155–165. https://doi.org/10.1007/s12649-017-0044-5

Luche, J.-L., 1998. Synthetic Organic Sonochemistry. Plenum Press, New York. https://doi.org/10.1007/978-1-4899-1910-6

Lunevich, L., 2020. Aqueous Silica and Silica Polymerisation, in: Desalination - Challenges and Opportunities. IntechOpen. https://doi.org/10.5772/intechopen.84824

Ma, Y., Sun, Q., Wu, D., Fan, W.-H., Deng, J.-F., 1999. A gel-oxalate co-precipitation process for preparation of $Cu/ZnO/Al_2O_3$ ultrafine catalyst for methanol synthesis from CO_2+H_2: (II) effect of various calcination conditions. Appl. Catal. A Gen. 177, 177–184. https://doi.org/10.1016/S0926-860X(98)00266-X

Macedo Neto, O.R., Ribeiro, N.F.P., Perez, C.A.C., Schmal, M., Souza, M.M.V.M., 2010. Incorporation of cerium ions by sonication in Ni–Mg–Al layered double hydroxides. Appl. Clay Sci. 48, 542–546. https://doi.org/10.1016/j.clay.2010.02.015

Madras, G., McCoy, B.J., 2003. Temperature effects for crystal growth: a distribution kinetics approach. Acta Mater. 51, 2031–2040. https://doi.org/10.1016/S1359-6454(02)00621-3

Mahammadunnisa, S., Manoj Kumar Reddy, P., Lingaiah, N., Subrahmanyam, C., 2013. $NiO/Ce_{1-x}Ni_xO_{2-\delta}$ as an alternative to noble metal catalysts for CO oxidation. Catal. Sci. Technol. 3, 730–736. https://doi.org/10.1039/C2CY20641B

Mahboob, S., Haghighi, M., Rahmani, F., 2017. Sonochemically preparation and characterization of bimetallic $Ni\text{-}Co/Al_2O_3\text{-}ZrO_2$ nanocatalyst: Effects of ultrasound irradiation time and power on catalytic properties and activity in dry reforming of CH_4. Ultrason. Sonochem. 38, 38–49. https://doi.org/10.1016/j.ultsonch.2017.02.039

Mahmoodi, N.M., Oveisi, M., Bakhtiari, M., Hayati, B., Shekarchi, A.A., Bagheri, A., Rahimi, S., 2019. Environmentally friendly ultrasound-assisted synthesis of magnetic zeolitic imidazolate framework - Graphene oxide nanocomposites and pollutant removal from water. J. Mol. Liq. 282, 115–130. https://doi.org/10.1016/j.molliq.2019.02.139

Mallaiah, M., Reddy, G.V., 2016a. Optimization studies on a continuous catalytic reactive distillation column for methyl acetate production with response surface methodology. J. Taiwan Inst. Chem. Eng. 69, 25–40. https://doi.org/10.1016/j.jtice.2016.10.007

Mallaiah, M., Reddy, G.V., 2016b. Optimization studies on a continuous catalytic reactive distillation column for methyl acetate production with response surface methodology. J. Taiwan Inst. Chem. Eng. 69, 25–40. https://doi.org/10.1016/j.jtice.2016.10.007

Manzoli, M., Bonelli, B., 2018. Microwave, Ultrasound, and Mechanochemistry: Unconventional Tools that Are Used to Obtain “Smart” Catalysts for CO_2

Hydrogenation. Catalysts 8, 262. https://doi.org/10.3390/catal8070262

Marafi, A., Stanislaus, A., Furimsky, E., 2010. Handbook of Spent Hydroprocessing Catalysts. Elsevier, Amsterdam.

Marafi, M., Stanislaus, A., 2011. Waste Catalyst Utilization: Extraction of Valuable Metals from Spent Hydroprocessing Catalysts by Ultrasonic-Assisted Leaching with Acids. Ind. Eng. Chem. Res. 50, 9495–9501. https://doi.org/10.1021/ie200789u

Marafi, M., Stanislaus, A., 2008. Spent catalyst waste management: A review. Resour. Conserv. Recycl. 52, 859–873. https://doi.org/10.1016/j.resconrec.2008.02.004

Margulis, M.A., 1995. Sonochemistry and Cavitation. Gordon and Breach Science Publishers.

Marshall, J.S., Wu, J., 2015. Acoustic streaming, fluid mixing, and particle transport by a Gaussian ultrasound beam in a cylindrical container. Phys. Fluids 27, 103601. https://doi.org/10.1063/1.4932232

Martin, C.A., Milinsk, M.C., Visentainer, J. V., Matsushita, M., De-Souza, N.E., 2007. Trans fatty acid-forming processes in foods: a review. An. Acad. Bras. Cienc. 79, 343–350. https://doi.org/10.1590/S0001-37652007000200015

Mason, T.J., 2003. Sonochemistry and sonoprocessing: the link, the trends and (probably) the future. Ultrason. Sonochem. 10, 175–179. https://doi.org/10.1016/S1350-4177(03)00086-5

Mason, T.J., 1992. Practical Sonochemistry: User's Guide to Applications in Chemistry and Chemical Engineering. Ellis Howood Ldt., New York.

Mason, T.J., Lorimer, J.P., 2002. Synthesis, in: Applied Sonochemistry: Uses of Power Ultrasound in Chemistry and Processing. Wiley-VCH Verlag GmbH & Co. KGaA, Weinheim, FRG, pp. 75–130. https://doi.org/10.1002/352760054X.ch3

Mason, T.J., Lorimer, J.P., 1988. Sonochemistry: Theory, Applications and Uses of Ultrasound in Chemistry. Ellis Horwood Publishers. https://doi.org/9780745802404

Mason, T.J., Peters, D., 2002. Practical Sonochemistry: Power Ultrasound Uses and Applications. Woodhead Publishing. https://doi.org/10.1002/352760054X

Mason, T.J., Petrier, C., 2004. Ultrasound Processes, in: Advanced Oxidation Processes for Water and Wastewater Treatment. IWA Publishing, pp. 185–208.

Mathure, P. V., Ganguly, S., Patwardhan, A. V., Saha, R.K., 2007. Steam Reforming of Ethanol Using a Commercial Nickel-Based Catalyst. Ind. Eng. Chem. Res. 46, 8471–8479. https://doi.org/10.1021/ie070321k

McArdle, S., Leahy, J.J., Curtin, T., Tanner, D., 2014. Hydrogenation of sunflower oil over Pt–Ni bimetallic supported catalysts: Preparation, characterization and catalytic activity. Appl. Catal. A Gen. 474, 78–86. https://doi.org/10.1016/j.apcata.2013.08.033

McClements, D.J., 1995. Advances in the application of ultrasound in food analysis and processing. Trends Food Sci. Technol. 6, 293–299. https://doi.org/10.1016/S0924-2244(00)89139-6

McNaught, A.D., Wilkinson, A., 1997. IUPAC Compendium of Chemical Terminology, 2nd ed. Blackwell Scientific Publications, Oxford.

Meister, E.C., Willeke, M., Angst, W., Togni, A., Walde, P., 2014. Confusing Quantitative Descriptions of Brønsted Lowry Acid Base Equilibria in Chemistry Textbooks - A Critical Review and Clarifications for Chemical Educators. Helv. Chim. Acta 97, 1–31. https://doi.org/10.1002/hlca.201300321

Mejía, C.H., Vogt, C., Weckhuysen, B.M., de Jong, K.P., 2018. Stable niobia-supported nickel catalysts for the hydrogenation of carbon monoxide to hydrocarbons. Catal. Today. https://doi.org/10.1016/j.cattod.2018.11.036

Mentler, A., Schomakers, J., Kloss, S., Zechmeister-Boltenstern, S., Schuller, R., Mayer, H., 2017. Calibration of ultrasonic power output in water, ethanol and sodium polytungstate. Int. Agrophysics 31, 583–588. https://doi.org/10.1515/intag-2016-0083

Merouani, S., Hamdaoui, O., Rezgui, Y., Guemini, M., 2013. Effects of ultrasound frequency and acoustic amplitude on the size of sonochemically active bubbles – Theoretical study. Ultrason. Sonochem. 20, 815–819. https://doi.org/10.1016/j.ultsonch.2012.10.015

Meshkani, F., Rezaei, M., 2015. Preparation of mesoporous nanocrystalline iron based catalysts for high temperature water gas shift reaction: Effect of preparation factors. Chem. Eng. J. 260, 107–116. https://doi.org/10.1016/j.cej.2014.08.080

Meshkani, F., Rezaei, M., 2011. Nickel catalyst supported on magnesium oxide with high surface area and plate-like shape: A highly stable and active catalyst in methane reforming with carbon dioxide. Catal. Commun. 12, 1046–1050. https://doi.org/10.1016/j.catcom.2011.03.013

Mile, B., Stirling, D., Zammitt, M.A., Lovell, A., Webb, M., 1988. The location of nickel oxide and nickel in silica-supported catalysts: Two forms of "NiO" and the assignment of temperature-programmed reduction profiles. J. Catal. 114, 217–229. https://doi.org/10.1016/0021-9517(88)90026-7

Mond, L., Langer, C., Quincke, F., 1890. L.—Action of carbon monoxide on nickel. J. Chem. Soc., Trans. 57, 749–753. https://doi.org/10.1039/CT8905700749

Montes, M., Penneman de Bosscheyde, C., Hodnett, B.K., Delannay, F., Grange, P., Delmon, B., 1984. Influence of metal-support interactions on the dispersion, distribution, reducibility and catalytic activity of Ni/SiO_2 catalysts. Appl. Catal. 12, 309–330. https://doi.org/10.1016/S0166-9834(00)81670-X

Moogi, S., Lee, I.-G., Park, J.-Y., 2019. Effect of La_2O_3 and CeO_2 loadings on formation of nickel-phyllosilicate precursor during preparation of Ni/SBA-15 for hydrogen-rich gas production from ethanol steam reforming. Int. J. Hydrogen Energy 44, 29537–29546. https://doi.org/10.1016/j.ijhydene.2019.03.053

Moosakazemi, F., Tavakoli Mohammadi, M.R., Zakeri, M., Esmaeili, M.J., Rafiei, H., 2020. Development of an environmentally friendly flowsheet for the hydrometallurgical recovery of nickel and aluminum from spent methanation catalyst. J. Clean. Prod. 244, 118731. https://doi.org/10.1016/j.jclepro.2019.118731

Moradiyan, E., Halladj, R., Askari, S., 2018. Beneficial Use of Ultrasound in Rapid-Synthesis of SAPO34/ZSM-5 Nanocomposite and Its Catalytic Performances on MTO Reaction. Ind. Eng. Chem. Res. 57, 1871–1882. https://doi.org/10.1021/acs.iecr.7b03772

Moulijn, J.., van Leeuwen, P.W.N.M., van Santen, R.A., 1993. Preparation of supported catalysts, in: Moulijn, J.., van Leeuwen, P.W.N.M., van Santen, R.A. (Eds.), Catalysis: An Integrated Approach to Homogeneous, Heterogeneous and Industrial Catalysis. Elsevier B.V., pp. 335–360.

https://doi.org/10.1016/S0167-2991(08)63813-6

Moulton, K.J., Koritala, S., Frankel, E.N., 1983. Ultrasonic hydrogenation of soybean oil. J. Am. Oil Chem. Soc. 60, 1257–1258. https://doi.org/10.1007/BF02702094

Munnik, P., de Jongh, P.E., de Jong, K.P., 2015. Recent Developments in the Synthesis of Supported Catalysts. Chem. Rev. 115, 6687–6718. https://doi.org/10.1021/cr500486u

Munnik, Peter, de Jongh, P.E., de Jong, K.P., 2015. Recent Developments in the Synthesis of Supported Catalysts. Chem. Rev. 115, 6687–6718. https://doi.org/10.1021/cr500486u

Nadeina, K.A., Kazakov, M.O., Kovalskaya, A.A., Danilevich, V.V., Klimov, O.V., Danilova, I.G., Khabibulin, D.F., Gerasimov, E.Y., Prosvirin, I.P., Ushakov, V.A., Fedotov, K.V., Kondrashev, D.O., Kleimenov, A.V., Noskov, A.S., 2019. Guard bed catalysts for silicon removal during hydrotreating of middle distillates. Catal. Today 329, 53–62. https://doi.org/10.1016/j.cattod.2018.11.075

Nares, R., Ramírez, J., Gutiérrez-Alejandre, A., Cuevas, R., 2009. Characterization and Hydrogenation Activity of Ni/Si(Al)- MCM-41 Catalysts Prepared by Deposition–Precipitation. Ind. Eng. Chem. Res. 48, 1154–1162. https://doi.org/10.1021/ie800569j

Nele, M., Vidal, A., Bhering, D.L., Carlos Pinto, J., Salim, V.M.M., 1999. Preparation of high loading silica supported nickel catalyst: simultaneous analysis of the precipitation and aging steps. Appl. Catal. A Gen. 178, 177–189. https://doi.org/10.1016/S0926-860X(98)00285-3

Neppiras, E.A., 1980. Acoustic Cavitation. Phys. Reports-Review Sect. Phys. Lett. 61, 159–251.

Nesterenko, A.I., Berlizov, Y.S., 2007. The possibility of cracking hydrocarbons with cavitation. A quantitative energy assessment. Chem. Technol. Fuels Oils 43, 515–518. https://doi.org/10.1007/s10553-007-0089-4

Nguyen, V.S., Rouxel, D., Hadji, R., Vincent, B., Fort, Y., 2011. Effect of ultrasonication and dispersion stability on the cluster size of alumina nanoscale particles in aqueous solutions. Ultrason. Sonochem. 18, 382–388. https://doi.org/10.1016/j.ultsonch.2010.07.003

Nikitenko, S.I., Moisy, P., Madic, C., 1999. Sonochemical Oxidation of Np(V) in Aqueous Nitric Acid Medium and Sonochemical Extraction of Np in two-Phase TBP (30 vol.%)-n-Dodecane/HNO3/H2O System. Radiochim. Acta 86. https://doi.org/10.1524/ract.1999.86.12.23

Nikitenko, S.I., Seliverstov, A.F., 2000. A synergetic effect in nitrous acid formation by sonolysis of nitric acid in the presence of nitrous oxide. Russ. Chem. Bull. 49, 2077–2079.

Nitta, Y., Imanaka, T., Teranishi, S., 1985. Preparation chemistry of precipitated $NiSiO_2$ catalysts for enantioselective hydrogenation. J. Catal. 96, 429–438. https://doi.org/10.1016/0021-9517(85)90312-4

Normann, W., 1903. Process for Converting Unsaturated Fatty Acids or their Glycerides into Saturated Compounds. GB190301515.

Novaes, L. da R., Pacheco, M.E., Salim, V.M.M., de Resende, N.S., 2017. Accelerated deactivation studies of hydrotreating catalysts in pilot unit. Appl. Catal. A Gen. 548, 114–121. https://doi.org/10.1016/j.apcata.2017.06.040

O'Brien, M.A., 1997. An Investigation into Coking on Catalyst Support Materials & Supported Metal Catalysts. Dublin City University.

Occelli, M.L., Psaras, D., Suib, S.L., Stencel, J.M., 1986. Metal contaminant effects on the properties of a silica-rich fluid cracking catalyst. Appl. Catal. 28, 143–160. https://doi.org/10.1016/S0166-9834(00)82499-9

Okamoto, Y., Nitta, Y., Imanaka, T., Teranishi, S., 1980. Surface state and catalytic activity and selectivity of nickel catalysts in hydrogenation reactions III. Electronic and catalytic properties of nickel catalysts. J. Catal. 64, 397–404. https://doi.org/10.1016/0021-9517(80)90512-6

Oruji, S., Khoshbin, R., Karimzadeh, R., 2019. Combination of precipitation and ultrasound irradiation methods for preparation of lanthanum-modified Y zeolite nano-catalysts used in catalytic cracking of bulky hydrocarbons. Mater. Chem. Phys. 230, 131–144. https://doi.org/10.1016/j.matchemphys.2019.03.038

Otterstedt, J.-E., Brandreth, D.A., 1998. Small Particles of Silica, in: Small Particles Technology. Springer US, Boston, MA, pp. 29–84. https://doi.org/10.1007/978-1-4757-6523-6_2

Oza, R., Patel, S., 2012. Recovery of Nickel from Spent Ni/Al_2O_3 Catalysts using Acid Leaching, Chelation and Ultrasonication. Res. J. Recent Sci. 1, 434–443.

Oza, R., Shah, N., Patel, S., 2011. Recovery of nickel from spent catalysts using ultrasonication-assisted leaching. J. Chem. Technol. Biotechnol. 86, 1276–1281. https://doi.org/10.1002/jctb.2649

Oza, R., Shah, N., Patel, S., 2010. Extraction of Nickel from Spent Catalyst Using EDTA as Chelating Agent. Nature, Environ. Pollut. Technol. 10, 197–200.

Panahi, P.N., Niaei, A., Salari, D., Mousavi, S.M., Delahay, G., 2015. Ultrasound-assistant preparation of Cu-SAPO-34 nanocatalyst for selective catalytic reduction of NO by NH 3. J. Environ. Sci. 35, 135–143. https://doi.org/10.1016/j.jes.2015.01.032

Pande, G., Akoh, C.C., Lai, O.-M., 2012. Food Uses of Palm Oil and Its Components, in: Palm Oil. Elsevier, pp. 561–586. https://doi.org/10.1016/B978-0-9818936-9-3.50022-8

Parhi, P.K., Park, K.H., Senanayake, G., 2013. A kinetic study on hydrochloric acid leaching of nickel from $Ni–Al_2O_3$ spent catalyst. J. Ind. Eng. Chem. 19, 589–594. https://doi.org/10.1016/j.jiec.2012.09.028

Patterson, H.B.W., 2011. The Hydrogenation Reaction, in: List, G.R., King, J.W. (Eds.), Hydrogenation of Fats and Oils. AOCS Press, Urbana, IL.

Pazos-Perez, N., Schäferhans, J., Skorb, E. V., Fery, A., Andreeva, D. V., 2012. Ultrasound driven formation of metal-supported nanocatalysts. Microporous Mesoporous Mater. 154, 164–169. https://doi.org/10.1016/j.micromeso.2011.08.011

Pecha, R., Gompf, B., 2000. Microimplosions: Cavitation Collapse and Shock Wave Emission on a Nanosecond Time Scale. Phys. Rev. Lett. 84, 1328–1330. https://doi.org/10.1103/PhysRevLett.84.1328

Pérez, A., Lamonier, J.-F., Giraudon, J.-M., Molina, R., Moreno, S., 2011. Catalytic activity of Co–Mg mixed oxides in the VOC oxidation: Effects of ultrasonic assisted in the synthesis. Catal. Today 176, 286–291. https://doi.org/10.1016/j.cattod.2010.11.088

Petrovic, S.J., Bogdanovic, G.D., Antonijevic, M.M., 2018. Leaching of chalcopyrite with hydrogen peroxide in hydrochloric acid solution. Trans. Nonferrous Met.

Soc. China 28, 1444–1455. https://doi.org/10.1016/S1003-6326(18)64788-0

Pettiti, I., Gazzoli, D., Benito, P., Fornasari, G., Vaccari, A., 2015. The reducibility of highly stable Ni-containing species in catalysts derived from hydrotalcite-type precursors. RSC Adv. 5, 82282–82291. https://doi.org/10.1039/C5RA13863A

Pfefferle, L., Fang, F., Iyyamperumal, E., Keskar, G., 2013. Nanostructures of Boron, Carbon and Magnesium Diboride for High Temperature Superconductivity. Argonne, IL (United States). https://doi.org/10.2172/1111414

Philipp, R., Fujimoto, K., 1992. FTIR spectroscopic study of carbon dioxide adsorption/desorption on magnesia/calcium oxide catalysts. J. Phys. Chem. 96, 9035–9038. https://doi.org/10.1021/j100201a063

Pimerzin, Aleksey, Roganov, A., Mozhaev, A., Maslakov, K., Nikulshin, P., Pimerzin, Andrey, 2018. Active phase transformation in industrial CoMo/Al_2O_3 hydrotreating catalyst during its deactivation and rejuvenation with organic chemicals treatment. Fuel Process. Technol. 173, 56–65. https://doi.org/10.1016/j.fuproc.2018.01.008

Pitto-Barry, A., Barry, N.P.E., 2019. Effect of Temperature on the Nucleation and Growth of Precious Metal Nanocrystals. Angew. Chemie Int. Ed. 58, 18482–18486. https://doi.org/10.1002/anie.201912219

Plourde, M., Belkacemi, K., Arul, J., 2004. Hydrogenation of Sunflower Oil with Novel Pd Catalysts Supported on Structured Silica. Ind. Eng. Chem. Res. 43, 2382–2390. https://doi.org/10.1021/ie030708x

Pokhrel, N., Vabbina, P.K., Pala, N., 2016. Sonochemistry: Science and Engineering. Ultrason. Sonochem. 29, 104–128. https://doi.org/10.1016/j.ultsonch.2015.07.023

Price, G.J., 1992. Current Trends in Sonochemistry. RSC, Cambridge.

Qiu, Y., Chen, J., Zhang, J., 2007. Effects of MgO promoter on properties of Ni/Al_2O_3 catalysts for partial oxidation of methane to syngas. Front. Chem. Eng. China 1, 167–171. https://doi.org/10.1007/s11705-007-0031-7

Qu, J., Li, W., Cao, C.-Y., Yin, X.-J., Zhao, L., Bai, J., Qin, Z., Song, W.-G., 2012. Metal silicate nanotubes with nanostructured walls as superb adsorbents for uranyl

ions and lead ions in water. J. Mater. Chem. 22, 17222. https://doi.org/10.1039/c2jm33178k

Quitete, C.P.B., Tavares, R.P.A., Bittencourt, R.C.P., Souza, M.M.V.M., 2016. Coking Study of Nickel Catalysts Using Model Compounds. Catal. Letters 146, 1435–1444. https://doi.org/10.1007/s10562-016-1773-y

Raba, D.N., Chambre, D.R., Copolovici, D.-M., Moldovan, C., Copolovici, L.O., 2018. The influence of high-temperature heating on composition and thermo-oxidative stability of the oil extracted from Arabica coffee beans. PLoS One 13, e0200314. https://doi.org/10.1371/journal.pone.0200314

Rahbar Shamskar, F., Meshkani, F., Rezaei, M., 2017. Ultrasound assisted co-precipitation synthesis and catalytic performance of mesoporous nanocrystalline NiO-Al_2O_3 powders. Ultrason. Sonochem. 34, 436–447. https://doi.org/10.1016/j.ultsonch.2016.06.021

Rahimi, G., Rastegar, S.O., Rahmani Chianeh, F., Gu, T., 2020. Ultrasound-assisted leaching of vanadium from fly ash using lemon juice organic acids. RSC Adv. 10, 1685–1696. https://doi.org/10.1039/C9RA09325G

Rahmani, F., Haghighi, M., Mahboob, S., 2016. CO_2 -enhanced dehydrogenation of ethane over sonochemically synthesized Cr/clinoptilolite-ZrO_2 nanocatalyst: Effects of ultrasound irradiation and ZrO_2 loading on catalytic activity and stability. Ultrason. Sonochem. 33, 150–163. https://doi.org/10.1016/j.ultsonch.2016.04.034

Raman, V., Abbas, A., 2008. Experimental investigations on ultrasound mediated particle breakage. Ultrason. Sonochem. 15, 55–64. https://doi.org/10.1016/j.ultsonch.2006.11.009

Ramesh, S., Koltypin, Y., Prozorov, R., Gedanken, A., 1997. Sonochemical Deposition and Characterization of Nanophasic Amorphous Nickel on Silica Microspheres. Chem. Mater. 9, 546–551. https://doi.org/10.1021/cm960390h

Ramos-Cano, J., González-Zamarripa, G., Carrillo-Pedroza, F.R., Soria-Aguilar, M. de J., Hurtado-Macías, A., Cano-Vielma, A., 2016. Kinetics and statistical analysis of nickel leaching from spent catalyst in nitric acid solution. Int. J. Miner. Process. 148, 41–47. https://doi.org/10.1016/j.minpro.2016.01.006

Rapaport, D., 2000. Are spent hydrocracking catalysts listed hazardous wastes? Hydrocarb. Process. 79, 49–53.

Razeghi, M., 2009. Semiconductor Characterization Techniques, in: Fundamentals of Solid State Engineering. Springer US, Boston, MA, pp. 1–29. https://doi.org/10.1007/978-0-387-92168-6_16

Retamal Marín, R., Babick, F., Lindner, G.-G., Wiemann, M., Stintz, M., 2018. Effects of Sample Preparation on Particle Size Distributions of Different Types of Silica in Suspensions. Nanomaterials 8, 454. https://doi.org/10.3390/nano8070454

Richards, W.T., Loomis, A.L., 1927. The chemical effects of high frequency sound waves I. A preliminary survey. J. Am. Chem. Soc. 49, 3086–3100. https://doi.org/10.1021/ja01411a015

Richardson, J., Scates, R., Twigg, M. V., 2003. X-ray diffraction study of nickel oxide reduction by hydrogen. Appl. Catal. A Gen. 246, 137–150. https://doi.org/10.1016/S0926-860X(02)00669-5

Richardson, J.T., 1989. Principles of Catalyst Development, in: Twigg, M.V., Spencer, M.S. (Eds.), Fundamental and Applied Catalysis. Plenum Press, New York.

Rifaya, M.N., Theivasanthi, T., Alagar, M., 2012. Chemical Capping Synthesis of Nickel Oxide Nanoparticles and their Characterizations Studies. Nanosci. Nanotechnol. 2, 134–138. https://doi.org/10.5923/j.nn.20120205.01

Rodríguez, E., Félix, G., Ancheyta, J., Trejo, F., 2018. Modeling of hydrotreating catalyst deactivation for heavy oil hydrocarbons. Fuel 225, 118–133. https://doi.org/10.1016/j.fuel.2018.02.085

Rosner, H., 2018. Palm oil is unavoidable. Can it be sustainable? [WWW Document]. Natl. Geogr. Mag. URL https://www.nationalgeographic.com/magazine/article/palm-oil-products-borneo-africa-environment-impact

Rufete-Beneite, M., Román-Martínez, M.C., 2019. Unraveling Toluene Conversion during the Liquid Phase Hydrogenation of Cyclohexene (in Toluene) with Rh Hybrid Catalysts. Catalysts 9, 973. https://doi.org/10.3390/catal9120973

Ruhr-Universitat, 2010. Microkinetic modeling of heterogeneous catalysts [WWW Document]. URL http://www.techem.ruhr-uni-bochum.de/index2.php?section=techem&ordner=research&group=group&sub=muhler&lang=en&page=microkinetic_modelling.html (accessed 7.4.18).

Ryabchuk, P., Agostini, G., Pohl, M.-M., Lund, H., Agapova, A., Junge, H., Junge, K., Beller, M., 2018. Intermetallic nickel silicide nanocatalyst—A non-noble metal–based general hydrogenation catalyst. Sci. Adv. 4, eaat0761. https://doi.org/10.1126/sciadv.aat0761

Rynkowski, J.M., Paryjczak, T., Lenik, M., 1993. On the nature of oxidic nickel phases in NiO/γ-Al_2O_3 catalysts. Appl. Catal. A Gen. 106, 73–82. https://doi.org/10.1016/0926-860X(93)80156-K

Sabatier, P., 1922. Catalysis in organic chemistry. D. Van Nostrand Company, New York.

Sabatier, P., Senderens, J.B., 1897. Action du nickel sur l'éthylène. Synthèse de l'éthane. C. R. Acad. Sci. Paris 124, 1358–1360.

Sádaba, I., López Granados, M., Riisager, A., Taarning, E., 2015. Deactivation of solid catalysts in liquid media: the case of leaching of active sites in biomass conversion reactions. Green Chem. 17, 4133–4145. https://doi.org/10.1039/C5GC00804B

Sadeghpour, P., Haghighi, M., Ebrahimi, A., 2021. Ultrasound-assisted rapid hydrothermal design of efficient nanostructured MFI-Type aluminosilicate catalyst for methanol to propylene reaction. Ultrason. Sonochem. 72, 105416. https://doi.org/10.1016/j.ultsonch.2020.105416

Sahoo, Y., He, Y., Swihart, M.T., Wang, S., Luo, H., Furlani, E.P., Prasad, P.N., 2005. An aerosol-mediated magnetic colloid: Study of nickel nanoparticles. J. Appl. Phys. 98, 054308. https://doi.org/10.1063/1.2033145

Sahu, K.K., Agarwal, A., Pandey, B.D., 2005. Nickel recovery from spent nickel catalyst. Waste Manag. Res. 23, 148–154. https://doi.org/10.1177/0734242X05052334

Salas, J.J., Bootello, M.A., Martínez-Force, E., Venegas Calerón, M., Garcés, R., 2021. High stearic sunflower oil: Latest advances and applications. OCL 28, 35. https://doi.org/10.1051/ocl/2021022

Sancheti, S. V., Gogate, P.R., 2017a. Ultrasound assisted selective catalytic transfer hydrogenation of soybean oil using 5% Pd/C as catalyst under ambient conditions in water. Ultrason. Sonochem. 38, 161–167. https://doi.org/10.1016/j.ultsonch.2017.03.004

Sancheti, S. V., Gogate, P.R., 2017b. A review of engineering aspects of intensification of chemical synthesis using ultrasound. Ultrason. Sonochem. 36, 527–543. https://doi.org/10.1016/j.ultsonch.2016.08.009

Santos, H.M., Loderiro, C., Capelo-Martinez, J.L., 2009. The Power of Ultrasound, in: Capelo-Martinez, J.L. (Ed.), Ultrasound in Chemistry: Analytical Applications. Wiley-VCH Verlag GmbH & Co. KGaA, Weinheim, pp. 1–16.

Schäferhans, J., Gómez-Quero, S., Andreeva, D. V., Rothenberg, G., 2011. Novel and Effective Copper-Aluminum Propane Dehydrogenation Catalysts. Chem. - A Eur. J. 17, 12254–12256. https://doi.org/10.1002/chem.201102580

Schlögl, R., 1997. Characterisation of solid catalysts, in: Ertl, G., Knözinger, H., Weitkamp, J. (Eds.), Handbook of Heterogeneous Catalysis. Wiley-VCH, Weinheim.

Schüth, F., Unger, K., 1997. Precipitation and coprecipitation, in: Ertl, G., Knözinger, H., Weitkamp, J. (Eds.), Handbook of Heterogeneous Catalysis. Wiley-VCH, Weinheim.

Scott, S.L., 2018. A Matter of Life(time) and Death. ACS Catal. 8, 8597–8599. https://doi.org/10.1021/acscatal.8b03199

Shahbudin, M.I., Jacob, D.M., Ameen, M., Aqsha, A., Azizan, M.T., Yusoff, M.H.M., Sher, F., 2021. Liquid value-added chemicals production from aqueous phase reforming of sorbitol and glycerol over sonosynthesized Ni-based catalyst. J. Environ. Chem. Eng. 9, 105766. https://doi.org/10.1016/j.jece.2021.105766

Shalvoy, R.B., Davis, B.H., Reucroft, P.J., 1980. Studies of the metal-support interaction in coprecipitated nickel on alumina methanation catalysts using X-ray photoelectron spectroscopy (XPS). Surf. Interface Anal. 2, 11–16. https://doi.org/10.1002/sia.740020104

Shalvoy, R.B., Reucroft, P.J., 1979. Characterization of coprecipitated nickel on silica methanation catalysts by X-ray photoelectron spectroscopy. J. Catal. 56, 336–348. https://doi.org/10.1016/0021-9517(79)90126-X

Sharahi, F.J., Shahbazi, A., 2017. Melamine-based dendrimer amine-modified magnetic nanoparticles as an efficient Pb(II) adsorbent for wastewater treatment: Adsorption optimization by response surface methodology. Chemosphere 189, 291–300. https://doi.org/10.1016/j.chemosphere.2017.09.050

Sharifi, M., Haghighi, M., Abdollahifar, M., 2014. Hydrogen production via reforming of biogas over nanostructured Ni/Y catalyst: Effect of ultrasound irradiation and Ni-content on catalyst properties and performance. Mater. Res. Bull. 60, 328–340. https://doi.org/10.1016/j.materresbull.2014.07.027

Shim, J.-O., Jeong, D.-W., Jang, W.-J., Jeon, K.-W., Kim, S.-H., Jeon, B.-H., Roh, H.-S., Na, J.-G., Oh, Y.-K., Han, S.S., Ko, C.H., 2015. Optimization of unsupported CoMo catalysts for decarboxylation of oleic acid. Catal. Commun. 67, 16–20. https://doi.org/10.1016/j.catcom.2015.03.034

Shimizu, R., Sawada, K., Enokida, Y., Yamamoto, I., 2005. Generation of Nitrous Acid by Ultrasound Irradiation in the Organic Solution Consisting of Tri- n -butylphosphate, Nitric Acid and Water. J. Nucl. Sci. Technol. 42, 979–983. https://doi.org/10.1080/18811248.2005.9711049

Shimura, K., Fujitani, T., 2019. Effects of promoters on the performance of a VO /SiO_2 catalyst for the oxidation of methane to formaldehyde. Appl. Catal. A Gen. 577, 44–51. https://doi.org/10.1016/j.apcata.2019.03.014

Shinde, V.M., Madras, G., 2014. Catalytic performance of highly dispersed Ni/TiO_2 for dry and steam reforming of methane. RSC Adv. 4, 4817. https://doi.org/10.1039/c3ra45961f

Sidik, S.M., Triwahyono, S., Jalil, A.A., Aziz, M.A.A., Fatah, N.A.A., Teh, L.P., 2016. Tailoring the properties of electrolyzed Ni/mesostructured silica nanoparticles (MSN) via different Ni-loading methods for CO_2 reforming of CH_4. J. CO2 Util. 13, 71–80. https://doi.org/10.1016/j.jcou.2015.12.004

Sing, K.S.W., Everett, D.H., Haul, R.A.W., Moscou, L., Pierotti, R.A., Rouquerol, J., Siemieniewska, T., 2008. Reporting Physisorption Data for Gas/Solid Systems, in: Handbook of Heterogeneous Catalysis. Wiley-VCH Verlag GmbH & Co. KGaA, Weinheim, Germany, pp. 1217–1230. https://doi.org/10.1002/9783527610044.hetcat0065

Singh, B., 2009. Treatment of spent catalyst from the nitrogenous fertilizer industry—A review of the available methods of regeneration, recovery and disposal. J. Hazard. Mater. 167, 24–37. https://doi.org/10.1016/j.jhazmat.2009.01.071

Singh, S.C., Zeng, H., Guo, C., Gopal, R., Cai, W., 2012. Introduction of Materials and Architectures at the Nanoscale, in: Singh, S.C., Zeng, H., Guo, C., Cai, W. (Eds.), Nanomaterials: Processing and Characterization with Lasers. Wiley-VCH Verlag GmbH & Co. KGaA, Weinheim, Germany, pp. 35–66.

https://doi.org/10.1002/9783527646821.ch2

Skorb, E. V., Baidukova, O., Andreeva, O.A., Cherepanov, P. V., Andreeva, D. V., 2013. Formation of polypyrrole/metal hybrid interfacial layer with self-regulation functions via ultrasonication. Bioinspired, Biomim. Nanobiomaterials 2, 123–129. https://doi.org/10.1680/bbn.13.00003

Skorb, E. V., Möhwald, H., Irrgang, T., Fery, A., Andreeva, D. V., 2010. Ultrasound-assisted design of metal nanocomposites. Chem. Commun. 46, 7897. https://doi.org/10.1039/c0cc00965b

Słowik, G., Gawryszuk-Rżysko, A., Greluk, M., Machocki, A., 2016. Estimation of Average Crystallites Size of Active Phase in Ceria-Supported Cobalt-Based Catalysts by Hydrogen Chemisorption vs TEM and XRD Methods. Catal. Letters 146, 2173–2184. https://doi.org/10.1007/s10562-016-1843-1

Smith, R.A.P., 2009. Surface Characterisation of Heterogeneous Catalysts by XPS: Part II. Platin. Met. Rev. 53, 109–110. https://doi.org/10.1595/147106709X432943

Smitha, S., Shajesh, P., Aravind, P.R., Kumar, S.R., Pillai, P.K., Warrier, K.G.K., 2006. Effect of aging time and concentration of aging solution on the porosity characteristics of subcritically dried silica aerogels. Microporous Mesoporous Mater. 91, 286–292. https://doi.org/10.1016/j.micromeso.2005.11.051

Soghrati, E., Ong, T.K.C., Poh, C.K., Kawi, S., Borgna, A., 2018. Zeolite–supported nickel phyllosilicate catalyst for CO hydrogenolysis of cyclic ethers and polyols. Appl. Catal. B Environ. 235, 130–142. https://doi.org/10.1016/j.apcatb.2018.04.053

Stanković, M., Čupić, Ž., Gabrovska, M., Banković, P., Nikolova, D., Jovanović, D., 2015. Characteristics and catalytic behavior of supported NiMgAg/D catalysts in the partial hydrogenation of soybean oil. React. Kinet. Mech. Catal. 115, 105–127. https://doi.org/10.1007/s11144-014-0829-5

Stanković, M., Krstić, J., Gabrovska, M., Radonjić, V., Nikolova, D., Lončarević, D., Jovanović, D., 2017. Supported Nickel-Based Catalysts for Partial Hydrogenation of Edible Oils, in: New Advances in Hydrogenation Processes - Fundamentals and Applications. InTech. https://doi.org/10.5772/66967

Stiles, B., Koch, T.A., 1995. Catalyst Manufacture, 2nd ed. M. Dekker, New York.

Sulman, M.G., 2000. Effects of ultrasound on catalytic processes. Russ. Chem. Rev. 69, 165–177. https://doi.org/10.1070/RC2000v069n02ABEH000543

Sulmonetti, T.P., Pang, S.H., Claure, M.T., Lee, S., Cullen, D.A., Agrawal, P.K., Jones, C.W., 2016. Vapor phase hydrogenation of furfural over nickel mixed metal oxide catalysts derived from layered double hydroxides. Appl. Catal. A Gen. 517, 187–195. https://doi.org/10.1016/j.apcata.2016.03.005

Suslick, K., Casadonte, D., Doktycz, S., 1989. The effects of ultrasound on nickel and copper powders. Solid State Ionics 32–33, 444–452. https://doi.org/10.1016/0167-2738(89)90254-3

Suslick, K.S., 1990. Sonochemistry. Science (80-.). 247, 1439–1445.

Suslick, K.S., 1989. The chemical effects of ultrasound. Sci. Am. 260, 80–86.

Suslick, K.S., Casadonte, D.J., 1987. Heterogeneous sonocatalysis with nickel powder. J. Am. Chem. Soc. 109, 3459–3461. https://doi.org/10.1021/ja00245a047

Suslick, K.S., Crum, L.A., 1997. Sonochemistry and Sonoluminescence, in: Crocker, M.J. (Ed.), Encyclopedia of Acoustics. Wiley-Interscience, New York, pp. 271–282.

Suslick, K.S., Didenko, Y., Fang, M.M., Hyeon, T., Kolbeck, K.J., McNamara, W.B., Mdleleni, M.M., Wong, M., 1999a. Acoustic cavitation and its chemical consequences. Philos. Trans. R. Soc. A Math. Phys. Eng. Sci. 357, 335–353. https://doi.org/10.1098/rsta.1999.0330

Suslick, K.S., Doktycz, S.J., 1990. Effects of ultrasound on surfaces and solids. Adv. Sonochemistry 1, 187–230.

Suslick, K.S., Doktycz, S.J., Flint, E.B., 1990. On the origin of sonoluminescence and sonochemistry. Ultrasonics 28, 280–290. https://doi.org/10.1016/0041-624X(90)90033-K

Suslick, K.S., Fang, M.M., Hyeon, T., Mdleleni, M.M., 1999b. Applications of Sonochemistry to Materials Synthesis, in: Sonochemistry and Sonoluminescence. Springer Netherlands, Dordrecht, pp. 291–320. https://doi.org/10.1007/978-94-015-9215-4_24

Suslick, K.S., Hammerton, D.A., Cline, D.E., 1986. The sonochemical hot spot. J. Am. Chem. Soc. 108, 5641–5645. https://doi.org/10.1021/ja00278a055

Suslick, K.S., Hyeon, T., Fang, M., 1996. Nanostructured Materials Generated by High-Intensity Ultrasound: Sonochemical Synthesis and Catalytic Studies. Chem. Mater. 8, 2172–2179. https://doi.org/10.1021/cm960056l

Suslick, K.S., Nyborg, W.L., 1990. Ultrasound: Its Chemical, Physical and Biological Effects. J. Acoust. Soc. Am. 87, 919–920. https://doi.org/10.1121/1.398864

Suslick, K.S., Price, G.J., 1999. Applications of ultrasound to materials chemistry. Annu. Rev. Mater. Sci. 29, 295–326. https://doi.org/10.1146/annurev.matsci.29.1.295

Syuhada, A., Ameen, M., Azizan, M.T., Aqsha, A., Yusoff, M.H.M., Ramli, A., Alnarabiji, M.S., Sher, F., 2021. In-situ hydrogenolysis of glycerol using hydrogen produced via aqueous phase reforming of glycerol over sonochemically synthesized nickel-based nano-catalyst. Mol. Catal. 514, 111860. https://doi.org/10.1016/j.mcat.2021.111860

Szöllösi, G., Török, B., Szakonyi, G., Kun, I., Bartók, M., 1998. Ultrasonic irradiation as activity and selectivity improving factor in the hydrogenation of cinnamaldehyde over Pt/SiO_2 catalysts. Appl. Catal. A Gen. 172, 225–232. https://doi.org/10.1016/S0926-860X(98)00132-X

Tahari, M.N.A., Yarmo, M.A., 2014. Adsorption of CO_2 on silica dioxide catalyst impregnated with various alkylamine. AIP Conf. Proc. 1614, 334–341. https://doi.org/10.1063/1.4895218

Takahashi, R., Sato, S., Tomiyama, S., Ohashi, T., Nakamura, N., 2007. Pore structure control in Ni/SiO_2 catalysts with both macropores and mesopores. Microporous Mesoporous Mater. 98, 107–114. https://doi.org/10.1016/j.micromeso.2006.08.027

Tamaru, Y. (Ed.), 2005. Modern Organonickel Chemistry. Wiley-VCH Verlag GmbH & Co. KGaA, Weinheim, FRG. https://doi.org/10.1002/3527604847

Tao, Q., Reddy, B.J., He, H., Frost, R.L., Yuan, P., Zhu, J., 2008. Synthesis and infrared spectroscopic characterization of selected layered double hydroxides containing divalent Ni and Co. Mater. Chem. Phys. 112, 869–875. https://doi.org/10.1016/j.matchemphys.2008.06.060

Tasker, S.Z., Standley, E.A., Jamison, T.F., 2014. Recent advances in homogeneous nickel catalysis. Nature 509, 299–309. https://doi.org/10.1038/nature13274

Thirunavukarasu, N., Panda, R.C., 2015. Modeling, identification, and control for the production of glycerol by the hydrolysis of tallow. Rev. Chem. Eng. 31. https://doi.org/10.1515/revce-2014-0047

Thommes, M., Kaneko, K., Neimark, A. V., Olivier, J.P., Rodriguez-Reinoso, F., Rouquerol, J., Sing, K.S.W., 2015. Physisorption of gases, with special reference to the evaluation of surface area and pore size distribution (IUPAC Technical Report). Pure Appl. Chem. 87, 1051–1069. https://doi.org/10.1515/pac-2014-1117

Thunyaratchatanon, C., Jitjamnong, J., Luengnaruemitchai, A., Numwong, N., Chollacoop, N., Yoshimura, Y., 2016. Influence of Mg modifier on cis-trans selectivity in partial hydrogenation of biodiesel using different metal types. Appl. Catal. A Gen. 520, 170–177. https://doi.org/10.1016/j.apcata.2016.04.019

Thyssen, V. V., Maia, T.A., Assaf, E.M., 2015. Cu and Ni Catalysts Supported on γ-Al_2O_3 and SiO_2 Assessed in Glycerol Steam Reforming Reaction. J. Braz. Chem. Soc. 26, 22–31. https://doi.org/10.5935/0103-5053.20140209

Thyssen, V.V., Georgetti, F., Assaf, E.M., 2017. Influence of MgO content as an additive on the performance of Ni/MgO SiO_2 catalysts for the steam reforming of glycerol. Int. J. Hydrogen Energy 42, 16979–16990. https://doi.org/10.1016/j.ijhydene.2017.05.180

Tian, X., Yin, C., Lv, D., Wang, P., Liu, G., 2018. Effect of Catalyst Deactivation on the Energy Consumption of Gasoline–Diesel Hydrotreating Process. Energy & Fuels 32, 10879–10890. https://doi.org/10.1021/acs.energyfuels.8b02442

Tiong, T.J., Chandesa, T., Yap, Y.H., 2017a. Comparison of sonochemiluminescence images using image analysis techniques and identification of acoustic pressure fields via simulation. Ultrason. Sonochem. 36, 78–87. https://doi.org/10.1016/j.ultsonch.2016.11.003

Tiong, T.J., Liew, D.K.L., Gondipon, R.C., Wong, R.W., Loo, Y.L., Lok, M.S.T., Manickam, S., 2017b. Identification of active sonochemical zones in a triple frequency ultrasonic reactor via physical and chemical characterization techniques. Ultrason. Sonochem. 35, 569–576. https://doi.org/10.1016/j.ultsonch.2016.04.029

Torres-Mancera, P., Ancheyta, J., Martínez, J., 2018. Deactivation of a hydrotreating catalyst in a bench-scale continuous stirred tank reactor at different operating conditions. Fuel 234, 326–334. https://doi.org/10.1016/j.fuel.2018.06.122

Toshtay, K., Auyezov, A.B., Bizhanov, Z.A., Yeraliyeva, A.T., Toktasinov, S.K., Kudaibergen, B., Nurakyshev, A., 2014. Effect of Catalyst Preparation on the Selective Hydrogenation of Vegetable Oil Over Low Percentage Pd/Diatomite Catalysts. Eurasian Chem. J. 17, 33. https://doi.org/10.18321/ectj192

Tyson, W.R., Miller, W.A., 1977. Surface free energies of solid metals: Estimation from liquid surface tension measurements. Surf. Sci. 62, 267–276. https://doi.org/10.1016/0039-6028(77)90442-3

Uchida, T., Kikuchi, T., 2013. Ultrasonic power measurement by calorimetric method using water as heating material, in: 2013 IEEE International Ultrasonics Symposium (IUS). IEEE, pp. 1657–1660. https://doi.org/10.1109/ULTSYM.2013.0422

van Eijk Van Voorthuijsen, J.J.B., Franzen, P., 2010. Structure and properties of compounds formed during the preparation of nickel-on-silica catalysts. Recl. des Trav. Chim. des Pays-Bas 70, 793–812. https://doi.org/10.1002/recl.19510700906

van Haasterecht, T., Swart, M., de Jong, K.P., Bitter, J.H., 2016. Effect of initial nickel particle size on stability of nickel catalysts for aqueous phase reforming. J. Energy Chem. 25, 289–296. https://doi.org/10.1016/j.jechem.2016.01.006

Vargas, E., Romero-Sáez, M., Denardin, J.C., Gracia, F., 2016. The ultrasound-assisted synthesis of effective monodisperse nickel nanoparticles: magnetic characterization and its catalytic activity in CO_2 methanation. New J. Chem. 40, 7307–7310. https://doi.org/10.1039/C6NJ01574C

Vásquez, M.C., Silva, E.E., Castillo, E.F., 2017. Hydrotreatment of vegetable oils: A review of the technologies and its developments for jet biofuel production. Biomass and Bioenergy 105, 197–206. https://doi.org/10.1016/j.biombioe.2017.07.008

Vavra, C., Koseoglu, S.S., 1994. Catalyst Removal from Hydrogenated Oils Using Membrane Technology, in: Developments in Food Engineering. Springer US, Boston, MA, pp. 683–685. https://doi.org/10.1007/978-1-4615-2674-2_221

Vedrine, J.C., Hollinger, G., Tran Minh Duc, 1978. Investigations of antigorite and

nickel supported catalysts by x-ray photoelectron spectroscopy. J. Phys. Chem. 82, 1515–1520. https://doi.org/10.1021/j100502a011

Veldsink, J.W., Bouma, M.J., Schöön, N.H., Beenackers, A.A.C.M., 1997. Heterogeneous Hydrogenation of Vegetable Oils: A Literature Review. Catal. Rev. 39, 253–318. https://doi.org/10.1080/01614949709353778

Venault, L., Moisy, P., Nikitenko, S.I., Madic, C., 1997. Kinetics of nitrous acid formation in nitric acid solutions under the effect of power ultrasound. Ultrason. Sonochem. 4, 195–204. https://doi.org/10.1016/S1350-4177(97)00010-2

Vidal, L., Gharzouni, A., Rossignol, S., 2016. Alkaline Silicate Solutions: An Overview of their Structure, Reactivity, and Applications, in: Handbook of Sol-Gel Science and Technology. Springer International Publishing, Cham, pp. 1–24. https://doi.org/10.1007/978-3-319-19454-7_88-1

Vizcaíno, A.J., Carrero, A., Calles, J.A., 2009. Ethanol steam reforming on Mg- and Ca-modified Cu–Ni/SBA-15 catalysts. Catal. Today 146, 63–70. https://doi.org/10.1016/j.cattod.2008.11.020

Vuyyuru, K.R., Pant, K.K., Krishnan, V. V., Nigam, K.D.P., 2010. Recovery of Nickel from Spent Industrial Catalysts Using Chelating Agents. Ind. Eng. Chem. Res. 49, 2014–2024. https://doi.org/10.1021/ie901406e

Wang, H.-Z., Sun, L.-L., Sui, Z.-J., Zhu, Y.-A., Ye, G.-H., Chen, D., Zhou, X.-G., Yuan, W.-K., 2018. Coke Formation on Pt–Sn/Al_2O_3 Catalyst for Propane Dehydrogenation. Ind. Eng. Chem. Res. 57, 8647–8654. https://doi.org/10.1021/acs.iecr.8b01313

Wang, H., Wang, Y., 2016. Characterization of Deactivated Bio-oil Hydrotreating Catalysts. Top. Catal. 59, 65–72. https://doi.org/10.1007/s11244-015-0506-6

Wang, J., Zeng, C., 2005. Al_2O_3 Effect on the Catalytic Activity of Cu-ZnO-Al_2O_3-SiO_2 Catalysts for Dimethyl Ether Synthesis from CO2 Hydrogenation. J. Nat. Gas 14, 156–162.

Wang, T., 2004. Soybean | Processing, in: Encyclopedia of Grain Science. Elsevier, pp. 159–168. https://doi.org/10.1016/B0-12-765490-9/00160-9

Wang, W., Yang, Y., Bao, J., Chen, Z., 2009. Influence of ultrasonic on the preparation

of Ni–Mo–B amorphous catalyst and its performance in phenol hydrodeoxygenation. J. Fuel Chem. Technol. 37, 701–706. https://doi.org/10.1016/S1872-5813(10)60016-3

Wang, X., Li, L., Zhang, T., Lin, B., Ni, J., Au, C.-T., Jiang, L., 2019. Strong metal–support interactions of Co-based catalysts facilitated by dopamine for highly efficient ammonia synthesis: in situ XPS and XAFS spectroscopy coupled with TPD studies. Chem. Commun. 55, 474–477. https://doi.org/10.1039/C8CC07130F

Wang, Yongzhao, Li, X., Lv, T., Wu, R., Zhao, Y., 2018. Effect of precipitants on the catalytic performance of Pd–Cu/attapulgite clay catalyst for CO oxidation at room temperature and in humid circumstances. React. Kinet. Mech. Catal. 124, 203–216. https://doi.org/10.1007/s11144-018-1355-7

Wang, Yanbing, Lin, F., Shang, B., Peng, B., Deng, Z., 2018. Self-template synthesis of nickel silicate and nickel silicate/nickel composite nanotubes and their applications in wastewater treatment. J. Colloid Interface Sci. 522, 191–199. https://doi.org/10.1016/j.jcis.2018.03.044

Webb, P.A., Orr, C., 1997. Analytical Methods in Fine Particle Technology. Micromeritics Instrument Corporation.

Wei, C., Shixing, W., Libo, Z., Jinhui, P., Gengwei, Z., 2015. The application of ultrasound technology in the field of the precious metal. Russ. J. Non-Ferrous Met. 56, 417–427. https://doi.org/10.3103/S1067821215040215

White, R.D., Bavykin, D. V., Walsh, F.C., 2013. Morphological control of synthetic $Ni_3Si_2O_5(OH)_4$ nanotubes in an alkaline hydrothermal environment. J. Mater. Chem. A 1, 548–556. https://doi.org/10.1039/C2TA00257D

Wilke, G., 1988. Contributions to Organo-Nickel Chemistry. Angew. Chemie Int. Ed. English 27, 185–206. https://doi.org/10.1002/anie.198801851

Wise, H., 1991. Mechanisms of Catalyst Poisoning by Sulfur Species, in: Catalyst Deactivation 1991, Proceedings of the 5th International Symposium. pp. 497–504. https://doi.org/10.1016/S0167-2991(08)62676-2

Wisniak, J., 2010. The History of Catalysis. From the Beginning to Nobel Prizes. Educ. Química 21, 60–69. https://doi.org/10.1016/S0187-893X(18)30074-0

Wong, E.L., 2021. MPOC: Palm oil production to increase to 19.6 million tonnes in

2021 [WWW Document]. Edge Mark. URL https://www.theedgemarkets.com/article/mpoc-palm-oil-production-increase-196-million-tonnes-2021 (accessed 7.1.21).

Wong, F.H., Tiong, T.J., Leong, L.K., Lin, K.-S., Yap, Y.H., 2018. Effects of ZnO on Characteristics and Selectivity of Coprecipitated Ni/ZnO/Al_2O_3 Catalysts for Partial Hydrogenation of Sunflower Oil. Ind. Eng. Chem. Res. 57, 3163–3174. https://doi.org/10.1021/acs.iecr.7b04963

Wu, C., Williams, P.T., 2010a. Investigation of coke formation on Ni-Mg-Al catalyst for hydrogen production from the catalytic steam pyrolysis-gasification of polypropylene. Appl. Catal. B Environ. 96, 198–207. https://doi.org/10.1016/j.apcatb.2010.02.022

Wu, C., Williams, P.T., 2010b. A Novel Nano-Ni/SiO_2 Catalyst for Hydrogen Production from Steam Reforming of Ethanol. Environ. Sci. Technol. 44, 5993–5998. https://doi.org/10.1021/es100912w

Wu, P.-Y., Jiang, Y.-P., Zhang, Q.-Y., Jia, Y., Peng, D.-Y., Xu, W., 2016. Comparative study on arsenate removal mechanism of MgO and MgO/TiO_2 composites: FTIR and XPS analysis. New J. Chem. 40, 2878–2885. https://doi.org/10.1039/C5NJ02358K

Wu, T.Y., Guo, N., Teh, C.Y., Hay, J.X.W., 2013. Theory and fundamentals of ultrasound, in: Advances in Ultrasound Technology for Environmental Remediation. Springer Netherlands, pp. 5–12. https://doi.org/10.1007/978-94-007-5533-8_2

Wu, Y., Liu, X., Han, D., Song, X., Shi, L., Song, Y., Niu, S., Xie, Y., Cai, J., Wu, S., Kang, J., Zhou, J., Chen, Z., Zheng, X., Xiao, X., Wang, G., 2018. Electron density modulation of $NiCo_2S_4$ nanowires by nitrogen incorporation for highly efficient hydrogen evolution catalysis. Nat. Commun. 9, 1425. https://doi.org/10.1038/s41467-018-03858-w

Wulfsberg, G., 2000. Principle of oxidation-reduction reactivity with applications to chemical safety, environmental chemistry and industrial chemistry, in: Inorganic Chemistry. University Science Books, Sausalito, California, pp. 243–297.

Wurster, O.H., 1940. Hydrogenation Of Fats. Ind. Eng. Chem. 32, 1193–1199. https://doi.org/10.1021/ie50369a029

Xin, Y., Jiang, P., Yu, M., Gu, H., Li, Q., Zhang, Z., 2014. A universal route to fabricate hierarchically ordered macro/mesoporous oxides with enhanced intrinsic activity. J. Mater. Chem. A 2, 6419. https://doi.org/10.1039/c3ta15060g

Xu, L., Zhao, H., Song, H., Chou, L., 2012. Ordered mesoporous alumina supported nickel based catalysts for carbon dioxide reforming of methane. Int. J. Hydrogen Energy 37, 7497–7511. https://doi.org/10.1016/j.ijhydene.2012.01.105

Yang, J., Hu, W., Wu, Y., Dai, X., 2012. Diffusion and growth of nickel, iron and magnesium adatoms on the aluminum truncated octahedron: A molecular dynamics simulation. Surf. Sci. 606, 971–980. https://doi.org/10.1016/j.susc.2012.02.017

Yang, L., Bukhovko, M.P., Malek, A., Li, L., Jones, C.W., Agrawal, P.K., Davis, R.J., 2020. Steam reforming of ethylene over nickel based spinel oxides. Appl. Catal. A Gen. 603, 117739. https://doi.org/10.1016/j.apcata.2020.117739

Yang, M., Wu, Huanhuan, Wu, Huayi, Huang, C., Weng, W., Chen, M., Wan, H., 2016. Preparation and characterization of a highly dispersed and stable Ni catalyst with a microporous nanosilica support. RSC Adv. 6, 81237–81244. https://doi.org/10.1039/C6RA15358E

Yao, D., Yang, H., Chen, H., Williams, P.T., 2018. Co-precipitation, impregnation and so-gel preparation of Ni catalysts for pyrolysis-catalytic steam reforming of waste plastics. Appl. Catal. B Environ. 239, 565–577. https://doi.org/10.1016/j.apcatb.2018.07.075

Yap, Y.H., Lim, M.S.W., Lee, Z.Y., Lai, K.C., Jamaal, M.A., Wong, F.H., Ng, H.K., Lim, S.S., Tiong, T.J., 2018. Effects of sonication on co-precipitation synthesis and activity of copper manganese oxide catalyst to remove methane and sulphur dioxide gases. Ultrason. Sonochem. 40, 57–67. https://doi.org/10.1016/j.ultsonch.2017.06.032

Yasui, K., Tuziuti, T., Sivakumar, M., Iida, Y., 2005. Theoretical study of single-bubble sonochemistry. J. Chem. Phys. 122, 224706. https://doi.org/10.1063/1.1925607

Yeong, S.K., Idris, Z., Hassan, H.A., 2012. Palm Oleochemicals in Non-food Applications, in: Palm Oil. Elsevier, pp. 587–624. https://doi.org/10.1016/B978-0-9818936-9-3.50023-X

Young, F.R., 1999. Cavitation. Imperial College Press, London.

Yu, F.W.S., Ameen, M., Aqsha, A., Izham, M., Azizan, M.T., Sher, F., 2021. Effects of ultrasound irradiations time over Ni–Mo/γ-Al_2O_3 catalyst synthesis for 1,3-Propanediol selectively via aqueous phase reforming of glycerol. Case Stud. Chem. Environ. Eng. 3, 100096. https://doi.org/10.1016/j.cscee.2021.100096

Zhang, G., Liu, J., Xu, Y., Sun, Y., 2019. Ordered mesoporous Ni/Silica-carbon as an efficient and stable catalyst for CO_2 reforming of methane. Int. J. Hydrogen Energy 44, 4809–4820. https://doi.org/10.1016/j.ijhydene.2019.01.017

Zhang, L., Lin, J., Chen, Y., 1992. Studies of surface NiO species in NiO/SiO_2 catalysts using temperature-programmed reduction and X-ray diffraction. J. Chem. Soc. Faraday Trans. 88, 2075. https://doi.org/10.1039/ft9928802075

Zhang, Y., Zhou, W., Yu, H., Feng, T., Pu, Y., Liu, H., Xiao, W., Tian, L., 2017. Self-templated Synthesis of Nickel Silicate Hydroxide/Reduced Graphene Oxide Composite Hollow Microspheres as Highly Stable Supercapacitor Electrode Material. Nanoscale Res. Lett. 12, 325. https://doi.org/10.1186/s11671-017-2094-9

Zhao, Y., Ren, Y., Zhang, R., Zhang, L., Yu, D., Jiang, L., Elfalleh, W., 2018. Preparation of hydrogenated soybean oil of high oleic oil with supported catalysts. Food Biosci. 22, 91–98. https://doi.org/10.1016/j.fbio.2018.01.010

Zhu, J., Peng, X., Yao, L., Shen, J., Tong, D., Hu, C., 2011. The promoting effect of La, Mg, Co and Zn on the activity and stability of Ni/SiO_2 catalyst for CO_2 reforming of methane. Int. J. Hydrogen Energy 36, 7094–7104. https://doi.org/10.1016/j.ijhydene.2011.02.133

Zhuang, S., Hu, Z., Huang, L., Qin, F., Huang, Z., Sun, C., Shen, W., Xu, H., 2018. Synthesis of ZSM-5 catalysts with tunable mesoporosity by ultrasound-assisted method: A highly stable catalyst for methanol to propylene. Catal. Commun. 114, 28–32. https://doi.org/10.1016/j.catcom.2018.06.001

Zisu, B., Bhaskaracharya, R., Kentish, S., Ashokkumar, M., 2010. Ultrasonic processing of dairy systems in large scale reactors. Ultrason. Sonochem. 17, 1075–1081. https://doi.org/10.1016/j.ultsonch.2009.10.014

Appendices

I. Iodine value (IV) test

Iodine value test procedure:

a) The hydrogenation product (oil sample) was melted to liquid form, filtered with ashless filter papers to remove impurities and moisture.
b) The liquid oil sample was weighed using a digital analytical weighing scale into a conical flask, with the mass in accordance with the recommended mass for the respective IV range listed in the table below.
c) 15 ml of a cyclohexane and acetic acid mixture (1:1 v/v) was added to the liquid oil to dissolve it.
d) 25 ml of Wijs solution (iodine monochloride, ICl) was added to the conical flask, stoppered and swirled vigorously to form an intimate solution, enabling the addition reaction to take place between the C=C double bonds present in the mixture.
e) Concurrently, a control blank set was prepared following steps c – d **without** the addition of the liquid oil sample.
f) Both sets were stored in the dark for 30 min at ambient conditions.
g) The flasks were titrated with a 0.1 M sodium thiosulphate solution until the mixture turned pale yellow.
h) 1 – 2 ml of 1 % starch solution was added to the pale-yellow mixture to form a blue-black solution due to the formation of tri-iodide complex, which served as an endpoint indicator.

i) The titration was continued until the blue-black solution turned colourless, an indication of the total reduction of I_2 and I_3^- species into I^-.

Table S1: Recommended mass of liquid oil samples for their respective expected iodine value ranges.

Iodine value range	Sample mass (g)
< 3	10 – 10
3	8.4613 – 10.576
5	5.0770 – 6.3460
10	2.5384 – 3.1730
20	0.8461 – 1.5865
40	0.6346 – 0.7935
60	0.4321 – 0.5288
80	0.3175 – 0.3969
90	0.2822 – 0.3528
100	0.2540 – 0.3175
110	0.2309 – 0.2886
120	0.2117 – 0.2646
130	0.1954 – 0.2442
140	0.1814 – 0.2268
150	0.1693 – 0.2116
160	0.1587 – 0.1984
170	0.1494 – 0.1868
180	0.1411 – 0.1764
190	0.1337 – 0.1671
200	0.1270 – 0.1587

A sample calculation of the iodine value for the hydrogenated oil sample obtained at 30 min for the hydrogenation run using sample A (Chapter 5) is demonstrated below with the following formula:

$$\text{Iodine value} = \frac{(\text{B} - \text{S})\text{x N x } 12.691}{\text{mass of sample, g}}$$

where:

B is the volume of titrant of blank set (ml); *S* is the volume of titrant of sample set (ml); *N* is the normality of the sodium thiosulphate solution.

$$\text{Iodine value} = \frac{(43.6 - 21.7)\text{x } 0.1 \text{ x } 12.691}{0.31}$$

$$\text{Iodine value} = 89.66$$

II. Gas chromatography

GC sample preparation:

a) The hydrogenation product (oil sample) was melted to liquid form, filtered with ashless filter papers to remove impurities and moisture.
b) 4 ml of 0.5 M potassium hydroxide in absolute methanol (KOH/MeOH) was added to approximately 0.2 ml of liquid oil sample and heated in reflux at 100 °C for 5 min.
c) 1.6 ml of aqueous hydrochloric acid in absolute methanol (HCL/MeOH, 4:1 v/v) was added to the reflux mixture and heated in reflux at 100 °C for another 15 min.
d) Heating is terminated and the reflux mixture is cooled.
e) 5 ml of deionised water and 10 ml of dichloromethane were added into the mixture.
f) The organic layer of the mixture was separated and extracted using a separatory funnel, which was further used for the GC analysis.

GC sample calculation:

A sample calculation of the fatty acids composition for the hydrogenated oil sample obtained at 30 min for the hydrogenation run using sample A (Chapter 5) is demonstrated below. Each retention time noted by the GC corresponds to a particular type of fatty acid, allowing one to determine the relative composition of each fatty acid via the peak area it occupies.

Table S2: Sample calculation of the fatty acids composition obtained for the hydrogenated oil sample at 30 min.

Retention time (min)	**Fatty acid**	**Peak area**	**Composition (%)**
22	C16:0	6848.7	7.15
30	C18:0	19908.3	20.78
32	*Trans*-C18:1	8465.1	8.83
33 – 34	*Cis*-C18:1	34144.1	35.63
39	C18:2	26462.4	27.61
40	C18:3	0	0
	TOTAL	**95828.6**	**100**

As an example, the relative percentage of C18:0 in this particular sample was calculated as follows:

$$\text{C18: 0 (\%)} = \frac{19908.3}{95828.6} \text{ x } 100$$

$$\text{C18: 0 (\%)} = 20.78\ \%$$

III. Deconvoluted TPR graphs

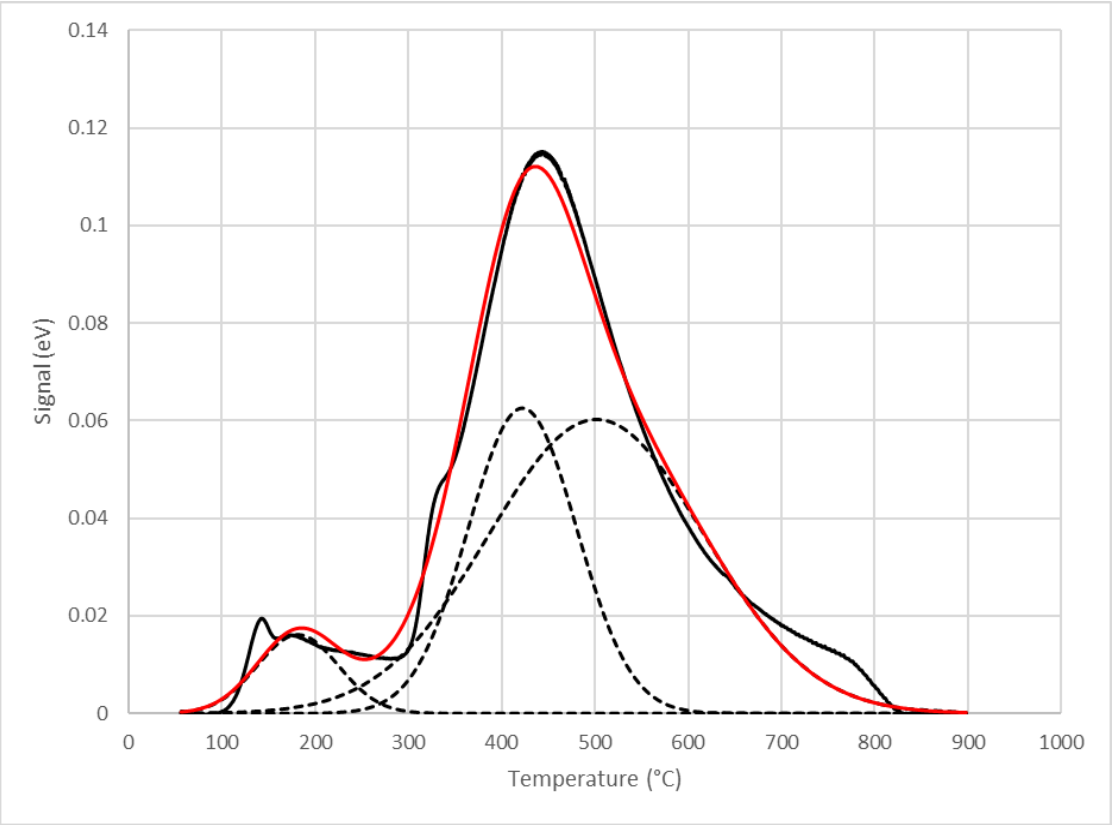


Figure S1: Deconvoluted TPR reduction curves for sample D.

Note: black solid lines represent raw curves; red solid lines represent fitted curves.

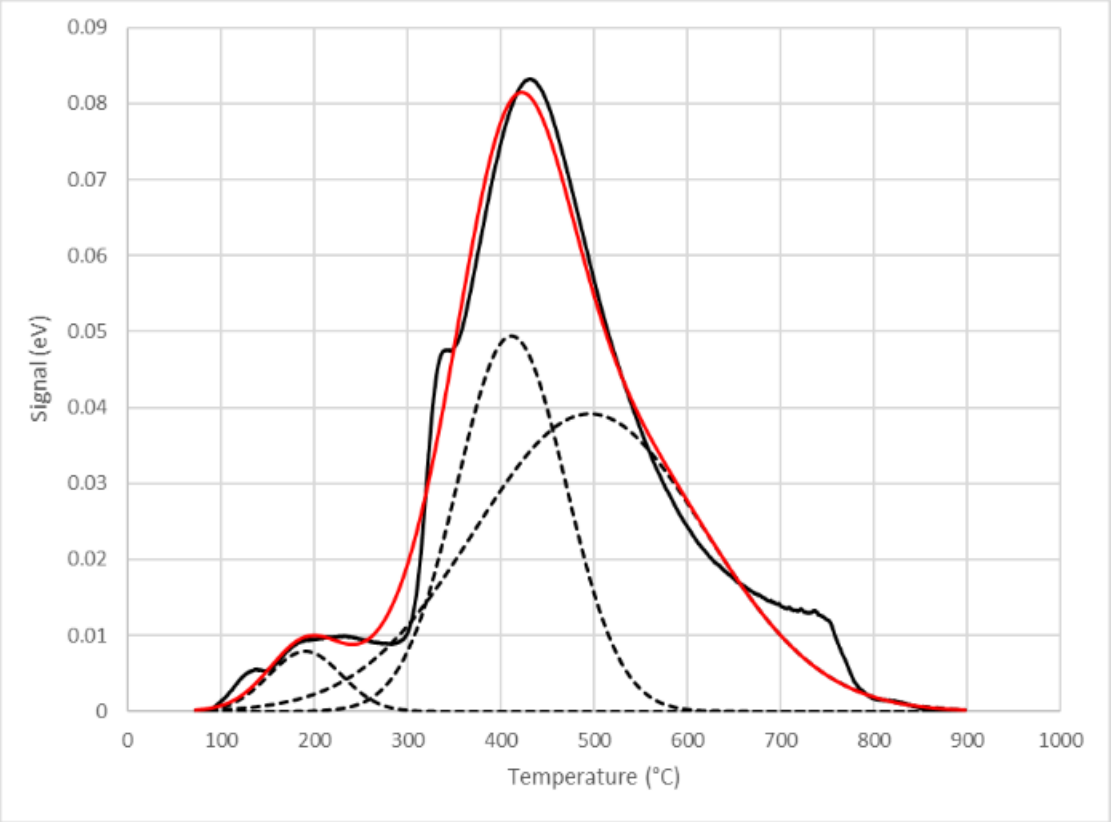


Figure S2: Deconvoluted TPR reduction curves for sample D_US20.

Note: black solid lines represent raw curves; red solid lines represent fitted curves.

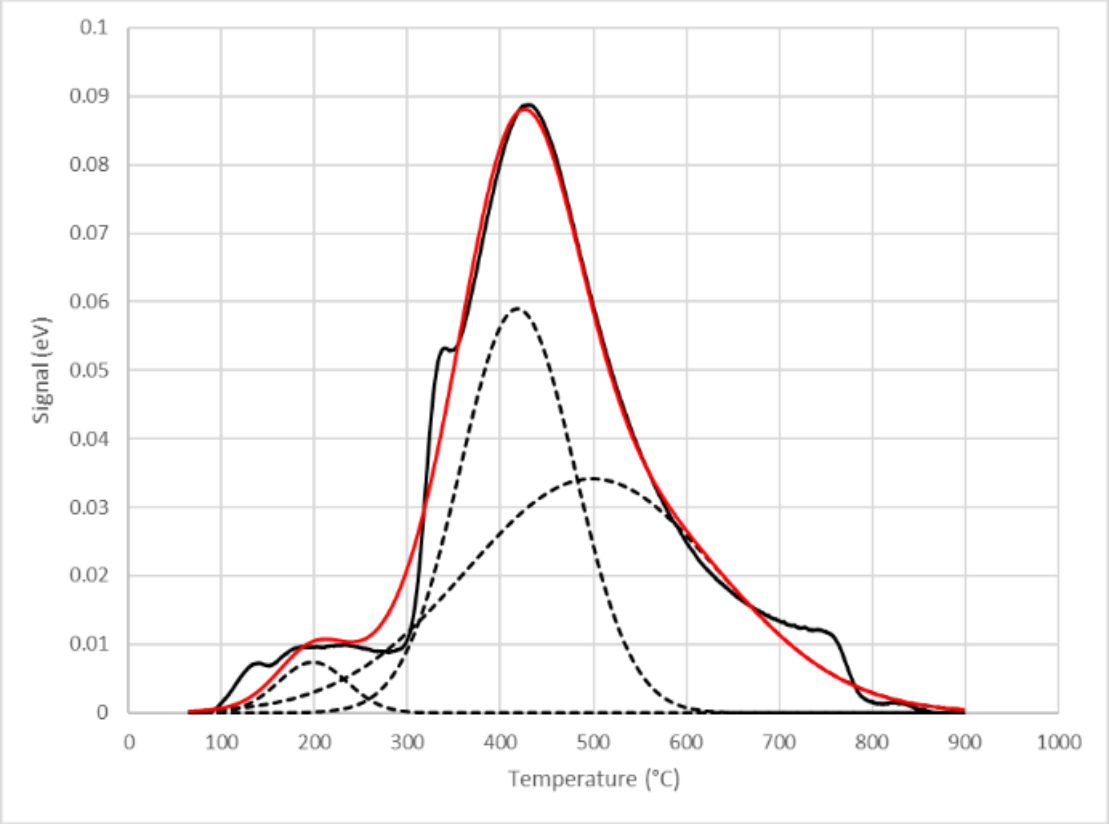


Figure S3: Deconvoluted TPR reduction curves for sample D_US30.

Note: black solid lines represent raw curves; red solid lines represent fitted curves.

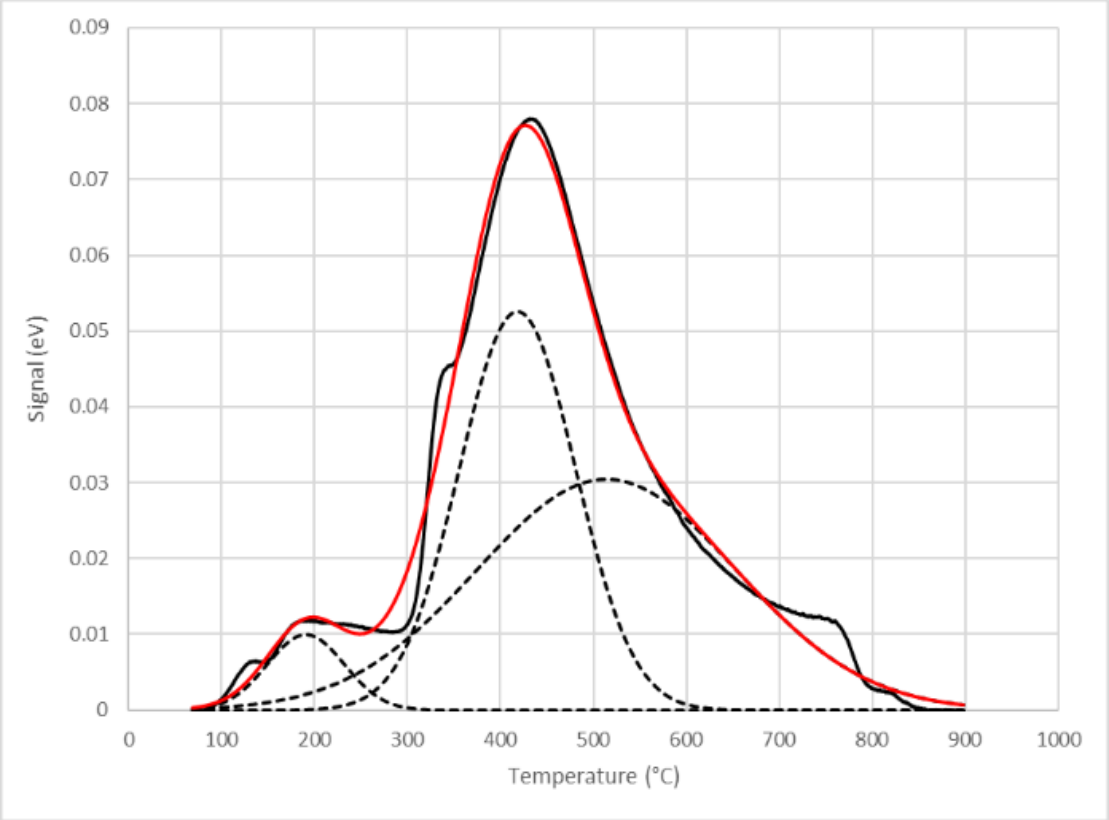


Figure S4: Deconvoluted TPR reduction curves for sample D_US40.

Note: black solid lines represent raw curves; red solid lines represent fitted curves.

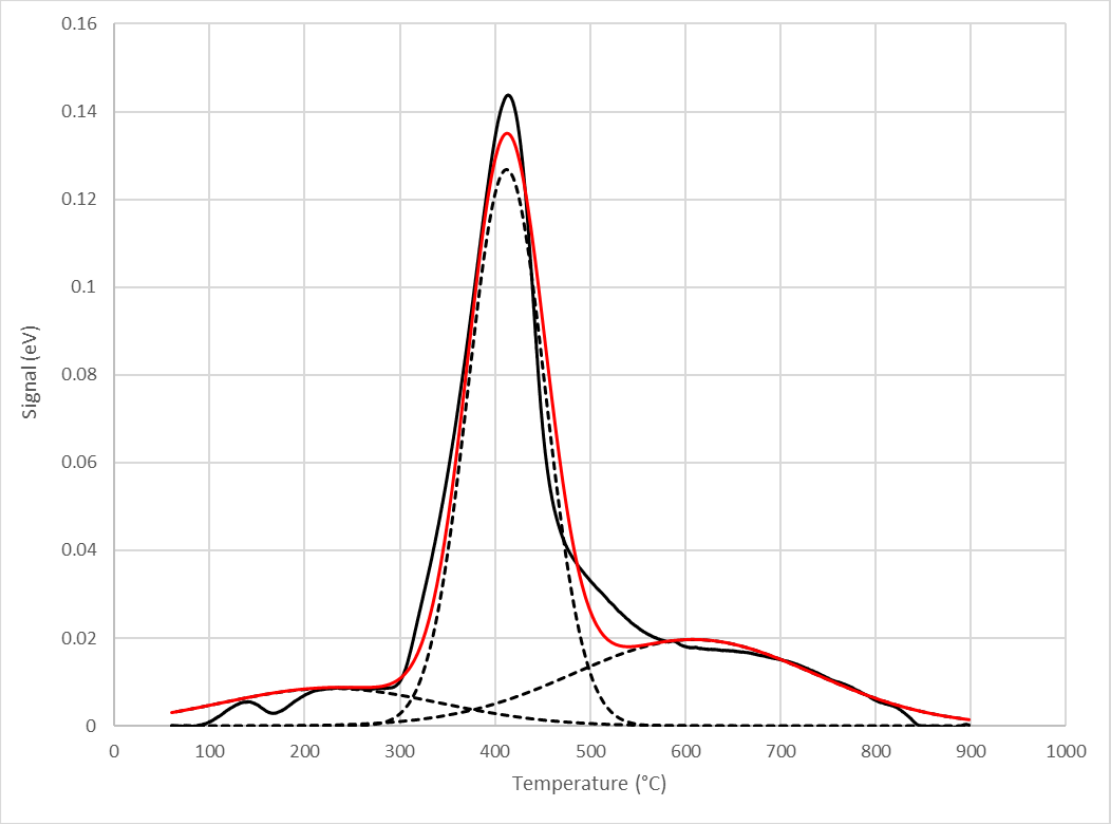


Figure S5: Deconvoluted TPR reduction curves for sample B.

Note: black solid lines represent raw curves; red solid lines represent fitted curves.

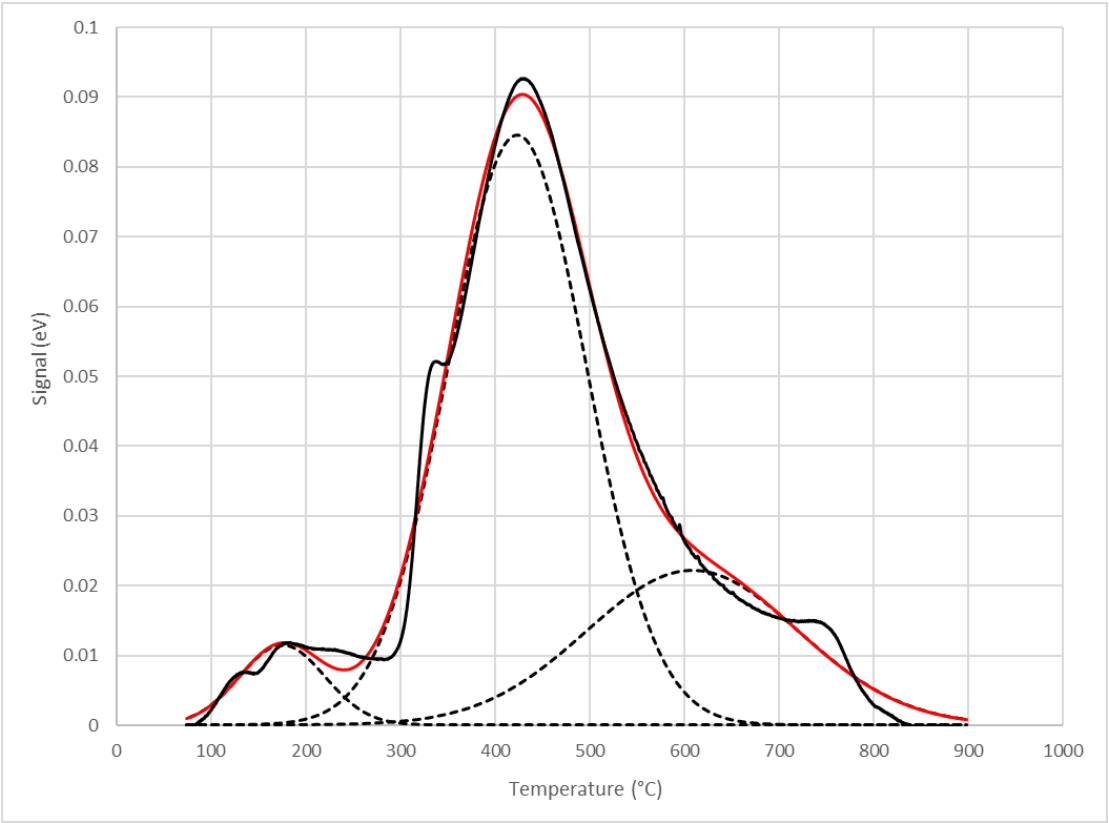


Figure S6: Deconvoluted TPR reduction curves for sample C.

Note: black solid lines represent raw curves; red solid lines represent fitted curves.

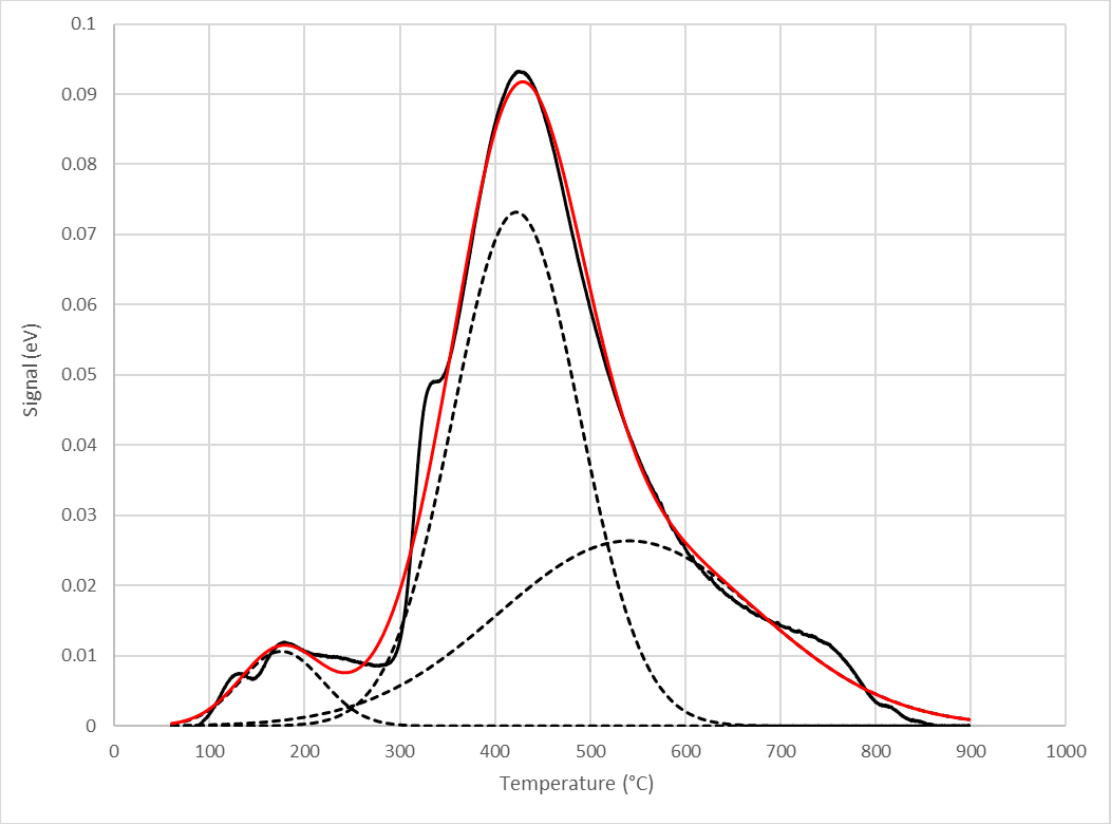


Figure S7: Deconvoluted TPR reduction curves for sample D.

Note: black solid lines represent raw curves; red solid lines represent fitted curves.